UNIL | Université de Lausanne

Unicentre
CH-1015 Lausanne
http://serval.unil.ch

Year : 2021

Geophysical Methods for Field-Scale Characterization of Soil Structure

Romero-Ruiz Alejandro

Romero-Ruiz Alejandro, 2021, Geophysical Methods for Field-Scale Characterization of Soil Structure

Originally published at : Thesis, University of Lausanne

Posted at the University of Lausanne Open Archive http://serval.unil.ch
Document URN : urn:nbn:ch:serval-BIB_9968EFF0673A7

Droits d'auteur
L'Université de Lausanne attire expressément l'attention des utilisateurs sur le fait que tous les documents publiés dans l'Archive SERVAL sont protégés par le droit d'auteur, conformément à la loi fédérale sur le droit d'auteur et les droits voisins (LDA). A ce titre, il est indispensable d'obtenir le consentement préalable de l'auteur et/ou de l'éditeur avant toute utilisation d'une oeuvre ou d'une partie d'une oeuvre ne relevant pas d'une utilisation à des fins personnelles au sens de la LDA (art. 19, al. 1 lettre a). A défaut, tout contrevenant s'expose aux sanctions prévues par cette loi. Nous déclinons toute responsabilité en la matière.

Copyright
The University of Lausanne expressly draws the attention of users to the fact that all documents published in the SERVAL Archive are protected by copyright in accordance with federal law on copyright and similar rights (LDA). Accordingly it is indispensable to obtain prior consent from the author and/or publisher before any use of a work or part of a work for purposes other than personal use within the meaning of LDA (art. 19, para. 1 letter a). Failure to do so will expose offenders to the sanctions laid down by this law. We accept no liability in this respect.

UNIL | Université de Lausanne

Faculté des géosciences et de l'environnement
Institut des sciences de la Terre

Geophysical Methods for Field-Scale Characterization of Soil Structure

Thèse de doctorat

Présentée à la
Faculté des géosciences et de l'environnement
Institut des sciences de la Terre
de l'Université de Lausanne
par

Alejandro Romero-Ruiz

Diplôme (M.Sc.) en Géophysique Appliquée
Division des Sciences de la Terre
CICESE Ensenada, Mexico

Jury

Prof. Dr. Dominique Arlettaz, président du jury
Prof. Dr. Niklas Linde, directeur de thèse
Prof. Dr. Dani Or, codirecteur de thèse
Prof. Dr. Thomas Keller, Expert
Dr. James Irving, Expert
Dr. Damien Jougnot, Expert

Lausanne, 2021

UNIL | Université de Lausanne
Faculté des géosciences et de l'environnement
bâtiment Géopolis bureau 4631

IMPRIMATUR

Vu le rapport présenté par le jury d'examen, composé de

Président de la séance publique :	M. le Professeur Dominique Arlettaz
Président du colloque :	M. le Professeur Dominique Arlettaz
Directeur de thèse :	M. le Professeur Niklas Linde
Co-directeur de thèse :	M. le Professeur Dani Or
Expert interne :	M. le Docteur James Irving
Expert externe :	M. le Docteur Thomas Keller
Expert externe :	M. le Docteur Damien Jougnot

Le Doyen de la Faculté des géosciences et de l'environnement autorise l'impression de la thèse de

Monsieur Alejandro ROMERO RUIZ

Titulaire d'un Master en sciences de la Terre
du Centro de Investigación Científica y de Educación Superior

intitulée

Geophysical Methods for Field-Scale Characterization of Soil Structure

Lausanne, le 26 mars 2021

Pour le Doyen de la Faculté des géosciences et de l'environnement

Professeur Dominique Arlettaz

Acknowledgements

It is with immense joy that I use this space to express my gratitude to the people that made it possible for me to swimmingly transit my PhD journey. It is because of these people that the journey, that now reaches its end, has been one of the most rewarding experiences of my life.

Special thanks go to my PhD supervisor Niklas Linde, my co-supervisor Dani Or and our close collaborator Thomas Keller. I thank them for their ever present support, guidance and patience during all my PhD days.

I am very grateful to Niklas. This thesis work would not have been possible without his tireless support and motivation. I thank him for offering me the opportunity to join his research group at the University of Lausanne. He dealt with the tough labor of guiding me to become a better scientist. I admire his evident expertise in countless research topics and it was a big pleasure (and luck) for me to work along his side. During all these years, I cannot find an example of a question or a problem he would not have a useful advise for. Knowing that I had his support gave me the confidence to move forward in hard times during my PhD. I thank him as well for always encouraging me to enjoy life, family and friends. It is hard to find the words to express my gratitude towards him.

I am lucky to have Dani as my thesis co-supervisor. Clearly, he has an outstanding vision about important soil-science related unresolved scientific problems and their prospective solutions. A good part of the scientific outputs of this thesis derived from discussions pivoting on his ideas. I thank him for always challenging me to think "outside the box" and to believe that I had the potential to do better. I further express my gratitude to him for offering financial support for my several visits to ETHZ, field trips to Agroscope, field material, scientific conferences and PhD schools.

Thomas was an excellent complement for improving my PhD research. I thank him for his always friendly manners to provide feedback on my PhD research. He would often rise "uncomfortable" comments that would force me to improve, to widen my perspective and reformulate my approach to explain or address a problem. Also, I am grateful to him for supporting our geophysical monitoring campaigns at the SSO.

I would like to thank those colleagues that were involved in activities related to data collection for my PhD. I thank Ludovic Baron from his enthusiastic help in designing, testing and placing our geophysical monitoring systems on the field. I owe it to him to be able to posses the interesting field datasets presented in this thesis. Dani Breitenstein is thanked for collecting field data set previous to the beginning of my PhD. I thank staff of Agroscope for offering technical and logistic support at the SSO, including Viktor Stadelmann, Celina Steffani, Selina Lutz, Rebecca Schneiter and Valerio Volpe. I am grateful to Simón Lissa for his help in field monitoring campaigns. I thank Damien Jougnot for providing his hydrogeophysical modeling

codes from which the part of the modeling work presented in the Chapter 4 of this thesis was build upon.

I am very happy to thank all my fellow PhD students and post-docs for being part of this journey. Specially, I thank my officemates Andrew Greengood and Santi Solazzi. The list is long and I do not want to risk missing a name so I extend my sincere gratitude to all of them without mentioning specific names.

My friends have been a very important pillar supporting my well-being during my PhD years. I thank my dear international friends Serdar, Nico, Solenne, Lissa, Santi, Sam and Julien for their friendship, for sharing amazing things about their cultures and for helping opening my mind. I am very grateful to my Mexican friends Mauro, Amira, Silver, Fer, Adrian, Ileana, Leslie and Erick for spicing up my life in Switzerland with their always joyful approach to life. My long-term friends Daniel, Pedro, Memo, David, David, Joseli and Diego for being close despite the physical distance and for making me feel at home again whenever I visit Mexico. I thank Andrea for being present and supportive in several good and bad moments during a good part of my PhD.

Finally, I express my gratitude to my family. I thank my parents Margarita and José and my siblings Nalle and Ed for giving me their love and support during my entire life. They are the most important people in my life.

Lausanne, 4 February 2021 Alejandro

Contents

Acknowledgements **i**

List of figures **vii**

List of tables **ix**

Résumé **xi**

Abstract **xiii**

1 Introduction **1**
1.1 Preamble . . . 1
1.2 Characterization of soil structure: Traditional methods . . . 5
1.2.1 Soil structure: metrics and challenges . . . 5
1.2.2 Soil core sampling . . . 6
1.2.3 *In-situ* soil measurements . . . 8
1.2.4 *In-situ* visual evaluation . . . 9
1.3 Geophysical methods for soil structure characterization . . . 10
1.3.1 Seismic methods . . . 11
1.3.2 DC-resistivity . . . 13
1.4 Conceptual model of soil structure . . . 15
1.5 Modeling tools for soil structure characterization . . . 17
1.5.1 Flow and transport modeling . . . 17
1.5.2 Pedophysical modeling . . . 18
1.5.3 Geophysical forward modeling . . . 19
1.6 The Soil Structure Observatory . . . 19
1.7 Objectives and outline . . . 22

2 A review of geophysical methods for soil structure characterization **25**
2.1 Introduction . . . 26
2.2 Geophysics for soil structure characterization: Concepts and challenges . . . 29
2.3 Geophysical methods in soil science . . . 33
2.3.1 DC-resistivity method and Electromagnetic Induction . . . 34
2.3.2 Induced Polarization . . . 39
2.3.3 Ground-Penetrating Radar . . . 40
2.3.4 Seismic methods . . . 43
2.3.5 Other geophysical methods . . . 46
2.4 Opportunities for geophysical soil structure characterization . . . 47
2.4.1 Petrophysical models of a structured soil: Pedophysical models . . . 47

2.4.2 Combination of geophysical measurement methods 50
2.4.3 Survey design and spatial scaling of soil structural features 51
2.4.4 Soil dynamic responses and hydrogeophysical modeling 52
2.4.5 Summary 55
2.5 Conclusions 55
2.6 Supplemental material 57

3 Seismic signatures reveal persistence of soil compaction 59
3.1 Introduction 60
3.2 Elastic properties of structured partially-saturated soil 61
3.2.1 Elastic properties of soil aggregates and soil frame 64
3.2.2 Elastic properties of the water-air fluid mixture 67
3.2.3 Elastic properties of structured partially-saturated soil 68
3.3 Field monitoring of seismic data 68
3.4 Effects of compaction and water content on measured seismic signatures . . . 70
3.4.1 S-wave and P-wave slowness variations with soil water content 71
3.4.2 Pedophysical parametrization of structured soil and treatments at the SSO 72
3.4.3 Pedophysical predictions of seismic velocities in soil 75
3.5 Discussion 77
3.6 Conclusions 81
3.7 Supplemental material 81

4 Lasting effects of soil compaction on soil water regime detected by geoelectrical monitoring 91
4.1 Introduction 92
4.2 Soil-structure-informed hydrogeophysical modeling 94
4.2.1 Pedophysical model of electrical conductivity 94
4.2.2 Hydrological process modeling in structured soils 97
4.2.3 Coupled hydrogeophysical modeling 101
4.2.4 Forward modeling of water flow and heat transfer 101
4.2.5 Inverse modeling of soil electrical data 101
4.3 Methods 103
4.3.1 Data monitoring 103
4.3.2 Impact of soil structure on measured apparent resistivity and soil water storage 105
4.3.3 Modeling of hydrogeophysical data 107
4.3.4 MCMC inversion of electrical properties 110
4.4 Results 110
4.4.1 Inverted electrical properties 110
4.4.2 Water content dynamics 112
4.4.3 Apparent electrical resistivity 112
4.5 Discussion 113
4.5.1 Long-term compaction effects revealed by geoelectrical data 113
4.5.2 Soil structure driven water dynamics captured by DC-resistivity data . . 116
4.5.3 Influence of compaction on water partitioning between soil and atmosphere 119

4.6 Conclusions 121

5 Conclusions and Outlook **123**
5.1 Conclusions 125
5.2 Outlook 126

Bibliography **151**

A Appendix A: Long-term soil structure observatory for monitoring post-compaction evolution of soil structure **153**

B Appendix B: Editor's Vox **171**

Curriculum Vitae **177**

List of Figures

1.1 Map of global annual ecosystem services and their economic values. 2
1.2 Conceptual representation of soil structure as affected by tillage and map of global tillage operations. 4
1.3 Metrics of non-compacted soil structure relative to compacted soil structure. . 6
1.4 Soil core sampling. 7
1.5 Examples of in-situ measurements of soil properties 8
1.6 Examples of visual evaluation methods. 10
1.7 Seismic refraction imaging. 12
1.8 DC-resistivity surveying. 14
1.9 Conceptual model of soil structure for predicting macroscopic geophysical properties. 15
1.10 Hydraulic conductivity function of structured soils as the superposition of soil matrix and soil structural pores. 17
1.11 Illustration of experimental setups for seismic and geoelectrical monitoring. . . 20
1.12 Summary of periods for geophysical monitoring 21

2.1 Schematic representation of soil structure along a transect. 30
2.2 Soil pore structure detectable by micro computed tomography for compacted and uncompacted bare soil. 31
2.3 Relationship between the inverse of the electrical formation factor and porosity in Archie's law. 35
2.4 Literature examples of DC-resistivity measurements for soil structure characterization. 37
2.5 GPR spatial identification of compacted zones in a compaction field experiment. 42
2.6 Literature examples of seismic methods for soil structure characterization. . . . 45
2.7 Diagram illustrating a bimodal pore network model. 48
2.8 Relative change in apparent resistivity as a function of saturated macroporosity. 49
2.9 Example of time-lapse changes in electrical resistivity for soil structure characterization. 54
2.10 Sketch of how to use geophysical methods for soil structure characterization. . 56

3.1 Conceptualization of soil structural elements and their integration within a self-consistent pedophysical model of macroscopic elastic properties. 63
3.2 Schematic representation of the soil compaction experiment at the SSO illustrating the seismic monitoring layout. 70
3.3 Time-series of estimated S-wave slowness and water content for full compacted ley, non-compacted ley, and full compacted bare soil. 71
3.4 Scatter plot of (a) P-wave and (b) S-wave slowness as a function of water content for all soil treatments. 72

3.5 Time series of modeled and measured P-wave and S-wave velocities. 76
3.6 Scatter plot of modeled and measured P-wave and S-wave velocities as functions of soil water content. 77
3.7 Dynamics of bulk density data and penetration resistance data measured at the SSO. 79
3.8 Comparison of the volumetric strain derived from bulk density data and the volumetric strain estimated from the pedophysical model of seismic data. . . . 80
3.9 Comparison of the volumetric content (WC) measured in block A and block C at the SSO. 82
3.10 Examples of seismic data recorded by the geophones at the six nearest offsets at arbitrary dates. 84
3.11 Examples of seismic data recorded by the geophones at the six nearest offsets at arbitrary dates. 85
3.12 Estimation of the depth of the first soil layer from time-lapse seismic data. . . . 87
3.13 Results of numerical modeling: comparison of true S-wave velocities versus S-wave velocities estimated from the zero-crossing method. 88

4.1 Conceptual figure of the pedophysical model of electrical properties for structured soils. 95
4.2 Flowchart for hydrogeophysical forward and inverse modeling including soil evaporation constrains. The flowchart is divided in blocks containing different modeling steps involved in the coupled model. 102
4.3 Schematic representation of the soil compaction experiment at the SSO illustrating the DC-resistivity monitoring layout. 104
4.4 Apparent electrical resistivity and soil water storage data collected for compacted and non-compacted soils. 106
4.5 Saturated hydraulic conductivity and macroporosity for compacted and non-compacted soils as a function of soil depth. 109
4.6 Results from MCMC inversion of geoelectrical data. 111
4.7 Modeled and measured dielectric constant, electrical resistivity and temperature of compacted and non-compacted ley soils. 114
4.8 Crossplots of modeled and measured apparent electrical resistivity and dielectric constant of compacted and non-compacted bare soil 115
4.9 Relative change in apparent electrical resistivity for compacted and non-compacted ley for the full monitored period. 117
4.10 Relative soil water content as a function of soil depth and time comparing compacted with non-compacted soils. 118
4.11 Measured total annual water losses in the top meter of soils and total annual water losses resulting from the Hydrus simulations. 120

5.1 Modeled and measured apparent resistivity against seismic velocities as a function of water content. 124

B.1 Illustration of tillaged and vegetated soils with different structure and functioning. 172
B.2 Schematic representation of soil structure. 173
B.3 Ponding water in compacted soils from farm fields. 174

List of Tables

3.1 Summary of the values of the parameters used for pedophysical prediction of seismic velocities of compacted and non-compacted soils. 74

4.1 Soil water retention, transport, evaporation, dielectric, electrical and other Hydrus properties considered in this study. 108

Résumé

Le sol est une ressource naturelle essentielle et le compartiment biologique le plus actif de la biosphère. Les sols sont les supports de l'agriculture et de la sylviculture, et ils abritent des processus hydrologiques qui contrôlent en grande partie la recharge des eaux souterraines. La structure ou l'architecture du sol, c'est-à-dire, la liaison et la disposition des constituants du sol entre eux, est un paramètre important pour les fonctions hydro-écologiques du sol. Malgré son importance, la structure du sol reste difficile à caractériser, en particulier à des échelles pertinentes pour les applications sur le terrain. Typiquement, la caractérisation de la structure du sol est faite à partir de mesures en laboratoire sur des échantillons de sol ou de mesures ponctuelles épisodiques, ce qui offre des perspectives limitées sur les variations spatiales et temporelles de la structure du sol. La motivation de cette thèse repose sur le besoin en techniques de caractérisation pour fournir des informations sur la structure du sol à des échelles spatiales pertinentes pour l'exploitation agricole et pour guider des stratégies de maintien de structure de sol favorable. Ainsi, l'objectif principal de cette thèse est d'évaluer le potentiel de l'utilisation des méthodes géophysiques pour la caractérisation de la structure du sol, soit directement (via l'impact des pores du sol, du transport et des propriétés mécaniques sur les signaux géophysiques), soit indirectement par la mesure de variables de substitution (humidité, taux de drainage). Premièrement, nous avons identifié les méthodes géophysiques qui présentent le plus grand potentiel pour caractériser les états mécaniques et hydrauliques liés à la structure du sol. Pour cela, nous avons choisi la méthode sismique pour sa sensibilité inégale aux caractéristiques mécaniques du sol et la méthode de résistivité en courant continu pour sa robustesse et sa sensibilité connue à la teneur en eau du sol et aux caractéristiques du réseau poreux. Nous présentons des avancées sur les approches intégratives combinant le suivi de données sur le terrain et la modélisation physique des signatures sismiques et géoélectriques qui permettent l'interprétation des signaux mesurés en termes de structure du sol. Ces systèmes ont été testés sur le site expérimental du Soil Structure Observatory (SSO), situé à proximité de Zürich, Suisse. Le SSO est un site d'études expérimentales sur le long terme conçu pour étudier l'évolution des propriétés du sol après un événement de compactage qui a eu lieu au printemps 2014. Nous avons collecté des données géophysiques au SSO en nous concentrant sur quatre parcelles expérimentales : sol nu non compacté et compacté, sol herbeux non compacté et compacté. Nous avons développé un nouveau modèle pédophysique pour interpréter les propriétés sismiques macroscopiques en termes de structure du sol. Basé sur des modèles de rhéologie du sol, notre modèle pédophysique capture les signatures mécaniques subtiles du sol en tenant compte de la déformation plastique du sol lors des événements de compactage. Ce modèle pédophysique est utilisé pour interpréter les vitesses des ondes P mesurées durant le printemps et l'été 2019. Les vitesses de l'onde P observées portaient une forte empreinte dûe au compactage du sol et étaient environ 30 % plus élevées pour les sols compactés que pour les sols non compactés. Les vitesses de l'onde P ont été bien prédites en utilisant la zone de contact entre les agrégats comme principale caractéristique pour identifier les structures du sol. Le modèle a inféré

des zones de contact entre les agrégats qui sont 2,9 fois plus grandes pour les sols compactés que pour les sols non compactés, ce qui indique que les sols ne se sont pas rétabli suite au compactage. Nous avons collecté les données de résistivité au cours du printemps et de l'été 2018. Afin d'interpréter ces données, nous avons développé une approche de modélisation qui combine un nouveau modèle pédophysique de propriétés électriques du sol avec un modèle unidimensionnel d'écoulement d'eau et de transfert de chaleur. Cette approche comprend un modèle d'évaporation spécifique à la structure du sol. Les données brutes de résistivité ont révélé que le compactage du sol entraîne une diminution persistante de la résistivité électrique du sol (~ 15%). Ces différences sont bien reproduites par notre modèle pédophysique en invoquant une réduction de la macroporosité et de sa connectivité par le compactage. Les données de réflectométrie temporelle (TDR) et de résistivité ont révélé que les sols compactés (sol nu et sol herbeux) sont généralement plus secs (i.e., ils présentent des pertes d'eau plus importantes) que les sols non compactés. Pour expliquer cela, nous invoquons des différences de propriétés d'évaporation pour reproduire qualitativement les différences de stockage de l'eau entre les sols compactés et non compactés. Ce travail de recherche est une première étape dans l'utilisation des méthodes géophysiques pour relever le défi de longue date qu'est la quantification de la structure du sol, pour pouvoir apporter des informations pour la recherche en agronomie, diagnostiquer la dégradation chronique du sol (compactage) et aider à calibrer les modèles de surface terrestre (Land Surface Model, LSM) qui reposent sur des informations incomplètes. La thèse fournit également un plan pour l'intégration future de la géophysique et de la recherche pédologique grâce au suivi des données combiné à la modélisation.

Mots clefs : Structure du sol, physique du sol, compactage du sol, méthodes géophysiques, pédophysique, suivi géophysique.

Abstract

Soil is a critical natural resource and the most biologically active compartment of the biosphere. Soils support global agriculture and forestry and they host hydrological processes largely controlling the recharge of the world's groundwater resources. Soil structure or architecture, referring to the binding and arrangement of soil constituents, is an important trait that supports a wide array of soil hydro-ecological functions. Despite its importance, soil structure remains difficult to define and characterize particularly at scales relevant to field applications. Typically, soil structure characterization relies on laboratory measurements on core samples or on episodic small scale field measurements, offering limited perspectives on the spatial and temporal variations of soil structure. The motivation of this thesis rests on the need for characterization techniques that provide soil structure information at relevant spatial scales (e.g., for applications in agricultural operation and management) and can guide strategies to maintain favorable soil structure. Thus, the main objective of this thesis is to evaluate the potential of harnessing geophysical methods to fill the scale-gap in characterization of soil structure and to propose a way forward in using geophysical methods to characterize soil structure directly (via impact of soil pores, transport and mechanical properties on geophysical signals), and indirectly by measurement of surrogate variables (wetness, rates of drainage). First, we identify the geophysical methods that hold the largest potential for characterizing soil structure-related mechanical and hydraulic states. For this, we chose the seismic method for its unmatched sensitivity to the soil mechanical traits and the Direct Current (DC)-resistivity method for its robustness and known sensitivity to the soil water content and pore network characteristics. We present advances on integrative frameworks combining field monitoring and physically-based modeling of seismic and geoelectrical signatures that enable interpretation of measured signals in terms of soil structure. These frameworks were tested at the Soil Structure Observatory (SSO) experimental field site, located in the vicinity of Zürich, Switzerland. The SSO is a long-term experiment designed to study the evolution of soil properties following a compaction event in the spring of 2014. We monitored geophysical data at the SSO focusing on four experimental plots: non-compacted and compacted bare soil and non-compacted and compacted ley. We developed a new pedophysical model to interpret macroscopic seismic properties in terms of soil structure. Based on soil rheology models, our pedophysical model captures subtle soil mechanical signatures by accounting for soil plastic deformation during compaction events. This pedophysical model is used to interpret P-wave velocities monitored in the spring and summer of 2019. The monitored P-wave velocities carried a strong imprint of soil compaction and were roughly 30% higher for compacted soils than for non-compacted soils. The P-wave velocities were well predicted using the contact area between aggregates as the main characterizing feature differentiating soil structure. The model inferred contact areas between aggregates that are 2.9 times larger for compacted than for non-compacted soils. We monitored DC-resistivity data in the spring and summer of 2018. In order to interpret these data, we developed a modeling scheme that combines a new pedophysical model of soil electrical properties and a one-dimensional water

flow and heat transfer model. This framework includes a soil-structure specific evaporation model. Raw DC-resistivity data revealed that soil compaction leads to a persistent decrease in soil electrical resistivity (~ 15%). These differences are well reproduced by our proposed pedophysical model by invoking a reduction of macroporosity and its connectivity by the compaction event. Time-Domain Reflectometry (TDR) and DC-resistivity data revealed that compacted soils (both bare soil and ley) are typically drier (i.e., present greater water losses) than non-compacted soils. To explain this, we invoke differences in evaporation properties to qualitatively reproduce differences in water storage between compacted and non-compacted soils. The monitored seismic and geoelectrical data suggest that soil properties have not yet recovered from compaction. The research reported here is a first step for harnessing geophysical methods to address a long standing challenge of soil structure quantification to inform agronomic activities, diagnose chronic soil degradation (compaction) and help calibrate Land Surface models that rely on currently incomplete soil information. Most importantly, the thesis provides a blueprint for future integration of geophysics and soil research through combined monitoring and modeling.

Key words: Soil structure, soil physics, soil compaction, geophysical methods, pedophysics, geophysical monitoring.

Chapter 1

Introduction

1.1 Preamble

Soils are remarkably complex systems. They form the most biologically active compartment of the Earth, they are the host that supports the formation and extraction of agricultural and forestry resources and serve as an interface for interactions between the atmosphere, biosphere, rhizosphere and lithosphere (thus, playing an important role in water, carbon and nutrient cycles). It is estimated that a ton of soil (~0.5 m^3) harbors up to four million different biological species (predominately bacteria), twice as many as those found in all oceans combined (*Curtis et al.*, 2002). Studies suggest that soil greenhouse gasses (GHG) emissions by bacterial activity (occurring under anaerobic conditions in about 1% of the soil volume) represent a substantial portion of the global GHG emissions (e.g., responsible for up to 60% of the global emissions of nitrous oxide; *Conrad*, 1996). Agricultural soils (about one third of all global terrestial surfaces; *Ramankutty et al.*, 2008) are essential for securing food demands of a growing population (*Blum and Swaran*, 2004). They store nutrients and water for plants and provide mechanical support for plant growth (*Aitkenhead et al.*, 2016), thereby, being essential for global agriculture. In addition, agricultural lands might serve as carbon sinks and could help mitigating climate change (*Whitmore et al.*, 2015). Fresh water resources conservation and management practices rely largely on key physical processes occurring in soil systems. Agricultural irrigation, rainfall water infiltration and drainage, soil evaporation and plant transpiration are processes affecting the Earth's water balance. Current practices of agriculture and water use may ultimately lead to depletion of groundwater resources (*Aeschbach-Hertig and Gleeson*, 2012; *Foster et al.*, 2017). *Costanza et al.* (2014) estimated the global economic value of soil services to average $125 trillion/year in 2011 (see Figure 1.1), exceeding the global gross domestic product (GDP) of $75 trillion/year for the same year. The value of soil services provided in the study by *Costanza et al.* (2014) are lower than previous estimations (*Costanza et al.*, 1997). By comparing both studies, *Costanza et al.* (2014) suggested that from 1997 to 2011 there was a loss in the economic value of soil services of $4.3-20.2 trillion/year due to land use change. The examples provided above illustrate how and why soils are of paramount importance for the World's ecology and human well-being (and economy). Humankind faces major challenges in developing strategies for sustainable use and management of soils. This relies on the identification of key attributes for healthy

soils and understanding how such attributes are impacted by land management practices and natural factors.

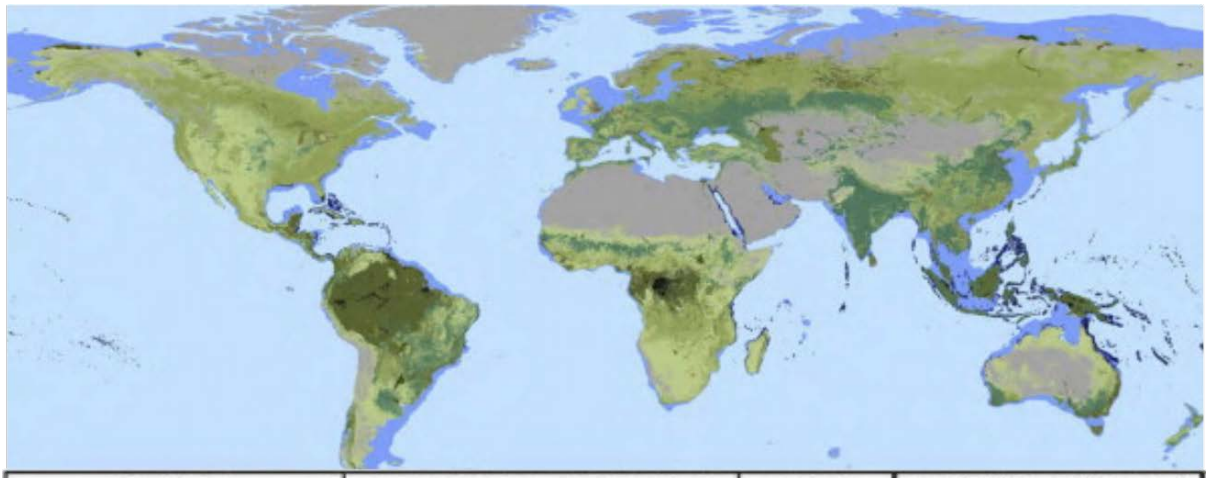

LandCover	Flow Value per Hectare per year	Legend	Area (millions of hectares)
Desert	$0		2159
Tundra	$0		433
Ice/Rock	$0		1640
Open Ocean	$491		33200
Marine Shelf	$2,222		2660
Grass/Rangelands	$2,871		4418
Temperate/Boreal Forest	$3,013		3003
Lakes/Rivers	$4,267		200
Tropical Forest	$5,264		1258
Cropland	$5,567		1672
Urban	$6,661		352
Swamps/Floodplains	$25,682		60
Tidal Marsh/Mangroves	$193,845		128
Coral Reefs	$352,249		28

Figure 1.1 – Map of global annual ecosystem services in 2011. Taken from *Costanza et al.* (2014).

Soil structure is a soil attribute with a major impact on soil functions (e.g., *Rabot et al.*, 2018). Soil structure refers to the spatial arrangement of solid constituents (minerals and organic matter) and voids of soil (*Dexter*, 1988). Soil hydro-mechanical traits are used as metrics for soil structure, including transport properties (saturated hydraulic conductivity, gas diffusivity, and infiltration capacity), water storage and mechanical penetration resistance (*Or et al.*, 2021). A desirable soil structure is a fragile product of biological activity including soil microbial communities (*Curtis et al.*, 2002), mesofauna (e.g. earthworms, termites) and vegetation (*Oades*, 1993). These organisms largely contribute to the development and maintenance of healthy soil structure (*Young et al.*, 1998; *Colombi et al.*, 2018). A well-developed healthy soil structure facilitates water and oxygen fluxes through the soil and makes these fluids available to plants, thereby, helping plant growth, promoting nutrient

recycling and groundwater recharge (*Maximilian et al.*, 2009; *Beven and Germann*, 2013; *Rabot et al.*, 2018).

In contrast with biotic processes promoting favorable soil structure, climatic factors (freezing-thawing, wetting-drying) or anthropogenic activities may produce soil structure breakage and/or degradation. Tillage operations are an example of soil structure breakage (Figure 1.2a), turning naturally developed soil structure volumes into small fragments (*Or et al.*, 2021). Similarly, soil compaction is an example of soil structure degradation with adverse environmental consequences. Soil compaction is produced by cattle movement, or usage of agricultural, forestry, military, construction and other off-road vehicles, leading to the collapse of biologically developed pore networks. Such poor soil structure restricts water infiltration and gas exchange, thereby, resulting in water runoff, soil erosion and unfavorable anoxic conditions that limit plant growth and may trigger greenhouse gas emissions by anaerobic bacterial respiration (*Jordanova et al.*, 2011; *Berisso et al.*, 2012; *Nawaz et al.*, 2013; *Chen et al.*, 2014). Several processes and mechanisms affect soil structure over multiple spatial and temporal scales. Despite the accumulated knowledge about soil structure degradation, our knowledge of soil structure generation, formation and recovery remains limited (*Keller et al.*, 2017). One reason for this is that methods for characterization of soil structure (based on soil sampling, laboratory measurements and point-wise field assessments) are invasive, provide fragmentary information in time and space and offer a limited capacity to evaluate soil structure evolution under natural conditions. Annual tillage operations (Figure 1.2b), the largest geo-engineering activity on Earth, illustrate the discrepancy between spatial scales for traditional characterization and the gigantic spatial scales at which soil structure are modified annually. This calls attention to the need of characterization methods operating at larger scales.

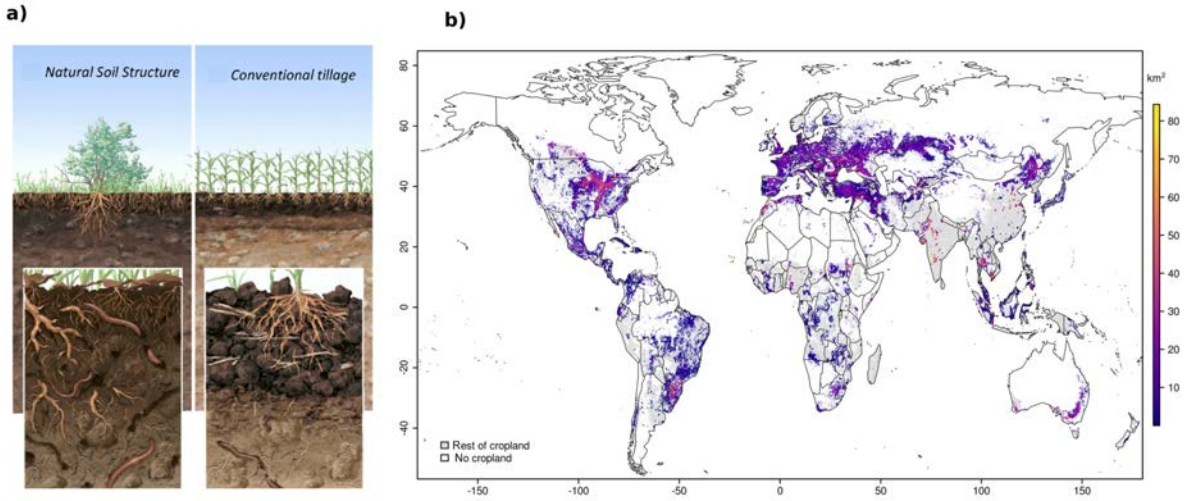

Figure 1.2 – (a) Conceptual representation of soil structure as affected by tillage showing natural soil structure shaped by soil-fauna-vegetation-climate feedbacks (left panel) and tilled soil structure characterized by mechanical fragmentation of the top layer (right panel) (from *Or et al.*, 2021). (b) Annual tillage area (km^2/pixel) in global agricultural lands (from *Porwollik et al.*, 2019).

This thesis aims at demonstrating how selected geophysical methods can be used to capture soil structural features, thereby, complementing traditional methods in a minimally invasive fashion. Geophysical methods can provide valuable complementary information for mapping dynamics and spatial variations of soil structure, and advance our understanding and monitoring capabilities of soil-structure driven physical processes. Thus, adapting geophysically-based soil structure characterization can help to bridge the gap in spatially and temporal limitations of traditional characterization methods. In order to harness geophysical methods for this challenging task, we developed frameworks that integrate geophysical monitoring with numerical modeling of soil processes and their geophysical signatures. The frameworks presented in this thesis include advances on pedophysical modeling linking soil structure with macroscopic geophysical properties. These models are based on conceptual geometrical models of soils. Specifically, we focused on seismic methods to characterize soil mechanical properties, and electrical methods to study soil structure effects on the soil water regime. The geophysical methods and associated frameworks presented in this thesis are used to interpret soil structure using geophysical data from compacted and non-compacted agricultural soils, yet, the methodologies are general and can be used in other contexts.

1.2 Characterization of soil structure: Traditional methods

1.2.1 Soil structure: metrics and challenges

Soil structure remains challenging to define and characterize. This is partly because soils sharing the same texture (size distribution and fractions of primary soil particles) and similar bulk properties may have substantially different in soil structure. In this thesis, we primarily consider soil structure represented by soil water and gas transport properties (saturated hydraulic conductivity and hydraulic conductivity function), soil water retention properties and soil mechanical impedance (penetration resistance) (*Or et al.*, 2021). Other surrogate variables in use are related to pore-network characteristics, the geometrical arrangement of the soil's solid phase and soil indicators of biological activity (*Kutílek*, 2004; *Rabot et al.*, 2018; *Or et al.*, 2021). Clearly, soil water transport and retention properties are strongly linked to pore size distribution and pore connectivity. The soil mechanical impedance, a proxy for the mechanical resistance of soils to mesofauna and plant root activity, is linked to the soil solid phase forming aggregates (primary soil particles held together by cohesive forces, secondary particles and organic matter) and the soil frame.

Figure 1.3 illustrates that soil structure is elusive, invisible to the eye and soil bulk properties may mask important soil structure aspects. The data are taken from a controlled soil compaction field experiment in which compaction by agricultural machinery was inflicted to selected soil plots. This experiment is described in detail by *Keller et al.* (2017), which is provided in Appendix A of this thesis. Figure 1.3 compares data from non-compacted and compacted agricultural soils, and illustrates the sensitivity of selected soil properties to soil structure variations by compaction. Soil compaction exerts a dramatic effect on soil surface water infiltration. Similarly, soil water and gas transport properties (relative gas diffusion coefficient and saturated hydraulic conductivity) and soil penetration resistance are strongly affected by soil compaction. In contrast, the soil bulk properties (soil bulk density and total porosity) present relatively-speaking small impacts on soil compaction. Data presented in Figure 1.3 were measured on soil samples in the laboratory, except for the penetration resistance and soil surface water infiltration that were measured *in-situ*.

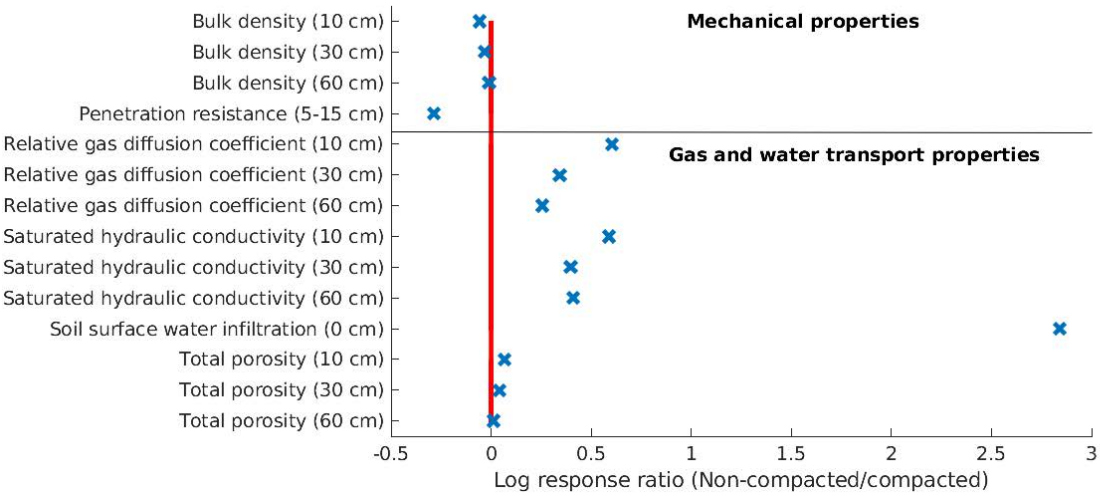

Figure 1.3 – Metrics of non-compacted soil structure relative to compacted soil structure. Data are from a soil compaction field experiment presented by *Keller et al.* (2017). Data from compacted soils were measured shortly after experimental compaction. The numbers in the parenthesis indicate the soil depth for soil samples. The values of soil penetration resistance are averaged between 5 and 15 cm. The horizontal value presents the log10 of the ratio between values from non-compacted and compacted soils.

An extended discussion concering general challenges related to soil structure characterization can be found in Chapter 2 and in *Or et al.* (2021). In the following, we provide a summary of operational principles of three traditional approaches for soil structure characterization: (1) methods based on soil sampling, (2) methods involving field assessment of soil physical properties and (3) visual evaluation methods. Relevant studies in which these methods are used are highlighted and the advantages and limitations of these methods are briefly discussed.

1.2.2 Soil core sampling

Soil sampling is one of the most common practices for characterization of soil properties. Sampling refers to the act of selecting a subset of elements (soil sample locations) whose properties are assumed to be representative of a given region (the targeted land area of study). Soil samples are typically collected with the core method (Figure 1.4a), in which a cylindrical metal sampler is driven into the soil to remove a known soil volume for further laboratory analysis. Sampling design (Figure1.4b) is the process of selecting the sampling locations (spatial coordinates) using a given approach. These approaches are often based on statistical methods, convenience, prior knowledge of the researcher or guided by the research goals of the study (*Carter and Gregorich*, 2007).

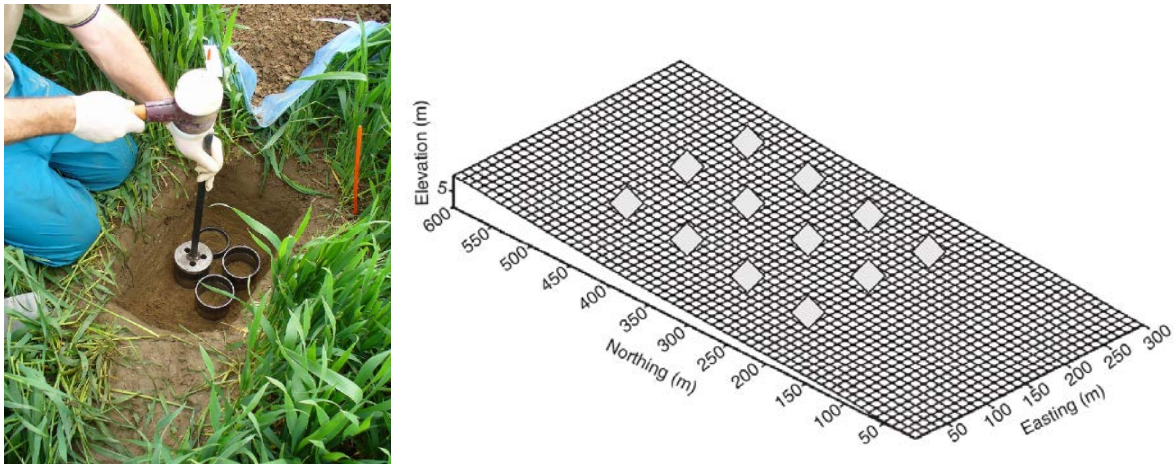

(a) (b)

Figure 1.4 – Soil core sampling. (a) Cylindrical soil sampler for obtaining undisturbed soil sample (from *Holpp et al.*, 2010). (b) Example of sampling design in a rectangular grid (from *Carter and Gregorich*, 2007). The diamond-shaped symbols represent the locations at which samples are collected.

Understanding water flow in partially-saturated soils is one of the major challenges in soil physics. Laboratory measurements advance such knowledge by offering detailed information of hydraulic properties. For this reason, laboratory measurements are commonly used to study soil structure dynamics and its impact on soil hydraulic properties, for example, in response to anthropogenic (*Peng and Horn*, 2008; *Martínez et al.*, 2016; *Keller et al.*, 2017) and biological perturbations (*Kroener et al.*, 2014). Similarly, laboratory measurements of bulk density are often used to study effects of soil compaction (*Håkansson and Lipiec*, 2000) and soil mesofauna in soil structure (*Stirzaker et al.*, 1996). In addition, X-ray computer tomography techniques provide very detailed information about the links between the intricate pore-system of soils and its hydraulic properties (*Helliwell et al.*, 2013; *Naveed et al.*, 2016; *Schlüter et al.*, 2014). However, there are a number of limitations that are inherent to soil sampling and related measurements of soil physical properties. Soil sampling provides only fragmentary information about the spatial variability and temporal variability of soil properties. It is invasive and measures soil properties in small volumes and under controlled (non-natural) conditions. Soil cores may not adequately represent the soil structure of the bulk soil, for example, because of dead-end pores resulting from the finite sample volume or alterations in soil structure due to sampling. This may lead to biased estimates of soil transport properties (*Mertens et al.*, 2005). More details about laboratory measurement techniques for saturated hydraulic conductivity, water retention properties, bulk density, total porosity, air permeability and gas diffusion can be found in *Carter and Gregorich* (2007); *Martínez et al.* (2016); *Klute and Dirksen* (1986).

1.2.3 *In-situ* soil measurements

Field-based methods measure soil properties under natural conditions, thereby, aiming at a more realistic quantification of *in-situ* soil properties and improved prediction capabilities of models of soil processes relying on such physical properties. Herein, we present two examples of such *in-situ* measurements of soil structure: soil mechanical impedance and soil surface infiltration.

Soil mechanical impedance is assessed in the field by the so-called cone penetrometer test (CTP, *Lunne et al.*, 1997). It utilizes a device consisting of a rod with a conical tip that is mounted onto a force transducer. The conical tip is pushed through the soil and the resulting force measured over the displaced depth is used to infer the cone penetration resistance stress, typically by dividing the force by the active area of the cone (Figure 1.5a). For practical applications, CPT is used to assess the suitability of soils for plant root growth and earthworm burrowing (*Bengough and Mullins*, 1990; *Ruiz et al.*, 2015). The test is often used to deduce the mechanical properties related to soil compaction (*Perdok et al.*, 2002; *Webb*, 2002; *Gregory et al.*, 2007; *Oleghe et al.*, 2017).

Figure 1.5 – Examples of in-situ measurements of soil properties. (a) Cone penetrometer test for measuring mechanical properties of soils. Photo from the experiment by *Keller et al.* (2017). (b) Disc permeameter for measuring surface infiltration and saturated hydraulic conductivity of soils. Credits to http://vro.agriculture.vic.gov.au.

There exist several field-based methods to estimate infiltration and soil hydraulic properties. Most methods involve controlled infiltration experiments with known flow geometry, intake area, flow rate and boundary conditions (see e.g., Figure 1.5b). Soil hydraulic properties are then inferred from time and flux measurements (*Perroux and White*, 1988). Although they offer advantages over soil sampling and associated laboratory measurements, information

derived from *in-situ* soil measurements remains limited in terms of spatial and temporal resolution, often involving invasive practices (e.g., excavation for measurements of hydraulic conductivity) and limited perspectives for understanding soil structure dynamics at the same locations.

1.2.4 *In-situ* visual evaluation

Visual soil evaluation (VSE) methods offer complementary information to asses of soil structure and soil characteristics at spatial scales that are typically larger than the above-mentioned methods (*Guimarães et al.*, 2017). VSE methods are subdivided into profile methods (Figure 1.6a) and spade methods (Figure 1.6b). Spade methods involve the extraction of a soil block from the soil surface with a spade, that is subsequently broken manually to produce aggregates. The aggregates are then described in terms of characteristics such as visual porosity, macroporosity and size of aggregates, and their mechanical resistance to manual breakage. These characteristics are classified using photographs for scoring the soil structure (*Munkholm*, 2000). Spade methods are relatively simple evaluation techniques for soil structure characterization. They require little methodological training for successful application (*Guimarães et al.*, 2017). Profile methods (e.g., "profil cultural", Figure 1.6a) aim at delineating lateral and vertical heterogeneities in soil structure along a soil profile that are typically associated with tillage, compaction and weathering. Some of the elements that are used for morphological discrimination of soil zones are the degree of compaction, spatial arrangement of clods (aggregate of large size), aggregates, voids, cracks and organic residues (*Boizard et al.*, 2017). Spade methods provide a rapid field assessment of soil structure, whereas soil evaluation methods offer valuable two-dimensional information of soil structure. This information can be used to improve our knowledge of management practices and the conceptual description of soils for numerical modeling of soil processes (*Keller et al.*, 2013a). Limitations of these methods are related to their highly invasive and subjective nature and that they only provide empirical information.

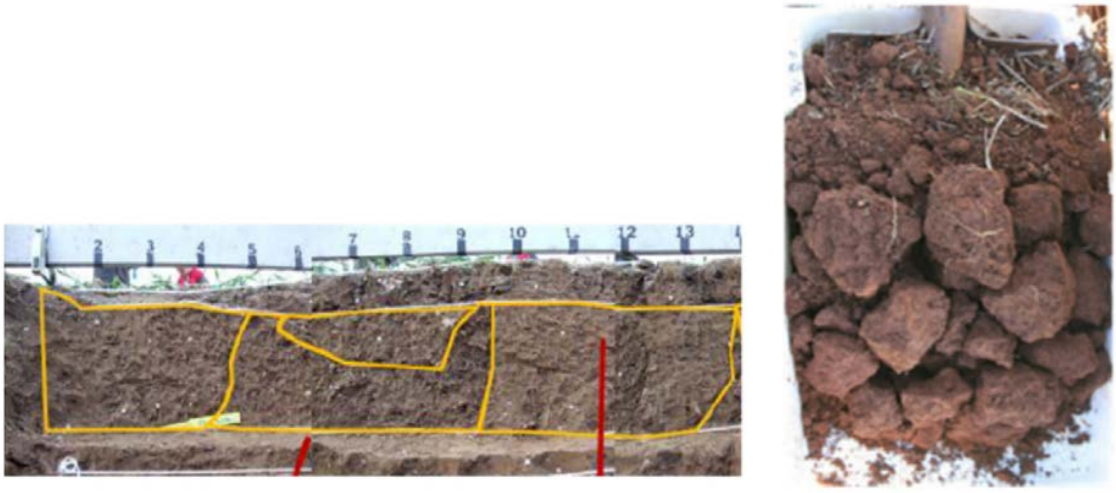

(a) (b)

Figure 1.6 – Examples of visual evaluation methods. (a) Detailed profile methods for delineating zones with soil different properties (from *Boizard et al.*, 2017). (b) Spade method for deriving statistical properties of soils (from *Guimarães et al.* (2017)).

1.3 Geophysical methods for soil structure characterization

Geophysical methods provide information about earth properties, lithological units, and processes that are often unavailable by any other means. Geophysical methods are used in many research fields including oil, gas and mineral exploration (*Telford et al.*, 1990), vulcanology studies (*Rosas-Carbajal et al.*, 2016), risk assessment of natural hazards (*Whiteley et al.*, 2019), groundwater exploration and management research (*Hubbard and Linde*, 2011; *Binley et al.*, 2015), critical zone research (*Parsekian et al.*, 2015) and soil science (*Grandjean et al.*, 2009a; *Allred et al.*, 2008).

In the context of soil science and soil structure, the vast majority of studies linking geophysical properties to soil structure are empirical and we lack a systematic approach to characterize soil structure with geophysical methods. In Chapter 2, we provide a comprehensive review of how geophysical methods can be used for soil structure characterization. Therein, we describe challenges associated with characterization of soil structure, we highlight selected geophysical methods and their potential for such tasks. We focus on the physical properties these methods are sensitive to and provide a discussion about the opportunities and potential research avenues for geophysical characterization of soil structure. The main opportunities can be summarized as:

1 **Pedophysical models.**
The development of specific pedophysical relationships is needed to include effects of soil structure on macroscopic geophysical properties and associated geophysical signatures.

2 **Combination of geophysical methods.**
Combining different geophysical methods can offer enhanced information of soil structure and/or related soil processes by capitalizing on complementary sensitivity to different soil properties or states.

3 **Survey design and spatial scaling of soil structural features.**
Geophysical methods could offer chracterization of soil structure over spatially extensive scales. For this, the development of mapping strategies are needed. The design of experimental setups and instruments using geophysical principles needs to be revised to enable accurate imaging at large horizontal scales.

4 **Soil dynamic responses and hydrogeophysical modeling.**
Soil structure can be indirectly inferred through geophysical monitoring. This is done by assessing its impact on soil states (e.g., water regime) captured by geophysical properties sensitive to such dynamics.

In the following, we provide basic principles pertaining to the geophysical methods employed in this thesis (the seismic method and the Direct Current (DC)-resistivity method). The focus is on geophysical imaging and links between the measured data and soil structure properties are highlighted.

1.3.1 Seismic methods

Seismic methods involve the measurement of components related to wave-fields produced by artificially or naturally generated seismic waves (e.g., pressure, shear and surface waves) propagating in the subsurface or near the soil surface. The velocity of the seismic waves can then be inferred from the measured signals along with other seismic attributes (amplitude and frequency). The velocities of seismic waves depends on the elastic moduli of the soil that, in turn, depends on the elastic properties of soil constituents and their spatial arrangement. For this reason, seismic methods may provide unique information about the variability of soil mechanical properties that can be linked to soil structural mechanical traits (e.g., penetration resistance). Seismic methods are currently underused for soil structure characterization (see discussion in Chapter 2). Seismic characterization and imaging can be achieved using a wide variety of methods and tools addressing wave phenomena (*Steeples*, 2005). Herein we describe basic principles of seismic imaging based on refraction of seismic waves at soil discontinuities. This principle is used in Chapter 3 for characterization of soil structure with field monitoring of seismic data.

Seismic refraction methods rely on ray theory (*Cerveny*, 2005). A transect of geophones is deployed on the soil surface, and a seismic source (typically a hammer impact on a plate for soil studies) is successively activated at different locations along the geophone transect. The geophones measure the vertical ground movement resulting from pressure and shear waves propagating through the soil, scattering at soil interfaces (referring to soil zones with different seismic properties) and surface waves propagating at the soil's surface. The resulting measured wavefields are called seismograms. P-waves are the fastest waves and, therefore, are the first ones being recorded on the seismograms. Seismic wave refraction occurs at the interface between soil layers when the underlying layer has a higher P-wave velocity (Figure 1.7a). At an incidence angle corresponding to the critical angle (given by Snell's law), the

refracted wavefront propagates along the interface at the velocity of the underlying layer (so-called head waves). Each point of the interface serves as a secondary source of waves that propagate back to the soil's surface at the critical angle (Figure 1.7a). The times of the first-arriving seismic waves of the different seismic shots are extracted from the measured seismograms and used as the data. The measured traveltimes are inverted to find a subsurface P-wave velocity model that honors the data and any imposed constraints (*Menke*, 2012).

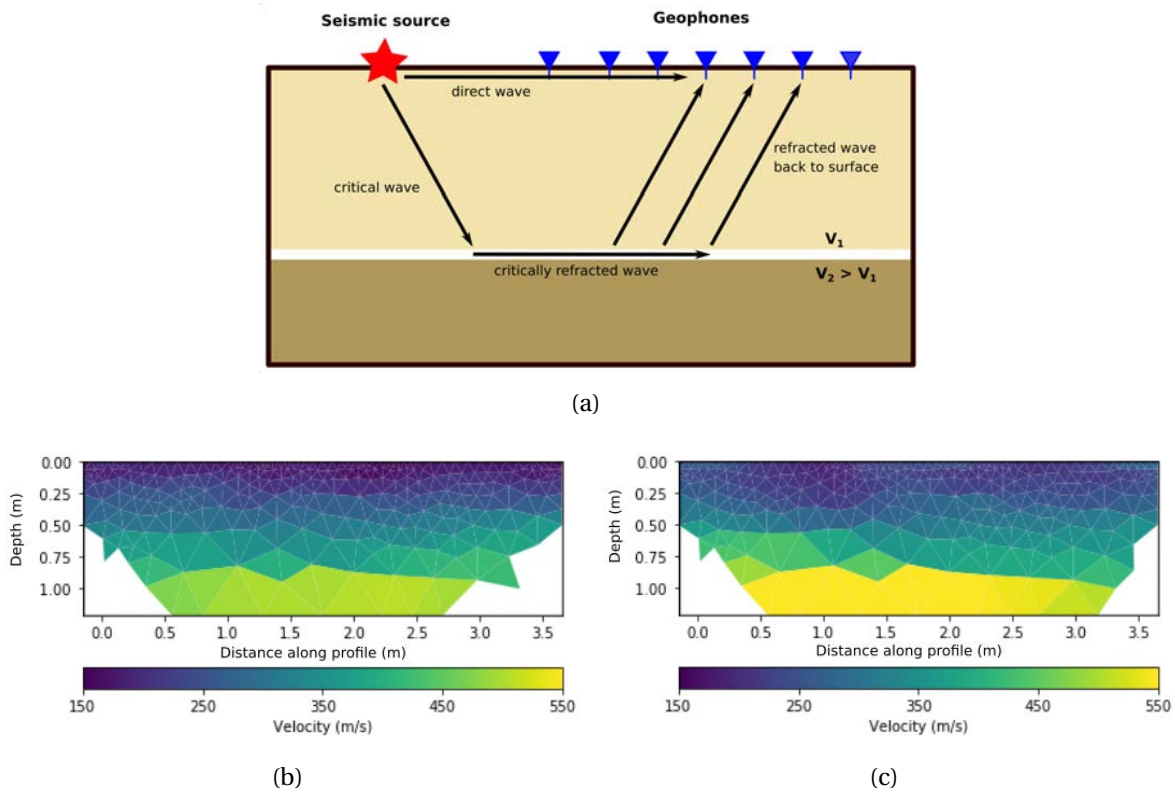

Figure 1.7 – Seismic refraction imaging. (a) Schematic representation of the seismic refraction ray-path. Inverted P-wave velocity sections from seismic refraction surveys collected in (b) non-compacted and (c) compacted bare soil with a loamy texture in the soil compaction experiment presented by *Keller et al.* (2017).

Figures 1.7b and 1.7c present examples of inferred P-wave velocity sections for non-compacted and compacted bare soil collected at the soil compaction experiment presented by *Keller et al.* (2017). The inferred P-wave velocities are generally greater for the compacted bare soil than for the non-compacted bare soil. From these sections, it appears reasonable that it is soil structure differences that produce the differences in seismic velocities. However, a detailed physical description that allows for a quantitative interpretation in terms of geometrical concepts of soil structure is needed. In Chapter 3, we deal with this problem and provide a pedophysical model for mechanistic prediction of seismic properties based on soil structure using first-arrival seismic monitoring.

1.3.2 DC-resistivity

The DC-resistivity method is one of the most widely used geoelectrical methods in soil studies and it holds potential to characterize soil structure (particularly, in relation to soil hydraulic properties) due to its sensitivity to soil water content, soil texture and the connectivity of electrical pathways for current flow (see discussions in Chapter 2). A typical DC-resistivity survey employs a four-electrode measurement configuration forming an electrical circuit in the subsurface with the electrodes deployed on the soil surface. Two electrodes act as a current source and sink in which a known low frequency (~1 Hz) square current waveform is applied. The other two electrodes measure the voltage at a given location (see Figure 1.8a). The measured current (I), the measured voltage (V) and a geometrical factor (k, which is a function of the electrode array geometry) are then used to calculate the apparent electrical resistivity of the soil ($\rho_a = k\frac{V}{I}$) (see more details in *Binley and Kemna*, 2005). The apparent resistivity refers to the resistivity of an equivalent homogeneous medium.

In modern DC-resistivity applications, data are acquired along a transect using multiple electrode locations and spacings (i.e., varying the penetration depth of electrical current). An electrode line is deployed (e.g., 24, 48 or 96 electrodes) and a resistivity meter executes a sequence of measurements involving different electrode quadripoles at selected locations and spacings from which apparent resistivities are measured (see Figure 1.8). Typically, a lateral position (given by the midpoint of the four electrodes) and a pseudo-depth level (related to the separation between current electrodes) are assigned to each measurements. This results in a pseudo-section of apparent resistivity that provides a qualitative view of the spatial variations of electrical resistivity in the subsurface. Subsequently, a resistivity distribution is inferred from apparent resistivity sections through an inversion process (*Menke*, 2012; *Rücker et al.*, 2006a). The resistivity section is inferred by modeling the forward response of a spatially discretized earth and finding a spatial distribution of electrical resistivity that honors the measured data. There is generally no unique solution to this problem and deterministic inversion approaches consider additional constraints to the inferred property model (e.g., smoothness constraints) (*Menke*, 2012).

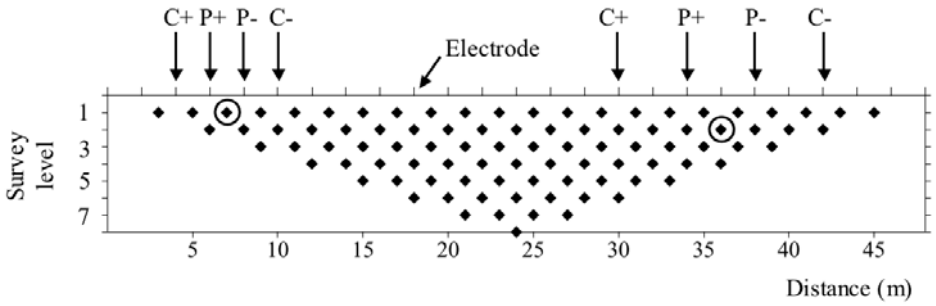

(a)

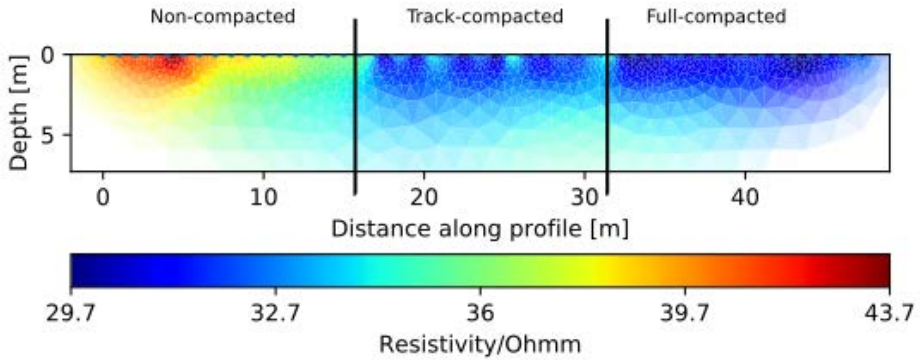

(b)

Figure 1.8 – DC-resistivity surveying. (a) Schematic representation of a DC-resistivity survey illustrating how a pseudo-section is built. The circles identify the locations of the two electrode configurations shown (from *Binley and Kemna* (2005)). (b) Inverted resistivity section from a soil compaction experiment by *Keller et al.* (2017). It illustrates spatial variations of electric resistivity in response to soil structure variations caused by compaction. The data correspond to the ley post-compaction management.

Chapter 2 presents a review of relevant studies that have used electrical resistivity surveys to interprete soil structure. For illustration purposes, we present here an example of an inverted resistivity section displaying spatial features that can be related to soil structure (Figure 1.8b). The data correspond to the soil compaction experiment described by *Keller et al.* (2017), in which a ley soil plot was compacted by an agricultural vehicle that was driven perpendicular to the direction of the presented section. Three compaction treatments are shown: no-compaction, track compaction and compaction over the whole soil surface (i.e., track by track). The pre-compaction history is the same for the three zones and we expect negligible lateral variations of soil texture. For this reason, we attribute variations of electrical resistivity to the compaction treatment. The inverted resistivity reveals that compacted zones present a decrease in electrical resistivity in relation to resistivity from non-compacted zones. Offering an interpretation for the compaction-associated drop in resistivity was part of the motivation for the study presented in Chapter 4. Therein, we utilize a soil-structure guided pedophysical model to explain the decrease in resistivity as a drop in macroporosity and its connectivity. Herein, we highlight that DC-resistivity imaging can

produce very useful qualitative information of soil structure at spatial scales that are larger than methods described in Section 1.2 in a minimally invasive way.

1.4 Conceptual model of soil structure

Conceptual models represent qualitative characteristics of a given system that ultimately help to better describe physical processes and build a physically-based interpretation of the macroscopic properties or outputs of such systems. Herein, we introduce basic concepts that are used in this thesis to build a conceptual model of structured soils in the context of geophysical methods. We aim at providing a framework for determining macroscopic geophysical properties of structured soils that are sensitive to (1) the physical properties of soil constituents (λ), (2) the volumetric proportions of soil constituents (V_λ) and (3) their spatial arrangement (S_λ).

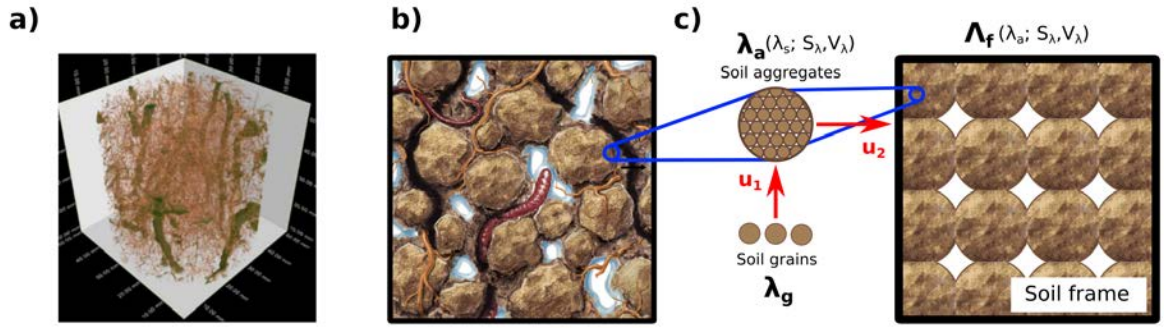

Figure 1.9 – Conceptual model of soil structure for determining macroscopic geophysical properties. (a) Computer tomography of a 100 cm^3 soil sample from an agricultural soil (voxel size 60 μm, corresponding to a minimum pore width of 120 μm) (from *Keller et al.*, 2017). (b) Conceptual illustration of a structured soil including aggregation and macroporosity created by biological activity (from *Romero-Ruiz et al.*, 2018). (c) Schematic representation of the upscaling of soil physical properties of structured soils from soil grains, to soil aggregates and ultimately to a soil frame. In these representations the soil is dry.

Soil bulk properties alone are insufficient to characterize soil structure (see Figure 1.3). Similarly, we postulate that predicting macroscopic geophysical properties by volumetric averaging alone is too limiting for quantitative applications. Instead, we employ a conceptual description of soil structure to compute macroscopic soil properties considering effects of soil structure. To achieve this, we consider two major aspects of soil structure: soil aggregation and macroporosity. The soil pore network is often determined by textural pores (i.e., those resulting from separation between soil solid grains) and structural pores (i.e., those resulting from aggregation and soil biological activity) (Figure 1.9a). Figure 1.9b illustrates how aggregates are connected in the soil, as well as their link with plant roots and earthworms penetrating the soil, ultimately generating biopores. Based on this, the soil is divided into two domains: (1) soil aggregates (comprising soil primary particles and intra-aggregate pore

space) and (2) soil inter-aggregate space. This leads naturally to a hierarchical approach in which soil primary particles (termed as "grains") are used as the building blocks to form soil aggregates, which in turn are the building blocks to form the soil frame (Figure 1.9c). The physical property of the aggregates (λ_a) is obtained by the upscaling procedure $\mathbf{u_1}$ using the physical properties and volumetric portions of the soil grains (λ_g and V_λ) and incorporating knowledge about their spatial structure (S_λ). Similarly, the macroscopic property of the soil frame (Λ_f) is obtained by the upscaling procedure $\mathbf{u_2}$ using the physical properties and volumetric proportions of the soil aggregates (λ_a and V_λ) and providing a given structure (S_λ). In order to simplify the illustration of these concepts, Figure 1.9c considers only a dry soil frame. Effects of water content can typically be considered in the upscaling processes $\mathbf{u_1}$ and $\mathbf{u_2}$ and/or in an additional upscaling process $\mathbf{u_3}$.

The concepts described above are widely accounted for to model macropore water flow. Water flow in soils is often considered to be a linear superposition of (1) relatively slow water flow in the soil matrix and (2) rapid water flow through soil macropores. For example, the soil hydraulic conductivity function is often modeled as:

$$K_{soil} = w_{sm}K_{sm}(h) + w_{mac}K_{mac}(h), \tag{1.1}$$

where w_{sm} and w_{mac} are the volumetric proportions of the soil matrix and soil macropore space, respectively, and K_{sm} and K_{mac} are their corresponding hydraulic conductivity functions. This equation explicitly accounts for the effect of soil structure in soil hydraulic properties. Figure 1.10, illustrates how the effects of soil structure (represented here as macropores) on the soil hydraulic conductivity as a function of the soil pressure head h (equation 1.1). The parametric functions proposed by *van Genuchten* (1980) are here used to model the hydraulic conductivity functions of the matrix and the soil macropores. In this example, the van Genuchten properties of the soil matrix are $\alpha_{sm} = 0.02\ cm^{-1}$ and $n_{sm} = 1.15$, while for soil macropores they are $\alpha_{mac} = 2\ cm^{-1}$ and $n_{mac} = 3$. The saturated hydraulic conductivity of the soil matrix and macropores are $K_{s_{sm}} = 3$ cm/h and $K_{s_{mac}} = 2500$ cm/h, respectively. The corresponding volumetric proportions are $w_{sm} = 0.96$ and $w_{sm} = 0.04\ cm^3/cm^3$. This example illustrates that a very small proportion of macropores can have a strong impact on transport properties and that domain separation can help modeling such effects.

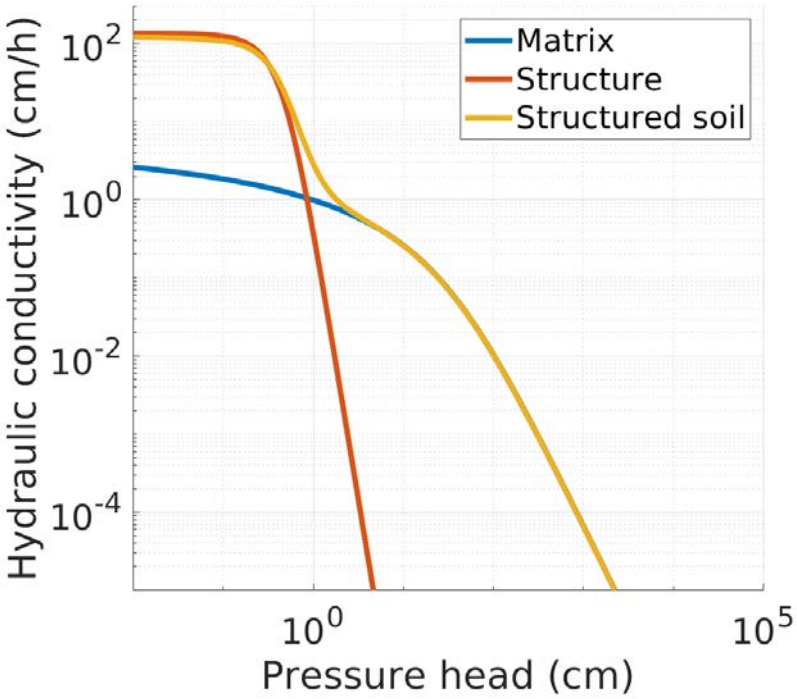

Figure 1.10 – Hydraulic conductivity function of structured soils as the superposition of soil matrix and soil structural pores. We used the parametric model of *van Genuchten* (1980) to model the hydraulic conductivity functions. The properties for soil matrix are: $\alpha_{sm} = 0.02$ cm^{-1}, $n_{sm} = 1.15$, $K_{s_{sm}} = 3$ cm/h, $w_{sm} = 0.96\ cm^3/cm^3$. The properties of the soil macropores are $\alpha_{mac} = 2\ cm^{-1}$, $n_{mac} = 3$, $K_{s_{mac}} = 2500$ cm/h, and $w_{sm} = 0.04\ cm^3/cm^3$.

In this thesis, we build models for macroscopic geophysical properties that are consistent with this representation and allow predicting signatures of soil structure on macroscopic geophysical properties. The developed pedophysical seismic and electrical models for soil structure are presented as parts of Chapter 3 and Chapter 4, respectively. Our work was based on previously proposed models for seismic properties of marine sediments (*Dvorkin et al.*, 1999), dielectric properties of highly heterogeneous porous rocks (*Blonquist Jr et al.*, 2006), and electrical signatures of solutes in dual-domain porous media (*Day-Lewis et al.*, 2017).

1.5 Modeling tools for soil structure characterization

1.5.1 Flow and transport modeling

One-dimensional water flow in unsaturated media is often expressed by Richards equation, written as *Richards* (1931):

$$\frac{\partial \theta}{\partial t} = \frac{\partial}{\partial z}\left[K_{soil}\left(\frac{\partial h}{\partial z} + 1\right)\right] - \Gamma, \tag{1.2}$$

where h is the soil pressure head, θ is the volumetric water content, z is the spatial coordinate, Γ is the sink term, and K_{soil} is the unsaturated hydraulic conductivity. Soil water flow and heat transfer are modeled in this thesis using the 1D finite-elements software HYDRUS-1D *Simunek et al.* (2013). To account for macropore water flow, we used the approach by *Durner* (1994). We use an in-house MATLAB script to change the input parameters, the boundary conditions, create the input files, run the code, and read the output files.

1.5.2 Pedophysical modeling

We developed new pedophysical models linking soil structure to soil seismic properties (Chapter 3) and soil electrical properties (Chapter 4). These models were based on the the Hertz-Mindlin (HM) contact theory and the Differential Effective Medium (DEM) theory, respectively.

The HM mechanical contact model is used to derive the elastic moduli of a random pack of spherical particles. These properties depend on the normal and tangential contact stiffness between adjacent particles (pp. 245-248 *Mavko et al.*, 2009). The elastic moduli are expressed in terms of the elastic properties of the particles and a confining pressure (P) as:

$$K_{mix} = \left[\frac{N^2(1-\phi)^2 G^2}{18\pi^2(1-\nu)^2} P \right]^{\frac{1}{3}}, \tag{1.3}$$

and,

$$G_{mix} = \frac{2+3f_1-(1+3f_1)\nu}{5(2-\nu)} \left[\frac{3N^2(1-\phi)^2 G^2}{2\pi^2(1-\nu)^2} P_e \right]^{\frac{1}{3}}, \tag{1.4}$$

where K_{mix} and G_{mix} are the bulk and shear moduli of the pack of particles, respectively. Furthermore, N is the average number of contacts per particle, G and ν are the shear modulus and Poisson's ratio of the particles, ϕ is the porosity of the particle pack and f_1 is the fraction of non-slipping particles.

The DEM theory is used to derive the electrical conductivity of a mixture of two media (host and inclusions) without imposing restrictive assumptions about electrical pathways in the mixture. The electrical conductivity of the mixture (σ_{mix}) is expressed as *Bussian* (1983):

$$\sigma_{mix} = \phi^m \sigma_2 \left(\frac{1-\sigma_1/\sigma_2}{1-\sigma_1/\sigma_{mix}} \right)^m, \tag{1.5}$$

where m is the so-called cementation exponent, σ_2 is the effective electrical conductivity of the inclusions and σ_1 is the electrical conductivity of the host.

Since we model Time-Domain Reflectometry (TDR) data, we provide the model used to convert water content to dielectric constant. For this, we used the volumetric mixing model

known as the Complex Reflective Index Model (CRIM) (*Roth et al.*, 1990). The dielectric constant of a mixture of n media is expressed as:

$$\sqrt{\kappa_{mix}} = \sum_{i=1}^{n} V_i \sqrt{\kappa_i}, \tag{1.6}$$

where κ_{mix} is the dielectric constant of the mixture, and κ_i and V_i are the dielectric constant and volumetric proportion of the i-th medium.

1.5.3 Geophysical forward modeling

In Chapter 3, we derive proxies of S-wave velocities from zero-crossing times obtained from field measurements. In order to assess the accuracy of our procedure for estimating S-wave velocities, we performed 2D numerical simulations of elastic wave propagation using the open-source code by *Bohlen* (2002). Additionally, for comparison purposes, we used the open-source code by *Wathelet et al.* (2020) to compute Rayleigh wave (R-wave) velocities for a two-layer velocity model. The inferred P-wave velocity models shown in Figures 1.7b and 1.7c were obtained using the refraction tomography module of Geophysical Inversion & Modeling Library (pyGIMLi) (see e.g., *Blazevic et al.*, 2020) that implements the algorithm by *Dijkstra et al.* (1959) for ray-tracing in the forward solver.

In Chapter 4, we model apparent resistivity data from one-dimnesional water content profiles resulting from Hydrus-1D simulations. For this, we solve the 1D DC-resistivity problem (e.g., *Parker*, 1984) using the implementation by *Ingeman-Nielsen and Baumgartner* (2006) based on digital filter theory. We used the pyGIMLi finite element electrical resistivity tomography (ERT) module (*Rücker et al.*, 2006b) to infer electrical resistivity sections, such as the one shown in Figure 1.8.

1.6 The Soil Structure Observatory

The Soil Structure Observatory (SSO) is an experimental field site located in the vicinity of Zürich, Switzerland (8^o31'04 E, 47^o25'39 N) (*Keller et al.*, 2017). It is a long-term experimental site designed to study the evolution of soil structure, following a compaction event in the spring of 2014, for different types of post-compaction management. The SSO has a strip-plot design with three blocks (replicates). We monitored geophysical data (DC-resistivity, seismics and TDR data) in experimental plots located in block A with two different covers (bare soil and ley soil) and two compaction treatments (compaction on the full surface and no compaction). The four corresponding soil cases are referred to as full compacted ley (grass-legume mixture), non-compacted ley, full compacted bare soil and non-compacted bare soil (see Figure 1.11). Since the soil properties (and texture) prior to the compaction event were similar at all monitoring sites (*Keller et al.*, 2017), we attribute differences in the monitoring geophysical signatures to the different soil covers and treatments.

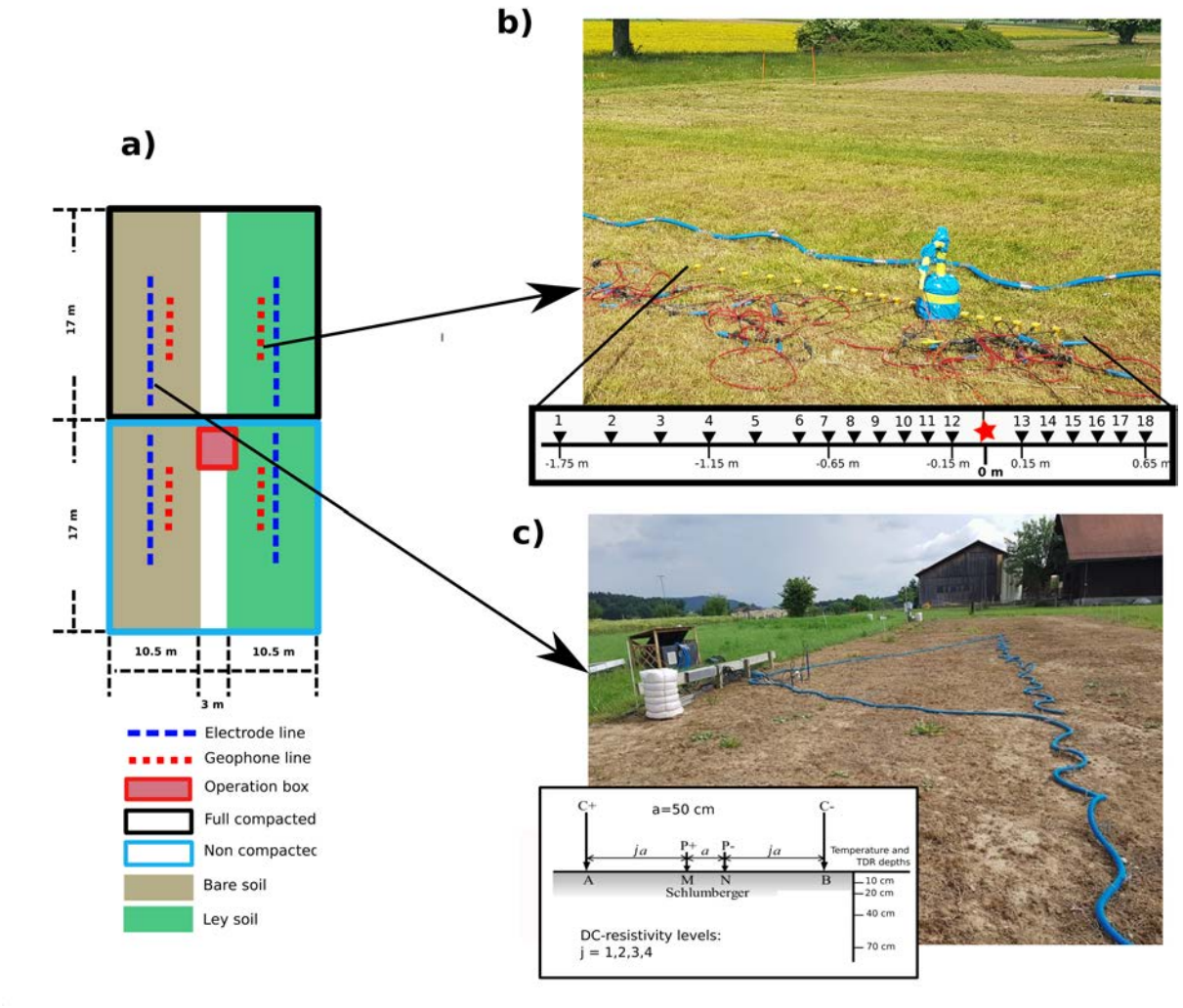

Figure 1.11 – (a) Schematic representation of the seismic lines deployed in block A. The seismic monitoring layout shown was established in the compacted ley. (b) Schematic representation of the DC-resistivity lines deployed in the block A. The DC-resistivity line shown is located in the bare soil.

Seismic monitoring

We conducted seismic monitoring in the spring and summer of 2018 (see summary in Figure 1.12). The seismic array comprised a line of 18 geophones (30 Hz SM-11 IO) deployed on both sides of an impact source (twelve on one side and six on the other side, Figure 1.11b). Two geophone spacings (Δx) were used: $\Delta x = 10$ cm for sensors with offsets shorter than 80 cm, and $\Delta x = 20$ cm for sensors with offsets longer than 80 cm. The sensors were connected to a Geode Exploration Seismograph located in an operation box at the edge of the soil plots. The Geode was controlled by a laptop operating the Seismodule Controller Software continuously during the full monitoring campaigns. An electromagnetic hammer (piston and base plate system driven by a 300 W audio speaker) was harnessed to provide an impact-like source that was activated at regular time intervals. The source frequency content was centered between

75 and 150 Hz. The hammer was controlled by a waveform generator (Agilent 33210A, located in the operation box) that was programmed to trigger an impact every 15 minutes. The function generator emitted a pulse waveform, with period of 15 minutes, high level of 4 V, low level of -1 V, width of 300 ms and edge time of 100 ns. Having only one source, the data were collected during three different time periods: from the 17th of May to the 26th of June (compacted ley), from the 26th of June to the 8th of July (non-compacted ley), and from the 25th of July to the 9th of August (compacted bare soil).

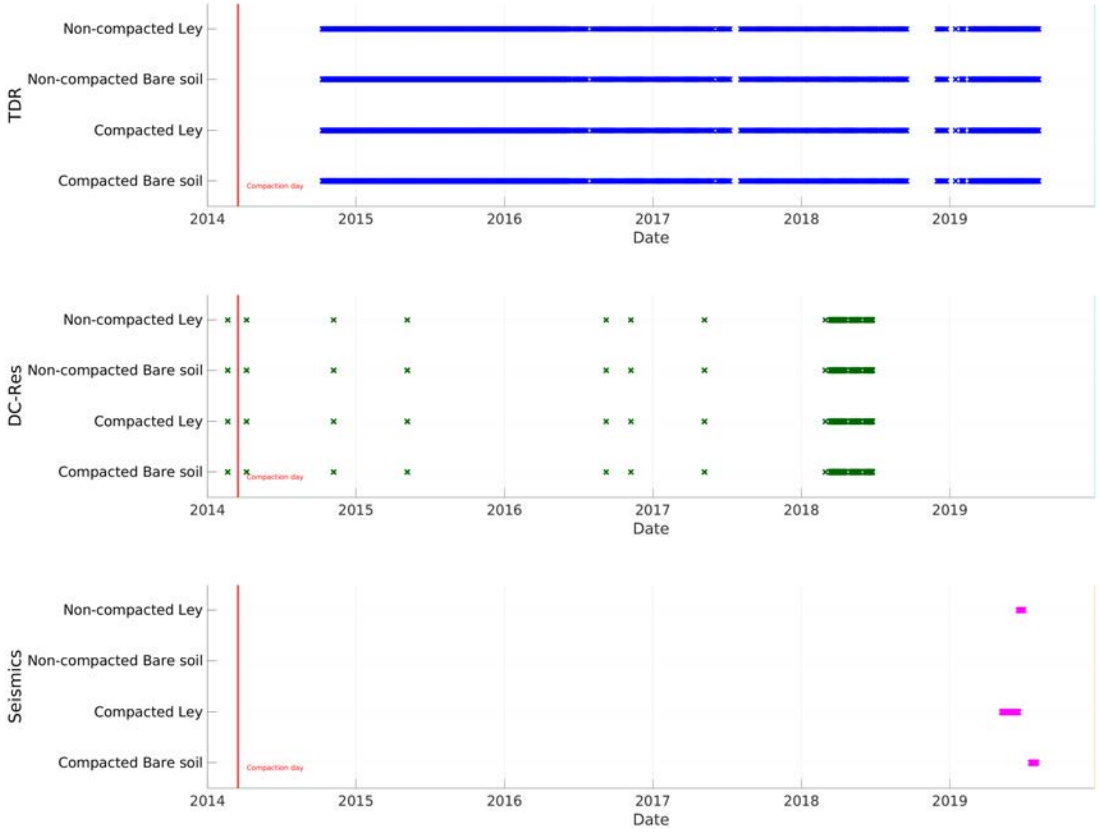

Figure 1.12 – Summary of periods for geophysical monitoring. We include data from DC-resistivity, seismic data and Time-Domain Reflectometry (TDR). The red line locates the day in which experimental compaction took place.

DC-resistivity monitoring

We performed seasonal (i.e., every six months or year) and hourly (i.e., every two hours) monitoring of DC-resistivity data (see summary in Figure 1.12). For the seasonal monitoring, the DC-resistivity acquisition array comprised two lines of 48 stainless steel electrodes: one line on the ley soil and the other on the bare soil. The electrode spacing was 1 m, resulting in 47.5 m long DC-resistivity lines (see Figure 1.8b). In order to improve spatial resolution, the electrode spacing was changed to 50 cm in the spring of 2015. With this change, 24 electrodes

were placed on the compacted treatment and 24 on the non-compacted treatment for each electrode line (see Figure 1.11a).

The hourly monitoring was conducted in the spring and summer of 2018 (see summary in Figure 1.12). The electrodes were connected to a 96-switch Syscal-Pro powered by a 12 V battery that were located in an operation box at the edge of the soil plots (see Figure 1.12). The Syscal-Pro was controlled by a laptop operating the Comsys-Pro geophysical software (see IRIS-instruments) continuously during the full monitoring campaigns. A DC-resistivity acquisition sequence was programed to be continuously repeated every two hours. More details of the DC-resistivity acquisition campaigns can be found in Chapter 4.

TDR

Time-domain reflectometry (TDR, TDR 100 by Campbell Scientific with MDX multiplexers) probes for soil water content measurements were installed in all plots, and were continuously collecting data at four different depths (10, 20, 40, and 70 cm).

1.7 Objectives and outline

Objectives

The main aim of this thesis was to advance non-invasive geophysical characterization of soil structure to complement established laboratory-based and field-based point-wise characterization approaches. For this, we set the following objectives:

- to identify the geophysical methods with the highest potential to characterize soil structure and areas of opportunity for the development of systematic characterization of soil structure.
- to develop frameworks for monitoring, modeling and interpretation in terms of soil structure for selected geophysical methods.
- to utilize the frameworks to interpret geophysical data acquired in a soil compaction experiment in terms of compaction effects and dynamics.

The geophysical methods selected for this thesis were the seismic method due to its sensitivity to the mechanical properties and contacts of porous media and the DC-resistivity method due to its sensitivity to pore space and water states.

Outline

In order to meet the established objectives, this thesis is structured as follows (the notation is different within each thesis chapter as Chapters 2-4 are reproduced article manuscripts):

- In **Chapter 2**, we present a review describing the role of geophysical methods in soil structure characterization. Within this review, we identified suitable geophysical methods that provide information about soil structural traits. We review past research regarding the correlation between geophysical responses and soil properties. Observation strategies and ways to establish theoretical links between detectable changes in geophysical properties and soil structure are also discussed. Finally, we propose an outlook of how geophysical observations can be used in combination with other measurements in order to quantify soil structural properties and dynamics.
- **Chapter 3** presents a field-based experimental study. It ultimately links soil mechanical traits derived from seismic monitoring and modeling with laboratory measurements of bulk density and field measurements of penetration resistance. We developed a pedophysical model that accounts for soil structure viscous deformation during compaction events and used the model to interpret seismic data monitored at the SSO. The model is used to interpret seismic signatures of persistent soil compaction five years after the compaction event at the SSO.
- In **Chapter 4**, we addressed the issue of soil structure characterization with geoelectrical methods. In this study, we aimed at understanding how geoelectrical monitoring can provide direct (via volumetric proportions and arrangement of constituents) and indirect (via impact on soil water dynamics) information about soil structure. We rely on a coupled hydrogeophysical modeling scheme to capture the prime signatures of soil structure on soil water dynamics and their corresponding geoelectrical signatures. To achieve this, we developed a suitable pedophysical model of electrical properties that provides a conceptual description of structured soils based on the connectivity between soil aggregates. The modeling framework is used to reproduce and interpret data from the SSO.
- Finally in **Chapter 5**, we summarize the main findings of this thesis and discuss possible research avenues that could further enrich soil structure characterization and evaluation with geophysical methods.

In **Appendix A**, we include the article by *Keller et al.* (2017). This scientific article describes the experimental design and monitoring concept of the SSO.

In **Appendix B**, we present an outreach article published in the Editors' Vox section of the news magazine Eos, published by the American Geophysical Union. The article follows the publication of our review article presented in Chapter 2, addressing the topic of soils structure characterization with geophysical methods in a Q&A format destined for large audiences. For the manuscripts presented in Chapters 2-4 and Appendix B, I contributed as the lead-author, while for the manuscript in Appendix A, I contributed as co-author.

Chapter 2

A review of geophysical methods for soil structure characterization

Alejandro Romero-Ruiz, Niklas Linde, Thomas Keller and Dani Or.

Published[1] in *Reviews of Geophysics* and herein slightly adapted to fit the theme of this thesis.

[1] Romero-Ruiz et al. (2020). A review of geophysical methods for soil structure characterization. *Reviews of Geophysics*, **56**(4) 672-697, doi:10.1029/2018RG000611

Abstract

The growing interest in the maintenance of favorable soil structure is largely motivated by its central role in plant growth, soil ecological functioning and impacts on surface water and energy fluxes. Soil structure pertains to the spatial arrangement of voids and solid constituents, their aggregation and mechanical state. As a fragile product of soil biological activity that includes invisible ingredients (mechanical and ecological states), soil structure is difficult to define rigorously, and measurements of relevant metrics often rely on core samples or on episodic point measurements. The presence of soil structure has not yet been explicitly incorporated in climate and Earth systems models, partially due to incomplete methodological means to characterize it at relevant scales and to parameterize it in spatially extensive models. We seek to review the potential of harnessing geophysical methods to fill the scale-gap in characterization of soil structure directly (via impact of soil pores, transport and mechanical properties on geophysical signals), or indirectly by measurement of surrogate variables (wetness, rates of drainage). We review basic aspects of soil structure and challenges of characterization across spatial and temporal scales and how geophysical methods could be used for the task. Additionally, we propose the use of geophysical models, inversion techniques, and combination of geophysical methods for extracting soil structure information at previously unexplored spatial and temporal scales.

2.1 Introduction

Soil structure is defined as the spatial arrangement of solid constituents (minerals and organic matter) and voids of soil (*Dexter*, 1988) and is a reflection of biological activity (earthworms, roots), abiotic factors (freezing-thawing, wetting-drying) or results from tillage operations in the soil. Soil structure dynamics occurs at vastly different temporal scales (seconds to centuries) and, although it fundamentally occurs at the pore scale, larger spatial scales (field, catchment, region) become relevant since a wide range of hydrological and ecological soil functions are governed by soil structure (*Stewart et al.*, 1990). A growing awareness of the key role that soil structure plays in providing soil ecosystem functions and services for all terrestrial surfaces (*Hamza and Anderson*, 2005; *Zhang et al.*, 2007; *Kibblewhite et al.*, 2008; *Nawaz et al.*, 2013; *Bronick and Lal*, 2005; *Keesstra et al.*, 2012; *Oertel et al.*, 2016) has motivated recent attempts to quantify this important but elusive soil trait at relevant spatial and temporal scales (*Besson et al.*, 2010a; *Keller et al.*, 2017; *Guimarães et al.*, 2017). For most of these services and functions, a desirable soil structure is one that is able to support a wide range of biological activity ranging from microbial communities (*Curtis et al.*, 2002) to mesofauna (e.g. earthworms, termites) and vegetation (*Oades*, 1993); organisms whose activity, in turn, contributes to the further development and maintenance of such desirable soil structure (*Young et al.*, 1998; *Colombi et al.*, 2018). This kind of well-developed soil structure facilitates fluxes of water and oxygen through the soil and makes these fluids available to plants, thereby, helping plant growth, promoting nutrient recycling and recharge of groundwater (*Maximilian et al.*, 2009; *Beven and Germann*, 2013; *Rabot et al.*, 2018). In contrast, a poor soil structure is one that restricts water infiltration and gas exchange, thereby, resulting in water runoff, soil erosion and unfavorable anoxic conditions that limit

plant growth and may trigger greenhouse gas emissions by anaerobic bacterial respiration (*Jordanova et al.*, 2011; *Berisso et al.*, 2012; *Nawaz et al.*, 2013; *Chen et al.*, 2014).

Several processes and mechanisms affect soil structure over multiple spatial and temporal scales. These processes are generally well known, including a reasonable level of quantitative understanding regarding soil structure degradation (e.g. compaction), however, our knowledge of soil structure generation, formation and recovery remains limited (*Keller et al.*, 2017). Mechanical and hydraulic stresses acting on or within the soil may generate or degrade soil structure. These stresses could either be produced by natural processes (both biotic and abiotic) or by human activity. Activities that cause degradation of soil structure include agricultural operations that may fragment aggregates and create compacted plow layers, compaction by heavy farm implements, and trampling by grazing animals (e.g. *Stewart et al.*, 1990; *Hamza and Anderson*, 2005; *Nawaz et al.*, 2013). Wetting-drying and freezing-thawing cycles induce swelling-shrinking effects in the soil and crack it. Biological activity plays a major role in soil structure formation and stabilization (*Dexter*, 1988; *Oades*, 1993). Earthworms and plant roots penetrate the soil and create biopores that provide preferential pathways for water and gas and help plants to proliferate their roots (*Bouchand et al.*, 2009; *Colombi et al.*, 2017; *Kroener et al.*, 2014; *Bottinelli et al.*, 2015; *Jarvis et al.*, 2016). Root exudates, bacterial fuselage and earthworm casting largely contribute to stabilization of soil structure (*Oades*, 1993). Soil structure generation and stabilization processes are slow and may take decades to centuries (*Håkansson and Reeder*, 1994; *Webb*, 2002). The large disparity between the characteristic time-scales of degrading processes (rapid compaction at the scale of seconds) and the exceedingly long regenerative processes (years to decades) has contributed to misconceptions regarding the nature of the damage. This is exemplified by contrasting the intensive efforts in quantifying compaction with the limited attention given to mechanisms of recovery during which the main damage and loss of productivity occur (*Keller et al.*, 2017). This bias propagates to reasonable characterization of compaction but virtually no measurements or metrics for soil structure recovery.

Quantifying soil structure non-invasively in space and time remains a challenge, involving the following four aspects: i) what are the soil properties that best represent soil structure? ii) how can we obtain information about these properties at the plot and field scale? iii) what is the characteristic spatial scale and variability of these properties? and iv) how do these properties evolve over time? Studies suggest that properties that capture the *soil structural form* (defined here as the pore size distribution, pore connectivity and pore stability) are important in many dynamic soil processes (*Stewart et al.*, 1990; *Keesstra et al.*, 2012; *Naveed et al.*, 2016; *Rabot et al.*, 2018). Laboratory measurements and imaging capabilities allow for detailed quantification of soil structure within individual soil samples (*Helliwell et al.*, 2013; *Schlüter et al.*, 2014). Such descriptions of soil structure are, however, obtained under laboratory (not *in-situ*) conditions. Furthermore, a major concern is that spatial and temporal undersampling is inevitable, which implies a limited capacity to infer spatial and temporal variations of soil structure and associated functions under natural conditions. In addition, there is limited knowledge on the potential bias occurring when findings from laboratory studies are extrapolated to *in-situ* conditions. Apart from inherent limitations of extrapolating soil structural information from point measurements, certain aspects of the system dynamic responses to rainfall or other forcings become observable only at certain scales (profile, plot,

catchment). Visual soil evaluation methods (e.g., *Guimarães et al.*, 2017) provide alternative means to examine the spatial variability of soil structure at the profile scale, yet, they are subjective, empirical, highly invasive and incapable of addressing soil structure dynamics. Considering the limitations of traditional characterization methods with reliance on point values and snapshots in time, we seek to expand the range of tools available for soil structure characterization at plot and field scales and across long time horizons by exploring the capabilities of geophysical methods to pick up signatures associated with structural features (rather than bulk properties).

In applied geophysics (e.g. *Telford et al.*, 1990) and hydrogeophysics (e.g. *Hubbard and Linde*, 2011), measurements of geophysical fields are used to infer spatial variations in the physical composition of the Earth in order to delineate geological boundaries, identify deposits of minerals, oil and gas, track the extent of groundwater and contaminants, etc. The analysis and interpretation of these upscaled geophysical-property models often relies on petrophysical relationships that link the inferred bulk geophysical properties with hydrological, transport and mechanical properties of interest (e.g. *Lesmes and Friedman*, 2005; *Mavko et al.*, 2009). Most such relationships were developed for consolidated porous rock formations, but their application has been widely extended to unconsolidated formations and soils. Efforts have been made in the last two decades to develop and standardize the use of geophysics for mapping soil properties (e.g. porosity, density, clay content) and state variables (e.g. water content, salinity). For instance, applications of geophysical methods to agricultural planning and management (farm and field scale) are extensively discussed in compilations by *Samouelian et al.* (2005) and *Allred et al.* (2008). The European Soil Data Centre published a series of reports containing detailed methodologies to systematically map soil properties using geophysical data (*Grandjean et al.*, 2009a,b; *Besson et al.*, 2010b). Geophysical methods have been used to delineate soil horizons (*Tabbagh et al.*, 2000; *Besson et al.*, 2004; *Muñiz et al.*, 2016), monitor water content (*Michot*, 2003; *Garré et al.*, 2011, 2013), map soil texture (*Sudduth et al.*, 2005; *Grote et al.*, 2010) and characterize the effect of tillage on soil properties (*Jonard et al.*, 2013). Most studies focus only on the estimation of soil bulk properties, which mask the *soil structural form* features that are critical for soil functioning. The application of geophysical methods to characterization of soil and near-surface fluxes seldom consider dynamic changes in the pore spaces in measurement interpretation (i.e., the soil domain is considered constant and unaltered).

Several studies have attempted to characterize soil compaction through effects of soil bulk density on changes in Direct Current-resistivity (DC-resistivity) (*Besson et al.*, 2013), by studying reflections of electromagnetic waves from soil compacted layers using Ground-Penetrating Radar (GPR) (*André et al.*, 2012; *Petersen et al.*, 2005; *Wang et al.*, 2016; *Muñiz et al.*, 2016) or by relating inferred seismic velocities to soil strength obtained from penetrometers (*Donohue et al.*, 2013; *Keller et al.*, 2013b). The motivation of most of the mentioned studies is grounded in the knowledge of how geophysical properties (e.g. electrical resistivity, dielectric permittivity, seismic velocities) respond to variations of soil bulk attributes (e.g., clay content, density, saturation). The impact of *soil structural form* properties (e.g., macroporosity and its connectivity) on geophysical data has not been considered systematically. Moreover, most laboratory experiments use soil samples that have been repacked (e.g., *Lu et al.*, 2004; *Seladji et al.*, 2010), thereby removing or suppressing the natural soil structure. Only a

few geophysical studies were devoted to investigate the sensitivity to soil structural form properties. For example, the detection of macropores using electrical measurements was studied by *Moysey and Liu* (2012) and the identification of preferential flow with electrical methods was reported by *Koestel et al.* (2008) and *Garré et al.* (2010).

Recent reviews (*Jayawickreme et al.*, 2014; *Parsekian et al.*, 2015; *Binley et al.*, 2015) describe how geophysics can be used to gain information about subsurface functions and processes in the critical zone. However, the scope and discussions in these reviews are general to bulk behavior of the shallow Earth (~ 100 m). Our review seeks to explore how geophysical techniques could complement traditional soil structure characterization techniques, help to obtain insights about soil structure and its dynamics and offer integrative ways of studying soil structure non-invasively at larger scales. For this, we seek to address three fundamental questions:

(a) are geophysical properties capable of providing information about structural features of soils beyond the already acknowledged links with soil bulk properties?
(b) what is the expected sensitivity of measured geophysical data to relevant soil structural properties?
(c) how to best combine different geophysical methods to obtain information on soil structure?

To address these questions we set the following objectives:

(I) to identify suitable geophysical methods that provide information about soil structural traits;
(II) to review past research regarding the correlation between geophysical responses and soil properties and the applications that have resulted from those relations;
(III) to devise observation strategies and ways to establish theoretical links between detectable changes in geophysical properties and soil structure;
(IV) to propose an outlook of how geophysical observations can be used in combination with other measurements in order to quantify soil structural properties and dynamics.

2.2 Geophysics for soil structure characterization: Concepts and challenges

Descriptions of soil structure focus either on representation of secondary pore spaces not associated with texture (e.g., biopores), or more generally, on the spatial arrangement, packing and mechanical properties of the solid phase such as aggregates and compacted layers (e.g., *Rabot et al.*, 2018). We will emphasize the pore space perspective due to its importance to soil ecological functioning (*Stewart et al.*, 1990; *Rabot et al.*, 2018), without neglect that compaction and aggregation are important soil structure components. The primary challenge is that bulk soil properties that are easy to measure (porosity or bulk density) offer limited insights about soil structure and functioning. To illustrate this, consider the schematic representation in Figure 2.1 (inspired by experimental observations presented by *Keller et al.* (2017)), in which the soil texture in the three panels is identical and the bulk porosity is similar,

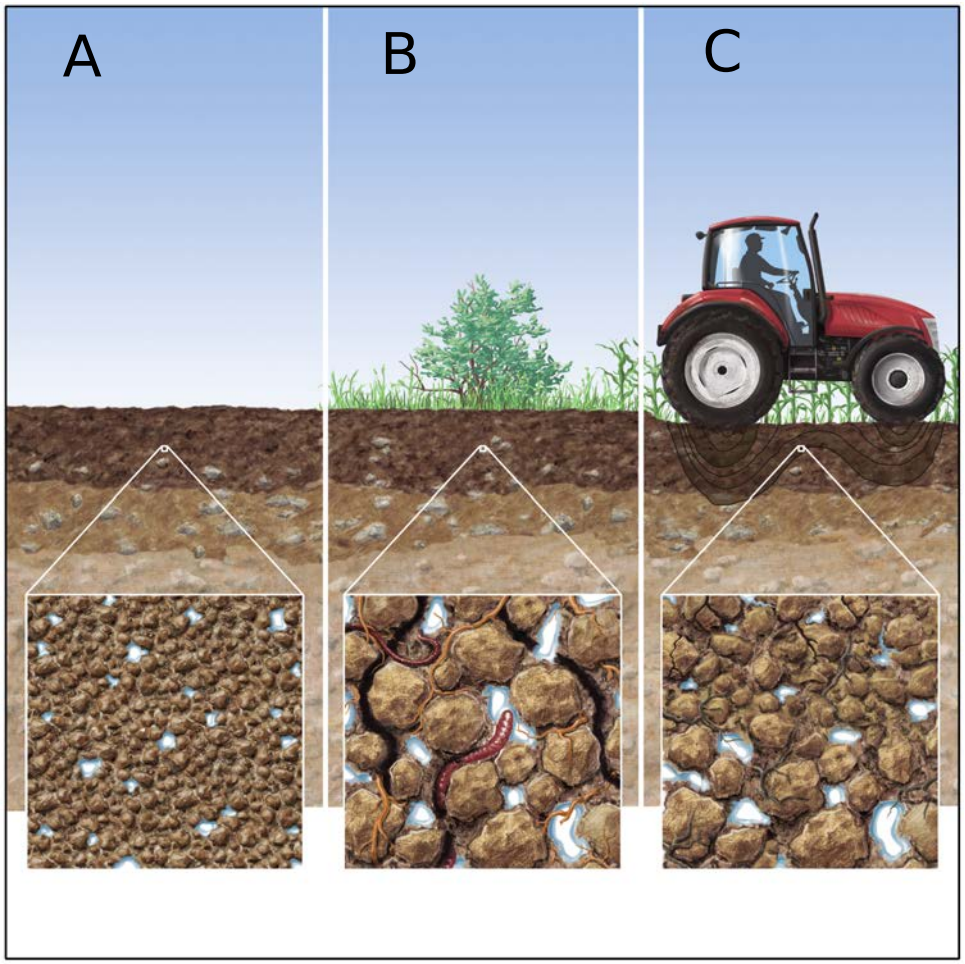

Figure 2.1 – Schematic representation of soil structure along a transect. Each panel corresponds to a different soil structure: homogeneous soil (A); the same soil with secondary biologically-induced structure (B) and soil structure from B as damaged by compaction (C).

the main difference is the different states of soil structure. Unfortunately, such nuanced views of structure related to soil pore spaces are difficult to quantify especially by geophysical methods that often cannot differentiate between soil traits of the different panels in Figure 2.1. Soils are likely to be treated as a homogeneous domain with no signatures of biological activity (our reference soil in Figure 2.1 depicted in panel A).

Soil structure is generally difficult to quantify, and selecting geophysical methods and measurement strategies for this task is not obvious. One approach is to capitalize on indirect effects of soil structure and select methods and observations sensitive to changes in soil structure (for example, enhanced drainage rates from soils with extensive biopores relative to soil with no structure or compacted). Such contrasting properties are schematically illustrated in comparison of panels A, which shows an homogeneous structure, and B, where earthworms and plants form channels and biopores and microorganisms stimulated by roots may excrete binding agents and promote aggregate formation. Soil biopores are an important element that differentiates soil structures. Despite contributing only to a small fraction of the entire soil porosity, soil biopores exert significant influence on water and gas transport and on

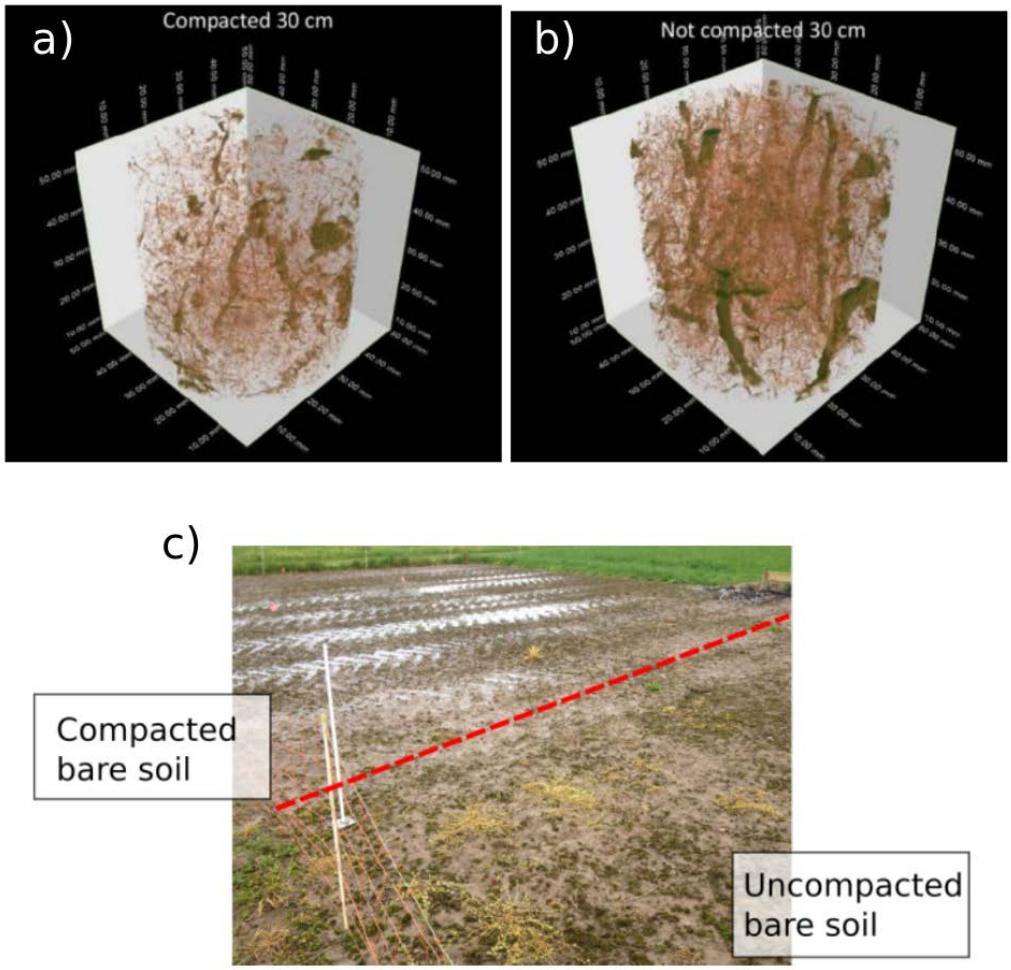

Figure 2.2 – Soil pore structure detectable by micro computed tomography (voxel size 60 μm, corresponding to a minimum pore width of 120 μm) of 100 cm^3 samples from (a) compacted and (b) uncompacted bare soil at 0.3 m depth sampled two weeks after the compaction event described by *Keller et al.* (2017). The samples were taken from the field shown in (c).

near surface hydrology and the mechanical environment for growing roots. For example, the biopores become preferential flow pathways for air and water, which may increase the overall saturated hydraulic conductivity of the soil by several orders of magnitude, thereby, increasing water and oxygen availability for plant roots. These channels may additionally facilitate formation of biological hotspots and regions of low mechanical impedance for roots to grow in. In panel C in Figure 2.1, we observe how a well structured soil has been degraded and compacted by the passage of farm implements. The stresses applied by the passing tractor have resulted in the collapse and disruption of the largest pores in the soil. This reduction in macropore volume leads to a concurrent decrease in saturated hydraulic conductivity and an increase in mechanical impedance to root growth. A key aspect that set the pore structure in Figures 2.1b and 2.1c apart from Figure 2.1a is the presence of heterogeneities in the pore network characteristics (e.g., structures of different sizes and tortuosities) that are clear in Figure 2.1b and diminished but still present in Figure 2.1c.

The effects of soil compaction on macroporosity are illustrated in the x-ray computer tomography images of soil samples from compacted (Fig. 2.2a) and uncompacted (Fig. 2.2b) soil in the same field experiment near Zürich, Switzerland (Fig. 2.2c) (*Keller et al.*, 2017). As the examples show, the reduction in overall porosities of the samples in Figs. 2.2a and b is only 0.04 (from 0.44 to 0.4) whereas the hydraulic conductivity has been reduced by half (from 195 to 78 mm/h), and the mechanical impedance measured by cone penetration nearly doubled (from 1.3 to 2.5 MPa). This example illustrate that compaction and subsequent soil structure recovery concern primarily soil macropores and the functionality they impart, and an important yet invisible ingredient, soil mechanical resistance. Our discussion of the impact of soil structure on geophysical signatures will be guided by this example where macroscopic properties routinely measured by geophysical methods show minute changes that do not capture the large impact on transport and mechanical behavior of the altered soil.

Considering the processes and interactions mentioned above, among the spectrum of geophysical methods, geoelectrical and electromagnetic methods with their inherent sensitivity to soil hydrological states are ideal candidates to asses the pore space and the influence of its different distributions on soil hydrology. Such methods include the DC-resistivity method (*Binley and Kemna*, 2005) targeting electrical conductivity, which depends strongly on pore space connectivity; the Induced Polarization (IP) method (*Kemna et al.*, 2012) that senses capacitive properties that depend on the pore size distribution; and the GPR method (*Annan*, 2005) that is sensitive to soil moisture, interfaces and cavities that could be associated with large roots or compacted layers.

Geoelectrical and electromagnetic methods, however, offer limited insights into the soil mechanical status. Soil mechanical properties (e.g., strength, elastic moduli) are better probed and characterized using shallow seismic methods (*Socco et al.*, 2010; *Foti et al.*, 2011; *Keller et al.*, 2013b; *Donohue et al.*, 2013). The sensitivity of seismic measurements to the mechanical states of the soil and wave interactions with inclusions offer opportunities for detection of compacted layers, aggregation and potentially large pores beyond what geoelectrical and electromagnetic methods provide. There is a wealth of experience and literature from geotechnical engineering on linking seismic signatures to soil mechanical states such as liquification resistance, penetrometer mechanical impedance, shear and bulk moduli, and soil density (e.g., *Sabba and Uyanik*, 2017; *Mandal et al.*, 2016; *Bhowmick*, 2017; *Yunmin et al.*, 2005). Additionally, cutting edge research into characterization of carbonate rock with vuggy pores (e.g., *Skalinski and Kenter*, 2014) offer a potential for using similar seismic measurements and methods for mapping large macropores.

A key step in the interpretation of geophysical methods is to define the links (and expressions) between the geophysical properties sensed and the soil properties and states of interest. In general, effective geophysical properties of a given heterogeneous volume composed by a multiphase porous medium (e.g. a soil) depend on two aspects: (i) a constitutive aspect, the geophysical property depends on the relative volumetric proportions of the constituents and their individual physical properties and (ii) a structural aspect, the geophysical property depends on the way in which the different constituents are spatially distributed in the volume and how they connect. Virtually all theoretically-based petrophysical models targeting electrical and mechanical properties were developed assuming an underlying structural model. However, emphasis in agricultural geophysics has been on estimating proportions

without always recognizing the impact of the structural model that is embedded in a given petrophysical model. Application of geophysical methods for the study of soil properties and structure hinges on the use and development of petrophysical models that consider changes in pore spaces, are sensitive to soil constituents, and account for structural features.

Intuitively, it is expected that a high seismic velocity is an indicator of a stiff soil rather than a loose soil, and that rapid rain infiltration as monitored by electrical methods suggests a well connected pore network and the presence of macropores. Such qualitative expectations exemplify the already discussed potential for using various geophysical measurements in space and time to infer soil structure. A major challenge is, however, the lack of a systematic quantitative approach in which geophysical methods are used to capture such signatures and interpret soil structure. In this context, advancing soil structure characterization requires a set of ingredients (some existing, some that require further development) that can be summarized as: (1) a set of geophysical methods that can sense the soil structural form (geoelectrical and electromagnetic methods) and the mechanical behavior (seismic methods) (2) a set of interpretation tools that focus on the signatures of the structural aspect of the geophysical response or property, (3) a framework of survey configurations, combination of methods and monitoring strategies that allow the inference of soil structure.

Soil structure information is important at the small scale of a plot or a field and at larger scales. For example, the parameterization of land-surface model often relies on the use of “pedotransfer functions" that relate soil attributes (often soil texture only) to hydraulic parameters. Recent studies have advocated for the urgent to include soil structure that could significantly affect infiltration and runoff in ways not predicted by soil texture (*Or et al.*, 2013; *Vereecken et al.*, 2016; *Hirmas et al.*, 2018). In addition, the trend of agricultural intensification and associated adverse impacts on soil compaction and structure are expected to affect food security (*Zhang et al.*, 2007). There is growing recognition for the importance of improving soil structure representation in Earth system models, geophysics may offer a critical role in providing such information at scales larger than the traditional point or sample scale measurements.

2.3 Geophysical methods in soil science

In the previous section, we described the general challenges and possibilities with soil structure characterization using geophysical methods. Here, we introduce selected studies that address soil properties using geophysical data. We discuss theoretical and empirical petrophysical relationships and supporting experimental evidence, as well as their use in a variety of soil science applications. The present literature review is not exhaustive, and we focus primarily on applications relevant to soil structure characterization. For more detailed introductions to the geophysical methods discussed herein, we refer to *Binley and Kemna* (2005) (DC-resistivity and IP), *Doolittle and Brevik* (2014) (EMI), *Annan* (2005) (GPR) and *Steeples* (2005) (seismic methods).

2.3.1 DC-resistivity method and Electromagnetic Induction

The DC-resistivity method is a method that measures spatially-distributed voltages resulting from current injections throughout an array of electrodes typically arranged on the soil surface or in boreholes. Electromagnetic induction (EMI) methods measure selected components of an electromagnetic (EM) field forming in the soil by induction in response to a prescribed EM field. Characteristics of the measured voltages or the induced EM field can be linked to subsurface electrical resistivity (*Telford et al.*, 1990). DC-resistivity and EMI are addressed together because they both respond to electrical resistivity (ρ) (or conductivity (σ), its inverse) although the underlying physical principles and sensitivity patterns are quite different.

Many authors (e.g. *Rhoades et al.*, 1976; *Corwin and Lesch*, 2003; *Samouelian et al.*, 2005; *Friedman*, 2005) discuss how soil electrical resistivity depends on the constitutive and structural aspects of soils that are captured by soil properties (e.g. bulk density and clay content) and state variables (e.g. soil salinity, water content, water saturation), their interactions and spatial arrangement. Significant research involving laboratory and field experiments has focused on the correlation between soil resistivity and one or more of these soil attributes. A suitable starting point is to combine the two experimental relations by *Archie* (1942) to express the impact of partial saturation on bulk electrical conductivity (σ) as:

$$\sigma = \phi^m S_w^n \sigma_w = \frac{1}{F} S_w^n \sigma_w, \tag{2.1}$$

where $F = \phi^{-m}$ is known as the electrical formation factor and quantifies the increase in resistivity of the porous volume due to the presence of the solid matrix (assumed an insulator). The dependence on the constitutive properties is given by the electrical conductivity of the pore fluid (strongly linked to the salinity) σ_w, the saturation S_w, and the interconnected porosity (porosity sensed by electrical current flow) ϕ. The cementation exponent m and the saturation index n account for the contribution related to the soil structural form. The parameter m, for example, can in combination with ϕ be used to predict tortuosity (*Nelson*, 1994). The physical meaning of the cementation exponent m was discussed by *Glover* (2009), in which the inverse of the formation factor is interpreted as the connectedness of the pore network. A higher value of m indicates a reduction in effective pore connectivity as exemplified by Figure 2.3 and is related to the geometry of solid particles (*Friedman*, 2005). In most published field studies, m and n are treated as known constants or as fitting parameters.

A major shortcoming of Equation 2.1 is that it ignores surface conductivity, which is significant in all soils and becomes an increasingly important contribution to bulk electrical conductivity with increasing clay content (*Revil et al.*, 2017). Multiple petrophysical models account for surface conductivity in saturated media (e.g., the empirical Waxman-Smits model, *Waxman and Smits*, 1968), in which surface conductivity (σ_s) acts in parallel to the conduction paths in the pore space (the so-called high-salinity limit). Other models are based on Effective Medium Theory (EMT) (e.g. *Bussian*, 1983). EMT models are preferred because they do not make restrictive assumptions implying that the pore and surface conductivity electrical current pathways are parallel. *Sen* (1997) used the EMT framework to discuss the effect of

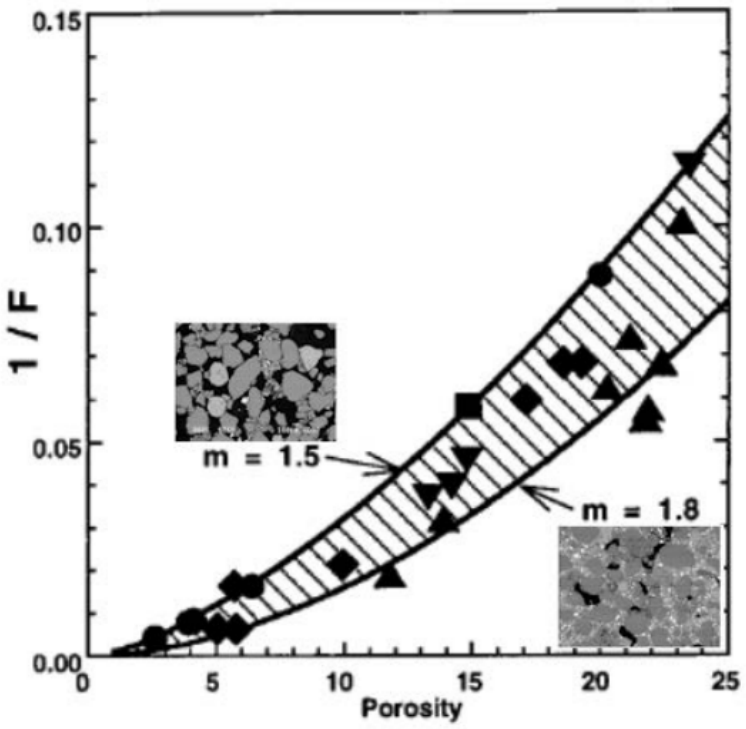

Figure 2.3 – Relationship between the inverse of the electrical formation factor and porosity in Archie's law (Equation 2.1). Two values of the cementation exponent are shown to illustrate how it affects the formation factor: $m = 1.5$ has a more connected pore network than $m = 1.8$ as shown in the photographies, where the pore space is black and the solid phase is gray. Modified from *Revil and Cathles* (1999)

different pore geometries and pore sizes on the electrical resistivity of rocks. In addition to the early work by *Waxman and Smits* (1968), models accounting for unsaturated conditions and surface conductivity (σ_s) have been proposed. For example, the model proposed by *Linde et al.* (2006):

$$\sigma = \frac{1}{F}\left[S_w^n \sigma_w + (F-1)\sigma_s\right], \tag{2.2}$$

was derived by volume averaging in the high-salinity limit. Other models can be found in *Wunderlich et al.* (2013) and *Cosenza et al.* (2009). Early models used to interpret electrical conductivity in soil science were often empirical (*Rhoades et al.*, 1989). Regardless of the considered parameters (and rules) that account for different structural forms, none of these petrophysical models considers explicitly the role of different types of heterogeneities in the pore network (e.g. biopores) nor makes a differentiation between pore sizes (e.g. micro and macroporosity).

Field and laboratory evidence of correlations between electrical resistivity and soil attributes abound. Note that some of the clear links presented below for well-controlled laboratory experiments are not easy to demonstrate under field conditions when soil moisture, pore properties and pore water conductivity change continuously and simultaneously. For example, *McCarter* (1984) measured the decrease in bulk resistivity with increasing water saturation by gradually compacting soil samples. The results suggest that the resistivity decreases with sample compaction. This is explained by increases in water saturation, and the growing contribution from surface conductivity. However, the relative change in resistivity caused by soil compaction is expected to be soil-dependent as many variables controlling electrical resistivity (e.g., porosity, pore connectivity, saturation, volumetric clay content) vary with compaction. For example, for the well structured agricultural soils shown in Figure 2.1b and Figure 2.2b, compaction reduces the percentage of macropores and its connectivity, but increases the contribution of surface conductivity. At a given partial saturation (implying unsaturated macropores) and salinity, the overall effect of compaction may, thus, be a decrease in the electrical resistivity of the soil. The work by *Doussan and Ruy* (2009) is intimately linked to soil structure. They demonstrate how unsaturated hydraulic conductivity can be predicted from electrical resistivity measurements at partial saturation by relating the pore diameter in the capillary equation with the characteristic pore diameter (proportional to the square root of the hydraulic conductivity) that results from applying percolation theory to porous media. Although their method requires exhaustive laboratory work (measurements of saturated hydraulic conductivity, electrical conductivity and clay content), their estimations of hydraulic conductivity are in good agreement with independent measurements. Laboratory experiments by *Moysey and Liu* (2012) demonstrated that the apparent electrical resistivity of samples decreased by 30% when adding 4% of saturated macroporosity (generated by removing rods and saturating the resulting pores). They proposed theoretical bounds for bulk electrical resistivity by considering the macropores as cylindrical tubes that fully penetrate a homogeneous soil matrix. They demonstrate that the relative effect of macropore activation on bulk resistivity depends on the ratio between the resistivity of the pore fluid and the bulk

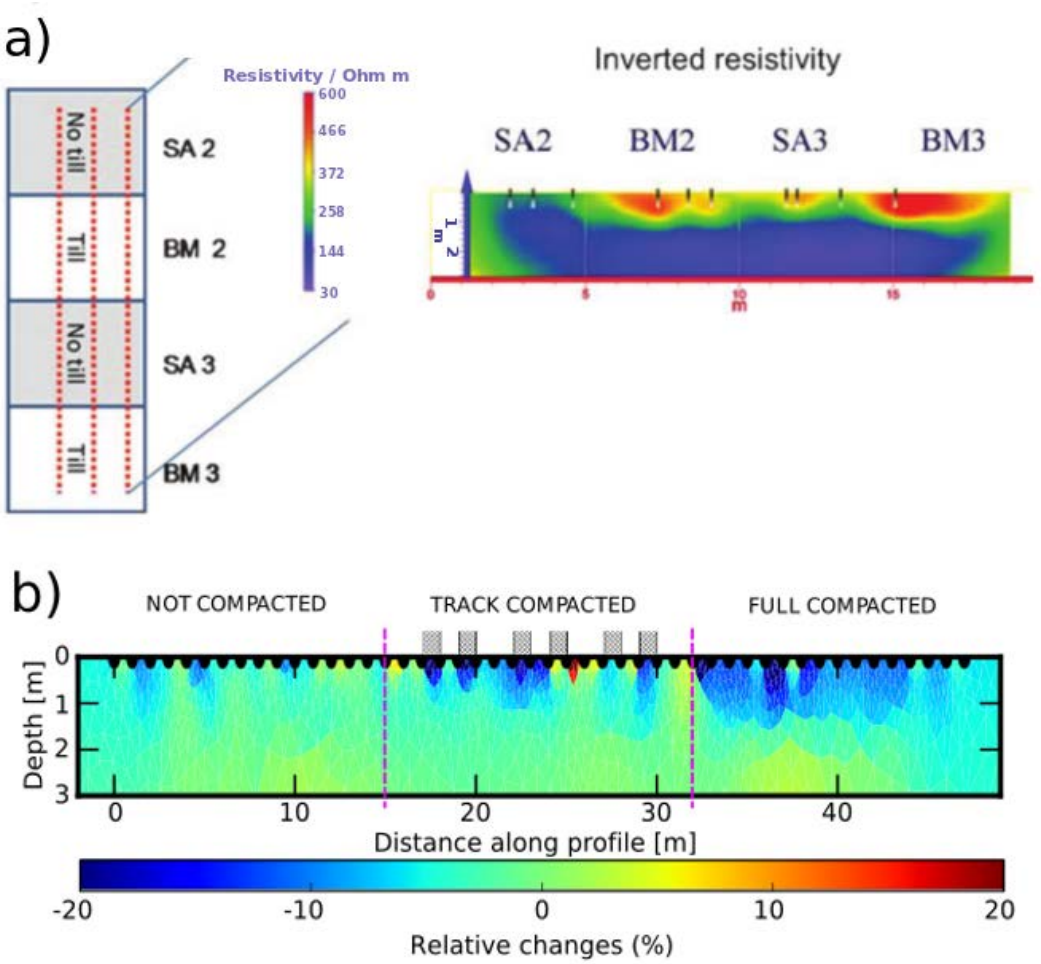

Figure 2.4 – (a) Experimental set-up of DC-resistivity measurements after the tillage experiment by *Rossi et al.* (2013a), soil electrical resistivity tomogram from data taken on one of transects in that cross the alternating tillage (BM2 and BM3) and non-tillage (SA2 and SA3) management regions. (b) Relative changes (before and after soil compaction) in inferred electrical resistivity of a soil (*Keller et al.*, 2017). Gray rectangles indicate track passages and the full compacted part was made by consecutive passages of tracks next to each other.

resistivity of the background soil. Note that the condition of “fully saturated macropores" may seldom apply to a real soil.

Several studies have observed a signature of soil compaction (e.g. decrease in macroporosity, increase in density, change in hydrological functions) on electrical resistivity. For example, *Michot* (2003) calibrated relationships between water content and resistivity for three different soil horizons and used them to obtain water content sections from DC-resistivity tomograms. After irrigating the field in the first day of the experiment, they monitored the water content sections for ten days and attributed low temporal variations of water content to zones that had undergone compaction. They discuss, how this could be attributed to a reduction in hydraulic conductivity; this is in agreement with results presented by *Richard et al.* (2001). As mentioned above, laboratory experiments by *McCarter* (1984) showed that soil resistivity decreases in response to an increasing effective saturation due to compaction

or increasing water content (especially for low moisture). These effects have also been captured in the field. *Besson et al.* (2004), for instance, studied the correlations of bulk density and electrical resistivity. They performed laboratory and field experiments to demonstrate that electrical resistivity is inversely correlated to changes in bulk density and, based on their observations, concluded that the DC-resistivity method has potential for delineating structural features such as the plough pan, wheel tracks and compacted soil lumps. The evolution of soil resistivity following compaction was studied in a one-year long field experiment by *Besson et al.* (2013). Along with DC-resistivity, they monitored soil water content and temperature, and performed periodic measurements of density via soil coring in compacted and non-compacted soils. Their results show that effects of compaction in electrical resistivity, attributed to changes in bulk density and water content, persisted after one year of monitoring. *Rossi et al.* (2013b) studied the effect that tillage has on DC-resistivity data. Their set-up contained DC-resistivity profiles located perpendicular to a plot with an alternating tillage pattern (Figure 2.4a); high resistivity anomalies are observed in the tilled zones. They suggested that the electrical heterogeneity was brought by soil break-up due to tillage, yet they emphasized the difficulty in recognizing effects of tillage as they were to some extent masked in the natural electrical variability of the soil. Clearly, this type of effects are best studied using a reference baseline prior to a perturbation (e.g., tillage or compaction). Figure 2.4b shows changes in electrical resistivity of a soil following compaction (see also *Keller et al.*, 2017). with electrical resistivity dropping up to 15 % in the compacted zones, which in this study was primarily attributed to increases in soil surface conductivity. It must be highlighted, however, that uncertainty in time-lapse DC-resistivity measurements increases when soil structure changes occur due to agricultural machinery, since the process of removing and replacing the electrodes will introduce position changes that may impact the data and subsequent inversion results. As discussed previously, changes in soil structure introduced by compaction and tillage are expected to affect electrical resistivity, and current petrophysical models (e.g., equations 2.1 and 2.2) may offer limited means to interpret these signatures.

Daily and seasonal variations in soil temperature are important to consider due to their potential effects on electrical resistivity (+1 ^{o}C may yield 2% decrease in electrical resistivity) and dielectric measurements by GPR and Time Domain Reflectometry (TDR) (*Or and Wraith*, 1999). To account for thermal effects on geophysical measurements, a correction is applied to measured electrical resistivity or dielectric permittivity (ϵ) values, these corrections are discussed in *Besson et al.* (2008) and in *Or and Wraith* (1999).

Considering the current state of the literature, we consider soil electrical resistivity as a valuable property for studying soil structure. It is one of the most commonly used geophysical properties in soil investigations and it carries information about a wide range of soil properties. This multitude of sensitivities can be seen both as an advantage and a disadvantage. We identify that there is a need to extend existing petrophysical relationships to consider aspects related to soil structure (e.g., macroporosity) together with associated laboratory experiments. Existing methodologies for estimating electrical resistivity (surface configuration, inversion techniques, etc.) are well developed and adapted to different spatial scales.

2.3.2 Induced Polarization

The induced polarization (IP) method is an extension of the DC-resistivity method. This method has a strong potential for soil structure characterization and deserves further attention, given that the mechanisms (e.g. polarization of grains and pore-throats) that govern the IP responses occur mainly at the interface between the pore space and the solid matrix (*Kemna et al.*, 2012). This should imply that IP properties are strongly linked to the structural aspect of the studied soils. For example, in the context of groundwater studies, *Slater* (2007) provides a discussion about the value of IP properties to estimate hydraulic conductivity in aquifers. In time-domain IP (TDIP), the main geophysical property targeted is the chargeability ($M = V_s/V_p$), defined as the ratio between the secondary voltage (voltage immediately after the current is shut off, V_s) and the primary voltage V_p (*Binley and Kemna*, 2005). In spectral IP (SIP), the frequency dependence of the complex electrical conductivity ($\sigma^* = 1/\rho^*$) is measured by applying alternating currents (*Kemna et al.*, 2012). Interested readers may refer to *Robinson et al.* (2008) for examples of different instruments. IP properties are very sensitive to the specific surface area of the soil, which is determined mainly by the clay content and clay type. Indeed, IP measurements complement DC-resistivity measurements by constraining the contribution of surface conductivity to electrical conductivity. As mentioned above, the IP method is an extension of the DC-resistivity method and measurements can be made using a typical four electrode configuration. Yet, obtaining high quality IP data is technically considerably more difficult since cable shielding and special electrodes need to be used to avoid capacitive coupling overruling the polarization effect from the soil.

Rather than studying the chargeability, authors have often focused on chargeability normalized by the electrical resistivity: the so-called normalized chargeability ($MN = M/\rho$), which is strongly correlated with the clay content of the soil (e.g. *Börner et al.*, 1996). Interestingly, the chargeability and resistivity do not carry conclusive information on soil clay when considered separately. The capability of the normalized chargeability to discriminate zones was studied by *Slater and Lesmes* (2002). They observed a clear lithological anomaly in their MN sections that was not present in their ρ and M sections. Thus, it is preferential to work with the normalized chargeability as it generally presents a linear dependence on the cation exchange capacity and clay per unit of volume (*Weller et al.*, 2013). The TDIP method is comparatively underused in soil science, partly because of the perceived difficulty to obtain high-quality field data (low signal-to-noise ratios and EM coupling effects) and the relative lack of predictive and robust petrophysical models that link IP parameters to soil properties. Recent laboratory studies on soil samples by *Revil et al.* (2017) are expected to promote its use.

We argue that SIP parameters have a great potential to offer insights about the structural form of the soil. The Cole-Cole model, for example, is an empirical model that links the frequency dependent complex electrical conductivity to a relaxation time (often assumed to depend on either the grain size or the pore size) and an exponent that depends on the width of the grain size distribution (*Friedman*, 2005). Qualitatively, *Ghorbani et al.* (2008) observed the effect of macroporosity on the complex electrical conductivity. In an infiltration experiment, they observed a drop in the phase of the complex conductivity that coincided with the time at which the macropores became saturated by the water front (as measured by a tensiometer).

This “two-stage" behavior of the phase data was interpreted as a decrease in the net polarization produced by the diffusion of ions from wet aggregates to the saturated macropores as they were filled with water. Based on this, they suggested that SIP parameters could be used to monitor the saturation and desaturation of macropores in soils. This result is in good agreement with laboratory work by *Breede* (2013). Here, the measured variations with saturation on SIP properties in repacked soil samples (mixtures of sand and clay) were qualitatively attributed to polarization effects related to saturation and desaturation of heterogeneous pore spaces.

The SIP method is still under development; the current state-of-the-art is reviewed by *Kemna et al.* (2012). The experimental evidence addressed in this section suggests that future developments and improved understanding of polarization properties of structured soils will eventually give IP methods a central role for characterization of the structural form of soils.

2.3.3 Ground-Penetrating Radar

GPR is a high-frequency EM method that is governed by a wave equation. In the typical set-up, an electromagnetic pulse is transmitted by a transmitter antenna placed in contact with the surface of the soil and the response is measured over time using a second receiving antenna placed at a fixed distance. The system is moved along a profile while repeating the measurements with a short measurement interval (for more details please refer to *Annan*, 2005). The GPR response is given by the interaction of EM waves at the soil-air interface, its propagation through the soil and scattering at interfaces. At GPR frequencies, the propagation velocity (v) and the reflexion coefficients of EM waves depend mainly on the relative permittivity of the medium in which it is traveling following (so-called dielectric constant). The dielectric constant is defined as the ratio between the dielectric permittivity of the medium (ϵ_{medium}) and vacum (ϵ_{vacum}) ($\kappa = \epsilon_{medium}/\epsilon_{vacuum}$). It is related to v as:

$$v = \frac{c}{\sqrt{\kappa}}, \tag{2.3}$$

where c is the speed of light in a vacuum. The dielectric constant of water ($\kappa \approx 80$) is widely different than the dielectric constant of both the matrix minerals ($\kappa \sim 5$) and the air ($\kappa \approx 1$). For this reason, the GPR propagation velocity is strongly dependent on the water content and the scattering of GPR signals are mainly caused by variations in water content.

Some of the most widely used models that relate the dielectric constant to the soil constituents are purely empirical. For example, the Topp model (*Topp et al.*, 1980), in which the predicted dielectric constant depends only on the soil water content through a polynomial relationship, is given by:

$$\kappa = 3.03 + 9.3\theta + 146\theta^2 - 76.7\theta^3. \tag{2.4}$$

More theoretically-based parametrizations are preferred as they consider different soil properties and assume a certain structure. For example the volume averaging relation proposed by *Linde et al.* (2006) connects the dielectric constant to soil properties by:

$$\kappa = \frac{1}{F}\left[S_w^n \kappa_w + (1 - S_w^n)\kappa_a + (F-1)\kappa_s\right], \tag{2.5}$$

where κ_w, κ_a and κ_s are the dielectric constant of water, air and the soil matrix, respectively; or the Lichteneker-Rother model (e.g., *Roth et al.*, 1990):

$$\kappa = \left[\theta \kappa_w^\alpha + (1-\phi)\kappa_s^\alpha + (\phi - \theta)\kappa_a^\alpha\right]^{\frac{1}{\alpha}}, \tag{2.6}$$

with typically $\alpha = 0.5$, more generally, $\alpha = 1/m$, where m is Archie's cementation exponent (*Brovelli and Cassiani*, 2008).

The applicability of GPR in soil-related field-based studies has been widely reported in the literature. For instance, *Grote et al.* (2003) derived a site-specific petrophysical relationship from soil samples and used it to investigate the accuracy of soil moisture estimations obtained from GPR surveys. The comparison between moisture estimations using GPR and sample measurements show correlation coefficients as high as 0.98 for 900 MHz data and 0.92 for 450 MHz data. The travel time to a reflected layer measured by GPR was used by *Lunt et al.* (2005) to estimate water content in a Californian vineyard where they had certain knowledge about the presence of a reflective layer in the soil. They calibrated a site-specific relationship between dielectric constant and water content and used it to map water content. *Krueger et al.* (2013) used a combination of EMI and GPR to map soil depth and used these estimations as input in a grain yield model. The accuracy of the model used to predict grain yield was improved by using such a geophysically-assisted approach. *André et al.* (2012) attributed GPR reflections in a transect across a vineyard to soil compaction. Zones with strong reflections present a compacted soil profile and a poor development of the vine in comparison to a weak reflection in an uncompacted zone where the vine presents a higher development. *Di Matteo et al.* (2013) discussed the effects of near-surface dielectric constant (with a sensitivity to depths on the same order of magnitude as the EM wavelength in the soil) on early time GPR amplitudes; these concepts were confirmed by numerical simulations. In fact, the dielectric constant is highly correlated to the amplitude of early GPR signals. These findings were used by *Algeo et al.* (2016) to map soil water content using GPR amplitudes in a field-scale experiment.

With respect to soil structure and compaction, *Petersen et al.* (2005) explored the value of GPR, EMI and refraction seismics to asses soil structural changes caused by soil compaction. For the compacted soil, they observed strong reflections in GPR signals under humid conditions. The contrast in dielectric constant that was causing these reflections was attributed to layers of variable water content that were considered indicators of soil compaction. *Wang et al.* (2016) used GPR data to study the correlation between soil properties and GPR wave speeds in compacted soils (both laboratory and field). Their results show that the wave speed (i.e. also

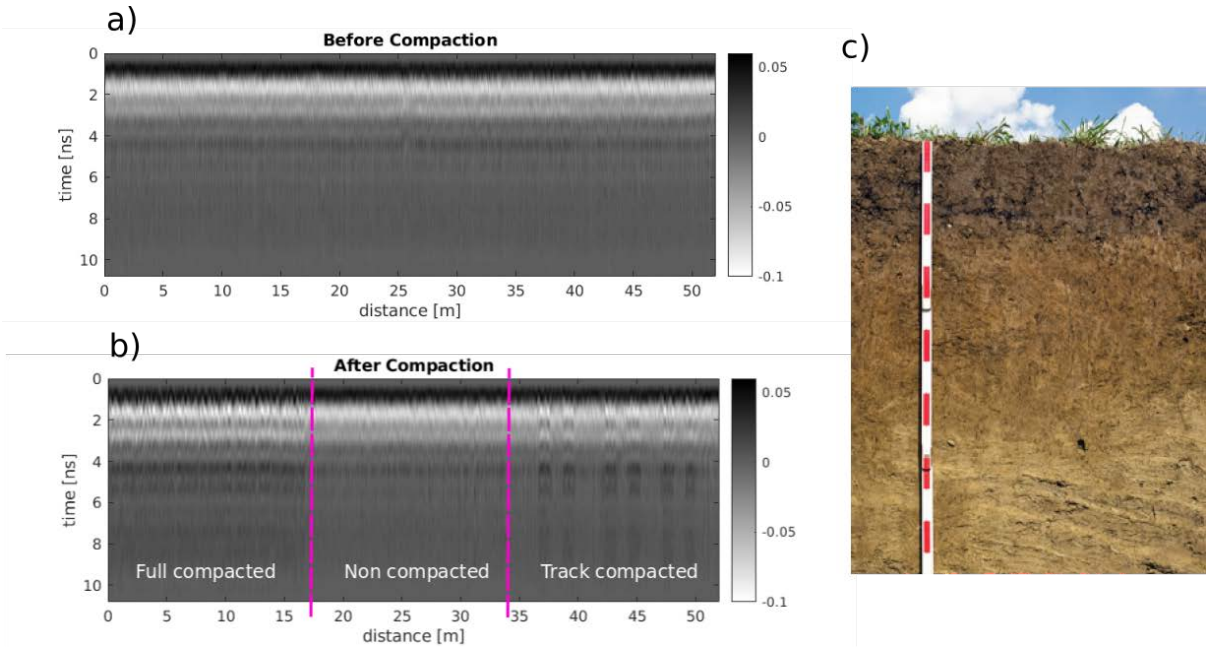

Figure 2.5 – GPR spatial identification of compacted zones in a compaction field experiment (described by *Keller et al.*, 2017) in Zürich, Switerland. (a) Data collected before the compaction event. (b) Data collected after the compaction event at the same location. (c) Soil profile from a non-compacted zone in the experimental field. The red and white color in the ruler alternate every 10 cm.

dielectric constant) is influenced by water content, bulk density and penetration resistance, they did not provide an equation describing these relationships because of insufficient data. Figure 2.5 shows GPR data collected with a 800 MHz monostatic antenna at the experimental field (soil profile similar to Figure 2.5c) described by *Keller et al.* (2017). The data were collected in a soil transect at two stages: before compaction (Figure 2.5a) and after (Figure 2.5b) the compaction of certain zones by a passing tractor. Note that the water content at the times of measurements of Figures 2.5a and 2.5b were similar in the non-compacted treatment. However, the water content of soil transects that underwent compaction is expected to be lower. A zero time correction was applied to the data, followed by DC-shift filter and a linear gain function. It is possible to identify the compacted zones based on features that appear in the data. For example, the post-compaction radargram shows an enhancement of signal amplitudes over the soil regions that underwent compaction.

The main value of the GPR method is its ability to estimate water content at a high spatial resolution (*Klotzsche et al.*, 2018). It offers estimates of soil moisture that are useful to account for dynamics of water losses (evaporation, root water uptake). Furthermore, it has have the potential of providing information related to natural layering and layering introduced by compaction. Survey designs and acquisition systems are relatively well developed, but readily-available and accurate techniques for quantitative interpretation of GPR data are more limited. A major limitation of the GPR method in soil science investigations is that the signal is highly attenuated in electrically conductive soils (high clay content).

2.3.4 Seismic methods

Seismic methods involve the measurement of ground displacement velocity (or acceleration) generated by compressional and shear waves produced by (most often) an artificial source (e.g., dynamite explosion or hammer impact). The use of seismic methods in soil science studies is not as common as electrical or EM methods. Nevertheless, seismic wave fields contain information about the mechanical properties of the subsurface and may offer insights about soil structure that other geophysical methods can not provide (*Keller et al.*, 2013a).

For an homogeneous media, seismic velocities (pressure wave v_p and shear wave v_s) are related to elastic moduli and density through:

$$v_p = \sqrt{\frac{K + 4/3\mu}{d}}, \tag{2.7}$$

and

$$v_s = \sqrt{\frac{\mu}{d}}, \tag{2.8}$$

where K is the bulk modulus (or compressibility modulus), μ is the shear modulus and d is the density. The elastic moduli of a porous medium (especially soils) are complex functions of the individual properties of the components of the mixture. Various relationships exist that link elastic moduli to, for example, porosity (see *Schmitt* (2015) for a review of the most common relationships). One of the most widely used are *Hashin and Shtrikman* (1963) (HS) relationships, which bound the elastic moduli of a mixture of grains and pores.

The bulk modulus of water is generally greater than that of the background dry matrix in unconsolidated soft materials like soils, so the impact of water content on the effective elastic properties of a soil is central, yet not fully understood and a cause of controversy in the scientific community (e.g. *Shin et al.*, 2016). The theory of elastic wave propagation through a multiphase porous material proposed by *Brutsaert and Luthin* (1964) is often used to study the influence of water content on p-wave velocity. It predicts:

$$v_p = \sqrt{\frac{0.306\, a\, p_e^{1/3} Z}{d\, \phi\, b^{2/3}}} = \sqrt{\frac{\frac{0.306\, a\, p_e^{1/3} Z}{\phi\, b^{2/3}}}{d}}, \tag{2.9}$$

where a and b are fitting parameters that largely depend on the elastic properties of the background dry matrix (*Shin et al.*, 2016), p_e is the effective pressure that depends on the capillary pressure (indirectly related to water content by the soil characteristic curve) and Z is a function of the degree of saturation or, more specifically, of the effective bulk modulus of the mixture of fluids (water and air) in the pore space. Equation 2.9 describes the dependency

of the p-wave velocity on the saturation (encoded in Z) and effective pressure. In such a description, the conceptualization underlying the calculation of the effective bulk modulus of the fluid mixture plays a predominant role and may determine the trend of the relationships between p-wave velocity and saturation. For instance, the effective bulk modulus will be very different if using arithmetic or harmonic (for which Z reduces to 1 for almost the entire range of saturations) weighted averages of the bulk modulus of the two fluids (*Domenico*, 1977). When measuring the p-wave velocity over a certain spatial and temporal scale, such simple assumptions do not well explain the actual water phase distribution as it is affected by many processes (infiltration, drainage, evapotranspiration) and it is very unlikely that the same mixing rules apply at all times (e.g. the empirical relation by *Brie et al.*, 1995). There are also other effects of water content (or saturation) on the p-wave velocity: indirectly by its impact on water potential and directly by its impact on density.

Lu and Sabatier (2009) performed a two-year long field experiment to study the above-mentioned effects of saturation and matric potential on the p-wave velocity by using Brutsaert and Luthin's theory. They instrumented a trench in a soil to measure p-wave velocity, water content and matric potential and back filled it with a soil mixture. They assume that $Z \approx 1$, which corresponds to a homogeneous distribution of the water in the pore space. Their results show that p-wave velocity relates to matric potential in good agreement with the predictions by *Brutsaert and Luthin* (1964). They observed a decreasing of p-wave velocity with increasing water content. Using Equation 2.9, this counterintuitive result can be understood as a consequence of the reduction of the capillary force acting on the soil particles and (to a lesser extent) an increase of the bulk density, leading to a decrease in the nominator (bulk moduli) and increase in the denominator of Equation 2.9 respectively. A more detailed discussion can be found in *Shin et al.* (2016). Brutsaert and Luthin's theory does not consider the relative movement between the solid and fluid phases, so dissipation of energy associated with such phenomena is ignored. Furthermore, the soil studies by *Lu and Sabatier* (2009) was performed on an artificial soil mixture, without a well-developed structural form; a situation for which it is reasonable to assume $Z = 1$ (c.f., panel A of Figure 2.1). Soil aggregation in a well-structured soil and consolidation of the solid matrix should reduce the relative effect of the capillary forces on the bonding of particles. *Flammer et al.* (2001) measured p-wave velocities and water content in undisturbed soil samples and observed a high sensitivity of the velocity to the distribution of water in the samples that was in turn influenced by preferential flow in macropores. For this reason, we expect Z to be a time-varying function and the appropriate way to derive it for a heterogeneous water-air mixture is an open question.

Unlike in geotechnical applications and reservoir characterization, seismic methods are relatively underused in soil characterization for ecological and agricultural applications. We have mentioned the potential adaptation of some of the methods to characterize soil compaction, and even soil structure by drawing analogies with petrophyiscal approaches used in characterization of carbonate reservoirs (*Skalinski and Kenter*, 2014). The Multichannel Analyses of Seismic Waves, has been widely applied in civil engineering studies (e.g. *Xia et al.*, 2000; *Park et al.*, 2002, 2007) to map shear wave velocities, known to be strongly linked to different soil mechanical properties (e.g., *Socco et al.*, 2010; *Foti et al.*, 2011). For example, the shear wave velocity has been related to the liquefaction resistance in soil samples by *Yunmin et al.* (2005). *Sabba and Uyanik* (2017) presented an empirical exponential relationship between

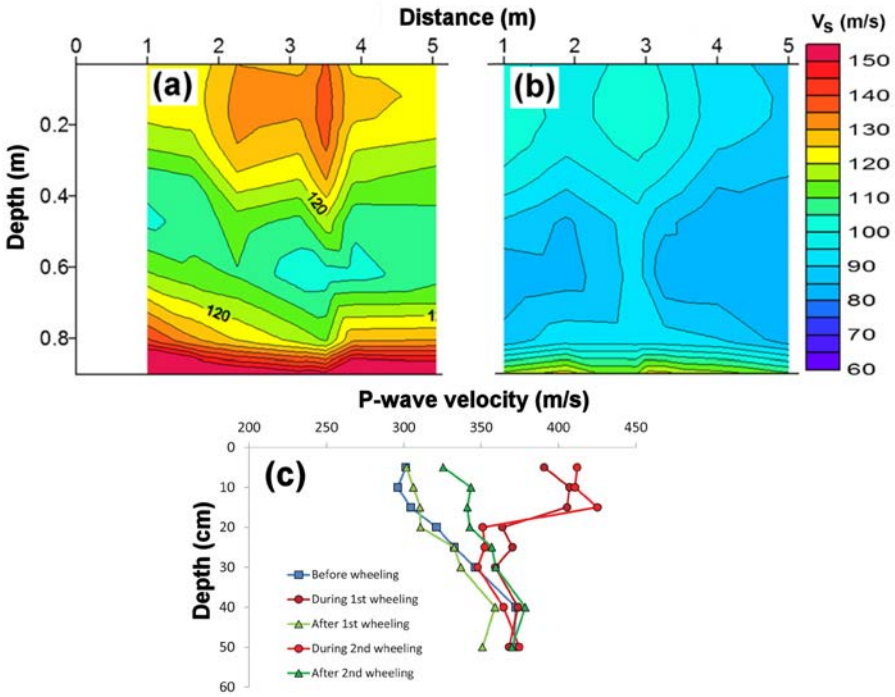

Figure 2.6 – The sensitivity of seismic measurements to soil compaction and load: S-wave sections from Multichannel Analysis of Seismic Waves (MASW) deduced from a compacted zone (a) and a non-compacted zone (b), note lower S-wave velocities for the non-compacted soil (from *Donohue et al.*, 2013); and (c) p-wave velocity with depth measured in a wheeling experiment marking changes during load application and after passage of the wheel (from *Keller et al.*, 2013b).

the uniaxial compressive strength (UCS) of samples of reinforced concrete and their shear-wave velocities ($R^2 \sim 0.90$). An interesting study for soil structure was presented by *Mandal et al.* (2016) for linking soil strength with p-wave velocities. They measured flexural strength and p-wave velocities of different types of soils that were stabilized with different binders. Their study shows that minute changes in soil bulk density may induce significant impact on seismic velocities. Similar effects are induced by soil biological activity with cementation and increase in strength and creation of stable aggregates. The principles of MASW methods have been successfully used for in-situ studies, for example, the methodology employed by *Ryden and Park* (2006) to determine the thickness and shear velocities of pavement layers. These concepts have already been used in other systems with similar characteristics (e.g. permafrost study by *Dou and Ajo-Franklin*, 2014).

Penetrometer mechanical impedance is an important soil trait that affect root growth and other aspects of soil biological activity (*Ruiz et al.*, 2015). In a manner similar to artificial cementing experiments of *Mandal et al.* (2016), near-surface seismic measurements offer a relatively direct window to quantify soil stabilization by biological agents. Some authors have proposed to use estimations of seismic velocities in combination with parameters derived from penetrometer resistance measurements to estimate bulk density by using empirical relationships (*Burns and Mayne*, 1996; *Mayne et al.*, 1999). For example, the dynamic resistance is related to the maximum shear modulus of the soil by *Lunne et al.* (1997)

and *Mayne and Rix* (1993). Then, the density could be derived by the combination of these empirical relations with Equation 2.8. More interestingly, seismic velocities have shown to be correlated with penetrometer resistance measurements, thereby, confirming the link between the seismic velocities and the mechanical impedance of soils. For example, *Donohue et al.* (2013) explored the possibility of using multichannel analysis of seismic waves for detecting soil compaction. They obtained a rather strong (R^2 = 0.66) correlation between inverted shear wave velocities and bulk density from sampled cores and penetration resistance taken in the field. The spatial distribution of the shear wave velocity is shown in Figure 2.6. Indeed, the soil in Figure 2.6a that was presumably compacted presents higher velocities and suggest the presence of a compacted layer in comparison with the soil in Figure 2.6b where a more homogeneous distribution of seismic velocities is observed. P-wave velocities were inferred during a wheeling experiment (passing of agricultural machinery) by *Keller et al.* (2013b). They inferred p-wave velocities at different depths along a soil profile crossing the traffic line at various stages (before, during and after wheeling). As shown in figure 2.6c, there is a strong increase in velocity during the first wheeling, a relaxation to its initial value between the first and second wheeling, a similar increment in velocity during the second wheeling and a relaxation to an intermediate value after the second wheeling. This illustrates the strong influence of soil structure on seismic velocities, yet quantitative interpretation is challenging with the existing tools. They also measured penetrometer resistance and took samples at various depths to measure bulk density. Their results show a correlation between p-wave velocity and bulk density and they reported a site-specific relationship between p-wave velocity and penetrometer resistance.

Despite the lack of a definitive understanding of the mechanisms that influence seismic velocities in soils, we argue that seismic methods are underused in studies of soil mechanical status and soil structure. In fact, the direct dependence of seismic waves on the soil mechanical properties make seismic methods essential for soil structure evaluation, given that they can resolve mechanical states that are not observable by other (e.g., geoelectrical) geophysical methods.

2.3.5 Other geophysical methods

We have discussed the geophysical methods that we consider best suited to address soil structure characterization. One should keep in mind, however, that a wide repertory of geophysical methods exist, and the usage of some of them may be relevant in this context (*Grandjean et al.*, 2009a; *Binley et al.*, 2015). For instance, the self potential (SP) method (*Revil et al.*, 2012) is a passive electrical method, in which naturally-occurring electrical potential differences are measured. The streaming potential contribution that is related to fluxes and water saturation is important in soils (*Doussan et al.*, 2002; *Jougnot et al.*, 2012, 2015) and can be associated to root water uptake or percolation following precipitation. Laboratory, borehole and surface based nuclear magnetic resonance (NMR) methods are sensitive to water content and, in some cases, to hydraulic conductivity (*Behroozmand et al.*, 2014; *Binley et al.*, 2015). Gravimetric measurements (especially time-lapse) can be useful to constrain estimates of hydraulic states and fluxes (*Blainey et al.*, 2007). The hyperspectral method uses the light reflected by the soil, which in turn is determined by its composition (texture, organic

matter, salinity) and could be useful to improve estimates of related properties (e.g., clay content) over large areas (*Ciampalini et al.*, 2015).

2.4 Opportunities for geophysical soil structure characterization

Following our review of geophysical methods and identification of current limitations for soil trait inferences, we evaluate next theoretical developments and applications of geophysical methods aimed specifically at resolving soil structural features directly or indirectly by examining the effects of soil structure on the soil system dynamics.

2.4.1 Petrophysical models of a structured soil: Pedophysical models

Petrophysical models are central to the interpretation of geophysical measurements. We have discussed some of their shortcomings for soil structure identification due to their reliance on volumetric proportions or neglect of key physical processes in their construction. A detailed treatment of the wide field that links geophysical responses with soil and geological material properties is beyond the scope of this review. We have presented several relationships for linking electrical conductivity to porosity (Equations 2.1 and 2.2), dielectric constant with water content (Equation 2.6) and seismic wave velocity with soil bulk density (Equation 2.9). However, the development of specific pedophysical relationships (associated to soils and not to rocks) is needed to include effects of soil structure on geophysical properties. A promising approach for incorporating soil structure is offered by effective medium theory (EMT) and related formalism (*Berryman*, 1995; *Friedman*, 2005).

In the absence of surface conductivity (a condition that hardly occurs in any soil), *Day-Lewis et al.* (2017) compared predictions of electrical petrophysical models that consider two porosity domains (Figure 2.7) with different salinities. One prediction is based on a simplified (assuming parallel conduction) weighted arithmetic average of the fluid conductivities and the other is derived using a variant of EMT called differential effective media (DEM) theory (*Bussian*, 1983). Predictions made by the latter model exhibit a very good match to pore network simulations of dual-domain solute transport. In this formulation, each porosity domain has its own cementation exponent (hence connectivity) and the interaction between the two conducting domains are accounted for. Furthermore, there is a functional relationship imposed between the two connectivities, thereby, limiting the number of free parameters. A similar parameterization could be pursued for aggregated soils by differentiating between inter and intra-aggregate pore space. Another example for which the shape and distribution of constituents has been studied extensively is dielectric mixtures (*Friedman*, 2005; *Wunderlich et al.*, 2013) where the arrangement of the phases or the shapes of the elements in the mixture affect the effective value of the upscaled petrophysical property (*Sihvola*, 1999).

The richness of EMT has been demonstrated by providing a rigorous basis for relationships that were proposed initially on empirical or ad-hoc basis. For example, the Hanai-Bruggeman

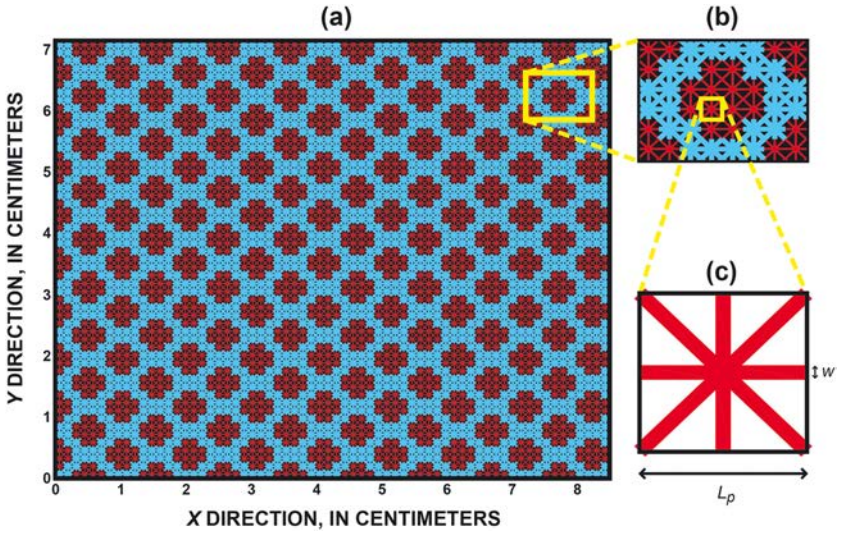

Figure 2.7 – (a) Diagram illustrating a bimodal pore network model (PNM) consisting of a pipe lattice with a given porosity (blue) between accumulations of zeolite grains (red) with (c) an internal porosity. From *Day-Lewis et al.* (2017).

mixing formula derived from DEM (e.g., *Bussian*, 1983), reduces to Archie's law when considering that conduction is dominated by the solute (see also *Sen et al.*, 1981). The exponent $m = 3/2$ results from considering spherical inclusions in the DEM formalism, and the different values of this exponent emanate from considering ellipsoidals with different eccentricities and orientations (*Cosenza et al.*, 2009). As for the high frequency permittivity, *Zakri et al.* (1998) demonstrated that the Lichteneker-Rother formula (Equation 2.6) can be derived from EMT by considering a symmetric Bruggeman mixing rule in which ellipsoidal inclusions parallel to the applied field are used and whose eccentricities follow a beta distribution. The inclusion of EMT formalism for soil structure characterization would require additional parameters and render the inference in field settings more complicated and less unique. To address some of this complexity, we will discuss shortly (Section 2.4.2) approaches that would harness concurrent measurements by different geophysical methods to better constrain the interpretation.

Laboratory investigations by *Moysey and Liu* (2012) show sensitivity of the electrical conductivity to the saturation of macropores in soil samples. This work (shown in Figure 2.8) demonstrated that even slight increases in active (saturated) macroporosity can produce considerable decreases in electrical resistivity and it proposed theoretical bounds by arithmetic and harmonic averages. These results illustrate that there is a measurable impact of macropores on electrical measurements and support our discussion that encourages the development of appropriate pedophysical models to capture such effects.

Mechanistic models describing IP responses are based on the assumption that the polarization process can be decoupled such that the contribution from each grain (or pore) can be summed up by a convolution operator. Furthermore, grain (and pore) polarization models are generally based on idealized geometrical shapes that might poorly describe actual pore structure. This might explain why the packing of identical matrix material has a strong IP effect, which cannot be captured by existing models (*Kemna et al.*, 2012; *Bairlein et al.*, 2014).

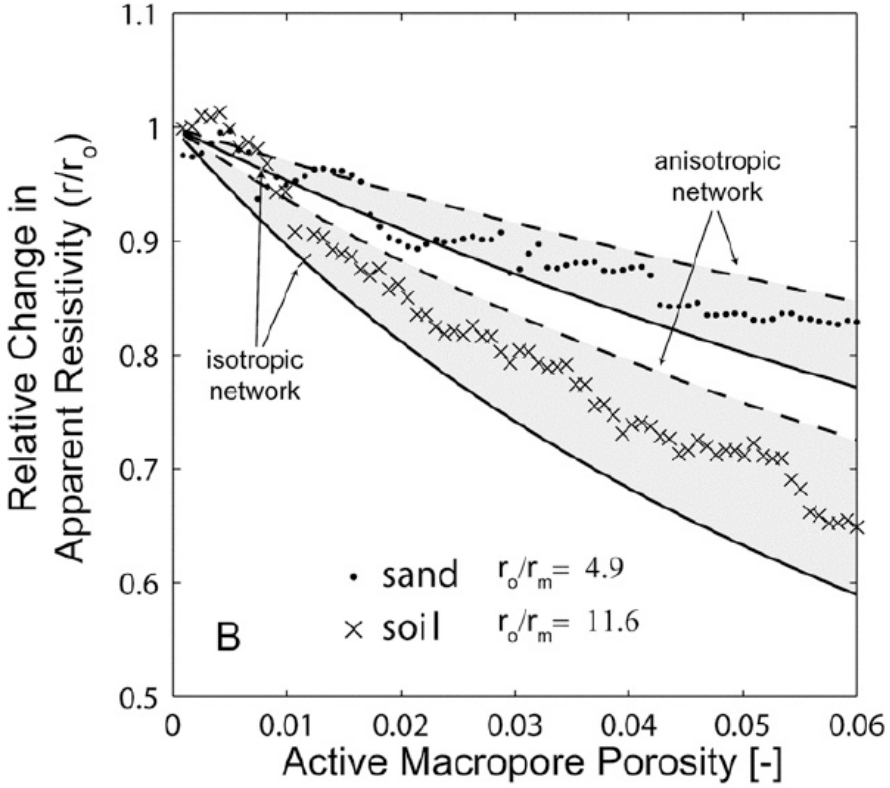

Figure 2.8 – Relative change in apparent resistivity as a function of saturated macroporosity. Symbols show experimental data for true (x) and sand (·) soils. Shaded areas indicate the region between the theoretical bounds derived for isotropic and anisotropic macropore networks. Here, r/r_0 is the ratio of the initial soil resistivity to the macropore resistivity (from *Moysey and Liu*, 2012).

To better understand the soil structure signature of the IP method, we suggest that laboratory work on undisturbed soil samples together with advanced soil structure imaging and modeling is needed.

Improving our understanding of the links between seismic properties and soil structure is an important and promising area that could enable non-invasive probing of the mechanical state of the soil by accounting for effects of structure on the seismic wave propagation. Changes in soil structure contain several invisible effects on soil function, primarily with loss of large pores and alteration of their topology (continuity), but even more subtle that these changes, are the alteration of soil mechanical resistance and strength that affect biological life in soil. The impacts of compaction and load on seismic velocities have been demonstrated in several studies including the aformentioned wheeling experiment (*Keller et al.*, 2013b) where p-wave velocities were sesnsitive to transient (load) and permanent changes in soil mechanical properties after wheel passage. The representation of such changes on seismic wave propagation hinges on advancing petrophysical modeling of commensurate changes in key variables (bulk density, soil stiffness, elastic moduli and more). *Markov et al.* (2005) used DEM theory to study a related problem, namely the sensitivity of effective elastic properties to porous heterogeneities in dual-porosity rocks. Their formulations include a homogeneous

porous host material with ellipsoidal and spheroidal inclusions representing vrugs and cracks in the rock, respectively. These ideas could be followed to include heterogeneities that are representative of macropores. For instance, it is already well established that thermal transport properties are critically dependent on the shape (e.g. spherical and cylindrical inclusions) of the grains and their spatial arrangement (*De Vries*, 1963). Similarly, *Berryman* (1995) reviews EMT approaches for modeling the elastic moduli of multiphase materials and illustrates how different inclusions shapes can be accounted for in such formulations. One could also explore advanced simulation methodologies. For example, *Rubino et al.* (2016) simulate the effective elastic properties of an experimental volume by considering attenuation and dispersion of seismic waves introduced by wave-induced fluid flow (see *Pride*, 2005) due to mesoscopic (larger than pore scale, smaller than the wavelength) heterogeneities within a porous media. By introducing heterogeneities that are representative of the structural form of a soil (e.g., a hole created by an earthworm), such methodologies could provide insights about the sensitivity of elastic properties (and seismic velocities) to structural form and water saturation.

2.4.2 Combination of geophysical measurement methods

Geophysical methods differ in their sensitivity to different soil physical properties, some respond primarily to interfaces (wave-based physics; seismic and GPR reflection methods) whereas others to bulk properties (diffusion-based physics; DC-resistivity and EMI). It is thus conceivable that the combination of geophysical methods may have a synergistic influence on the inferences especially as related to an elusive trait such as soil structure. We discriminate below between multi-method approaches that (i) provide information about soil structure properties and (ii) delineate zones with different soil properties.

The first category is motivated by the fact that a single geophysical property is often insufficient to draw reliable conclusions about soil structure. For instance, the IP method provides information about the conductive and capacitive properties of a soil. Compared to DC-resistivity data that only sense conductive properties, this makes it much easier to attribute responses to salinity, clay or water content variations (*Revil et al.*, 2017). Similarly, estimations of water content using GPR may be useful to constrain the interpretation not only of electrical resistivity sections (or maps) derived from DC-resistivity (or EMI) but also of seismic velocities.

The second category is motivated by the fact that certain methods (e.g., seismics and GPR) have superior resolution, while the physical property of interest is primarily sensed by a lower-resolution method. As an example, one could improve the information content of DC-resistivity data by constraining its interpretation to soil layers derived from GPR or seismic data (see *Doetsch et al.* (2010) for a hydrogeological example). This could help to better constrain hydrological dynamics in time-lapse studies (discussed in Section 2.4.4). Another option would be to combine GPR reflectivity patterns and seismic bulk properties to differentiate between loose and compacted soil zones. Similar combinations of GPR and seismics might help to localize large root volumes in forest soils.

Inversion (e.g. *Menke*, 2012) is needed to translate geophysical data into geophysical properties. The resolution and robustness of geophysical inversion results are often improved by considering multiple data sets or information gained from other types of geophysical data (*Linde and Doetsch*, 2016). A more advanced approach would, therefore, be to jointly invert the data by directly targeting properties of interest. For instance, both DC-resistivity and GPR data are highly sensitive to porosity (Equations 2.1 and 2.5). This suggests that joint inversion schemes combined with appropriate pedophysical parametrizations of soil (in order to target, say, macroporosity rather than total porosity) would be possible. Joint inversion implementations remain challenging since data errors and sensitivities are different for different methods.

Similarly, joint inversion could be used to (i) better understand field-scale petrophysical relationships (e.g., *Linde and Doetsch*, 2010) and to (ii) enable clustering into zones of distinct soil structure. One way to achieve this is joint inversion using structural constraints in which no petrophysical relationship is imposed (*Gallardo and Meju*, 2003; *Doetsch et al.*, 2010). *Gallardo and Meju* (2003) pioneered such an approach by jointly inverting DC-resistivity data and seismic travel-time data. By observing the resulting cross-plot of electrical resistivity and p-wave velocity, they recognized segregation of the scattered points into different zones with different trends suggesting local field-scale petrophysical relationships. *Doetsch et al.* (2010) used such plots as input to clustering algorithms that provided a zonation of the subsurface.

2.4.3 Survey design and spatial scaling of soil structural features

Geophysics may offer extensive spatial coverage that provides a more integrative view of the subsurface than what can be obtained by sparse soil sampling or deployment of point sensors. In general, the support volumes of geophysical data and corresponding property estimates obtained by inversion are often much larger than the Representative Elementary Volume (REV) scale at which petrophysical models are defined. Any attempts to describe processes or downscale geophysical information to finer spatial scales should consider a certain level of stochasticity. Geostatistical theory offers means to explicitly account for spatial averaging and support volume (*Kyriakidis*, 2004). Ignoring the scale disparity between geophysical estimates and variables of interest is known to bias results (*Day-Lewis et al.*, 2005) and it might lead to false conclusions. Hence, once a clearer understanding on the signatures of soil structure in geophysical signals is developed, geophysics could help bridging the spatial gap between the very small support-volume offered by spatially-undersampled subsurface soil sensors and the larger scales that are relevant for land management and climate modeling. Such methods are not yet developed, and refinement of geophysical methods and interpretation would be required to allow for large-scale investigations at high resolution (also with depth).

The main challenge with high-resolution geophysical imaging of soils over large scales is that the horizontal scales are much larger (kilometric or more) than the vertical scale (decimetric to metric) of interest. Exhaustive representation of such landscapes at the resolution relevant to soil structure studies would require the acquisition and processing of massive amounts of measurements (both are time and cost extensive). Experimental setups would also need to be adapted to enable accurate imaging of features at scales of decimeters or less (e.g., account for electrode shape (*Rücker and Günther*, 2011) and use non-standard high-frequency seismic

sources *Ryden and Lowe* (2004). In addition, noise becomes an issue at these scales, at which electrode contact, exact electrode locations (and their variation over time) and microtopography may introduce considerable errors and mislead interpretations. Drone-based geophysics or instruments that are towed or attached to agricultural machinery (or autonomous vehicles) is likely to become increasingly available and alleviate some of challenges of data acquisition (e.g., http://vulcanuav.com/, https://gamaya.com/) (*Rapstine et al.*, 2017) (the processing remains a challenge). Other surrogate variables may help indicating presence and influence of soil structure from rapid infiltration or no runoff (local gravity methods); manipulative experiments with large scale salt application to monitor rate of removal and potential pathways; use of near-surface seismic surveys to establish baseline compaction levels in agricultural regions. To address the data processing and information extraction burden, we envision the use of hierarchical approaches that retain essential soil structural features based on the intended application. The potential of information compression (similar to image compression) could be useful in communicating such large soil structural data sets. We suggest further that low-resolution mapping with EMI or satellite-based remote sensing (that only senses land-surface properties) can be used both to guide the locations of such detailed surveys and to interpolate in-between (*Dafflon et al.*, 2017). Versatile geostatistical techniques that can handle incomplete sampling and different support-scales need to be further developed and demonstrated for this type of problem (*Straubhaar et al.*, 2016). We also expect that recent advances in deep-learning can help to address downscaling using image super-resolution methods (*Lu et al.*, 2018; *Shen*, 2018).

2.4.4 Soil dynamic responses and hydrogeophysical modeling

Repeated geophysical surveys or semi-permanent geophysical monitoring make it possible to deduce influences of soil structure indirectly via its impact on various soil dynamic processes. Examples include the activation of macropores (*Moysey and Liu*, 2012), rapid drainage, salinity changes due to root water uptake, abrupt changes in seismic or GPR signals following compaction. Given their larger spatial footprint, time-lapse geophysics may offer insights that are impossible when using individual point sensors. In the vein of hydrogeophysics (*Binley et al.*, 2015), we propose to capitalize on the combination of spatial coverage and dynamic monitoring to differentiate geophysical responses related to the presence or absence of certain structural features. We highlight that the relevant time scales might be years, even decades (aggregation, soil structure formation and regeneration), and that geophysical monitoring can be achieved over such time-scales. Having the possibility of gathering dynamic responses enhances the value of geophysical methods as tools for soil structure characterization. Current instrumentation may not be well suited for such challenging task, the creation of new autonomous machines specifically designed to monitor large areas over long time periods may substantially improve monitoring capabilities.

As an example, we present a week-long time-lapse DC-resistivity monitoring experiment carried out in September 2017 at the Soil Structure Observatory in Zürich, Switzerland (see *Keller et al.* (2017) for experimental details and Section 2.6). Figure 2.9 presents relative variations (and associated standard deviations) of apparent resistivities (Figure 2.9a) corresponding to electrodes separated by 50 cm (so-called Wenner array) and volumetric water content esti-

mated using Topp's equation from measurements of TDR probes at a depth of 20 cm (Figure 2.9b). The data were acquired in four subplots with different characteristics: non-compacted bare soil (yellow), compacted bare soil (brown), non-compacted soil under grassland (mixture of grass and legumes, light green) and compacted soil under grassland (mixture of grass and legumes, dark green). These results obtained 3.5 years after the compaction event can be interpreted by qualitative arguments. The grass-covered zones respond much more to the rainfall on September 17 than the zones with bare soil. This confirms that the bare soil is nearly water-saturated before this precipitation event (see Figure 2.9b). In contrast, the grass covered zones present a lower initial water saturation/content (more evapotranspiration and faster downward percolation). Additionally, note how Figure 2.9 resembles the results obtained by *Moysey and Liu* (2012) (Figure 2.8); normalized apparent resistivity decreases as the biopores created by the grass and legume roots gradually become active in response to the rainfall. This is not evident for the bare soil, where root-introduced biopores is not present. The only clear discriminator between the subplots is their structural form, and yet, the DC-resistivity data presented here and in Figure 2.4b could capture aspects related to soil structure (compacted vs. non-compacted) and management (bare vs. grass-covered soil). These observations were obtained from one geophysical method and interpretations were made with the help of TDR data and based on prior knowledge about the characteristics of the controlled experiment. This enhances the value of the combination of geophysical methods with other sources of information. Additionally, we expect that the combination of methods (see Section 2.4.2) can guide interpretations at locations with more limited prior knowledge about the soil and its history. This example emphasizes the lack of quantitative tools to interpret the observations and reinforces the need for developments described in this section.

The anecdotal applications described above, clearly point to the need for methods that fuse spatial and temporal geophysical information to derive quantitative metrics related to soil structure. Such methods could be fashioned after large scale hydrological and climate models (*Van Looy et al.*, 2017), or in the context of geophysics, could use coupled hydrogeophysical inversion to infer subsurface properties (*Linde and Doetsch*, 2016). In such an approach, the inverse problem is parameterized in terms of hydrological properties. The mismatch between the observed geophysical data and those predicted from the hydrological forward response (using a petrophysical relationship and a geophysical forward model) is used to iteratively infer a set of hydrological parameters that honor the data (*Kowalsky et al.*, 2004; *Jougnot et al.*, 2015; *Tran et al.*, 2016; *Kuhl et al.*, 2018). Thus, the dynamic geophysical response to soil state is used to infer soil properties of interest. Such coupled inversion methodologies have the potential of providing valuable information about the evolution of soil structure and, in the case of degradation, the major aspects influencing its recovery. A further step would be to shift emphasis from parameter estimation towards a framework of formal testing of competing hypotheses of the mechanisms governing soil structure and its development. This can be addressed by model selection techniques that use geophysical data to discriminate among multiple competing conceptual soil models (*Linde*, 2014; *Brunetti et al.*, 2017).

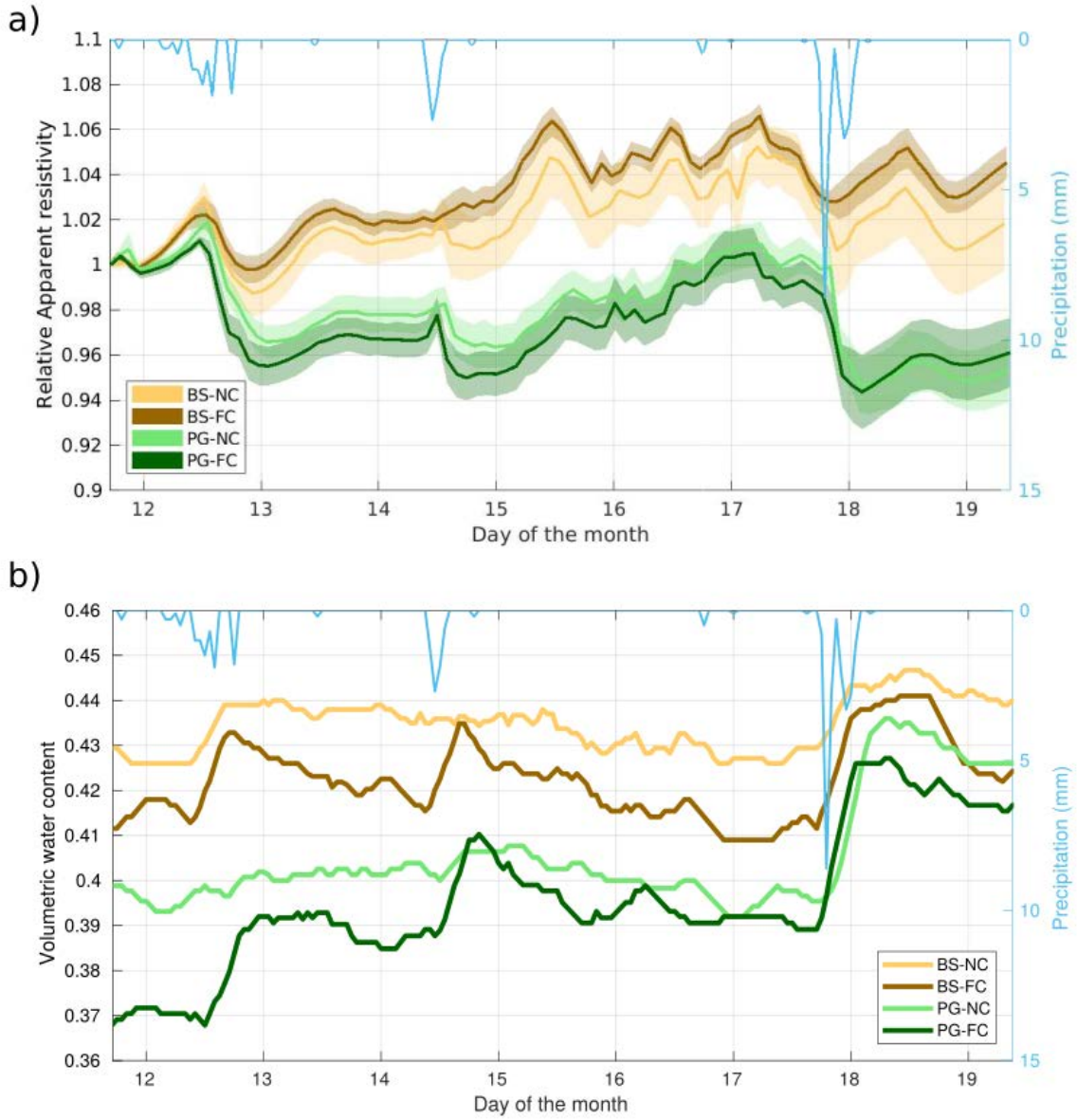

Figure 2.9 – (a) Relative time-lapse changes in electrical resistivity of the first level of the Wenner array for bare soil compacted (BS-FC), bare soil non compacted (BS-NC), permanent grass compacted (PG-FC) and permanent grass non compacted (PG-NC). (b) Volumetric water content estimated from TDR measurements at 20 cm depth, located in the same plots as in (a).

2.4.5 Summary

This section presents an overview of geophysical methods and models (petrophysical and inversion strategies) for soil structure characterization that have not been yet fully developed, yet they deem to hold most promise for progress in this area. In particular, the harnessing of combination of methods with different sensitivities to soil structure attributes and placing these on a soil structure-aware modeling framework that capitalizes on spatial or temporal signatures (i.e., system dynamics). As a specific example, Figure 2.10 shows how DC-resistivity and GPR methods can be used to characterize the evolution of different soil structures in relation to soil compaction and soil management (see also Section 2.6). The experimental field presents different compaction patterns as well as different soil post-compaction treatments. The characterization of soil surfaces using GPR and DC-resistivity arrays at sufficient spatial resolutions have been shown to identify zones affected by soil compaction. Shortly after the compaction event, these zones would appear as high electrical conductivity (e.g., due to relatively higher saturation levels and volumetric clay content) or increase the amplitude of GPR signals in the radargram at the same spatial locations. Such spatial characterization is not strongly dependent on the dynamics of soil processes and we thus term this class of characterization "static". In contrast, repetitive measurements in time could be acquired (for example using time-lapse DC-resistivity) with the explicit objective of capturing dynamic (and relatively rapid) changes in the hydrogeophysical state of the soil system. These changes could be fed into a modeling framework that explicitly considers soil structure effects on soil dynamic processes and thus we may use these geophysical observations (and inversion framework) to distinguish different integrative signatures of soil structure. The success of new geophysical applications is also critically dependent on developing new and well-tested pedophysical relations that link soil structure states with geophysical measurements.

2.5 Conclusions

Soil structure governs a wide range of hydrological and ecological soil functions, but there are currently no satisfying ways to measure it non-invasively and at relevant field-scales. We have examined how geophysics, with its ability to image large spatial and temporal domains, can be used to obtain insights about soil structure. Many geophysical properties respond to soil structure, but there is a lack of petrophysical (pedophysical) models that relate them to soil structure attributes (e.g., macroporosity and its connectivity). We highlight the need to reduce interpretation ambiguity and increase image resolution by combining multiple geophysical data types. We suggest that indirect inference of soil structure by relating the geophysical time-lapse response to the dynamics of state variables together with appropriate hydro-mechanical and biological modeling offer multiple possibilities for quantitative assessments of soil structure. Given the many factors that may influence geophysical responses, we suggest that geophysical methodologies for soil structure characterization are first developed and tested at well-instrumented field sites.

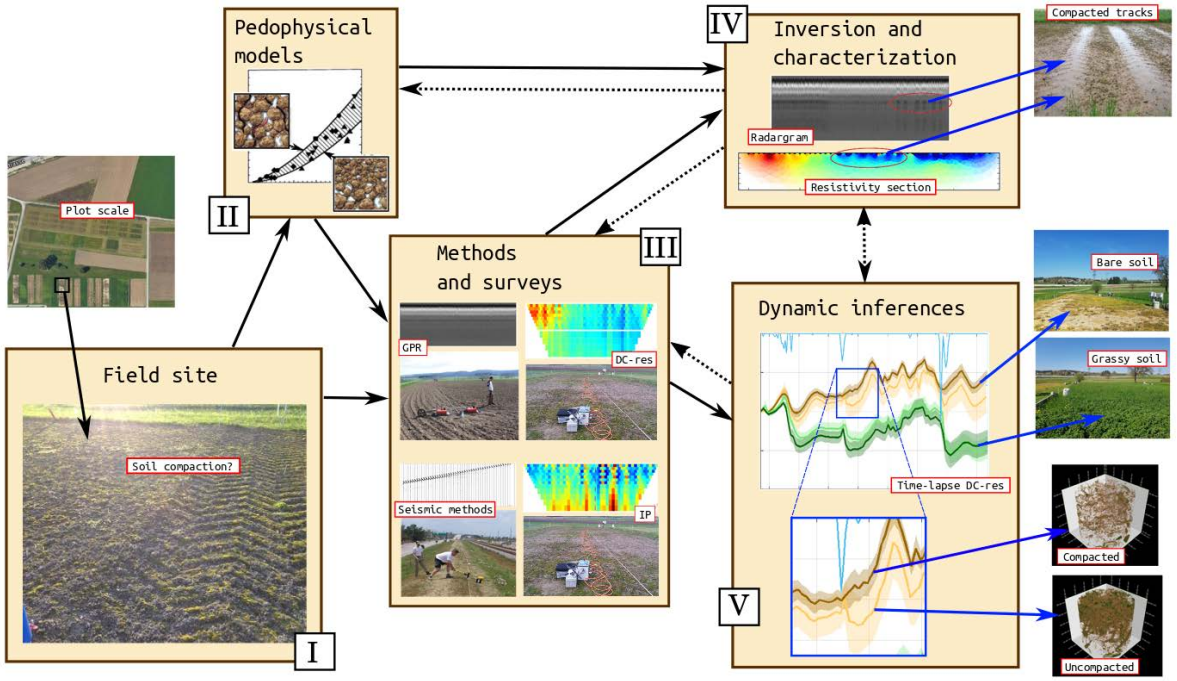

Figure 2.10 – Sketch of how to use geophysical methods for soil structure characterization: a soil compaction example. Solid black lines represent the information flow, dashed black lines represent feedbacks between activities and blue lines represent inferences of soil structure. (I) The example shows how geophysical methods can be used to infer information related to soil compaction in an agricultural field. (II) Knowledge about the pedophysical links between geophysical properties and soil structural properties is used to guide the selection of methods and help interpretation. (III) DC-resistivity, IP, GPR and seismic methods are suitable for obtaining information about soil structure. (IV) The spatial distribution of compaction is captured by the inverted and/or processed geophysical data: track compacted zones produce more conductive regions (DC-resistivity) and enhancement of GPR early-signals (see blue arrows). (V) Time-lapse changes in apparent resistivity due to the soil hydrological response to precipitation help to discriminate between soil structures: the grassy soil is highly responsive to rain relative to bare soil and the uncompacted bare soil is more responsive to rain than the compacted bare soil (blue arrows).

2.6 Supplemental material

Soil Structure Observatories

Field-scale research observatories help to advance science as they concentrate research resources to specific areas where researchers have access to long-term time-series and other supporting data sources. Multiple large-scale initiatives related to critical zone science (http://criticalzone.org/national/), climate change (http://www.tereno.net/overview-en?set_language=en) and hydrogeology (http://hplus.ore.fr/en/) have been developed. Similar observatories that are dedicated to soil structure would facilitate the development of geophysical approaches for soil structure characterization. The research opportunities highlighted above would all be facilitated by working on sites where:

1. The experimental design can be controlled (or at least having detailed knowledge);
2. There is easy access to multiple types of data to improve interpretations and, if possible, guide survey design;
3. There is access to laboratory measurements to better understand site pedophysics;
4. It is possible to perform long-term monitoring of soil structure evolution without removing the sensors.

The Soil Structure Observatory *Keller et al.* (2017) established in the vicinity of Zurich, Switzerland, seeks to study the evolution of soil structure by measuring different soil properties with point probe measurements, soil sampling, weather measurements and geophysical techniques. Figures 2.4 and 2.9 represent preliminary analysis of ERT insights related to soil structure and Figure 2.5 presents the GPR patterns due to compaction. Clearly, different climates and textures will influence the development of soil structure and responses of soils to deformations, the time needed for them to regenerate after a plastic deformation and the relative relevance of the different processes that act on them. Consequently, additional SSO's that are representative for other soil types and climatic conditions would be most useful.

Chapter 3

Seismic signatures reveal persistence of soil compaction

Alejandro Romero-Ruiz, Niklas Linde, Ludovic Baron, Santiago G. Solazzi, Thomas Keller and Dani Or.

Submitted to [1] to *Vadose Zone Journal*

[1] Romero-Ruiz et al. (2021). Seismic Signatures Reveal Persistence of Soil Compaction. *Vadose Zone Journal*, submitted

Abstract

Soil structure is a key attribute of a productive and functioning soil. Evidence shows that subtle changes in the spatial arrangement and binding of soil constituents impart large changes in soil mechanical and hydraulic properties and associated ecological services. However, these features remain difficult to quantify at spatial scales relevant for agricultural management. In this work, we propose a pedophysical model to interpret macroscopic seismic properties in terms of soil structure. The model captures subtle soil mechanical traits accounting for soil plastic deformation due to compaction. In order to evaluate the model, we use data from field monitoring at an experimental site that revealed elevated seismic velocities in plots that were compacted five years prior to our measurements. Our results show that P-wave velocities carry a strong imprint of soil compaction and are well predicted by the proposed model. The model infers contact areas between aggregates that are nearly threefold larger for compacted than for non-compacted soils, indicating that soils have not recovered from compaction. The study illustrates the potential of seismic methods to identify chronic compaction at field scale.

3.1 Introduction

Soil structure refers to the spatial organization of a soil's solid constituents (minerals and organic matter) and voids resulting from bioturbation, abiotic processes (e.g., wetting-drying and freezing-thawing), and soil management practices (*Oades*, 1993; *Gregory et al.*, 2009; *Or et al.*, 2021). Soil structure is critical for determining a soil's macroscopic transport and mechanical properties. Well developed and stable soil structure plays a central role in supporting soil ecosystem services, including climate regulation (*Hirmas et al.*, 2018; *Fatichi et al.*, 2020), groundwater recharge (*Keesstra et al.*, 2012), carbon cycling (*Follett*, 2001; *Green et al.*, 2019), and agricultural production (*Zhang et al.*, 2007). In contrast, degradation of soil structure may trigger processes with adverse environmental and economical consequences (*Graves et al.*, 2015), such as soil erosion (*Nawaz et al.*, 2013), increased greenhouse gas emissions (*Oertel et al.*, 2016), reduced crop productivity (*Håkansson and Reeder*, 1994), and landslides (*Toll et al.*, 2012).

Soil compaction is a major soil structure-degrading hazard that results from use of agricultural, forestry, military, construction, and other off-road vehicles under mechanically-sensitive soil conditions. It adversely impacts soils as habitats for soil animals and plants due to increased mechanical impedance and loss of porosity and hydrological functions (*Nawaz et al.*, 2013). The quantification of compaction remains a challenge, particularly at the field scale. Moreover, favorable soil structure takes decades to develop primarily by biological processes, whereas compaction may occur in a few seconds with its adverse impacts on soil functions lasting for many years thereafter (*Håkansson and Reeder*, 1994; *Webb*, 2002). Thus, gaps in our understanding of long-term dynamics of soil structure can be associated to (1) the disparities in the time-scale of degradation and generation processes, and (2) the lack of characterization methods capturing the relevant temporal and spatial scales (*Keller et al.*, 2017). For these reasons, the global extension of soil compaction in all terrestrial surfaces

remains unknown and challenging to assess. Three decades ago, *Oldeman* (1992) estimated that 68 Mha of arable lands were compacted globally. Recent estimations indicate that about 25-40% of all arable land is compacted in the United Kingdom (*Graves et al.*, 2015), Denmark (*Schjønning et al.*, 2015) and the Netherlands (*Brus and Van Den Akker*, 2018).

Characterization of the structure and mechanical status of a soil often relies on pointwise on-site measurements (e.g., cone penetrometer testing; *Lunne et al.*, 1997), or on highly invasive soil evaluation methods (*Guimarães et al.*, 2017), often involving time intensive characterization based on soil sampling (*Peng and Horn*, 2008). Such invasive approaches provide fragmentary information in time and space and offer a limited capacity to evaluate soil structure evolution under natural conditions. Recently, geophysical methods have been proposed to add complementary information to traditional techniques and to bridge the gap from point to field scales at relevant temporal scales (see review by *Romero-Ruiz et al.*, 2018). Because of the direct link between seismic velocities and soil elastic moduli, seismic methods hold a particular promise for minimally invasive characterization of variations in soil mechanical status at field scales and at highly resolved time scales. On-site applications of shallow seismic methods and monitoring have increased in the last decades including monitoring of thawing in Artic environments (*Wu et al.*, 2017; *Stemland et al.*, 2020), landslide monitoring (*Chen et al.*, 2018; *Whiteley et al.*, 2020) and characterization of soil compaction (*Uyanik and Ulugergerli*, 2008; *Uyanik*, 2011; *Donohue et al.*, 2013; *Keller et al.*, 2013b). These studies highlight that seismic methods can provide valuable information pertaining to soil structure. However, existing studies that analyze soil structure based on seismic velocities are largely empirical, soil specific and lack descriptions of arrangement of soil components and the mechanisms behind the soil structure state (for linking deformation, macroporosity, and mechanical state with seismic signals). The development of seismic-based practices for characterization of soil structure at relevant scales will largely rely on continued improvements in our understanding of the relationships between the macroscopic seismic properties of structured soils and the spatial arrangement and binding of soil constituents.

In this study, we seek to improve mechanistic understanding regarding the potential of seismic methods in quantifying the mechanical impacts of soil compaction. The objectives of this study are: (1) to develop a soil-structure informed pedophysical model that accounts for soil structure deformation; (2) to monitor seismic signatures of different states of soil compaction at a long-term Soil Structure Observatory (SSO) established in Zürich, Switzerland (*Keller et al.*, 2017); and (3) to apply the model to interpret seismic signatures of persistent soil compaction five years after a compaction event at the SSO.

3.2 Elastic properties of structured partially-saturated soil

Seismic induced compressional wave (P-wave, V_p) and shear wave (S-wave, V_s) velocities can be expressed as functions of soil's elastic moduli and bulk density ρ_b. For isotropic elastic

media, the seismic velocities are expressed as:

$$V_p = \sqrt{\frac{K_{soil} + \frac{4}{3}G_{soil}}{\rho_b}}, \tag{3.1}$$

$$V_s = \sqrt{\frac{G_{soil}}{\rho_b}}, \tag{3.2}$$

where K_{soil} and G_{soil} are the macroscopic soil bulk and shear moduli, respectively. Relating these properties to their microscopic counterparts remains challenging for structured soils as they depend on both (1) the elastic properties and volumetric fractions of the soil phases (solids, water and air), and (2) the spatial distribution of the soil constituents and their corresponding mechanical bonds.

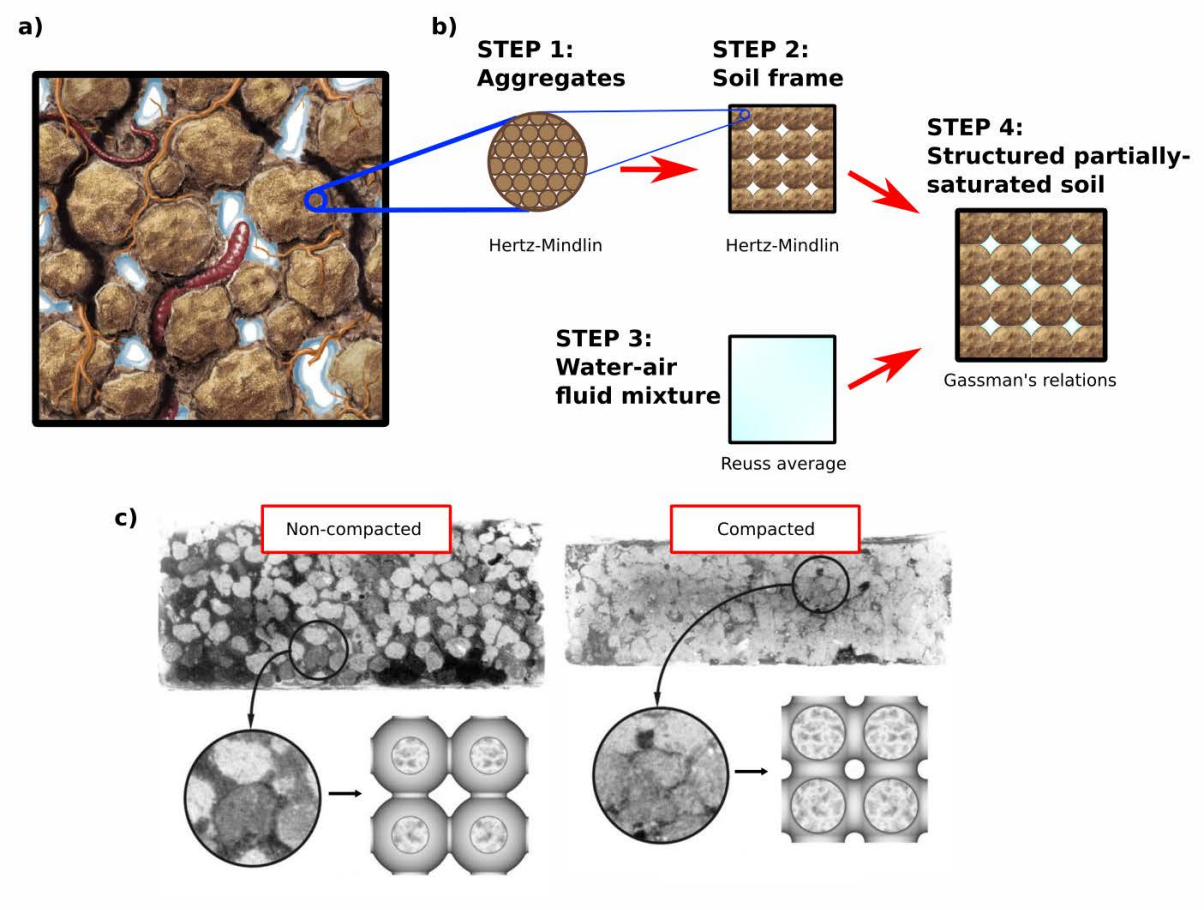

Figure 3.1 – Conceptualization of soil structural elements and their integration within a self-consistent pedophysical model of macroscopic elastic properties. (a) Schematic representation of a structured soil displaying aggregation (taken from *Romero-Ruiz et al.*, 2018). (b) Sketch of the four mixing steps used to predict the elastic properties of partially-saturated structured soils with the model type used at each step. (c) Schematic representation of aggregate geometries as conceptualized in step 2 (modified from *Ghezzehei and Or*, 2003).

In this work, the incorporation of salient features of soil structure for predicting seismic response of unsaturated soils is based on self-consistent mixing of soil constituents which, in turn, is based on a conceptual model of their arrangement. We conceptualize the soil as a composite dual-domain medium (Fig. 3.1a). Such a dual-domain representation of rocks and soils has been succesfully employed to model seismic (*Dvorkin et al.*, 1999), hydraulic (*Durner*, 1994; *Tuller and Or*, 2002), dielectric (*Blonquist Jr et al.*, 2006), and electrical properties (*Day-Lewis et al.*, 2017). The dual-domain pedophysical model proposed herein accounts for soil structural features by considering four mixing steps (Fig. 3.1b). These steps are described in the following sections.

3.2.1 Elastic properties of soil aggregates and soil frame

The elastic properties of the soil frame are obtained by applying the Hertz-Mindlin (HM) model in two consecutive steps. First, we obtain the elastic properties of soil aggregates (step 1), and then we consider a geometrical arrangement of aggregates (step 2). The dual-porosity soil with total porosity of ϕ_T comprises an intra-aggregate domain and an inter-aggregate domain occupying volumetric fractions w_m and $w_M = 1 - w_m$, respectively. The aggregates are composed by pores and solid particles and have an intra-aggregate porosity of ϕ_m. The inter-aggregate domain (space between aggregates) is composed by void space only (thus, making $\phi_M = 1$). The total porosity can thus be expressed as:

$$\phi_T = w_m \phi_m + w_M \phi_M. \tag{3.3}$$

The HM mechanical contact model is used to derive the elastic moduli of an aggregate (step 1 in Figure 3.1b) that depend on the normal and tangential contact stiffness between adjacent particles (pp. 245-248 *Mavko et al.*, 2009). The elastic moduli are expressed in terms of the elastic properties of the particles and a confining pressure P_e as:

$$K_{agg} = \left[\frac{N_m^2 (1-\phi_m)^2 G_s^2}{18\pi^2 (1-\nu_s)^2} P_e \right]^{\frac{1}{3}}, \tag{3.4}$$

and,

$$G_{agg} = \frac{2 + 3f_m - (1+3f_m)\nu_s}{5(2-\nu_s)} \left[\frac{3N_m^2 (1-\phi_m)^2 G_s^2}{2\pi^2 (1-\nu_s)^2} P_e \right]^{\frac{1}{3}}, \tag{3.5}$$

where K_{agg} and G_{agg} are the bulk and shear moduli of the aggregate, respectively. Furthermore, N_m is the average number of contacts per particle, which can be considered a function of the intra-aggregate porosity (p. 232-234 *Mavko et al.*, 2009). In addition, G_s and ν_s are the shear modulus and Poisson's ratio of the particles, and f_m is the fraction of non-slipping particles (see *Bachrach et al.*, 2000).

The elastic properties of the soil frame (step 2) are obtained by considering an assembly of spherical aggregates, whose homogeneous isotropic and elastic properties are given by equations 3.4 and 3.5. For this purpose, we use the HM model once again. The elastic properties of the soil frame are then expressed as:

$$K_{frame} = \left[\frac{{N_M}^2 (1-w_M)^2 G_{agg}^2}{18\pi^2 (1-\nu_{agg})^2} P_a \right]^{\frac{1}{3}}, \tag{3.6}$$

and

$$G_{frame} = \frac{2+3f_M-(1+3f_M)\nu_{agg}}{5(2-\nu_{agg})}\left[\frac{3{N_M}^2(1-w_M)^2G_{agg}^2}{2\pi^2(1-\nu_{agg})^2}P_a\right]^{\frac{1}{3}}, \tag{3.7}$$

where K_{frame} and G_{frame} are the bulk and shear moduli of the soil frame, ν_{agg} is the Poisson's ratio of the aggregates, N_M is the average number of contacts per aggregate, f_M is the fraction of non-slipping aggregates, and P_a is the HM confining pressure. The confining pressure P_e is used as in traditional geophysical applications of the HM framework, attributed to overburden pressure and suction stress for partially saturated media (see Section 3.2.1). In this study, we expand the interpretation by introducing P_a to relate HM elastically deformed soil aggregate contacts and permanently (viscous) deformed soil aggregate contacts due to compaction induced by a transient vertical stress (see Section 3.2.1). Hence, these signatures of soil compaction are interpreted via their elastic equivalence in the HM framework that, in turn, affects the seismic response.

Effects of hydration status on the elastic properties of the soil frame

The elastic moduli of the soil frame (eqs. 3.6 and 3.7) are strongly dependent on the elastic properties of the aggregates, which depend on the confining pressure P_e (eqs. 3.4 and 3.5). Research shows that P_e and, therefore, the elastic moduli of the frame, are affected by the hydration status in soils (*Brutsaert and Luthin*, 1964; *Lu*, 2011; *Shin et al.*, 2016). A frame softening effect is related to the decrease in the aggregate matric suction through the concept of effective stress (*Bishop and Blight*, 1963; *Nuth and Laloui*, 2008; *Lu et al.*, 2010). As proposed by *Shen et al.* (2016), we account for soil frame softening by adding a suction stress term ($\chi(u_a-u_w)$) to the HM pressure appearing in equations 3.4 and 3.5:

$$P_e = \sigma - u_a + \chi(u_a-u_w) = \sigma - u_a + \chi\psi_{agg}, \tag{3.8}$$

where $\sigma = \rho_b g Z_0$ is the overburden pressure, $u_a = \rho_a g Z_0$ is the air pore pressure, u_w is the water pore pressure, $\psi_{agg} = u_a - u_w$ is the matric suction of the aggregates, g is the gravitational acceleration, and Z_0 is the depth of investigation. The effective stress parameter χ is a function of the effective saturation of the aggregates $S_{e_{agg}}$ and varies between 0 and 1. In its simplest form, it is expressed as $\chi = S_{e_{agg}}$ (*Nuth and Laloui*, 2008), yet the dependence of χ with saturation may vary with the soil type (*Khalili and Khabbaz*, 1998). The bulk density is defined as

$$\rho_b = (1-\phi_T)\rho_s + \phi_T(S\rho_w + (1-S)\rho_a), \tag{3.9}$$

where ρ_s, ρ_w and ρ_a are the densities of soil particles, water and air, respectively, and S ($=\theta/\phi_T$) is the total soil saturation defined as the ratio between total water content θ and total porosity.

Consequently, the effective moduli of the soil aggregates become water-content dependent through the water retention curve of the aggregates. The matric suction of the aggregates ψ_{agg} can be expressed as a function of effective water saturation of the soil aggregates $S_{e_{agg}}$ as (*van Genuchten*, 1980):

$$\psi_{agg} = \frac{g\rho_w}{\alpha_m}\left[S_{e_{agg}}^{\frac{n_m}{1-n_m}} - 1\right]^{\frac{1}{n_m}}, \tag{3.10}$$

where α_m is related to the inverse of the air-entry pressure of the aggregates, and n_m is the Van Genuchten exponent, which is related to the pore size distributions of the intra-aggregate space (*Mualem*, 1976; *van Genuchten*, 1980). The effective saturation in the aggregates is a function of the residual water content θ_r, the intra-aggregate porosity ϕ_{agg} and the intra-aggregate water content ($S_{e_{agg}} = (\theta_{agg} - \theta_r)/(\phi_{agg}(1 - w_M) - \theta_r)$). In our model, the intra-aggregate water content is obtained from the soil total water content (θ, e.g., from TDR data) and the volumetric proportion of intra-aggregate pore space. If the total soil water content is lower or equal than the volumetric proportion of intra-aggregate pore space ($\theta < \phi_{agg}(1 - w_M)$), the water content in the aggregates is the total water content in the soil ($\theta_{agg} = \theta$). For a total soil water content higher than the proportion of intra-aggregate pore space ($\theta > \phi_{agg}(1 - w_M)$), the water content in the aggregates is equal to the volumetric proportion of intra-aggregate pore ($\theta_{agg} = \phi_{agg}(1 - w_M)$).

Soil compaction effects on the elastic properties of the soil frame

In the framework of the HM theory expressed by equations 3.6 and 3.7, the soil frame is represented as an assembly of soil aggregates with contacts elastically deforming in the presence of a confining pressure P_a. In reality, the aggregate contacts in soils deform plastically due to soil stresses induced by abiotic processes (e.g., wetting-drying and freezing and thawing cycles), anthropogenic activities (e.g., passages of agricultural vehicles) and/or biological activity (e.g., penetrating earthworms and growing roots) producing aggregate coalescence. In the following, we describe how to account for permanent deformation of the soil frame using the HM framework through equations 3.6 and 3.7 via the relationship between P_a and the corresponding contact areas between aggregates.

The application of a transient load (e.g., passage of a tractor) results in an elastic (temporary) and a viscous (permanent) deformation of the soil frame producing an axial strain $\epsilon = \epsilon_e + \epsilon_v$ (see *Ghezzehei and Or*, 2003), where ϵ_e and ϵ_v are the elastic and viscous strains, respectively. The lasting effect of a soil compaction event is associated with irreversible deformation comprised in ϵ_v, which can be modeled using information on the initial (prior to compaction) strain ϵ_0, the axial load and duration of stress application (i.e., tractor weight and speed) and the soil rheological properties represented by the Bingham model (*Ghezzehei and Or*, 2001). The post-compaction viscous component of the strain (reflecting irreversible soil deformation) ϵ_v is related to the contact area between aggregates A_c through the approximation:

$$A_c = \pi a^2 \approx 2\pi R^2 \epsilon_v, \tag{3.11}$$

where a and R are the radii of the contact area and the aggregate, respectively. We do not seek to reconstruct the deformation process (*Ghezzehei and Or*, 2001; *Or and Ghezzehei*, 2002) but to infer from the primarily elastic nature of seismic methods what is the representative contact area between aggregates based on the HM contact theory. To build such a pedophysical model, we rely on the contact area (eq. 3.11) that is permanent in nature, yet, for convenience, it is treated here as an elastic deformation in the context of the HM theory. This allows expressing P_a in terms of the contact radius a by (p. 246 *Mavko et al.*, 2009):

$$P_a = \frac{2N_M(1-w_M)G_{agg}}{3\pi(1-\nu_{agg})}\left(\frac{a}{R}\right)^3. \tag{3.12}$$

To assess compaction independently of the aggregate size, we define the relative contact radius $R_{rel} = \frac{a}{R}$ as the ratio between the radius of the contact area and the radius of the aggregates, which can be related to the viscous strain using equation 3.11:

$$\epsilon_v \approx \frac{1}{2}R_{rel}^2. \tag{3.13}$$

Note that, similarly to what is described for P_e, a suction stress associated with the inter-aggregate pore space must exist and should be comprised in P_a. However, the large size of the macropores generally results in small inter-aggregate suction stress that is much lower than compaction stresses and, thus, the contribution of such stress to P_a is assumed negligible.

3.2.2 Elastic properties of the water-air fluid mixture

The effective bulk modulus of the fluid mixture (step 3 in Figure 3.1b) is required for evaluating the elastic moduli of a partially water-saturated structured soil. In the low frequency limit, wave-induced pore fluid pressure gradients induced by the propagating seismic wavefield have sufficient time to equilibrate in the pore space (pp. 174-175 *Mavko et al.*, 2009). This allows representing the elastic properties of the fluid mixture as properties of an effective fluid (composed by water and air) using the Reuss isostress average, which is based on an harmonic mean (*Reuss*, 1929) and relates the bulk modulus of the fluid mixture K_{fluid} to the saturation ($S = \theta/\phi_T$) by:

$$K_{fluid} = \left[\frac{S}{K_w} + \frac{1-S}{K_a}\right]^{-1}, \tag{3.14}$$

where K_w and K_a are the bulk moduli of water and air, respectively. Due to the low frequencies used in this study (i.e., wavelengths are much larger than the inter- and intra-aggregate pore radii), the effective fluid is considered to be occupying both inter and intra-aggregate pores.

3.2.3 Elastic properties of structured partially-saturated soil

Gassmann's low-frequency fluid substitution relationships (*Gassmann*, 1951) are widely used to systematically incorporate the effects of a saturating fluid in the elastic moduli of porous materials (*Bachrach and Nur*, 1998; *Pasquet et al.*, 2016). Gassmann's relationships can be used to predict the elastic moduli of soils by considering the elastic moduli of (1) the soil frame (eqs. 3.6 and 3.7), (2) the soil solid constituents forming the soil frame K_s, and (3) the saturating fluid (eq. 3.14). Effects of partial water-saturation are modeled by considering an effective saturating fluid, whose properties are given by equation 3.14 (e.g., *Johnson*, 2001). In this framework, the elastic moduli of the partially saturated structured soil are expressed as (p. 273 *Mavko et al.*, 2009):

$$K_{soil} = K_{frame} + \frac{\left(1 - \frac{K_{frame}}{K_s}\right)^2}{\frac{\phi_T}{K_{fluid}} + \frac{1-\phi_T}{K_s} - \frac{K_{frame}}{K_s^2}}, \tag{3.15}$$

and

$$G_{soil} = G_{frame}. \tag{3.16}$$

Equations 3.15 and 3.16 are valid in the so-called *relaxed state*. This implies that pore fluid pressures are equilibrated throughout the pore space (*Berryman*, 1999). Dissipative effects associated with the relative motion between the saturating fluids and the frame, which are commonly considered in the context of Biot's poroelasticity theory (*Biot*, 1962), are thus assumed to be negligible in the frequency range employed in our study. Note that the macroscopic elastic properties (and seismic velocities) of the soil are sensitive to changes in water content (1) through the water retention relationship of the aggregates which determines their effective stress (eq. 3.8), and (2) through the impact of water saturation in the elastic properties of the fluid mixture (eq. 3.14).

3.3 Field monitoring of seismic data

We conducted seismic monitoring to evaluate long-term effects of soil compaction and analyze potential recovery for different soil cover. Monitoring was carried out in the spring and summer of 2019 at an experimental field site located in the vicinity of Zürich, Switzerland (8^o31'04 E, 47^o25'39 N) (*Keller et al.*, 2017). This soil structure observatory (SSO) is a long-term experiment designed to study the evolution of soil structure, following a compaction event in the spring of 2014, for different types of post-compaction management. The SSO has a strip-plot design with three blocks (replicates, see Figure 3.2a). We monitored the seismic response of experimental plots (located in block A) with different covers (bare soil and vegetated soil) and compaction treatments (compaction on the full surface and no compaction). The corresponding soil treatments are referred to as full compacted ley (grass-legume mixture),

non-compacted ley, and full compacted bare soil (Fig. 3.2b). Since the soil properties (and texture) prior to the compaction event were similar at all monitoring sites (*Keller et al.*, 2017), we attribute differences in the corresponding seismic signatures to the different soil covers and treatments.

The seismic array comprised a line of 18 geophones (30 Hz SM-11 IO) deployed on both sides of an impact source (twelve on one side and six on the other side, Figure 3.2c). Two geophone spacings were used: Δx = 10 cm for sensors with offsets shorter than 80 cm, and Δx = 20 cm for sensors with offsets longer than 80 cm. The sensors were connected to a Geode Exploration Seismograph located in an operation box at the edge of the soil plots. The Geode was controlled by a laptop operating the Seismodule Controller Software continuously during the full monitoring campaigns. The geophone array was not symmetric due to the limited length of the seismic cable used in our experiment. As shown in Figure 3.2b, the operation box controlling the seismic monitoring experiment was placed at an untreated soil area located a few meters away from the seismic lines. In order to connect the geophones to the Geode (located in the operation box), part of the seismic cable was used as an extension, which prohibited us from using six outtakes of the cable.

An electromagnetic hammer (piston and base plate system driven by a 300 W audio speaker) was harnessed to provide an impact-like source that was activated at regular time intervals. The source frequency content was centered between 75 and 150 Hz. The hammer was controlled by a waveform generator (Agilent 33210A, located in the operation box) that was programmed to trigger an impact every 15 minutes. The function generator emitted a pulse waveform, with period of 15 minutes, high level of 4 V, low level of -1 V, width of 300 ms and edge time of 100 ns. The seismic source is considered a point source, as shown in the schematic representation of the seismic array presented in Figure 3.2c. Having only one source, the data were collected during three different time periods: from the 17th of May to the 26th of June (compacted ley), from the 26th of June to the 8th of July (non-compacted ley), and from the 25th of July to the 9th of August (compacted bare soil). All these periods contain significant rainfall events followed/preceded by dry periods with associated changes in soil hydration status. Figure 3.2c presents a photography from May of 2019 of the seismic monitoring layout deployed in the compacted ley.

Time-domain reflectometry (TDR, TDR 100 by Campbell Scientific with MDX multiplexers) probes for soil water content measurements were installed in all plots, and were continuously collecting data at four different depths (10, 20, 40, and 70 cm). Due to a technical issue, TDR data were not available from block A in 2019. For this reason, we considered TDR data collected at the TDR banks in block C (see Figure 3.2a). TDR data from previous years in block C are in good agreement with data from block A (see Section 3.7). The soil properties are assumed to vary only as a function of depth within each of the soil treatments.

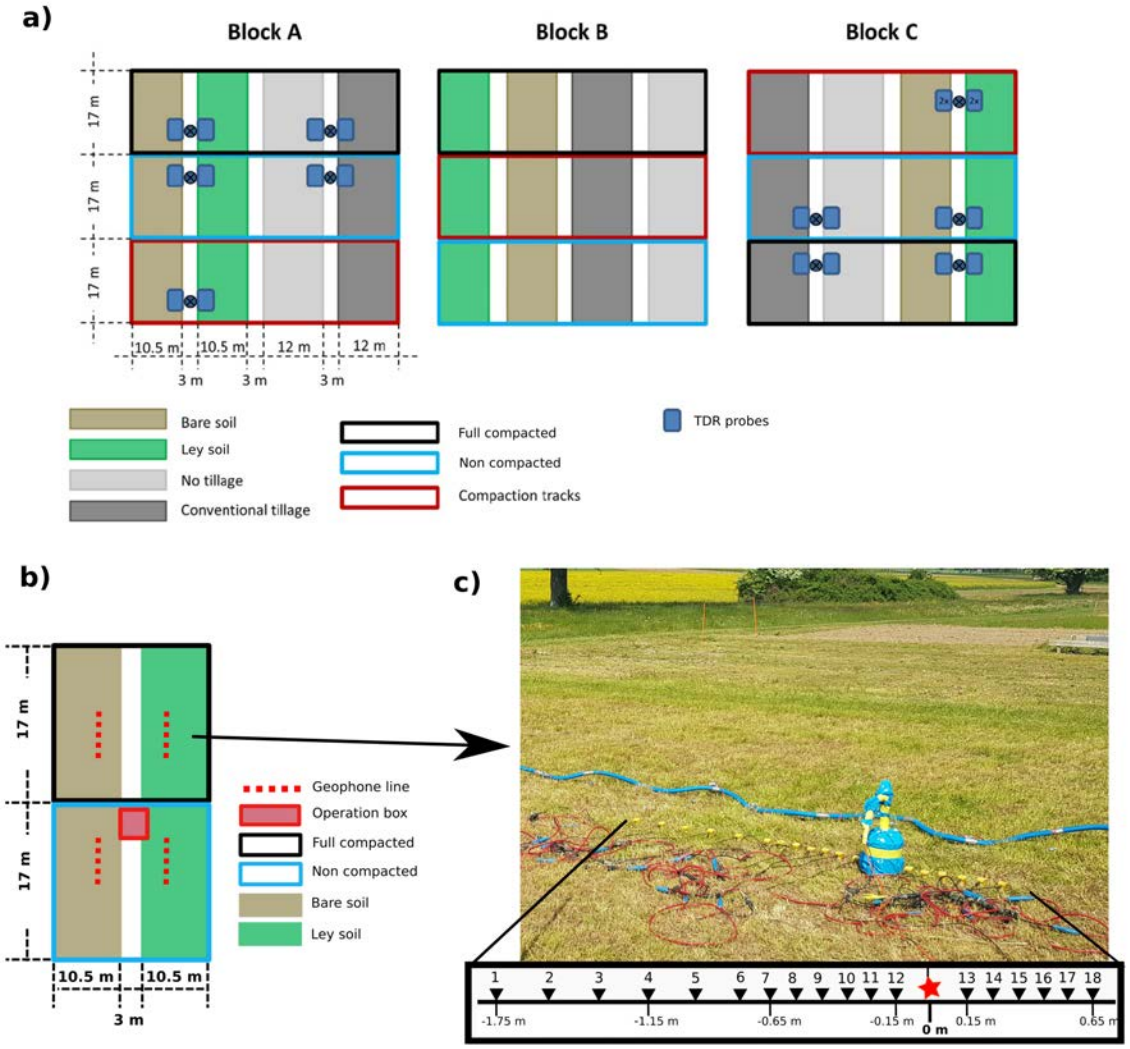

Figure 3.2 – (a) Schematic representation of the soil compaction experiment showing the different compaction treatments and post-compaction managements strategies at the SSO (adapted from *Keller et al.*, 2017). (b) Schematic representation of the seismic lines deployed in block A. (c) Seismic monitoring layout established in the compacted ley.

3.4 Effects of compaction and water content on measured seismic signatures

The seismic velocities derived from the seismic monitoring data are contrasted with predictions made by feeding the pedophysical model with water content θ data derived from TDR sensors at 10 cm depth. The P-wave velocities were approximated by first-break picking and the S-wave velocities by picking the first zero-crossing in the signal, respectively (see Section 3.7). The zero-crossing velocities were found, for this specific experimental setting, to provide

a proxy to the S-wave velocities (see Section 3.7), denoted here as V_s^*. The seismic velocities are representative of the first soil layer with an estimated thickness of 20 cm obtained from first arrivals by solving for the depth to the first refractor (see Section 3.7). In the following, we present the mean values and standard deviations of the estimated seismic velocities at different offsets.

3.4.1 S-wave and P-wave slowness variations with soil water content

We compared time-series of estimated S-wave slowness together with TDR-derived water content using Topp's equation (*Topp et al.*, 1980) for compacted ley (Fig. 3.3a), non-compacted ley (Fig. 3.3b), and compacted bare soil (Fig. 3.3c). The S-wave slowness and the water content showed a remarkable correlation regardless of the studied soil treatment, with correlation coefficients of $r = 0.94$, $r = 0.97$, and $r = 0.97$ for compacted ley, non-compacted ley and compacted bare soil, respectively. The correlations with water content were weaker for P-wave slowness with corresponding correlation coefficients of $r = 0.7$, $r = 0.95$, and $r = 0.85$ for compacted ley, non-compacted ley, and compacted bare soil, respectively (see Fig. 3.4).

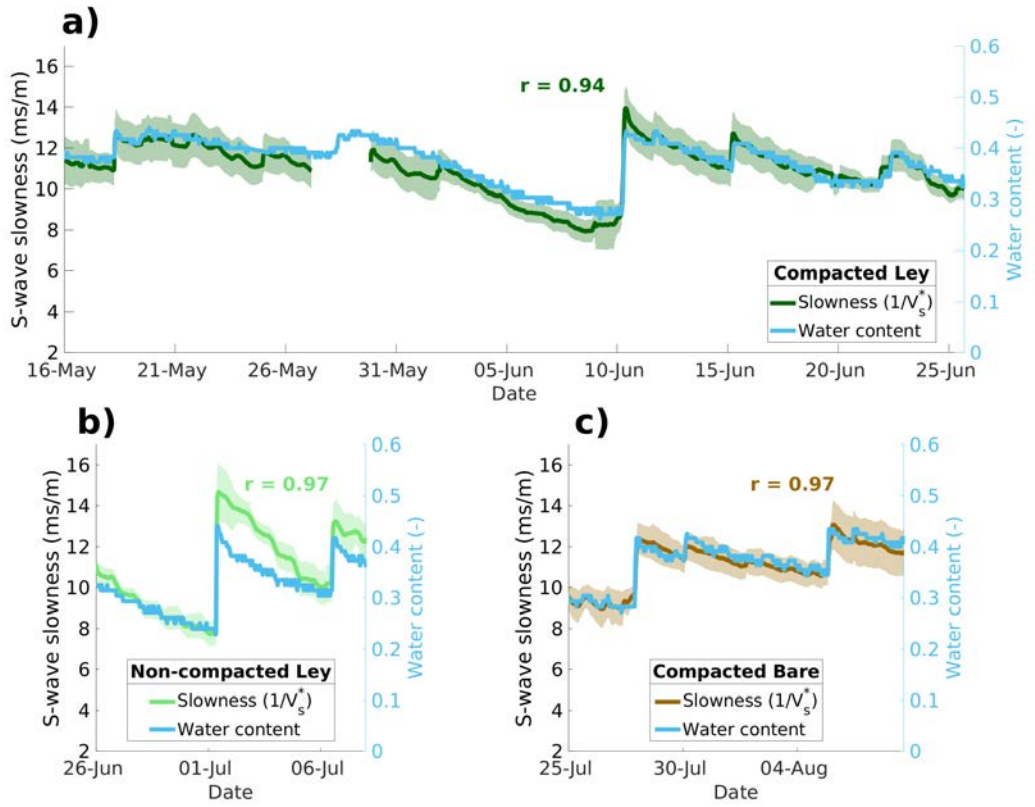

Figure 3.3 – Time-series of estimated S-wave slowness and water content for: (a) full compacted ley, (b) non-compacted ley, and (c) full compacted bare soil. Note that slowness and water content correspond to different time-periods for the different soil treatments.

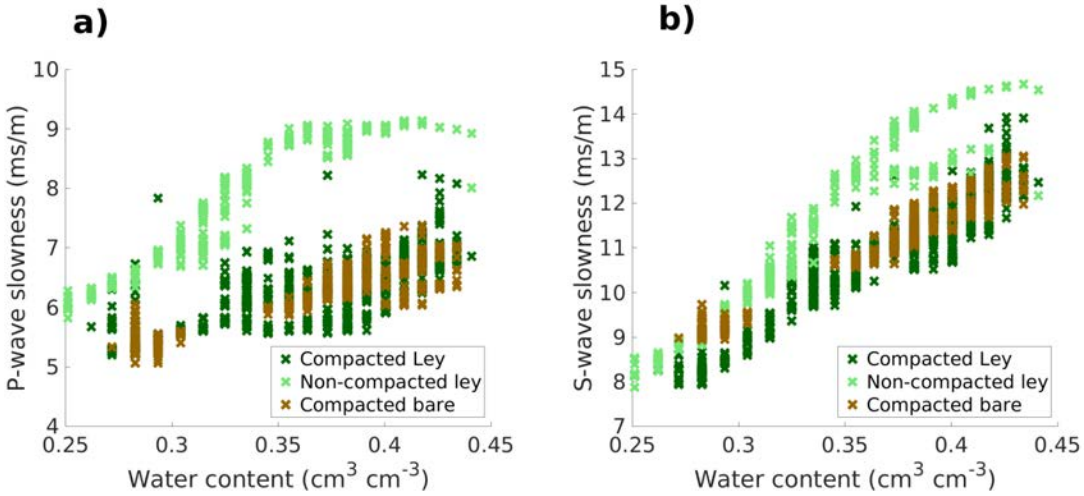

Figure 3.4 – Scatter plot of (a) P-wave and (b) S-wave slowness as a function of water content for all soil treatments.

3.4.2 Pedophysical parametrization of structured soil and treatments at the SSO

Our pedophysical model was developed to deduce information related to soil structure from the measured seismic signatures. In applying the model, we first identified the properties that are linked to compaction states and those related to soil texture. The different soil plots at the SSO present negligible differences in soil texture and the same pre-compaction history (*Keller et al.*, 2017). Thus, we assumed that differences in soil structure for the studied soils are manifested primarily via differences in the compaction-induced contact area A_c (eq. 3.12) and the inter-aggregate space w_M (eqs. 3.6, 3.7 and 3.12). We considered that the aggregate properties (eqs. 3.4 and 3.5) are unaffected by compaction and the same for all soil treatments. In the following, we present the values of the model parameters used (see also Table 3.1).

The properties of water (K_w = 2.2 GPa and ρ_w = 1 g/cm^3) and air (K_a = 0.101 MPa and ρ_a = 1.29 mg/cm^3) were taken from the literature (p. 176, p. 468 *Mavko et al.*, 2009). The elastic properties of the grain mixture (K_s = 36.5 and G_s = 27.6 GPa) were chosen to be representative of the soil texture with roughly 25% sand, 25% clay and 50% silt (*Keller et al.*, 2017). As suggested by *Gurevich and Carcione* (2000), we modeled the grains as a mixture of quartz (sand) and clays using the Hashin-Shtrikman lower bound (*Hashin and Shtrikman*, 1963), implying that the softer material (clays) acts as the primary load-bearing material. The silt fraction was split in equal parts between clay and sand leading to a mixture containing 50% clays and 50% quartz. The dominant clay minerals at the SSO are illite and smectite, thus, we used the elastic properties of an illite-smectite mixture (K_{clay} = 36 and G_{clay} = 18 GPa) reported by *Wang et al.* (2001). The elastic moduli of quartz (K_{quartz} = 37 and G_{quartz} = 44 GPa) were taken from the literature (Table A.4.1 in *Mavko et al.*, 2009). The Poisson ratio of grains and aggregates (ν_s and ν_{agg}) were computed from their corresponding

elastic moduli assuming homogeneous isotropic elastic properties. The highest values of water content measured in 2019 were 0.44, 0.46 and 0.44 for compacted ley, non-compacted ley and compacted bare soil, respectively. To account for air entrapment (i.e., the total porosity is higher than the maximum in-situ water content derived from TDR measurements) (*Faybishenko*, 1995; *Sakaguchi et al.*, 2005), we assumed the total porosities to be 0.47, 0.49 and 0.47 for compacted ley, non-compacted ley and compacted bare soil, respectively. For simplicity, the depth of investigation Z_0 was set to 10 cm in agreement with the depth of TDR measurements. Yet, the velocities reported herein are to be considered as apparent velocities (i.e., averaged velocities over the first soil layer), and Z_0 should be considered a pseudo-depth.

Table 3.1 – Values of the parameters used for pedophysical model predictions for compacted ley (CL), non-compacted ley (NL) and compacted bare soil (CB). Only one value is reported when the model parameter is the same for all soil treatments. Eq. indicates the equation where the parameter is used. The comments specify if the parameters were taken from literature values, calculated from a given model or assumed.

Parameter	Value CL	Value NL	Value CB	Eq.	Comments
STEP 1					
K_{clay} (GPa)		36		-	from *Wang et al.* (2001)
G_{clay} (GPa)		18		-	from *Wang et al.* (2001)
K_{quartz} (GPa)		36		-	from table A.4.1 *Mavko et al.* (2009)
G_{quartz} (GPa)		44		-	from table A.4.1 *Mavko et al.* (2009)
K_s (GPa)		36.5		3.4-3.5	*Hashin and Shtrikman* (1963) lower bound
G_s (GPa)		27.63		3.4-3.5	*Hashin and Shtrikman* (1963) lower bound
ϕ_m (–)		0.46		3.4-3.5	assumed parameter
N_m (–)		6.5		3.4-3.5	from *Manegold and von Engelhardt* (1933)
f_m (–)		0.5		3.5	from *Bachrach et al.* (2000)
ρ_s (g/cm^3)		2.6		3.8	from p. 176 *Mavko et al.* (2009)
ρ_w (g/cm^3)		1		3.8	from p. 176 *Mavko et al.* (2009)
ρ_a (mg/cm^3)		1.29		3.8	from p. 468 *Mavko et al.* (2009)
ϕ_T (–)	0.47	0.49	0.47	3.8	assumed from TDR measurements
S (–)		θ/ϕ_T		3.8	from TDR water content time-series
Z_0 (m)		0.1		3.8	depth of TDR sensors
χ (–)		$S_{e_{agg}}$		3.8	based on *Nuth and Laloui* (2008)
α_m (cm^{-1})		0.02		3.10	assumed based on *Carsel and Parrish* (1988)
n_m (–)		1.25		3.10	assumed based on *Carsel and Parrish* (1988)
$S_{e_{agg}}$ (–)		$(\theta_{agg}-\theta_r)/(\theta_s-\theta_r)$		3.10	based on *van Genuchten* (1980)
θ_s (–)		$\phi_m(1-w_M)$		-	assumed parameter
θ_r (–)		0.08		-	assumed based on *Carsel and Parrish* (1988)
STEP 2					
w_M (–)	0.018	0.055	0.018	3.6-3.7,3.11	from equation 3
N_M (–)	10.44	10.14	10.44	3.6-3.7,3.11	from model by *García and Medina* (2006)
f_M (–)		0.5		3.7	from *Bachrach et al.* (2000)
R_{rel} (–)	0.162	0.095	0.166	3.11	fitting parameter
R (mm)		5		-	assumed based on Marquez et al. (2006)
ϵ_v (%)	1.3	ϵ_0 =0.45	1.4	-	from equation 3.13
P_a (MPa)	1.23	0.21	1.3	3.6-3.7,3.11	mean values from equation 3.11
A (mm^2)	2.06	0.70	2.16	-	-
STEP 3					
K_w (GPa)		2.2		3.14	from p. 176 *Mavko et al.* (2009)
K_a (MPa)		0.101		3.14	from p. 468 *Mavko et al.* (2009)
S (–)		θ/ϕ_T		3.14	from TDR water content time-series
STEP 4					
K_s (GPa)		36.5		3.15	*Hashin and Shtrikman* (1963) lower bound
ϕ_T (–)	0.47	0.49	0.47	3.15	assumed from TDR measurements
K_{fluid} (GPa)		eq. 13		3.15	-
K_{frame} (GPa)		eq. 6		3.15	-
G_{frame} (GPa)		eq. 7		3.16	-

For simplicity, we took the effective stress parameter χ to be equal to $S_{e_{agg}}$. As suggested by *Bachrach et al.* (2000), the fraction of non-slipping particles and aggregates were taken as $f_m = f_M = 0.5$ for all soil treatments to account for the fact that some contacts have zero tangential stiffness. The water retention properties of the aggregates are based on the measurements reported by *Carsel and Parrish* (1988) on clay-loam soils sharing a similar texture as the soil studied here ($n_m = 1.25$ and $\alpha = 0.02\ cm^{-1}$). The intra-aggregate porosity $\phi_m = 0.46$ was assumed based on TDR measurements. The fraction of inter-aggregate porosity w_M was calculated from the intra-aggregate porosity and the total porosity (eq. 3.3). The average number of contacts per particle $N_m = 6.5$ was chosen according to data by *Manegold and von Engelhardt* (1933).

The average number of contacts per aggregates were calculated using the equation for dense packings proposed by *García and Medina* (2006) as $N_M = 4.46 + 9.7(0.384 - w_M)^{0.48}$, resulting in $N_M = 10.44$ for the compacted treatments and $N_M = 10.14$ for the non-compacted treatment. We used the relative contact radius (R_{rel}, see equation 3.12) as a fitting parameter. For each soil treatment, a grid search was performed to minimize the L_2 norm of the misfit between modeled and observed P-wave velocities. Minimum values were obtained when the relative contact radii were 0.162, 0.095 and 0.166 for compacted ley, non-compacted ley and compacted bare soil, respectively, which corresponds to viscous strains of $\epsilon_v = 1.3\%$, $\epsilon_v = \epsilon_0 = 0.4\%$ and $\epsilon_v = 1.4\%$. Assuming a cubic packing of aggregates (*Or*, 1996), we inferred a volumetric strain (non-compacted vs compacted) of roughly 3%. When considering an aggregate radius of $R = 5$ mm (e.g., *Márquez et al.*, 2004), the corresponding contact areas were 2.06, 0.70 and 2.16 mm^2 (see equation 3.12). The average confining pressures P_a (eq. 3.11) were about 1.23 and 0.21 MPa for compacted and non-compacted ley, respectively, with corresponding standard deviations of 0.5 and 0.1 MPa.

3.4.3 Pedophysical predictions of seismic velocities in soil

All soil covers and treatments display gradual increases in seismic velocities during drying periods associated with increasing matric suction and decreasing bulk density (eq. 3.9) (Figs. 3.5a, 3.5b, and 3.5c). Conversely, seismic velocities decrease sharply following rain events which, in turn, are associated with a rapid increase in water content and bulk density, and a decrease in matric suction. P-wave velocities are higher for the compacted soils (see Figure 3.4a). In particular, the highest P-wave velocities were measured in the compacted bare soil treatment, and the lowest in the non-compacted ley treatment. Considering periods with overlapping water content values, the P-wave velocities of compacted ley are on average 31% higher than non-compacted ley and 1.7% lower than compacted bare soil. The S-wave velocities of compacted ley are on average 13.5% higher than for non-compacted ley and 2.5% higher than for compacted bare soil. At water content close to field capacity ($\theta \sim 0.35\ cm^3 cm^{-3}$), the seismic velocities of compacted treatments were higher (41.1% for P-wave velocities and 17.7% for S-wave velocities) than for the non-compacted treatment. These results provide evidence concerning the effects of persistent soil compaction on the seismic data. For saturation values close to one, the P-wave velocity is expected to increase sharply in response to a rapid increase of the bulk modulus of the effective fluid (eq. 3.14). However, our measurements never reached such high saturation levels. For this reason, we only observe

a decreasing trend in seismic velocities with increasing water content due to a decreasing suction stress and an increasing bulk density.

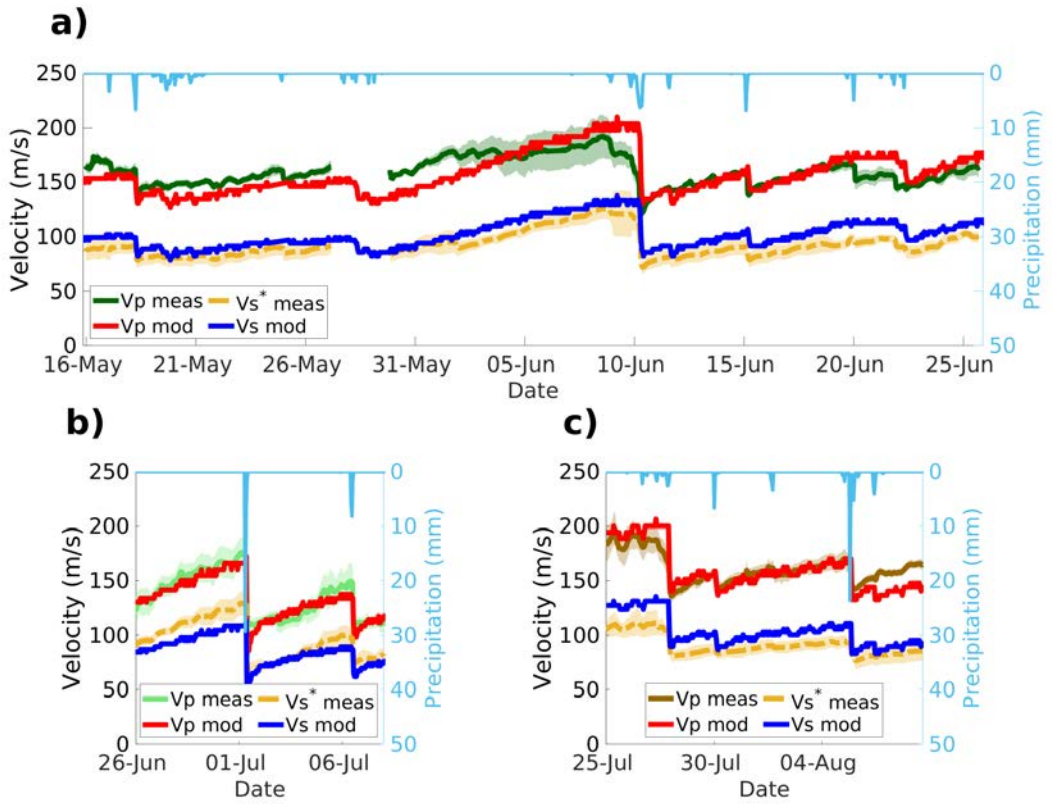

Figure 3.5 – Time series of modeled (mod) and measured (meas) P-wave and S-wave velocities for (a) compacted ley, (b) non-compacted ley and (c) compacted bare soil along with precipitation data (light blue right hand axes).

Our pedophysical predictions of P-wave and S-wave velocity reproduce the main trends in the dynamics of the measured data such as those related to large rain events or drying periods (Figs. 3.5 and 3.6). We evaluate the capacity of the model for reproducing the trend and fitting the observations with correlation coefficients and the weighted root-mean-square-error (WRMSE) values between observed and modeled P-wave velocities for each soil treatment. The correlation coefficients between predicted and measured P-wave velocities were $r = 0.71$ for compacted ley, $r = 0.95$ for non-compacted ley and $r = 0.87$ for compacted bare soil. The corresponding WRMSE were 1.6, 1.08, and 1.3, assuming relative data errors of 5%. We did not include S-wave velocities in the our fitting procedure for obtaining R_{rel}. Yet we observe high correlation coefficients and moderately high WRMSE values between observed and modeled S-wave velocities. The correlation coefficients were $r = 0.94$ for compacted ley, $r = 0.96$ for non-compacted ley and $r = 0.97$ for compacted bare soil. The corresponding WRMSE were 2.35, 2.16, and 2.93, assuming relative data errors of 5%. The slope of the seismic velocity-water content curve is controlled by the Van Genuchten exponent n_m, which is the same for all treatments. As our model does not consider hysteresis in the water retention

curve, a unique value of seismic velocity is predicted for each water content (see Figures 3.6a, 3.6b, and 3.6c). The model predictions slightly overestimate the S-wave velocities (V_s^*) for compacted soils and underestimate them for non-compacted treatments.

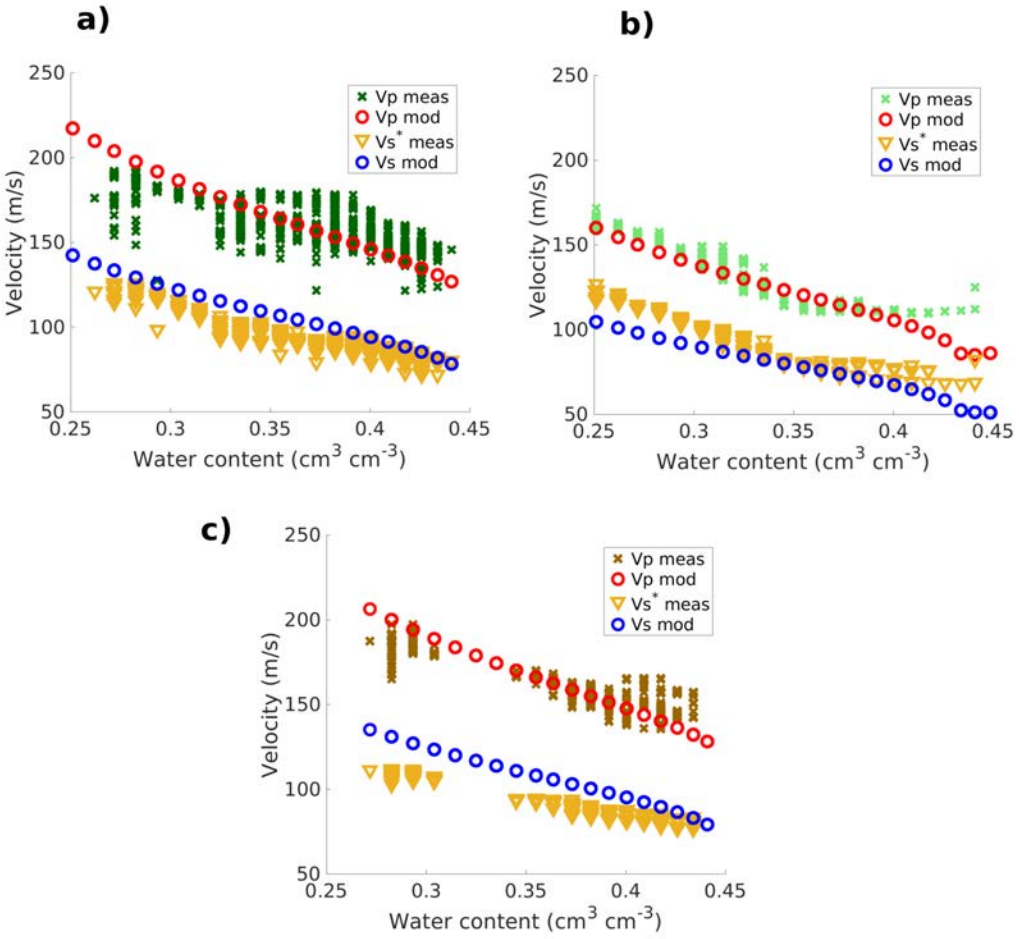

Figure 3.6 – Scatter plot of modeled and measured P-wave and S-wave velocities as functions of soil water content for (a) compacted ley, (b) non-compacted ley and (c) compacted bare soil.

3.5 Discussion

This study presents a method for quantifying the compaction state of a soil from its seismic response. Particularly, we present a pedophysical model for interpretation of seismic measurements in terms of soil aggregate contacts. The model was tested in a field experiment where we monitored seismic properties and water content, associated with rain events and subsequent drying. We compared seismic velocities of different soil plots at the same water content (or saturation) over a wide range of values. Consequently, effects of soil compaction

on mechanical properties can be distinguished from water content effects. For water contents between 0.3 and 0.4 cm^3 cm^{-3}, the pedophysical model predicts a decrease of about 2.5% in both P-wave and S-wave velocities in response to a 0.01 cm^3 cm^{-3} increase in soil water content.

Our results suggest that compacted soil structure has not yet recovered from the effects of compaction as indicated by higher P- and S-wave velocities measured in plots that were compacted five years prior to our measurements. For a given water content, the seismic velocities are similar in compacted ley and compacted bare soil (only 1.7% difference on average), suggesting that the presence of ley has not had a significant effect on the recovery of mechanical properties towards non-compacted conditions. This agrees with on-site point measurements of dry bulk density (soil cores sampled a 10 cm depth) and penetration resistance (average from 5 cm to 15 cm depth) at the SSO presented in Figure 3.7. Figure 3.7 includes observations in the non-compacted bare soil, where seismic monitoring was not carried out. Figures 3.7c and 3.7d present the ratios of compacted vs non-compacted dry bulk density and penetration resistance data by soil cover measured at the same time after compaction. These relative values provide insights of how mechanical properties recover from compaction with respect to the soil cover and suggest that (i) the soil cover does not have a strong influence on the recovery of soil mechanical properties towards non-compacted states, and that (ii) soil mechanical properties still show a significant imprint of soil compaction four years after the compaction event.

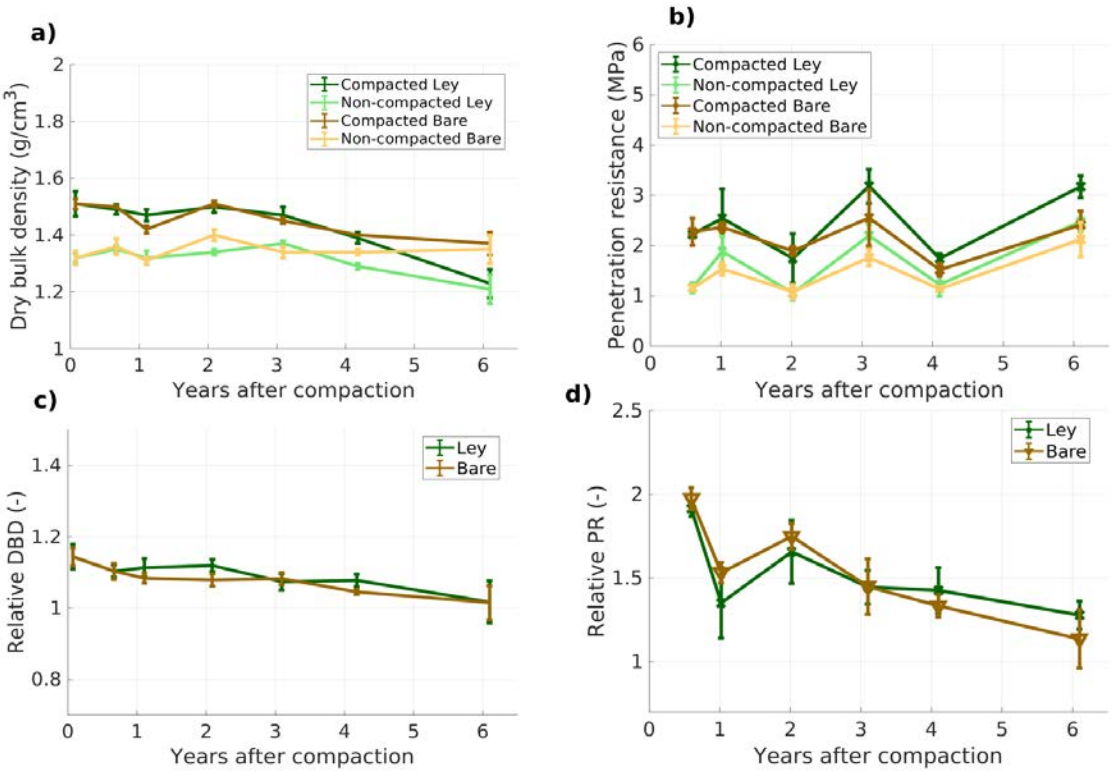

Figure 3.7 – (a) Dry bulk density data as a function of the time since the compaction event for compacted ley, non-compacted ley, compacted bare soil, and non-compacted bare soil. (b) Penetration resistance as a function of the time since the compaction event for compacted ley, non-compacted ley, compacted bare soil, and non-compacted Bare soil. (c) Relative dry bulk density (DBD) as a function of years since compaction for ley and bare soil. (d) Relative penetration resistance (PR) as a function of years after compaction for ley and bare soil. Error bars correspond to the standard error of the measured dry bulk densities and standard deviation of measured penetration resistance. The relative values were calculated as the ratio between the compacted treatment and its corresponding non-compacted treatment measured at the same time. For comparison, note that the seismic monitoring results were acquired 5 years after the compaction event.

Five years after compaction, using our pedophysical model and the retrieved seismic data, we inferred contact areas that are 2.9 larger for compacted than for non-compacted soils. This corresponds to a seismic-inferred volumetric strain of ~ 3% for compacted soils. In this context, Figure 3.8 presents long-term volumetric strains derived from dry bulk density data measured in the compacted ley and compacted bare soil and data measured in their corresponding non-compacted treatments at the same time after compaction. For further information regarding the volumetric strain calculations we refer the reader to Section 3.7. The volumetric strains resulting from pedophysical modeling five years after compaction (~ 3%) fit nicely the post-compaction decreasing trend observed in volumetric strains computed from dry bulk density data (~ 7 % for four years after compaction and ~ 1.5 % for six years after compaction). Our model considers the aggregates as elastic spheres, for which the

confining pressure P_a (~ 1.2 MPa for compacted soils) is required to maintain the inferred contact areas. This pressure should not be confused with the stress applied during visco-elastic deformation of the aggregates during compaction, that was much lower (~ 150 KPa at 10 cm depth, see *Keller et al.*, 2017).

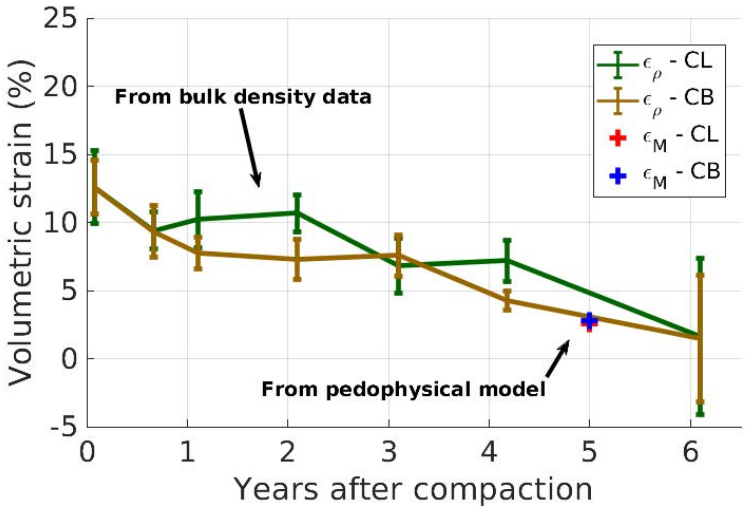

Figure 3.8 – Comparison of soil volumetric strain derived from dry bulk density data (ϵ_ρ) as a function of the time since the compaction event and the volumetric strain estimated from inferences of axial strains obtained from the pedophysical model and seismic data (ϵ_M). The volumetric strains from bulk densities and pedophysical model were obtained by comparing compacted ley (CL) and compacted bare soil (CB) with non-compacted ley at the same time after the experimental compaction event.

Our results show that combined seismic monitoring and pedophysical modeling can provide information related to soil compaction. In well-controlled field experiments such as the SSO, our framework of combined measurements and modeling could be used to evaluate the evolution of the mechanical status of soils at the plot scale by studying the long-term evolution of inferred aggregate contact area. Due to the low frequencies used, the small scale of the experiment and the target soil volume (first soil layer), the approach presented does not consider vertical variations of the overburden pressure and rather offers a simplified description of the effective compaction properties (i.e., contact area) of the first soil layer. This already provides useful insights on the compaction state of soils. A detailed one-dimensional analysis of soil compaction would require the water content at all depths. Soil-structure based concepts might be further developed to advance other applications of seismic monitoring.

3.6 Conclusions

We monitored seismic signatures of soils with different compaction treatments and covers at a controlled experimental field site, in which a compaction event took place five years prior to the presented seismic monitoring. We found that inferred S-wave slownesses strongly correlate with water content in all soil treatments, while P-waves carried a stronger imprint of soil compaction. Furthermore, no significant differences were observed between soil cover (ley vs. bare soil), implying that the ley did not play a crucial role on the recovery of soil mechanical properties. Significantly higher P-wave velocities observed in the compacted plots suggested that the soils are still appreciably impacted by the compaction event and that soil structure recovery is a slow process. The seismic velocities were well reproduced with a newly proposed dual-domain pedophysical model accounting for soil plastic deformation due to soil compaction events. The model inferred contact areas between aggregates that are 2.9 times larger for compacted than for non-compacted soils. Based on our results, we suggest that seismic methods are suitable for characterizing soil structure, partly by offering a link to soil hydration status and partly by providing a direct link to soil mechanical properties that other geophysical methods do not respond to.

3.7 Supplemental material

Comparison of volumetric water content between block A and block C at the SSO

In this study we infer effective seismic velocity from seismic measurements conducted in 2019 in block A of the Soil Structure Observatory (SSO). The inferences were based on application of a pedophysical model informed by water content measurements derived from Time Domain Reflectometry (TDR) probes installed in the soil profile. Due to a technical issue, TDR data were not available for block A in 2019. For this reason we used TDR data from adjacent block C (with similar replicated treatments) subjected to similar climatic conditions over a relatively uniform field. In the following, we compare TDR data from block A and block C of the SSO from 2015-2018. Figure 3.9 presents crossplots of TDR soil water content measured in block A and block C in the SSO for all the soil treatments considered in this study. The data were collected from 2015 to 2018. The correlation coefficient between data measured in the block C and block A were 0.93, 0.85, 0.97 and 0.94 for compacted bare soil, non-compacted bare soil, compacted ley and non-compacted ley, respectively. The weighted root-mean-square-error (WRMSE) between data measured in the block C and block A were 1.05, 1.61, 1.04 and 1.66 considering 5% of data error for compacted bare soil, non-compacted bare soil, compacted ley and non-compacted ley, respectively.

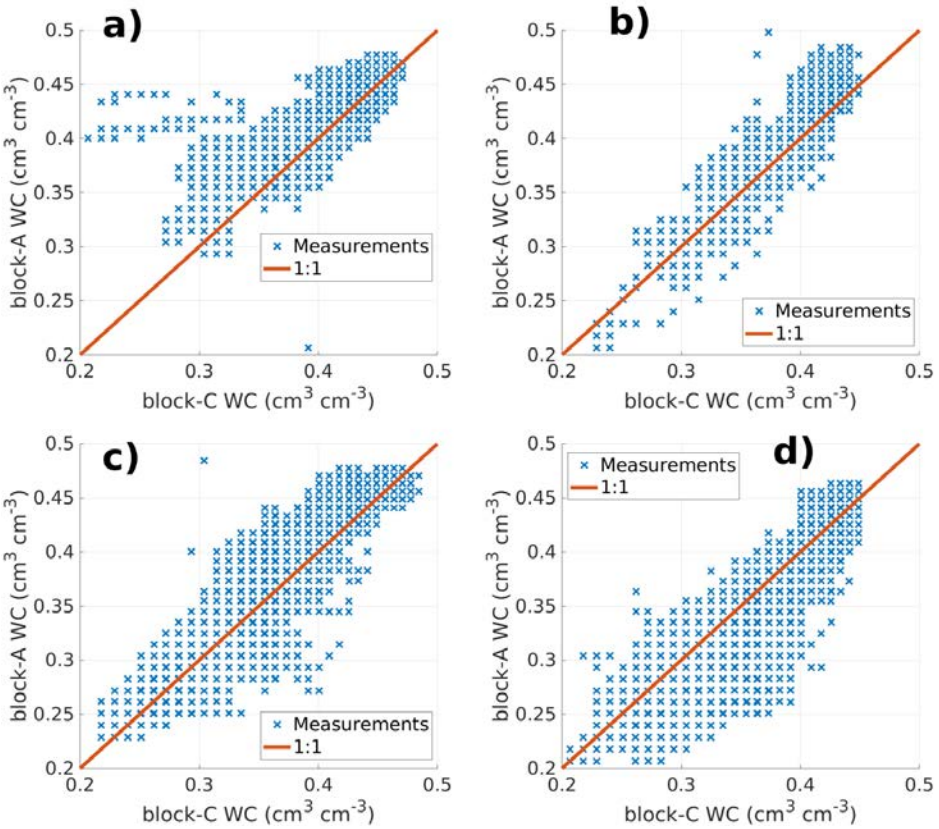

Figure 3.9 – Comparison of the volumetric content (WC) measured in block A and block C for (a) compacted bare soil, (b) non-compacted bare soil, (c) compacted ley and (d) non-compacted ley. The crossplots present data from 2015 to 2018.

Determination of seismic velocities from the measured seismic signals

P-wave velocities

P-wave velocities were estimated by standard picking of first-arrivals from the time-lapse seismic records. We selected the traces corresponding to offsets of 0.35 m, 0.45 m, 0.55 m and 0.65 m to estimate the seismic velocities for all treatments (see Figures 3.10a, 3.10b and 3.10c). Due to noise, the traces corresponding to the 0.35 m offset from compacted bare soil were discarded. The first arrivals were defined as the time at which the absolute value of a normalized trace is higher than the threshold of 0.01 (normalized units). A 1D median filter (with a width of ten samples corresponding to a time period of 150 minutes) was applied to the time-series of the picked times to filter out outliers. A geophone screwed to the top of the seismic source was used to trigger acquisition and to register the reference impact time. Yet it was common to encounter negative times at the shortest offset (0.15 m). A time delay t_0 was added to the picked times to account for this error, which we estimated as a time-invariant constant for each monitoring period of a given soil treatment. The time delay was obtained by (1) referencing the picked times to a given t_0 to obtain corrected picked times, (2) fitting a straight line by regression to the corrected picked times that passes through the origin and (3) using the value of t_0 that minimizes the misfit of the corrected picked times

and the theoretical times predicted by the straight line. This procedure was done for each soil treatment considering picked times from both sides of the source and for all acquisition times. The optimal values of t_0 were 1.06, 1.56 and 1.06 ms for the compacted ley, non-compacted ley and compacted bare soil, respectively.

The time series of the picked times for each treatment were referenced to their corresponding optimal value of t_0 (see Figures 3.10d, 3.10e and 3.10f). In order to have a more robust estimation of our seismic velocities, we estimated them with two different approaches. For each treatment, the corrected picked times were used to calculate the time series of P-wave velocities (1) for each individual geophone, defined by the ratio between its offset and its picked time, and (2) for the group of geophones, defined by the slope of the straight line that passes by the origin and gives the best fit to the four picked times. This process was done for each side of the seismic source, leading to ten time-series of seismic velocities for each plot. Figures 3.10g, 3.10h and 3.10i show the time-series of estimated P-wave velocities corresponding to the sensors of one side of the seismic source for compacted ley, non-compacted ley and compacted bare soil, respectively. Mean values and standard deviations of the P-wave velocities reported in our study were calculated by averaging the ten time-series of P-wave velocities estimated within each treatment.

S-wave velocities

The S-wave velocities were estimated based on the first zero-crossings. This procedure was based on the assumption that, at the scale of our experiments and for the conditions prevailing at the SSO, the first zero-crossing was dominated by a combination of S-wave and surface waves that share similar velocities (the validity of this assumption is assessed by modeling in the following section). Similarly to the first-break picks, we selected the traces at 0.35 m, 0.45 m, 0.55 m and 0.65 m to calculate our S-wave velocities for all treatments (see Figures 3.11a, 3.11b and 3.11c). The first zero-crossing times were defined as the first time at which the signal changes its polarity from negative to positive. A 1D median filter (with a width of ten samples corresponding to a time period of 150 minutes) was applied to the time-series of the picked times to filter out outliers. We corrected the time series of the picked times by referencing them to the previously estimated values of t_0 (see Figures 3.10d, 3.10e and 3.10f).

Similarly to the procedure to obtain P-wave velocities, we used the corrected picked times to calculate the time series of S-wave velocities (1) for each individual geophone, defined by the ratio between its offset and its picked time, and (2) for the group of geophones, defined by the slope of the straight line that passes by the origin and gives the best fit to the four picked times. This was done for sensor on each side of the source, resulting in ten time-series of estimated velocities. Figures 3.11g, 3.11h and 3.11i show the time-series of estimated S-wave velocities corresponding to the sensors of one side of the seismic source for compacted ley, non-compacted ley and compacted bare soil, respectively. The mean values and standard deviations of the S-wave velocities reported in our study were calculated by averaging the ten time-series of S-wave velocities within each treatment.

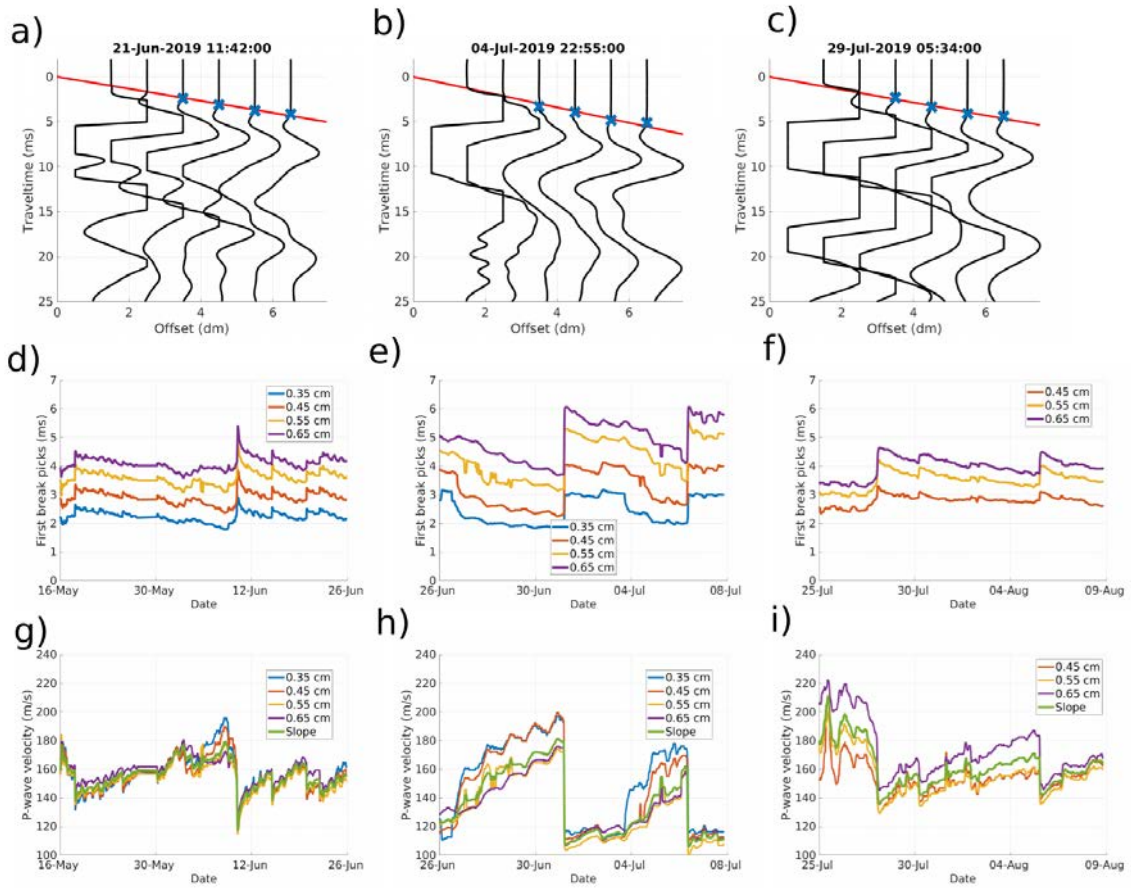

Figure 3.10 – Examples of seismic data recorded by the geophones at the six nearest offsets at an arbitrary date from (a) compacted ley, (b) non-compacted ley and (c) compacted bare soil. The blue crosses correspond to the first-break picks used to calculate the P-wave velocities from to the slope of the red line. Time-series of the picked first-break times for different offsets in the (d) compacted ley, (e) non-compacted ley and (f) compacted bare soil. Time series of the calculated P-wave velocities for different offsets along with the velocity calculated with the slope method for (g) compacted ley, (h) non-compacted ley and (i) compacted bare soil.

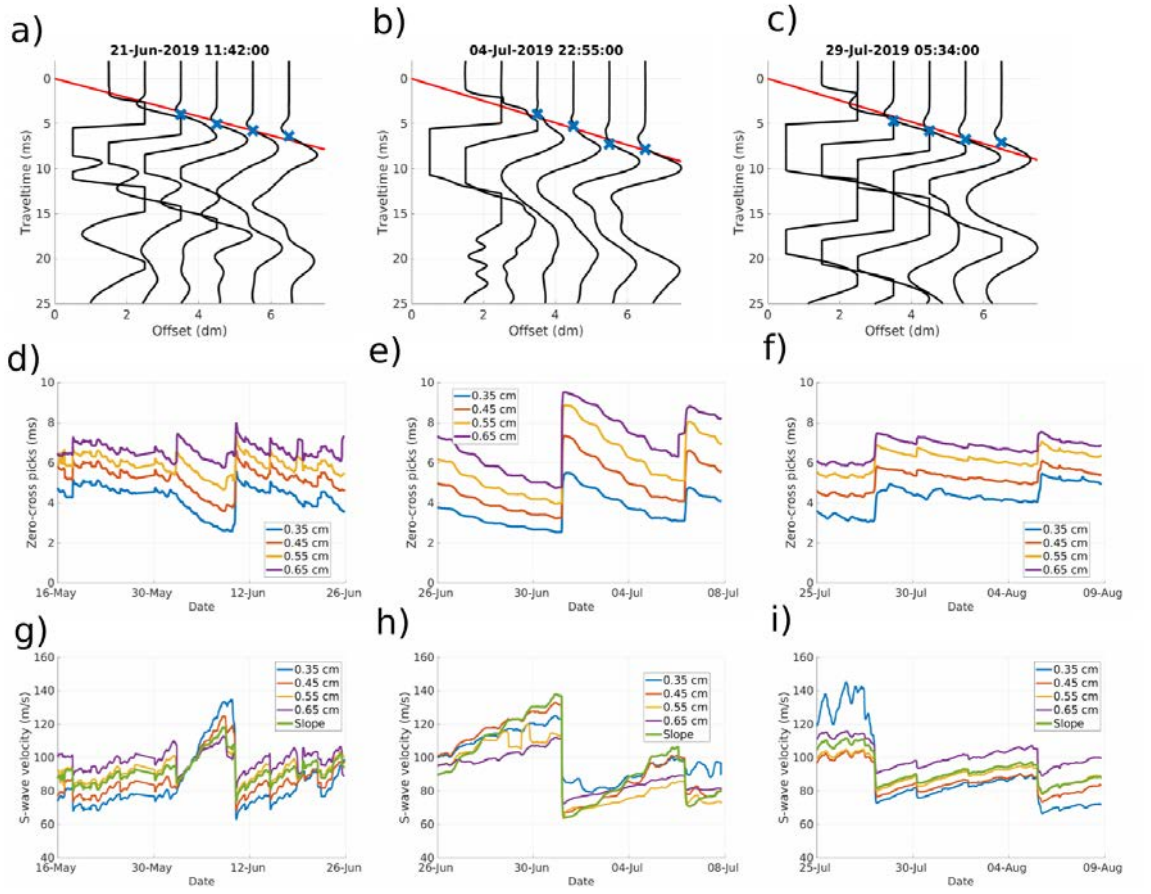

Figure 3.11 – Examples of seismic data recorded by the geophones at the six nearest offsets at an arbitrary date from (a) compacted ley, (b) non-compacted ley and (c) compacted bare soil. The blue crosses correspond to the first-break picks used to calculate the S-wave velocities from the slope of the red line. Time-series of the picked first-break times for different offsets in the (d) compacted ley, (e) non-compacted ley and (f) compacted bare. Time series of the calculated S-wave velocities for different offsets along with the velocity calculated with the slope method for (g) compacted ley, (h) non-compacted ley and (i) compacted bare soil.

Assessing the accuracy S-wave velocity estimation by numerical modeling of wave propagation

In order to assess the accuracy of our procedure for estimating S-wave velocities, we performed 2D numerical simulations of elastic wave propagation using the open-source code by *Bohlen* (2002). Zero-crossing velocities (V_{zc}) were estimated from the generated seismic data using the same procedure as for the field data and compared to the true (provided as input to the modeling code) underlying velocities used in the numerical model and theoretical velocities of Rayleigh waves (R-waves) for a two-layer velocity model. The R-wave velocities (V_r) were computed with the open-source code by *Wathelet et al.* (2020).

The soil was represented by a simplified two-layer velocity model that is representative of the soil conditions at the SSO. We aimed at testing our procedure for estimation of S-wave velocities considering realistic variations of seismic velocities at the SSO. For this, we considered 72 different combinations of P- and S-wave velocities for the top layer and, thus, performed 72 wave propagation simulations. The velocities were selected from estimations of seismic velocities in the SSO, specifically, in the compacted ley. The values of the ratio between seismic velocities (V_p/V_s) are within the range of values reported for soils (e.g., *Uyanik*, 2010). The bulk density of the top layer were estimated from TDR data assuming the values for the total porosity and densities of the soil solid phase, water and air that are presented in Table 1. To estimate the layer thickness in our numerical simulations, we solved the refractor problem from field data at the compacted ley to estimate time-series of the depth of the refractor (see Figure 3.12) and its P-wave velocity. In the following, the P-wave velocity of the underlaying half-space was kept fixed to the average velocity of the first refractor (~280 m/s). In order to obtain a reasonable corresponding S-wave velocity, we assumed a constant ratio between seismic velocities of $V_p/V_s \sim 1.75$. The bulk density of the underlaying half-space was set to 1.8 g/cm^3.

The space domain of the numerical simulation extended horizontally from 0 to 5 m and vertically from 0 to 2 m. The grid size was 1 cm × 1 cm. The free surface condition was set at the top of the model domain, whereas perfectly matched layer (PML) boundary conditions were used for the remaining boundaries. The parameters of the PML boundaries were chosen, according to recommendations by *Komatitsch and Martin* (2007), to 20 grid elements and a velocity of 150 m/s. In the considered two-layer velocity model, it is expected that the source wavelet and its central frequency exert an effect on the estimated zero-crossing velocities. However, the source wavelet is difficult to determine from the field data and its parameters are typically inferred from the seismic data (e.g., *Asnaashari et al.*, 2013). Since we lack information about the exact source wavelet and its central frequency, we considered two different source wavelets and frequencies. We used Füchs-Müller (FM) type sources with central frequencies of 75 and 150 Hz (Figure 3.13a) and Ricker (RI) type sources with central frequencies of 75 and 150 Hz (Figure 3.13b). Figures 3.13c and 3.13d present the estimated zero-crossing velocities as a function of the true S-wave velocities of the top-layer for 75 and 150 Hz, respectively. In order to evaluate whether the zero-crossing velocities were related to the velocities of R-wave, we added the theoretical R-wave velocities corresponding to the two-layer system as a function of the true S-wave velocities of the top-layer. Theoretical values of R-wave velocities were computed for 75 and 150 Hz with the module **gpdc** included

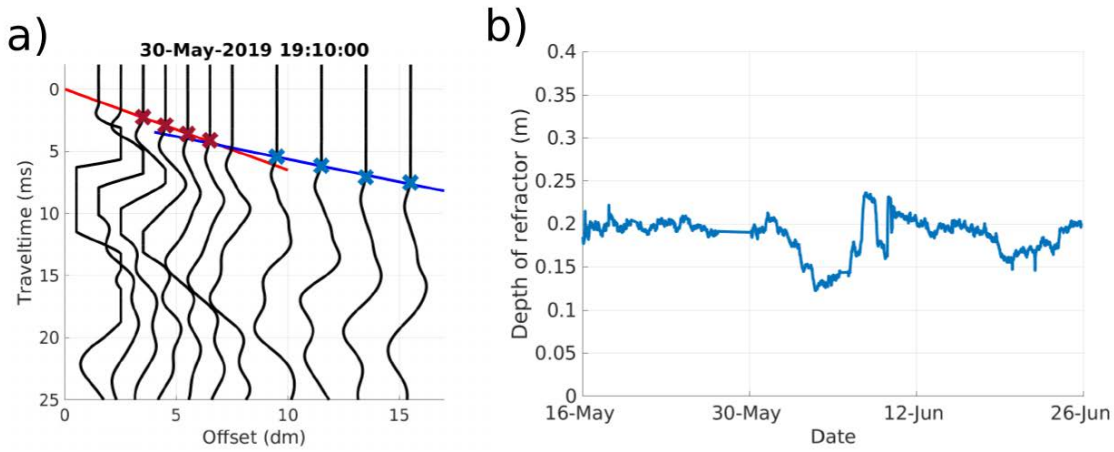

Figure 3.12 – (a) Example of seismic data recorded by the geophones at the twelve nearest offsets, at an arbitrary date, from compacted ley used to solve for the depth of the refractor. The red crosses represent the first-break picks used to calculate the P-wave velocities of the top layer (slope of the red line). The blue crosses represent the first-break picks used to calculate the P-wave velocities of the refracted wave (slope of the blue line). (b) Time series of the estimated depth of the refracting layer for the compacted ley.

in GEOPSY (see *Wathelet et al.*, 2020), developed to calculate dispersion curves of surface waves. The zero-crossing velocities are sensitive to the source wavelet and its frequency, tending towards higher values for lower frequencies. Figures 3.13c and 3.13d demonstrate that our procedure of estimating S-wave velocities lead to slightly biased estimates that are bounded between the true R-wave and S-wave velocities. The correlation coefficient between zero-crossing velocities and true S-wave velocities were 0.95, 0.99, 0.96 and 0.98 for the FM 150 Hz, FM 75 Hz, RI 150 Hz and RI 75 Hz wavelets, respectively.

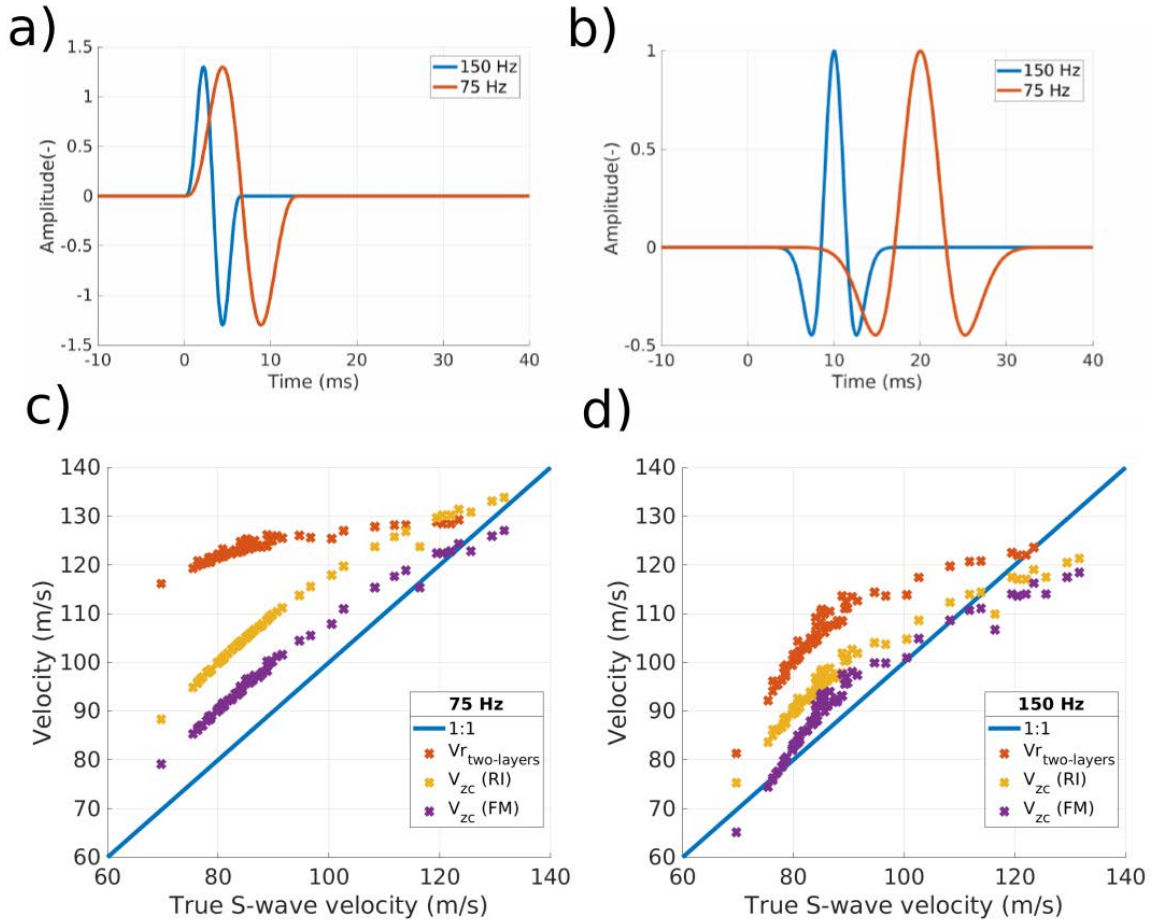

Figure 3.13 – (a) Füchs-Müller and (b) Ricker wavelets with central frequencies of 75 and 150 Hz. Comparison of true vs. estimated S-wave velocities in a two-layer media for two different source wavelets and two different central frequencies: (c) 75 Hz and (d) 150 Hz. In (c) and (d), the true R-wave velocity (V_r) is shown for comparison purposes.

We have demonstrated that there is a high correlation between true S-wave velocities and estimated zero-crossing velocities for different source wavelets and frequencies. Because of sensitivity to R-wave velocities, our velocity estimation procedure provides zero-crossing velocities that slightly overestimate the true S-wave velocities. In this study, we can thus use the zero-crossing velocities as proxies of S-wave velocities. We stress that this estimation procedure is site-specific and it cannot be assumed to apply at other conditions.

Volumetric strain from dry bulk density data and seismic measurements

The volumetric strain from dry bulk density data is calculated as:

$$\epsilon_\rho = 1 - \frac{\rho_{NC}}{\rho_{FC}}, \tag{3.17}$$

where ρ_{NC} and ρ_{FC} are the dry bulk densities of the non-compacted soil and full-compacted soil, respectively. The volumetric strain from dry bulk density data (equation 3.17) was calculated by comparing dry bulk densities measured in the full compacted ley with dry bulk densities measured in the non-compacted ley and full compacted bare soil with non-compacted bare soil at the same time after the experimental compaction event.

The volumetric strain is derived from seismic measurements by considering a cubic arrangement of soil aggregates. In such case, the axial strain derived for non-compacted ($\epsilon_{v_{NC}}$) and full-compacted soils ($\epsilon_{v_{FC}}$) are related to their corresponding bulk densities (ρ_{NC} and ρ_{FC}) by (see *Or*, 1996):

$$\epsilon_{v_{NC}} = 1 - \left(\frac{\rho_i}{\rho_{NC}}\right)^{\frac{1}{3}}, \tag{3.18}$$

and

$$\epsilon_{v_{FC}} = 1 - \left(\frac{\rho_i}{\rho_{FC}}\right)^{\frac{1}{3}}, \tag{3.19}$$

where ρ_i is the reference pre-compaction bulk density, which is assumed to be the same for the non-compacted and compacted soil treatments given that they share the same pre-compaction history. Rearranging equations 3.18 and 3.19, we obtain a model-estimate of the volumetric strain (ϵ_M) that is a function of the axial strains as:

$$\epsilon_M = 1 - \frac{\rho_{NC}}{\rho_{FC}} = 1 - \left(\frac{1-\epsilon_{v_{FC}}}{1-\epsilon_{v_{NC}}}\right)^3. \tag{3.20}$$

The volumetric strain from pedophysical model (equation 3.20) were obtained by comparing compacted ley and compacted bare soil with non-compacted ley.

Chapter 4

Lasting effects of soil compaction on soil water regime detected by geoelectrical monitoring

---

Alejandro Romero-Ruiz, Niklas Linde, Ludovic Baron, Daniel Breitenstein, Thomas Keller and Dani Or.

In preparation for submission to *Water Resources Research*.

Abstract

Despite the central role of soil structure in hydrological and ecological soil functioning, its quantification in the field remains a challenge. Traditional characterization of soil structure relies on point-wise measurements and complementary methods for systematic soil structure characterization that are minimally invasive, operate at field scales, and can deliver information under natural conditions are lacking. We propose the use of geoelectrical monitoring as a means for observing indirect effects of soil structure on the soil water regime (infiltration and drainage rates, evaporation, etc.). We developed a modeling scheme combining a new pedophysical model of soil electrical properties and a one-dimensional water flow and heat transfer model that incorporate a physically-based and structure-specific model of soil evaporation that is soil structure-specific. The model was used to interpret Direct Current (DC)-resistivity and Time-Domain Reflectometry (TDR) monitoring data from the Soil Structure Observatory (SSO) located in the vicinity of Zürich, Switzerland. The SSO is a long-term experiment designed to study the evolution of soil properties following a compaction event in the spring of 2014. We focus on four experimental plots: non-compacted and compacted bare soil and non-compacted and compacted ley. DC-resistivity data revealed that soil compaction leads to a persistent decrease in soil electrical resistivity. This decrease is mainly attributed to increasing connectivity of soil aggregates due to compaction as predicted by soil rheology models. Our work advances the ability to characterize soil structure at the field scale with electrical methods by offering a physically-based explanation of the impact of soil compaction on electrical properties and by showing how DC-resistivity data senses soil water dynamics that depends on soil structure.

4.1 Introduction

Soil structure refers to the spatial arrangement and binding of soil constituents that develops in response to biological activity, seasonal cycles of wetting and drying, freezing and thawing and anthropogenic activities (*Dexter*, 1988). Earthworms moving through the soil combined with decaying roots generate biopores networks in the soil (*Oades*, 1993; *Bottinelli et al.*, 2015) that have a strong impact on soil hydraulic properties and related soil ecological services (*Gerke et al.*, 2010; *Vereecken et al.*, 2007; *Jarvis et al.*, 2016). In addition, soil texture influences soil evapotranspiration, thereby, impacting water and energy partitions at the soil-atmosphere interface (*Lawrence et al.*, 2007; *Lehmann et al.*, 2018). The notion of soil structure remains elusive and despite the growing recognition of soil structure as a determinant agent affecting hydraulic processes at the landscape scale, current climate models used in Earth System Science rely on pedotransfer functions that often consider soil texture only (*Van Looy et al.*, 2017), thereby, overlooking the important impact of soil structure (*Fatichi et al.*, 2020).

Characterizing soil structure at the field scale remains a challenge due to the reliance of invasive point measurements offering limited prospects for studying soil structure over larger spatial scales relevant to land management. *Romero-Ruiz et al.* (2018) proposed using geophysical methods to complement such traditional techniques for soil structure characterization. Electrical methods offer a great potential for capturing and monitoring effects of

soil structure on soil water regimes that cannot be deduced from bulk soil properties. Electrical properties of porous materials are widely used for capturing and characterizing water flow under different conditions (*Binley et al.*, 2015; *Binley and Slater*, 2020). There is extensive evidence demonstrating that electrical properties of soil are sensitive to the volumetric fractions and electrical properties of the soil constituents and their spatial arrangement (*Bussian*, 1983; *Glover et al.*, 2000; *Glover*, 2009; *Cosenza et al.*, 2009; *Moysey and Liu*, 2012; *Day-Lewis et al.*, 2017). For this reason, electrical methods have been used extensively to quantify water content in soils (*Doolittle and Brevik*, 2014) and to quantify compaction states (*Besson et al.*, 2013), mainly by capitalizing on the sensitivity of electrical properties to the volumetric fraction of soil constituents. Recently, *Blanchy et al.* (2020) demonstrated the potential of electromagnetic induction (EMI) and DC-resistivity methods to monitor the impact of agricultural practices and identify soil compaction. Despite the accumulated wealth of studies relating soil electrical properties to various soil properties and states, providing a physically based description of how soil structure impacts electrical resistivity remains an open question.

Soil structure influences soil electrical resistivity by (1) the direct impact of the arrangement and volumetric fractions of soil constituents and (2) the indirect impact of the arrangement of soil constituents on soil water dynamics. Soil compaction is a common modifier of soil structure that adversely impacts soil functioning and its water regime (*Hamza and Anderson*, 2005). Disentangling effects of soil compaction on geoelectrical signatures is challenging due to its multiple effects on pore geometry, pore connectivity and its role in determining the volumetric proportion of the conducting liquid phase. Soil compaction reduces the capacity of the soil to provide water and air to plant roots for their development. It produces a reduction and disruption of the soil pore system (particularly biopores), which leads to a reduction in soil transport properties and might impact soil evaporation (*Assouline et al.*, 2014) and decrease soil surface water infiltration. The effect of soil compaction on soil mechanical properties limit the ability of plant roots to reach larger soil volumes and extract water (*Bengough et al.*, 2011). All these interacting processes ultimately determine the resulting soil water dynamics. Coupled hydrogeophysical modeling (e.g., *Kowalsky et al.*, 2004) is expected to enhance our quantitative understanding of the influence of soil structure on such natural processes and their corresponding effect on soil water dynamics and related geoelectrical signals. In this context, it is important to consider a soil-structure based integrative modeling framework that accounts for soil electrical properties and the controlling soil processes impacting soil water dynamics (infiltration, drainage and evapotranspiration).

In this study, we focus on how geoelectrical monitoring can provide direct (via volumetric portions and arrangement of constituents) and indirect (via impact on soil water dynamics) information about soil structure. We rely on a coupled hydrogeophysical modeling scheme to predict the prime signatures of soil structure on soil water dynamics and their corresponding geoelectrical properties. At its core, it relies on a new pedophysical model of electrical properties that considers a conceptual description of structured soils. We further infuse knowledge of how soil water retention and transport properties impact soil evaporation in order to constrain the choices of physical parameters and incorporated the corresponding evaporation properties in a one-dimensional water flow model. This modeling framework was used to reproduce and interpret data from a soil compaction experiment at the Soil

Structure Observatory (SSO) located in the vicinity of Zürich, Switzerland. We analyzed four different cases (combinations of two compaction treatments and two soil covers) presenting different responses but sharing the same soil texture.

4.2 Soil-structure-informed hydrogeophysical modeling

Our hydrogeophysical modeling scheme is based on a new pedophysical model of electrical properties that is combined with 1D simulations of water-flow and heat transfer in a layered soil profile. We account for macropore water flow (*Durner*, 1994) and use soil-specific evaporative properties to define water loss functions. The water flow model considers soil structure-specific evaporation properties that are derived from water retention and transport properties (e.g., van Genuchten properties, *van Genuchten*, 1980) using the model by *Lehmann et al.* (2020). We converted modeled time-series of water content to their corresponding soil dielectric permittivity for comparison with Time-Domain Reflectometry (TDR) measurements of dielectric permittivity. Our new pedophysical model is used to calculate electrical conductivity profiles from soil properties, water content and temperature profiles resulting from the water-flow and heat-transfer simulations. The electrical conductivity profiles were then used to calculate apparent electrical resistivity for comparison with measured data. Subsequently, Markov chain Monte Carlo (MCMC) is used to infer posterior probability density functions of unknown parameters of interest. Details of our modeling scheme are described below.

4.2.1 Pedophysical model of electrical conductivity

The electrical properties of structured soils are modeled with a new pedophysical model that account for the arrangement of soil constituents. The soil electrical conductivity is predicted by considering the combined impact of the soil matrix and soil macropores (see also *Day-Lewis et al.*, 2017). The soil matrix is composed by a water-air fluid mixture containing soil inclusions, while the macroporous region is composed by a water-air fluid-mixture. The total porosity (ϕ_T) is expressed as a function of the soil matrix porosity (ϕ_{sm}) and the macroporous region ($\phi_{mac} = 1$), and the volumetric fraction occupied by the soil macropores (w_{mac}) and the soil matrix ($1 - w_{mac}$):

$$\phi_T = (1 - w_{mac})\phi_{sm} + w_{mac}\phi_{mac}. \tag{4.1}$$

The predicted electrical conductivity of the soil is obtained by applying three main mixing steps (Figure 4.1a) to derive: (1) the electrical conductivity of the partially saturated soil matrix, (2) the electrical conductivity of the partially saturated macropores and (3) the electrical conductivity of the structured soil (soil matrix with embedded macropores).

We first model the electrical conductivity of the soil matrix (σ_{sm}). In this context, soil surface conductivity (σ_s) plays an important role in determining the electrical conducitivity of soils

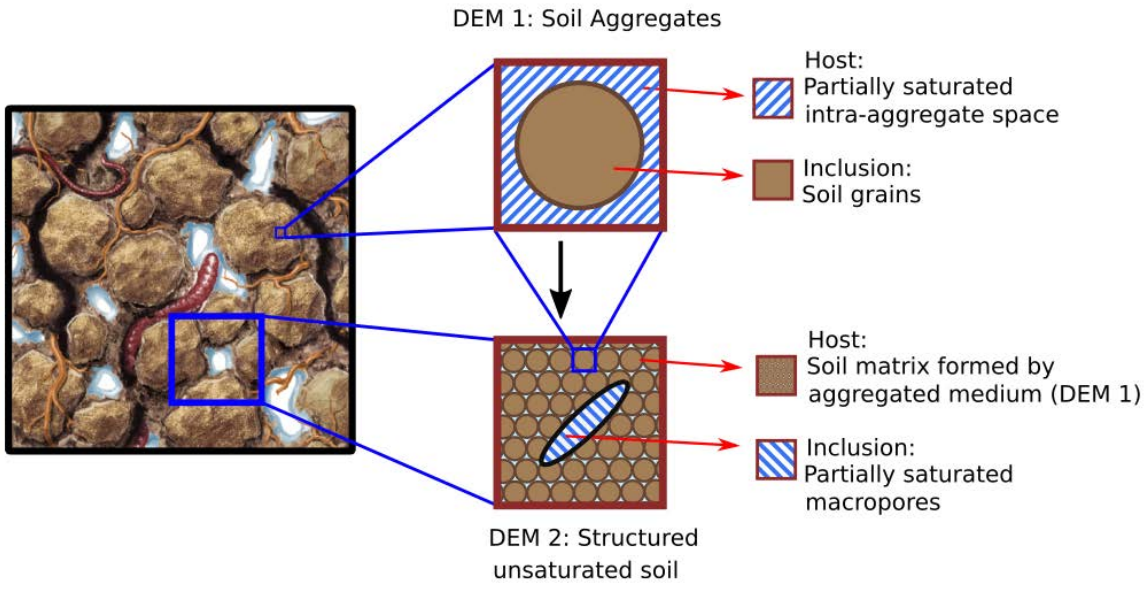

(a)

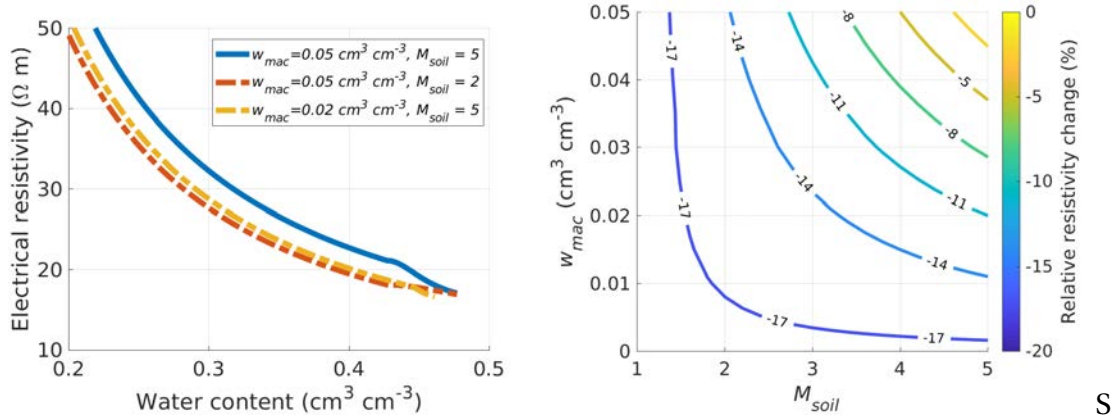

(b) (c)

Figure 4.1 – (a) Simplified conceptual illustration of the pedophysical model used to predict electrical properties for structured soils. The electrical conductivity of the soil aggregates is modeled by considering a fluid mixture with inclusions of soil grains. The electrical conductivity of the structured soil is modeled by considering the soil as soil porous matrix (formed by aggregates) with inclusions representing soil macropores. The electrical conductivity of the partially saturated inter-aggregate space and macropores are modeled using Archie's second law. (b) Comparison of electrical resistivity as a function of water content for three combinations of the M_{soil} exponent (M_{soil}=5, 2 and 5) and macroporosity (w_{mac} = 0.05, 0.05 and 0.02 cm^3cm^{-3}). The soil matrix porosity (ϕ_{sm} = 0.46 cm^3cm^{-3}), matrix cementation exponent (m_{sm} = 2), saturation exponents ($N_{sm} = N_{mac}$ = 2), the water conductivity (σ_w = 0.03 S/m) and the surface conductivity (σ_s = 0.1 S/m) are the same for the three cases. (d) Relative change of electrical resistivity calculated at a water content of θ = 0.38 cm^3cm^{-3} as a function of M_{soil} and w_{mac} with respect to the base case (M_{soil}=5 and w_{mac} = 0.05 cm^3cm^{-3}).

with high clay contents (e.g., agricultural soils *Friedman*, 2005). Traditional electrical models by *Archie* (1942) were developed for highly resistive rock formations and ignore the contribution of surface conductivity.5 Surface conductivity is often accounted for in pedophysical models by considering that electrical pathways of soil grains and pore spaces are parallel (i.e., the high salinity limit *Waxman and Smits*, 1968; *Linde et al.*, 2006). Dispite such restrictive assumptions, these models are widely used in soil science and hydrogeophysics (*Seladji et al.*, 2010; *Linde et al.*, 2006; *Tran et al.*, 2017). In this work, we propose to account for surface conductivity without imposing restrictive assumptions of being in the high salinity limit using Differential Effective Medium theory (*Bussian*, 1983). We modeled the electrical conductivity of the partially saturated soil matrix (σ_{sm}) as:

$$\sigma_{sm} = \phi_{sm}^{m_{sm}} \sigma_{f_{sm}} \left(\frac{1 - \sigma_s/\sigma_{f_{sm}}}{1 - \sigma_s/\sigma_{sm}} \right)^{m_{sm}}, \tag{4.2}$$

where m_{sm} is the cementation exponent of the soil matrix, $\sigma_{f_{sm}}$ is the effective electrical conductivity of the fluid mixture in the soil matrix and σ_s is the surface conductivity of the soil grains.

The effective electrical conductivity of the matrix fluid mixture is given by (*Archie*, 1942):

$$\sigma_{f_{sm}} = \left(\frac{\theta_{sm}}{(1 - w_{mac})\phi_{sm}} \right)^{N_{sm}} \sigma_w, \tag{4.3}$$

where θ_{sm} is the volumetric water content of the soil matrix, N_{sm} is the saturation exponent that accounts for the water distribution of the soil matrix, and σ_w is the electrical conductivity of the pore water. Similarly, the electrical conductivity of the macropores can be expressed as:

$$\sigma_{mac} = \left(\frac{\theta_{mac}}{w_{mac}} \right)^{N_{mac}} \sigma_w, \tag{4.4}$$

where θ_{mac} is the water content filling the macropores and N_{mac} is the saturation exponent describing the water phase in the macropores. Finally, the electrical conductivity of the soil is obtained by applying DEM theory once again in order to predict the combined effects of the electrical conductivity of the soil matrix and the electrical conductivity of the macropores:

$$\sigma_{soil} = (1 - w_{mac})^{M_{soil}} \sigma_{sm} \left(\frac{1 - \sigma_{mac}/\sigma_{sm}}{1 - \sigma_{mac}/\sigma_{soil}} \right)^{M_{soil}}, \tag{4.5}$$

where M_{soil} is an exponent that is inversely related to the connectivity between soil aggregates. The symbol is capitalized here to better differentiate it with the more traditional cementation exponent m_{sm} for which large data sets are available (see *Bussian*, 1983; *Lesmes and Friedman*, 2005; *Friedman*, 2005; *Cosenza et al.*, 2009). Equation 4.5 implies that the

presence of macroporosity (when unsaturated, which is the most common state) hinders electrical conduction in the structured soil by (1) decreasing the volumetric proportion of the electrically conductive soil matrix ($1 - w_{mac}$) and (2) by interrupting electrical pathways between soil aggregates (M_{soil}).

We tested the sensitivity of the model to changes in w_{mac} and M_{soil} by predicting the electrical resistivity of a soil as a function of water content (Figure 4.1b) considering three different combinations of M_{soil} and w_{mac} : a base case (M_{soil}=5, w_{mac} = 0.05 cm^3cm^{-3}), a reduction in M_{soil} (M_{soil}=2, w_{mac} = 0.05 cm^3cm^{-3}), and a reduction of macroporosity (M_{soil}=5, w_{mac} = 0.02 cm^3cm^{-3}). The remaining parameters were kept constant and chosen as typical values found in the literature: the soil matrix porosity (ϕ_{sm} = 0.46 cm^3cm^{-3}), aggregate cementation exponent (m_{sm} = 2), the saturation exponents ($N_{sm} = N_{mac}$ = 2), the water conductivity (σ_w = 0.03 S/m) and the surface conductivity (σ_s = 0.1 S/m). At full water saturation, the electrical resistivity is the same for all cases. The decrease of electrical resistivity with a decreasing water content is increased both by reducing M_{soil} and reducing w_{mac} as expected in response to soil compaction. Correspondingly, the model predicts a decrease in electrical resistivity of soils in response to soil compaction when considering a constant water content. This behvior is in agreement with laboratory and field observations reported in the literature (*Seladji et al.*, 2010; *Besson et al.*, 2013; *Keller et al.*, 2017). Figure 4.1c illustrates the relative impact of combined changes in M_{soil} and w_{mac} on electrical resistivity. The values were calculated at a water content close to field capacity in agricultural soils ($\theta \sim 0.38$ cm^3cm^{-3}) using the base case (M_{soil}=5, w_{mac} = 0.05 cm^3cm^{-3}) as the reference. For this example, the combined effects of reductions in M_{soil} and w_{mac} lead to a decrease of electrical resistivity by up to 20%.

4.2.2 Hydrological process modeling in structured soils

Soil water flow and heat transfer were performed using the 1D finite-difference software HYDRUS-1D (*Simunek et al.*, 2013).

Water flow modeling

One-dimensional water flow in unsaturated media is governed by Richards equation, written as (*Richards*, 1931):

$$\frac{\partial \theta}{\partial t} = \frac{\partial}{\partial z}\left[K_{soil}\left(\frac{\partial h}{\partial z} + 1\right)\right] - \Gamma, \tag{4.6}$$

where h is the water pressure head, θ is the volumetric water content, z is the spatial coordinate, Γ is the sink term, and K_{soil} is the unsaturated hydraulic conductivity. To account for macropore water flow, we used the approach by *Durner* (1994), which considers the porous medium to be divided by two overlapping domains representing (1) the pore system in the soil matrix and (2) the macropore system. In this parametrization, the water retention and the

hydraulic conductivity function of the soil are expressed as a combination of the functions ascribed to the two considered domains:

$$S_e = \frac{\theta - \theta_r}{\theta_s - \theta_r} = w_{sm}[1 + (\alpha_{sm} h)^{n_{sm}}]^{1-\frac{1}{n_{sm}}} + w_{mac}[1 + (\alpha_{mac} h)^{n_{mac}}]^{1-\frac{1}{n_{mac}}}, \tag{4.7}$$

and

$$K_{soil} = r_k K_{sm} \frac{\left(w_{sm} S_{e_{sm}} + w_{mac} S_{e_{mac}}\right)^{0.5}}{(w_{sm}\alpha_{sm} + w_{mac}\alpha_{mac})^2} \left(w_{sm}\alpha_{sm} \left[1 - \left(1 - S_{e_{sm}}^{\frac{n_{sm}}{n_{sm}-1}} \right)^{1-\frac{1}{n_{sm}}} \right] + w_{mac}\alpha_{mac} \left[1 - \left(1 - S_{e_{mac}}^{\frac{n_{mac}}{n_{mac}-1}} \right)^{1-\frac{1}{n_{mac}}} \right] \right)^2, \tag{4.8}$$

where S_e is the effective saturation of the soil, $\theta_s = \phi_T$ is the soil saturated water content (i.e., the total porosity), θ_r is the residual water content, n_i is the van Genuchten exponent (which is related to soil texture) and α_i is the inverse of the air-entry pressure. The saturated hydraulic conductivity of the soil $K_{SS} = r_k K_{sm}$ is defined as the product of the saturated hydraulic conductivity of the soil matrix K_{sm} and the ratio r_k ($= K_{SS}/K_{sm}$) which is a function of the soil macroporosity. The indices $i = sm$ and $i = mac$ represent the soil matrix and the macroporous region, respectively.

Increased saturated hydraulic conductivity in structured soils is often an effect of macropore networks created by bioturbation (earthworm moving and decaying roots). Soil biological activity and related soil organic matter decays exponentially with respect to soil depth (*Kramer and Gleixner*, 2008; *Hobley and Wilson*, 2016). For this reason, we consider that the saturated hydraulic conductivity of the soil K_{SS} decays exponentially with soil depth to the saturated hydraulic conductivity of the soil matrix K_{sm} as:

$$K_{SS}(z) = K_{sm} + a_{K_0} e^{-z/\lambda_K}, \tag{4.9}$$

where a_{K_0} is the increase in saturated hydraulic conductivity at the soil surface due to macroporosity and λ_K is the depth at which macroporosity-induced increase has reduced by a factor 1/e.

Representing soil structure effects on evapotranspiration

Soil surface evaporation is spatially limited by the so-called soil evaporation characteristic lenght (L_C) (*Lehmann et al.*, 2008; *Or and Lehmann*, 2019), which is soil structure-specific and represents the limiting depth at which there is an interruption in soil capillary flow that supports the so-called Stage-I evaporation, which is much more efficient than the diffision limited Stage-II evaporation (see more details about soil surface evaporation in *Or et al.*, 2013). Similarly, it exists an associated critical pressure head (h_{crit}) that marks the disruption of soil capillary paths. We employed the physical model by *Lehmann et al.* (2008) to calculate soil evaporation properties (L_C and h_{crit}) as a function of the water retention and hydraulic properties of the soil matrix. This is then used to define soil evapotranspiration functions

that are, in turn, used in the water-flow model. The soil evaporation characteristic length can be expressed as (*Or and Lehmann*, 2019):

$$L_c = \frac{h_{crit} - h_b}{1 + \frac{E_0}{4K_{soil}(h_{crit})}} = \frac{\frac{1}{n_{sm}\alpha_{sm}}\left(1 + \frac{n_{sm}}{n_{sm}-1}\right)^{(2-\frac{1}{n_{sm}})}}{1 + \frac{E_0}{4K_{soil}(h_{crit})}}, \tag{4.10}$$

where E_0 is the Stage I evaporation rate typically taken as the mean potential yearly evapotranspiration. The critical pressure head h_{crit} can be written as:

$$h_{crit} = \frac{1}{\alpha_{sm}\left(\frac{n_{sm}-1}{n_{sm}}\right)^{2-\frac{1}{n_{sm}}}}. \tag{4.11}$$

For interpretative purposes, we will sometimes present results in terms of a critical water content $\theta_{crit}(h_{crit})$.

The characteristic evaporation length (equation 4.10) and the critical pressure head (equation 4.11) are used in combination with soil potential evapotranspiration (ET_p) to define treatment-specific (vegetated and bare soil, compacted and non-compacted) potential evaporative water losses. We modeled the potential water losses as the product of: (1) a linear combination of a root density function that is depth-dependent ($RU(z)$) and a soil evaporation function that draws water from different depths (compacted and non-compacted soil) ($SE(z)$); (2) a scaling function varying between zero and one that depends on the soil pressure head ($\beta(h)$) and (3) surface potential evapotranspiration rate determined by meteorological conditions as:

$$\Gamma_{ET} = \beta(h)\left((1-\chi_{ev})\frac{RU(z)}{\int_0^Z RU(z)dz} + \chi_{ev}\frac{SE(z)}{\int_0^Z SE(z)dz}\right)ET_p(t), \tag{4.12}$$

where Z is the depth of the soil profile, χ_{ev} is the percentage of flux associated with soil evaporation. The potential evapotranspiration ET_p is calculated using the empirical function based on soil temperature by *Jensen and Haise* (1963). For simplicity, the depth dependent evaporation function is defined as a function of the soil characteristic evaporation depth that is normalized. It is expressed as:

$$SE(z) = \begin{cases} \frac{5}{3L_c} & z < 0.2L_c \\ \frac{2.0833}{L_c}\left(1 - \frac{L_c - z}{L_c}\right) & 0.2L_c < z < L_c \\ 0 & z > L_c. \end{cases} \tag{4.13}$$

The depth dependent root distribution function is chosen as an exponential function decaying with depth (e.g., *Zuo et al.*, 2006):

$$RU(z) = RU_0 e^{-z/\lambda_{roo}}, \tag{4.14}$$

where RU_0 is the root density at the soil surface and λ_{roo} is the depth at which root density has decayed to 1/e of RU_0. We defined the scaling function $\beta(h)$ as a S-shape function:

$$\beta(h) = \frac{1}{1 + \left(\frac{h}{h_{50}}\right)^p}, \tag{4.15}$$

the exponent p determines how fast β drops for increasing pressure head and h_{50} is the pressure head at which β is equal to 0.5 (*Feddes*, 1982).

For bare soil, we have that $\chi_{ev} = 1$ (i.e., no transpiration) and the function β can be used to approximate the soil evaporation function representing the transition from Stage-I evaporation to Stage-II evaporation. In such case, we approximated the h_{50} as the critical capillary pressure h_{crit}. Conversely, $1 - \chi_{ev}$ determines the fraction of water available for root-water uptake in vegetated soils and β represents the so-called root water stress function (see *Van Genuchten*, 1987).

Heat transfer modeling

Heat transfer is described by a convection-dispersion equation, defined for a one-dimensional system as:

$$C_p(\theta)\frac{\partial T}{\partial t} = \frac{\partial}{\partial z}\left[\lambda(\theta)\frac{\partial T}{\partial z}\right] - C_w q\frac{\partial T}{\partial z}, \tag{4.16}$$

where T is the temperature, $\lambda(\theta)$ is the coefficient of the apparent thermal conductivity of the soil, C_p and C_w is the volumetric heat capacity of the porous media and the water, respectively, and q is the Darcy fluid flux. The volumetric heat capacity of the soil can be expressed as (*De Vries*, 1963):

$$C_p(\theta) = (1 - \phi_T)C_s + \theta C_w, \tag{4.17}$$

C_s and C_a are the volumetric heat capacity of the soil solid phase and the air, respectively.

4.2.3 Coupled hydrogeophysical modeling

A coupled hydrogeophysical modeling scheme is used to investigate the soil structure signatures on soil water dynamics (see Section 4.2.2) and their corresponding geoelectrical signatures (see Section 4.2.1). The modeling is divided in two main steps (see Figure 4.2) that are described below.

4.2.4 Forward modeling of water flow and heat transfer

The soil hydraulic and transport properties are used to compute the soil evaporative properties. All properties are used to model water-flow in Hydrus 1D. From this, we obtain soil evapotranspiration, time-series of water content and temperature at specific depths and profiles of water content and temperature. The time series of water content at specific depths are converted to a dielectric constant by using a volumetric mixing model known as the Complex Reflective Index Model (CRIM) (*Roth et al.*, 1990). The dielectric constant of the soil is expressed as:

$$\sqrt{\kappa_{soil}} = f_s\sqrt{\kappa_s} + f_w\sqrt{\kappa_w} + f_a\sqrt{\kappa_a} + f_i\sqrt{\kappa_i}, \tag{4.18}$$

where κ_{soil}, κ_s, κ_w, κ_a, κ_i are the dielectric constants of the soil, the soil grains, the soil water, the air and the ice, respectively. Similarly, $f_s = 1-\phi_T$, $f_w = \theta(1-S_{ice})$, $f_a = \phi_T - \theta$ and $f_i = \theta S_{ice}$ refer to the fraction of soil grains, water, air and ice, respectively. The ice saturation (S_{ice}) is approximated at a given time as a linear function of the mean soil temperature from the previous 24 hours at the evaluated soil depth. The onset for obtaining non-zero values in ice content was defined when the mean temperatures fell bellow 0.5 ^{o}C.

4.2.5 Inverse modeling of soil electrical data

The simulated water content profiles are fed to the pedophysical model (equation 4.5) to derive electrical resistivity profiles. Subsequently, the temperature profiles are used to calculate profiles of electrical resistivity accounting for temperature effects with the model by *Campbell et al.* (1948). Finally, the apparent resistivities are simulated for a desired electrode array. In this study, we solved the 1D DC-resistivity problem (e.g., *Parker*, 1984) for a Wenner-Schlumberger array using an electrode spacing of $a = 50$ cm and various current-electrode spacings ($(2j+1)a$). This was achieved using the implementation by *Ingeman-Nielsen and Baumgartner* (2006) that is based on digital filter theory.

The pedophysical electrical properties (**P**) are inferred using the Markov-chain Monte Carlo (MCMC) method by *Laloy and Vrugt* (2012) (the so-called differential evolution adaptive

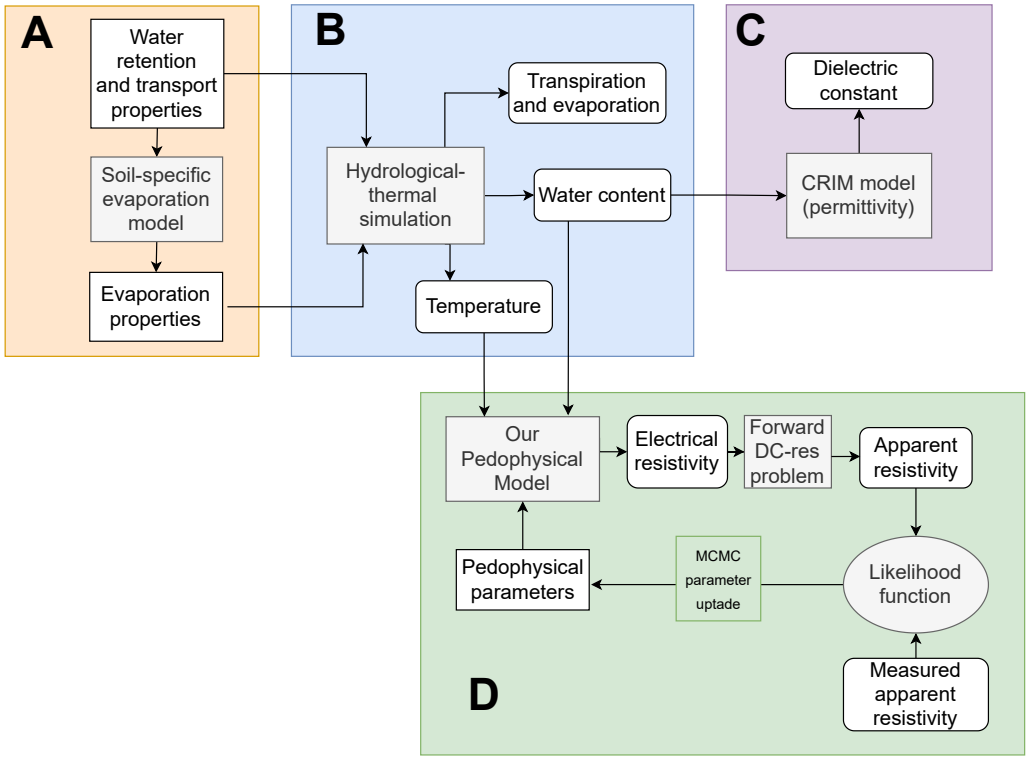

Figure 4.2 – Flowchart for hydrogeophysical forward and inverse modeling including soil evaporation constrains. The flowchart is divided in blocks containing different modeling steps involved in the coupled model. In A, water retention and transport properties are used to calculate treatment-specific evaporation properties. The water retention, transport and evaporation properties are used to perform a hydro-thermal simulation with Hydruys-1D resulting in soil water fluxes, water content and temperature. In C, the water content time-series are used with the CRIM model to model dielectric constant for comparison with TDR data. The inverse modeling of the electrical data is presented in D. The water content and temperature are used with the new pedophysical model to compute electrical resistivity profiles that are in turn used to compute apparent electrical resistivity. The pedophysical electrical properties are inferred using MCMC.

Metropolis, DREAM$_{(ZS)}$) to infer the posterior probability density function of the electrical properties using the following likelihood function

$$L(\mathbf{P}|\mathbf{d}) = \left(\sqrt{2\pi\sigma_{\mathbf{d}}}\right)^{-n} exp\left[-\frac{1}{2}\sum_{i=1}^{n}\left(\frac{F_i(\mathbf{P}) - d_i}{\sigma_{\mathbf{d}}}\right)^2\right], \tag{4.19}$$

where $F(\mathbf{P};\theta,T)$ and $\mathbf{d}$ are the simulated and measured apparent resistivity, respectively, $\sigma_{\mathbf{d}}$ is the standard deviation of the apparent resistivity data error and n is the number of data.

4.3 Methods

4.3.1 Data monitoring

DC-resistivity monitoring at the Soil Structure Observatory

To evaluate the value of electrical resistivity monitoring for capturing long-term effects of soil compaction and soil structure effects on soil moisture dynamics, we conducted monitoring (seasonal and hourly) of geoelectrical data. The monitoring was carried out at an experimental field site located in the vicinity of Zürich, Switzerland (8^o31'04 E, 47^o25'39 N) (*Keller et al.*, 2017). This Soil Structure Observatory (SSO) is a long-term experiment designed to study the evolution of soil structure, following a compaction event in the spring of 2014, for different types of post-compaction management (see Figure 4.3). The SSO has a strip-plot design with three blocks (replicates). Each strip-plot corresponds to a different post-compaction management, their area is evenly divided in the three compaction treatments (compaction on the full surface, compaction by tracks and no experimental compaction) and they are separated by a 2 m wide space of untreated soil. We monitored the DC-resistivity response of experimental plots with two different covers (bare soil and ley soil) and two compaction treatments (compaction on the full surface and no compaction). The four combinations are referred to as full compacted ley (grass-legume mixture), non-compacted ley, full compacted bare soil and non-compacted bare soil. The soil properties (and texture) prior to the compaction event were similar at all monitoring sites (*Keller et al.*, 2017) allowing us to attribute differences in the corresponding electrical signatures to different soil covers and treatments. For the seasonal monitoring, the DC-resistivity acquisition array comprised two lines of 48 stainless steel electrodes: one line on the ley soil and the other on the bare soil. The electrode spacing was 1 m, resulting in 47.5 m long DC-resistivity lines. In order to improve spatial resolution, the electrode spacing was changed to 50 cm in the spring of 2015. With this change, 24 electrodes were placed on the compacted treatment and 24 on the non-compacted treatment for each electrode line in the ley and bare soil. The seasonal campaigns extend from March 2014 (a few weeks before the compaction event) until March 2021.

For hourly monitoring, the electrodes were connected to a 96-switch Syscal-Pro powered by a 12 V battery located in an operation box at the edge of the soil plots (see Figure 4.3). The Syscal-Pro was controlled by a laptop operating the Comsys-Pro geophysical software (see http://www.iris-instruments.com/download) continuously during the full monitoring campaigns. A DC-resistivity acquisition sequence was programmed to be continuously repeated every two hours. Data were first collected from the bare soil profile and consecutively from the ley soil profile. The same subsequence (considering only 48 electrodes) was applied to both lines: from 1 to 48 for the bare soil and from 49 to 96 for the ley soil. A full DC-resistivity acquisition consisted of 464 data points (no stacking) for each profile, the duration of the current injection cycle was set to 250 ms and the full acquisition was completed roughly in one and a half hours. We used a Wenner-Schlumberger electrode array with 50 cm spacing between potential electrodes and four different spacings ($(2j+1)a$) for current electrodes corresponding to j =1, 2, 3 and 4 (see Figure 4.3c). As the soil treatments are assumed to be laterally homogeneous and we focused on larger-scale differences at the plot scale, the

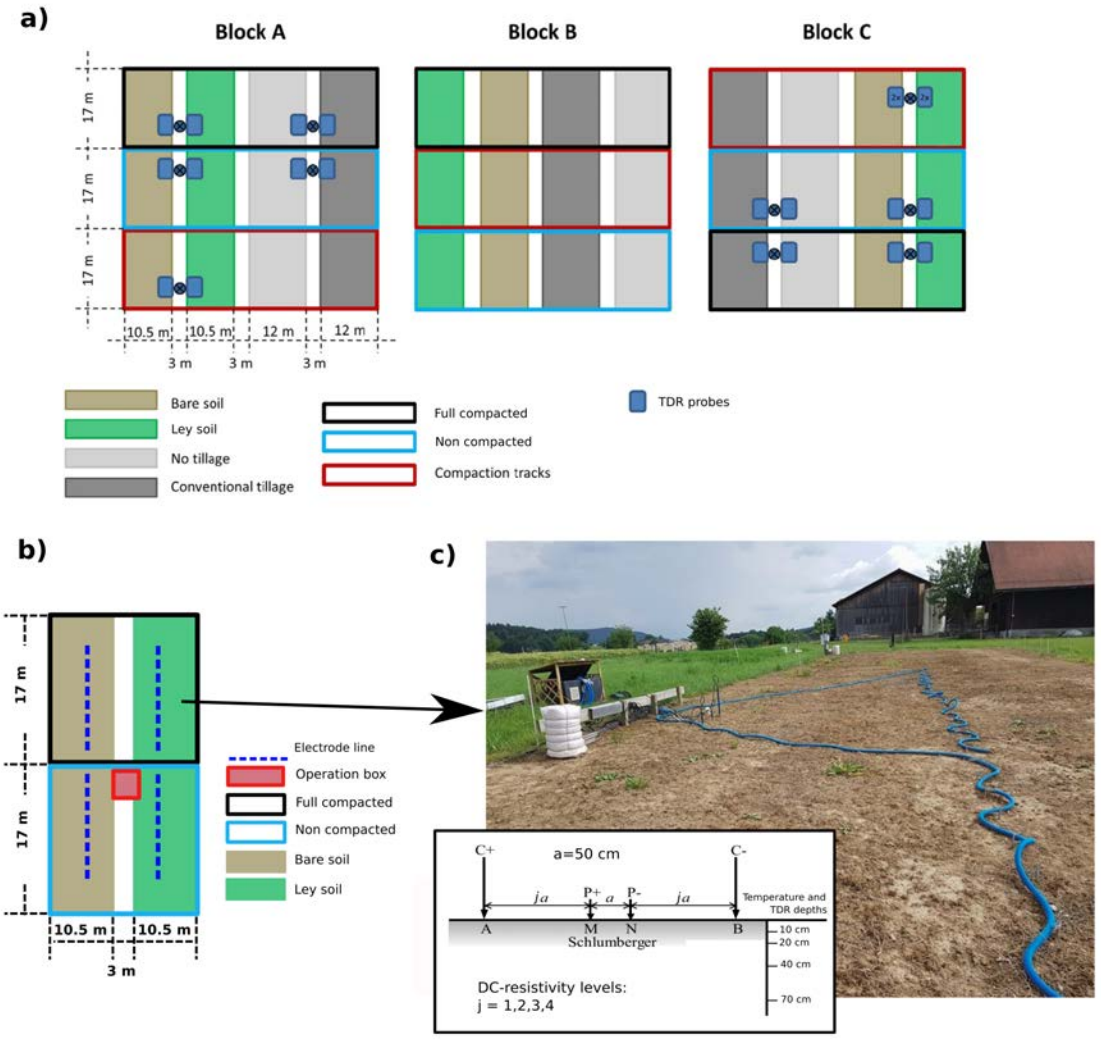

Figure 4.3 – (a) Schematic representation of the soil compaction experiment showing the different compaction treatments and post-compaction management strategies at the Soil Structure Observatory. (b) Schematic representation of the DC-resistivity lines deployed in the block A. (c) DC-resistivity line located in the bare soil.

different lateral values of apparent resistivity were averaged to obtain one value for each level at each plot at a given acquisition time. Data were collected from the 15th of February to the 8th of July of 2018.

Time-Domain Reflectometry and Temperature

Time-domain reflectometry (TDR, TDR 100 by Campbell Scientific with MDX multiplexers) probes for soil water content measurements and temperature probes were installed in all plots, and were continuously collecting data every hour at four different depths (10, 20, 40, and 70 cm, Figure 4.3c). Meteorological data were continuously monitored at an on-site station.

Ancillary data

Aboveground biomass was measured in the ley treatments for all blocks to evaluate soil compaction effects on plant growth. Measurements were made in the Spring of 2017 only. Hereafter we will present values averaged values considering all blocks for each treatments.

4.3.2 Impact of soil structure on measured apparent resistivity and soil water storage

Figure 4.4a presents the apparent resistivity time-series (j=1 of Wenner-Schlumberger array) for all soil cases and Figure 4.4b presents corresponding soil water storage storage estimated from TDR data. We used a one-year long time window from August 2017 to August 2018. No clear differences in apparent resistivity data are observed for the different soil covers during wet periods (i.e., high values of water storage for all treatments, before March 31). The apparent resistivity clusters according to the compaction treatment, presenting higher values for non-compacted ley and bare soil than for compacted ley and bare soil. Under these conditions (see data before March 31 in Figure 4.4a), the effect of soil compaction can be clearly identified as a decrease in soil electrical resistivity ($\sim$ 15%). This effect continues to be present during the full monitoring period in the bare soil, in which apparent resistivities of compacted bare soil are consistently shifted to lower values compared with non-compacted bare soils. The apparent electrical resistivity of the bare soil follows a mainly temperature-driven seasonal trend. The apparent resistivity of ley soil strongly responds to water storage variations during dry periods in May, June and July 2018. Therein, differences in water dynamics (see Figure 4.4b), according to the compaction treatment, impact the electrical resistivity producing similar values for compacted and non-compacted ley (see e.g., the last data points in Figure 4.4). The differences in water storage between compacted and non-compacted ley are larger. For this reason, the values of apparent resistivity may be similar or higher for compacted ley than for non-compacted ley during this period.

The compacted ley soil is persistently drier than the non-compacted ley soil during long dry periods as indicated by the monitored apparent electrical resistivity and TDR data. The measured aboveground biomass averaged for all blocks in compacted ley (85 $g/0.25$ cm^2) was approximately 70% of the biomass measured in the non-compacted ley (125 $g/0.25$

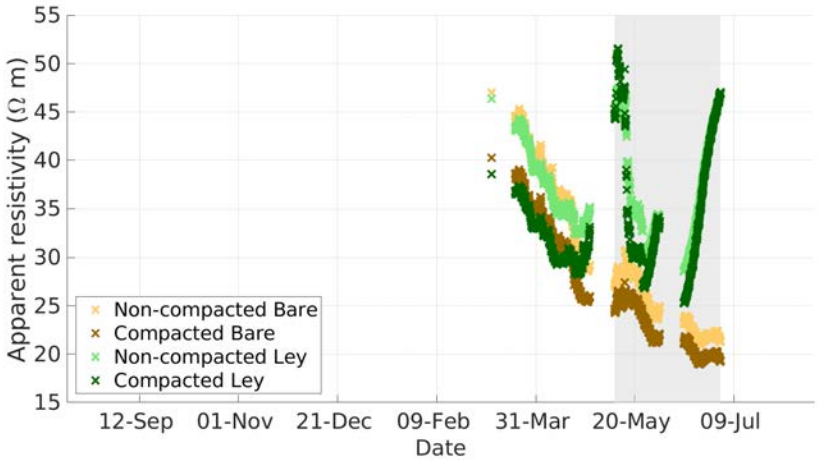

(a)

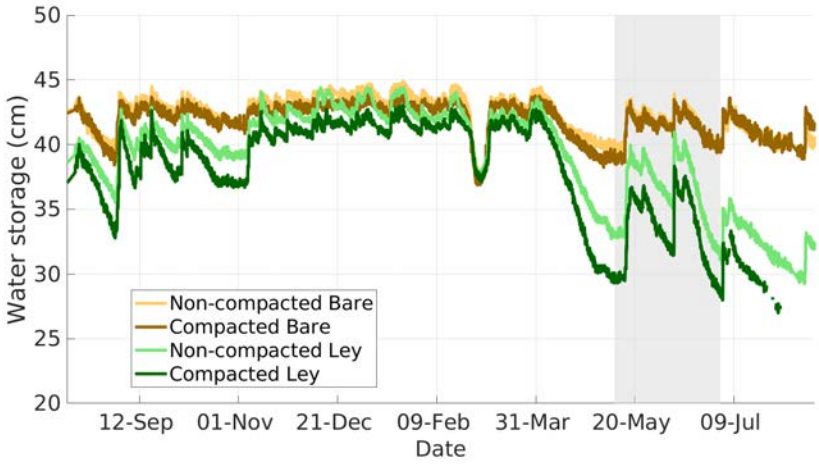

(b)

Figure 4.4 – (a) Apparent electrical resistivity time series collected for all soil treatments corresponding to j=1 of the Wenner-Schlumberger array. (b) Soil water storage in the upper one meter of the soil calculated from TDR data for all soil treatments presented in this study. The time axis goes from the middle of 2017 to the middle of 2018.

cm^2) implying that plant transspiration in the compacted ley is roughly 70% of the plant transpiration in non-compacted ley (see e.g., *Steduto et al.*, 2007).

4.3.3 Modeling of hydrogeophysical data

The selection of soil water retention and hydraulic properties for the different soil cases was based on qualitative expectations based on observations in Section 4.3.2 and our knowledge of soil hydraulic properties for compacted and non-compacted soils at the SSO informed by the laboratory measurements by *Keller et al.* (2017). We use a simple parametrization to differentiate between soil structure effects of compacted and non-compacted only in terms of: (1) the saturated hydraulic conductivity as a function of soil depth, (2) the macroporosity as a function of soil depth and (3) the Van Genuchten parameter α_{sm} that is constant with depth. The remaining model parameters are considered constant with depth and the same for compacted and non-compacted soils. The choices of soil model parameters are summarized in Table 4.1 and detailed below.

We assume that the saturated hydraulic conductivity of the soil matrix K_{sm} is the same for compacted and non-compacted soils. Based on this, the saturated hydraulic conductivity $K_{SS}(z)$ of both compacted and non-compacted soils are modeled by equation 4.9 with a common K_{sm}. The parameters of equation 4.9 were obtained by fitting laboratory data of saturated conductivity of compacted and non-compacted soil at the SSO (*Keller et al.*, 2017) (see Figure 4.5a). We obtained K_{sm} = 5.7 cm/h for both compacted and non-compacted soils and λ_K = 31 and 44 cm; and a_{K_0} = 8.3 and 34.6 cm/h for compacted and non-compacted soils, respectively.

The macroporosity as a function of soil depth is obtained from the derived $K_{SS}(z)$ (Figure 4.5a). Equation 4.8 is a simplified parametric expression to account for macropore water flow. To link K_{SS} with soil macroporosity, we impose that the hydraulic conductivity function used here (Equation 4.8) approximates a linear superposition (weighted by their volumetric fractions) of (1) the hydraulic conductivity function of the soil matrix $K_{matrix}(h,z)$ and (2) the hydraulic conductivity function of the macropore system $K_{macropore}(h,z)$ as:

$$K_{soil} = w_{sm}K_{matrix}(h,z) + w_{mac}K_{macropore}(h,z). \tag{4.20}$$

With such assumptions, we infer a macroporosity at the soil surface of 1.1 and 3.1 % for compacted and non-compacted soils, respectively (see Figure 4.5b).

We hypothesized that soil structure and compaction status play an important role on soil evaporation and soil transpiration. Soil evaporation properties strongly depend on three main properties: (1) the van Genuchten exponent n_{sm}, (2) the inverse of the air-entry pressure of α_{sm} and (3) the hydraulic conductivity of the soil matrix K_{sm} (equations 4.10 and 4.11). The exponent n_{sm} is often regarded as a surrogate variable for soil texture which is approximately the same for the soil treatments studied here (roughly 25% clay, 25% sand and 50% silt, see *Keller et al.*, 2017) and is, consequently, considered the same for all soil cases. We account for subtle soil compaction impacts on the soil matrix using the parameter α_{sm}.

Table 4.1 – Soil water retention, transport, evaporation, dielectric, electrical and other Hydrus properties considered in this study for non-compacted ley (NL), compacted ley (CL), non-compacted bare soil (NB) and compacted bare soil (CB). The properties showing a value are fixed during the inversion whereas the properties showing an x_i are considered unknown. Note that there are properties that are common and properties that are different for each soil structure in both variable and fixed properties. Additionally we added the number of equation in which all properties are used in commented on the motivations for electing these properties.

Water retention, transport and evaporation properties

	NL	NB	CL	CB	Equation	Comments
θ_r (cm^3cm^3)	0.08				4.13	from *Carsel and Parrish* (1988)
ϕ_{sm} (cm^3cm^3)	0.47		0.45		4.1,4.2,4.3	from *Carsel and Parrish* (1988)
θ_s (cm^3cm^3)	$(1-w_{mac})\phi_{sm}+w_{mac}$				4.13,4.17	computed
a_{K_0} (cm/h)	31		8.3		4.9	assumed property
α_{sm} (cm^{-1})	0.04		0.02		4.13,4.8,4.10,4.11	assumed property
n_{sm} $(-)$	1.15				4.13,4.8,4.10,4.11	assumed property
K_{sm} (cm/h)	5.7				4.8,4.10,4.11	based on lab data
α_{mac} (cm^{-1})	1				4.13,4.10,4.11	assumed property
n_{mac} $(-)$	2				4.13,4.8,4.10,4.11	assumed property
h_{crit} (cm)	250		500		4.10,4.11	computed
θ_{crit} (cm^3cm^{-3})	0.35		0.33		-	computed
L_c (cm)	31		63		4.10	computed

Other Hydrus-1D properties

	NL	CL	NB	CB	Equation	Comments
λ_{RU} (cm)	20				4.14	assumed property
λ_K (cm)	44		31		4.9	assumed property
p $(-)$	2				4.15	assumed property
h_{50} (cm)	10^5	10^5	h_{crit}	h_{crit}	4.15	approximated
C_s $(Jm^{-3}{}^oC^{-1})$	1.92×10^6				4.17	from *De Vries* (1963)
C_w $(Jm^{-3}{}^oC^{-1})$	4.18×10^6				4.17	from *De Vries* (1963)

Dielectric properties

	NL	CL	NB	CB	Equation	Comments
κ_s $(-)$	5				4.18	from *Annan* (2005)
κ_w $(-)$	80				4.18	from *Annan* (2005)
κ_a $(-)$	1				4.18	from *Annan* (2005)
κ_i $(-)$	3.4				4.18	from *Evans* (1965)

Electrical properties

	NL	CL	NB	CB	Equation	Comments
M_{soil} $(-)$	x_1		x_2		4.5	inverted properties $[1,5]$
σ_s (Sm)	x_3				4.2	inverted property $[0,0.25]$
σ_w (Sm)	x_4				4.3,4.4	inverted property $[0.02,0.05]$
M_{sm} $(-)$	x_5				4.2	inverted property $[1.5,2.5]$
N_{sm} $(-)$	2				4.3	assumed property
N_{mac} $(-)$	2				4.4	assumed property

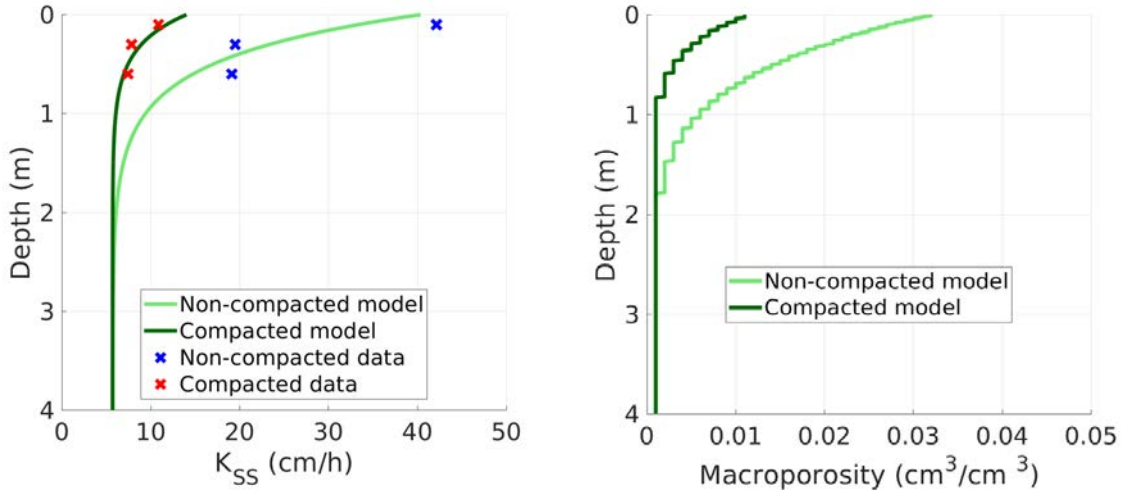

(a) (b)

Figure 4.5 – (a) Measured and modeled saturated hydraulic conductivity as a function of soil depth for compacted and non-compacted soils. (b) Estimated macroporosity as a function of soil depth for compacted and non-compacted soils.

Therefore, we assign the same α_{sm} for a compaction treatment regardless of soil cover. This assumption can be linked the existence of subtle changes in mesoporosity (pore diameters in the range of 30-100 μm) between compacted and non-compacted soils. This is supported by observations by *Meurer et al.* (2020) who found differences in mesoporosity of compacted and non-compacted soils at the SSO. Here, we do not explicity account for three domains (micro-, meso- and macropores) as done by *Meurer et al.* (2020). To simplify the analysis, we account for mesoporosity reduction as a reduction of α_{sm} for compacted soils and incorporate its corresponding effects in evaporation properties (equations 4.10 and 4.11). The parameter α_{sm} should decrease with compaction due to the closure of mesopores in the matrix induced by the applied stresses. The selected properties were $\alpha_{sm} = 0.04\ cm^{-1}$ for non-compacted soils, $\alpha_{sm} = 0.02\ cm^{-1}$ for compacted soils. These values are within the range of properties for loamy-clay soils reported by *Carsel and Parrish* (1988). The exponent was set $n_{sm} = 1.15$ for all soil treatments. The resulting evaporation properties are $L_C = 31\ cm$ and $h_{crit} = 250\ cm$ for non-compacted soils, and $L_C = 63\ cm$ and $h_{crit} = 500\ cm$ for compacted soils. The macroporosity, the total porosity (equation 4.1) and saturated hydraulic conductivity of the soil vary with the soil depth. We selected a $\alpha_{mac} = 1\ cm^{-1}$ and $n_{mac} = 2$, leading to a pore size distribution of the soil macroporosity with a maximum pore radius of 1.5 mm.

Water flow and heat transfer simulations were made in a 3.5 m deep soil profile. We discretized the soil in 20 different soil layers. Based on the TDR data, we assumed that the growing season (i.e., period in which both evaporation and transpiration are active in the ley soil) begins on the second week of April and ends on the third week of September.

The dielectric properties of the soil are considered the same for all soil treatments. The dielectric properties of soil solid constituents, water, air and ice were taken from the literature (*Annan*, 2005; *Evans*, 1965). Similarly, the values of the volumetric heat capacity of water and

soil solids were chosen as typical values reported in the literature (*De Vries*, 1963). These values are reported in Table 4.1.

4.3.4 MCMC inversion of electrical properties

All electrical properties were considered to be constant with soil depth. The inversion strategy for electrical data considers that most electrical properties are the same for all soil treatments and data from all soil treatments are considered together in the data vector **d**. As mentioned before, the exponent M_{soil} represents the connectivity of electrical pathways (inversely related to the connectivity between soil aggregates) in the structured soil that is hindered by the presence of macroporosity. Thus, the exponent M_{soil} was set to be the distinctive property for the compaction state of the soils. In contrast, the surface conductivity (σ_s), the water conductivity (σ_w), the cementation exponent of the soil matrix m_{sm} were set to be same for all soil cases. For simplicity, the saturation exponents ($n_{sm} = n_{mac} = 2$) appearing in equations 4.3 and 4.4 were considered the same for all soil cases. The ranges of the uniform prior probability density functions of the inversion parameters are provided in Table 4.1. The data error was selected as 10% of each data point and the scale of the model proposal in the DREAM$_{(ZS)}$ algorithm was tuned to achieve an adequate acceptance rate. Figures 4.6a and 4.6b present the log-likelihood and the $\hat{R}$-diagnostic (*Gelman and Rubin*, 1992) of the inverted parameters as a function of the number of model evaluations in the MCMC inversion process. The $\hat{R}$-diagnostic criteria by *Gelman and Rubin* (1992) was used to declare convergence when it is below 1.2 for all variables.

4.4 Results

4.4.1 Inverted electrical properties

Figures 4.6c, 4.6f, 4.6g and 4.6f present the posterior samples after burn-in (the first 5000 iterations). Figure 4.6d and 4.6e show the difference and the crossplot, respectively, of the sampled values for exponents M_{soil} of compacted and non-compacted soils. The exponents M_{soil} presents mostly lower values for compacted soils (Figure 4.6d). This indicates that soil aggregates of compacted soils are more connected (i.e., the macroporosity is less connected) than for non-compacted soils. The reduction of M_{soil} together with the inferred decrease in macroporosity explain the observed lower values of electrical resistivity of compacted soils even for similar values of water storage (see apparent resistivity data and water storage in Figure 4.4). The sampled values of water conductivity and surface conductivity fall within reasonable ranges according to the work of *Farahani et al.* (2018) and *Revil et al.* (2017), respectively. The posterior mean of the cementation exponent of the soil matrix is 1.65.

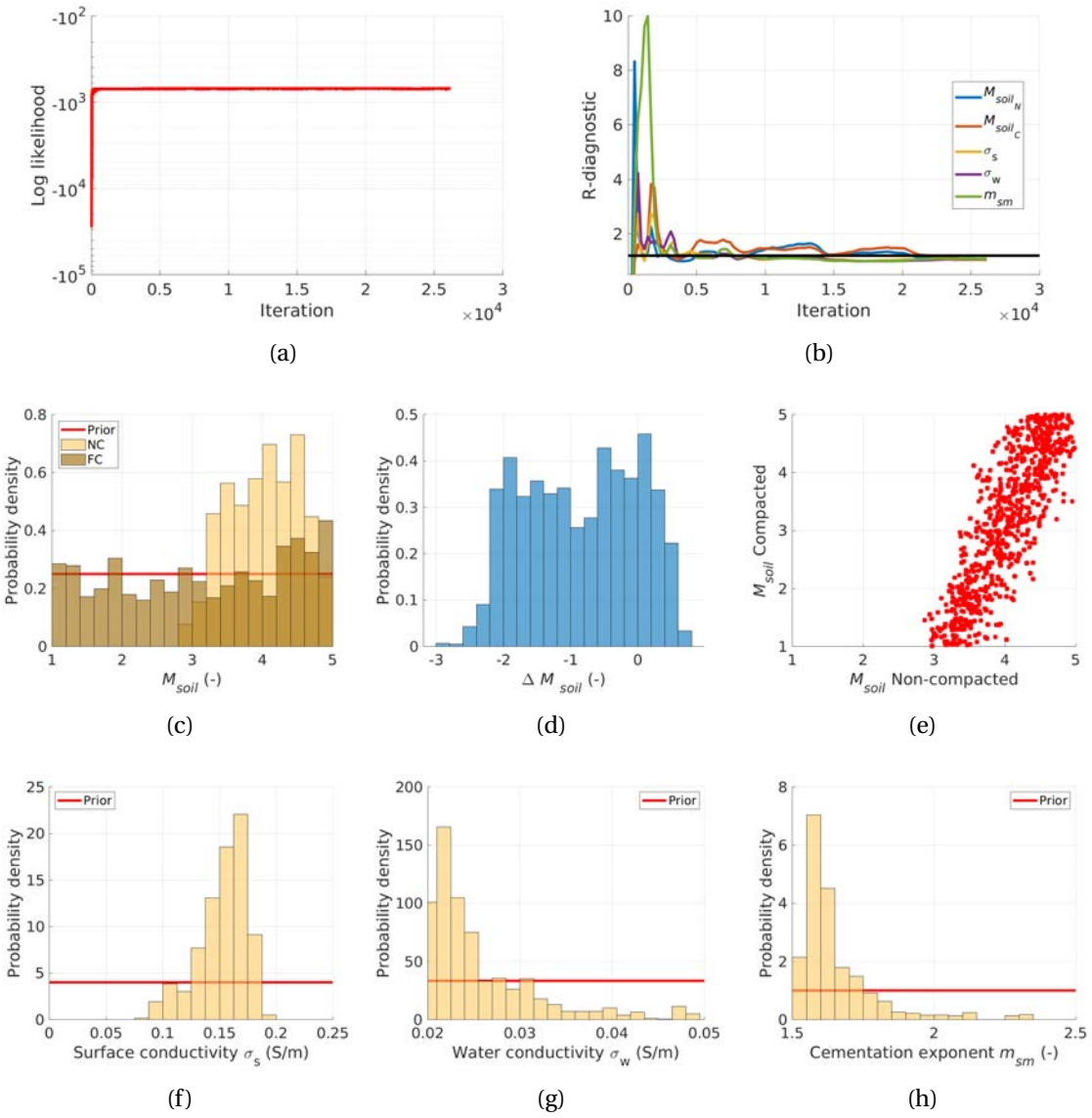

Figure 4.6 – Results from MCMC inversion of geoelectrical data. (a) Log-likelihood function and (b) $\hat{\mathrm{R}}$-diagnostic for 24000 iterations. MCMC sampled values after the iteration 5000 for (c) the exponent M_{soil} for non-compacted and compacted soil, (f) the surface conductivity (σ_s), (g) water conductivity (σ_w) and (h) the cementation exponent (m_{sm}). The latter three properties are shared for non-compacted and compacted soils. (d) Difference between sampled values of M_{soil} for non-compacted and compacted soils. (e) Crossplot of the sampled values of M_{soil} for non-compacted and compacted soils.

4.4.2 Water content dynamics

The dielectric constant is measured directly by the TDR probes. For this reason, we chose to present bulk dielectric constant data instead of water content data. We first focus on the simulated dielectric constant of the bare soil (Figures 4.7a and 4.7b). The simulated dielectric constant captured the small differences between compacted and non-compacted bare soil observed in the data. Differences during wet periods can be interpreted as slight differences in total porosity between the two compaction treatments. The differences in the dry periods are linked to the differences in evaporation properties. The lower values of dielectric constant are linked with the critical water content at which Stage-I evaporation is interrupted. The computed critical water contents are $\theta_{crit} = 0.35\ cm^3 cm^{-3}$ for non-compacted soils and $\theta_{crit} = 0.33\ cm^3 cm^{-3}$ for compacted soils. The simulated dielectric constant underestimates the measured dielectric constant for some drying events, particularly evident at 40 cm depth (see Figures 4.7b). Our strategy to estimate the dielectric permittivity of soils with partially frozen water volumes well reproduced the freezing-thawing events (see Feb-Mar in Figures 4.7a and 4.7b).

The simulated dielectric constant captured the small differences between compacted and non-compacted ley observed in the data (Figures 4.8a and 4.8b). Differences during wet periods can be interpreted as slight differences in total porosity between the two compaction treatments. The lower values of dielectric constant are associated with the combined effect evapotranspiration. At 10 cm depth, the differences in dielectric constant are small, and in agreement with the measured data (Figure 4.8a). These differences are determined by the evapotranspiration function defined in equation 4.12. Here, the lowest values of dielectric permittivity are initially limited by the pressure head at which root-water uptake rate is reduced by half (h_{50}) which is the same for compacted and non-compacted ley. These slight differences are driven by differences in the evaporation depth L_C that influences the evaporation function (equation 4.13). This is more evident at 40 cm depth (Figure 4.8b) where the differences between simulated dielectric constant of compacted and non-compacted ley are more visible. The simulated differences are not as large as those observed by TDR data. As before, our strategy to estimate the dielectric permittivity of soils with partially frozen water well reproduced the freezing-thawing events (see Feb-Mar in Figure 4.8a).

4.4.3 Apparent electrical resistivity

The predicted apparent resistivity is adversely impacted by the discrepancies of the modeled and observed soil moisture dynamics discussed above. Yet, the main features observed in the measured apparent electrical resistivity are qualitatively well reproduced by our modeling scheme and parametrization. Figures 4.7c and 4.7d present measured and simulated apparent resistivity for non-compacted and compacted bare soil for $j = 1$ and $j = 3$, respectively. The shift towards lower apparent resistivities for compacted soils is qualitatively well reproduced by the model. There are two primary competing factors influencing the dynamics of soil apparent resistivity: soil temperature and soil water storage. For low temperatures and high water storage, temperature effects dominate the apparent electrical resistivity. Conversely, for low water storage and high temperatures, soil water storage dominates the

electrical resistivity. Since the soil water storage varies within moderate to high values in the bare soil during the monitored period (see Figure 4.4a), the corresponding measured apparent resistivity is mainly responsive to the temperature-driven trends (see also Figures 4.7e and 4.7f). The model overestimated the measured apparent resistivity in early July as soil water losses are overestimated during this period (see Figure 4.7b).

Figures 4.8c and 4.8d present measured and simulated data of apparent resistivity for non-compacted and compacted ley soil for $j = 1$ and $j = 3$, respectively. The measured apparent resistivity in the ley soil is strongly influenced by changes in soil water storage in the beginning of May and in the beginning of July (see also Figures 4.8a and 4.8b). These drying events are qualitatively well captured in the modeled apparent resistivity. The measured apparent resistivity in the compacted ley soil switches from being lower than non-compacted ley at wet conditions to being higher at dry conditions (Figures 4.8c and 4.8d). This suggests that the compacted ley presents higher water losses during these dry periods. These effects are not clearly visible in the modeled apparent resistivity, as the modeled differences in water losses between compacted and non-compacted ley are underestimated.

4.5 Discussion

Field monitoring of apparent electrical resistivity revealed (1) a persistent effect of soil compaction leading to a decrease in electrical resistivity of compacted soils and, (2) a strong influence of soil structure in soil water dynamics in the ley soil driven mainly by evapotranspiration.

4.5.1 Long-term compaction effects revealed by geoelectrical data

Compacted soils have lower apparent electrical resistivities than non-compacted soils for the same soil water storage. In apparent resistivity data, of compacted and non-compacted soils, this effect can be masked if, at a given monitoring time, differences in water storage are sufficiently large (see Figure 4.4). This suggests that detecting soil compaction with geoelectrical methods can be better achieved under wet conditions (i.e., when evapotranspiration is negligible). Decreasing resistivities in compacted soils have been widely reported in the literature (e.g., *Séger et al.*, 2009; *Besson et al.*, 2013), including at the SSO (*Keller et al.*, 2017). Four years after the experimental compaction, we observed up to a 15% decrease in apparent electrical resistivity in compacted soils. This is similar to the changes in inverted electrical resistivity of compacted treatments (a few days after compaction) compared to their pre-compaction states at the SSO reported by *Keller et al.* (2017). Figure 4.9 presents the relative differences in apparent resistivity data ($j = 1$, $a = 1$ m) considering compacted vs non-compacted bare soil and compacted vs non-compacted ley soil measured at the same date and time. We included data from the onset of the experimental compaction and until March 2021 (~7 years after compaction). Relative differences from 2018 and 2021 remain similar to those measured shortly after the compaction event (about 10% decrease). A 10% decrease in apparent resistivity was captured by long-term simulations of apparent resistivity (from 2013 to 2019) using the electrical properties inferred for 2018 (Figure 4.9). As suggested

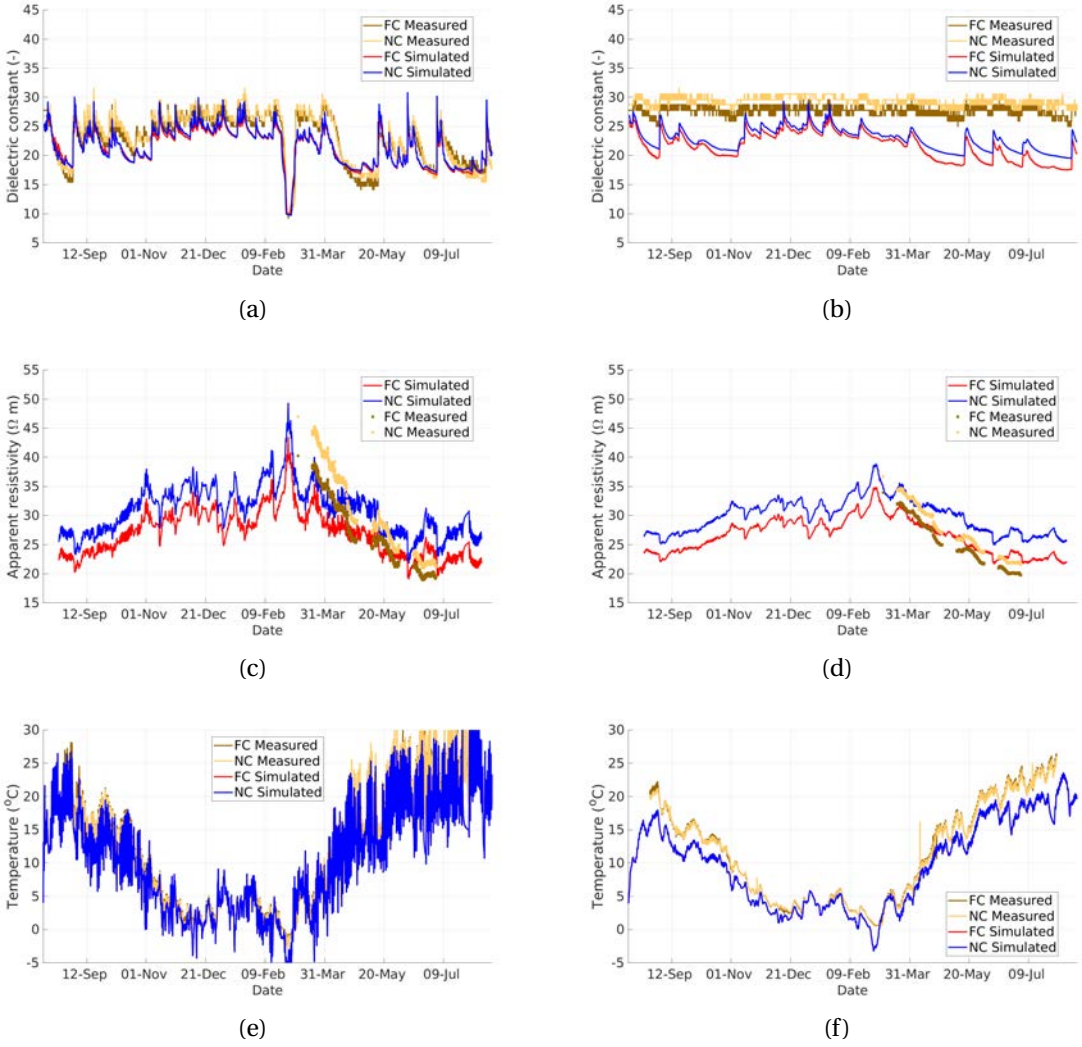

Figure 4.7 – Modeled and measured dielectric constant of compacted and non-compacted bare soil at (a) 10 cm and (b) 40 cm depth. Modeled and measured electrical resistivity of compacted and non-compacted bare soils using (c) j=1 and (d) j=3 in the Wenner-Schlumberger array. Modeled and measured temperature of compacted and non-compacted bare soils at (e) 10 cm and (f) 40 cm depth. The time axis goes from the middle of 2017 to the middle of 2018.

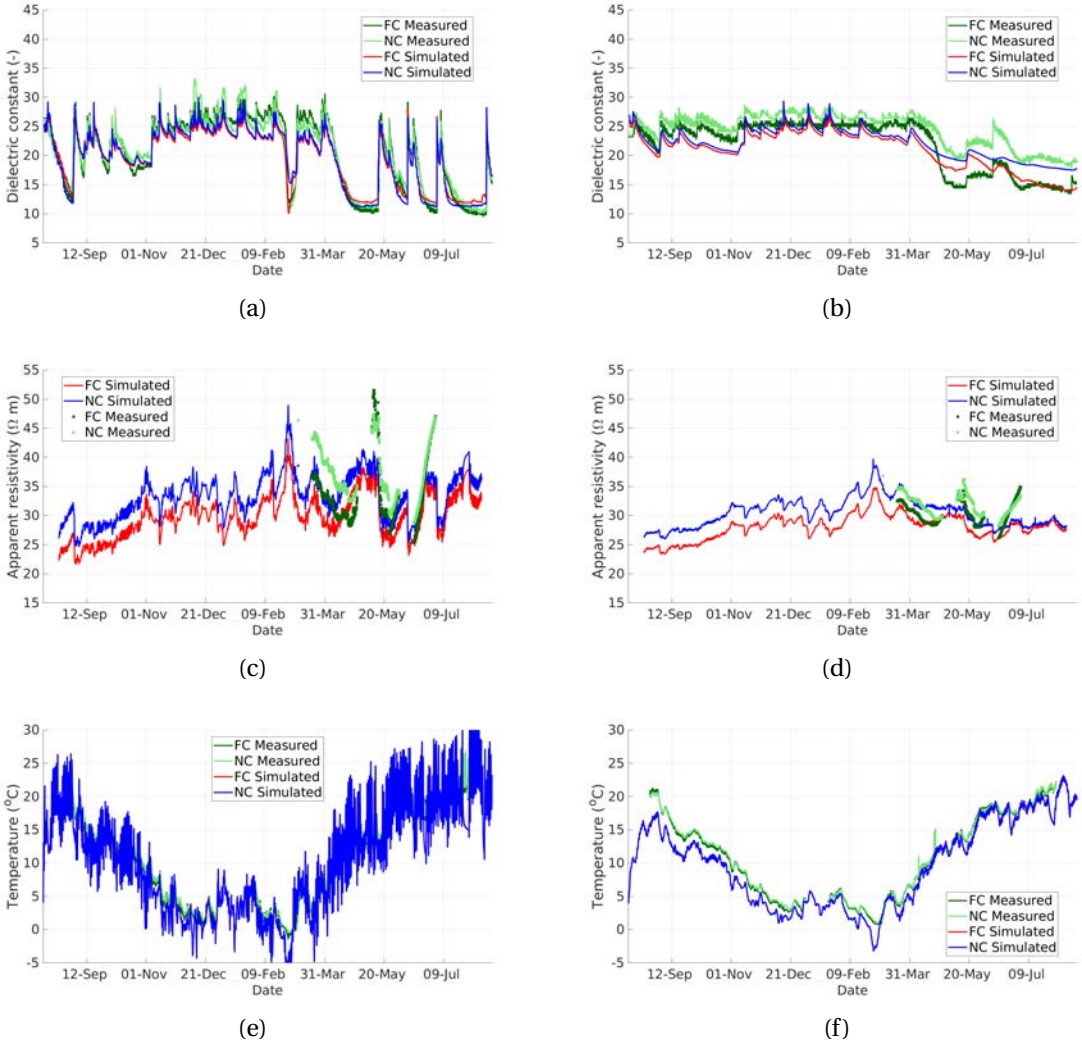

Figure 4.8 – Modeled and measured dielectric constant of compacted and non-compacted ley soils at (a) 10 cm and (b) 40 cm depth. Modeled and measured electrical resistivity of compacted and non-compacted ley soils using (c) j=1 and (d) j=3 in the Wenner-Schlumberger array. Modeled and measured temperature of compacted and non-compacted ley soils at (e) 10 cm and (f) 40 cm depth. The time axis goes from the middle of 2017 to the middle of 2018.

by the modeled results, the 10% differences are mostly seen during wet periods (e.g., winter months) and may be masked during drier periods (e.g., during spring and summer) due to the larger differences in water contents. Our results suggest a limited recovery of electrical properties of the compacted soils.

The prescribed differences in macroporosity are not enough to describe the decrease in electrical resistivity of compacted soils (see e.g., Figure 4.1c). In addition, we need to account for an increase in connectivity of the soil aggregates (comprised by a decrease in the exponent M_{soil}). This implies a decrease of connectivity of the macroporosity as a result of soil compaction. The posterior distribution of M_{soil} for the compacted soils is centered at values in-between those for the cementation exponent of the soil matrix m_{sm} and the exponent M_{soil} for non-compacted soil. The interpretation of an increase aggregate connectivity for compacted soils is consistent with expectations about the dynamics of soil aggregate contacts in response to compaction controlled by soil rheological properties (see e.g., *Or and Ghezzehei*, 2002). In addition, similar effects have been observed for hydraulic properties of partially saturated soils. *Carminati et al.* (2007) showed that hydraulic conductivity increases with increasing hydraulic contacts between soil grains. We highlight that a similar result was observed for soil seismic properties by *Romero-Ruiz et al.* (2021). Therein, the differences in seismic velocities (strongly sensitive to mechanical resistance of soils) of compacted and non-compacted soils were interpreted as increased contact area between soil aggregates.

4.5.2 Soil structure driven water dynamics captured by DC-resistivity data

The apparent electrical resistivity monitoring in 2018 revealed a persistent decrease in electrical resistivity for compacted soils described in the previous section and captured difference in soil water dynamics associated with soil structure. Additionally, the proposed pedophysical parametrization and the modeling approach were capable of qualitatively and quantitatively describe effects for the different soil treatments. The difference in soil water dynamics between compacted and non-compacted bare soil were insufficient to produce distinguishing changes in the measured apparent resistivity. The data followed a temperature driven trend that the model was able to reproduce (see Figure 4.7d) with some discrepancies observed during the dry periods. The discrepancies might be attributed to overestimation of water losses in the bare soil (see 4.11b) and changes in the electrical conductivity of soil water which are not accounted for in our pedophysical model. Furthermore, we did not identify a strong effect of macropore water flow in the measured and modeled water contents (see Figure 4.10a) and the related geoelectrical signal. During the monitored period (Spring a Summer), water flow occurred mainly in the soil matrix.

In the ley soil, we observed a relatively larger influence of soil compaction on soil water dynamics that was captured by the measured data (Figure 4.4). The model did not entirely reproduce the dynamics of electrical resistivity of compacted ley compared to non-compacted ley during dry periods, that changed from values of apparent electrical resistivity that were relatively lower to relatively higher than for non-compacted soils (see Figures 4.8c and 4.8d). However, the differences in modeled electrical resistivity of compacted and non-compacted ley diminished considerably during dry periods, which is consistent with observations. This slight discrepancy in modeled and observed apparent resistivity might be attributed to the

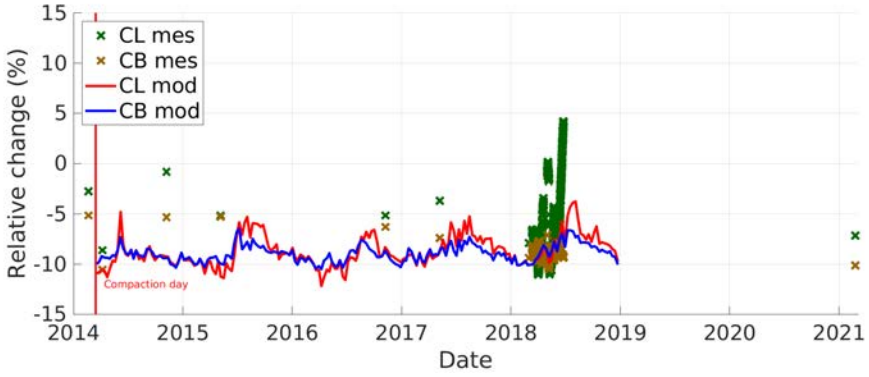

(a)

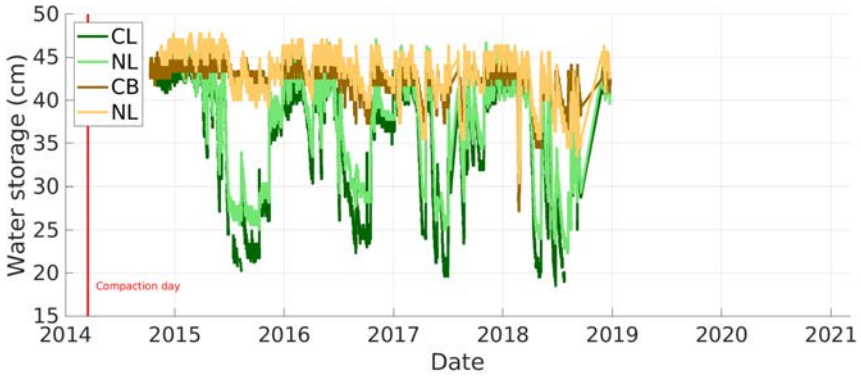

(b)

Figure 4.9 – (a) Measured (mes) and modeled (mod) relative change in apparent electrical resistivity for compacted and non-compacted ley (CL) and bare soil (CB). (b) Water storage calculated from TDR data for Compacted Ley (CL), Non-compacted ley (NL), Compacted bare soil (CB), and Non-compacted bare soil (NB).

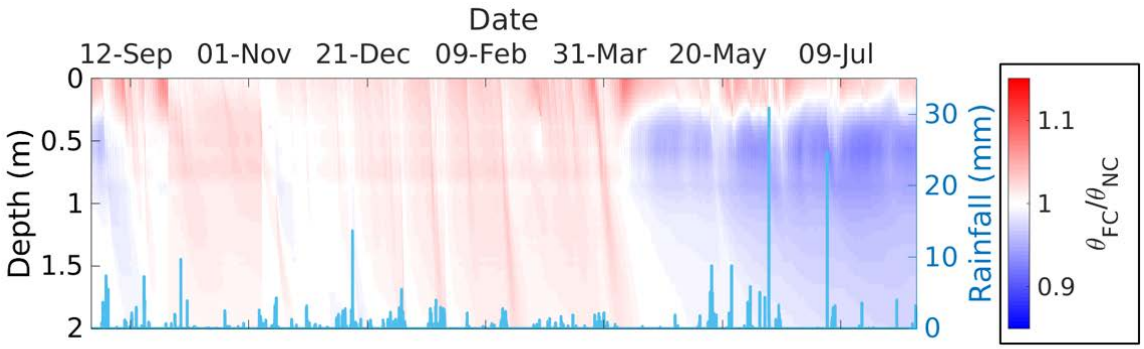

(a)

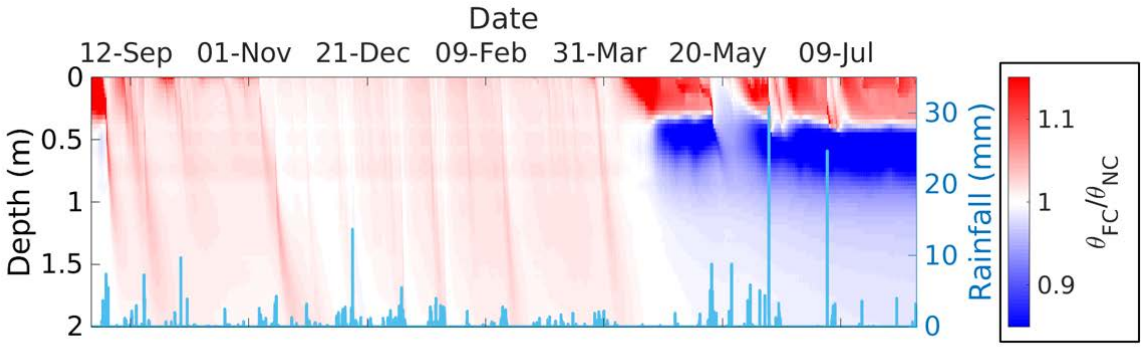

(b)

Figure 4.10 – Relative soil water content as a function of soil depth and time for (a) bare soil and (b) ley. The plots present relative value between water content modeled in compacted soils (θ_{FC}) and non-compacted soils (θ_{NC}). Monitored rainfall data are included.

previously discussed underprediction of the differences in water storage of compacted ley relative to non-compacted ley as shown in Figures 4.11a and 4.11b. The main process dominating water content dynamics in the ley soil were soil evaporation and plant transpiration (see Figure 4.10b). Similarly to the bare soil, we did not observe a major effect of differences in macropore water flow in the measured and simulated water content and corresponding electrical signatures.

4.5.3 Influence of compaction on water partitioning between soil and atmosphere

The modeling framework and monitored data are used to assess the potential implications of soil compaction on soil water partitions between soil and atmosphere (Figure 4.11a). For this purpose, we estimated water losses from TDR data and compare them with the simulated water losses resulting from Hydrus-1D simulations.

Bare soil water losses in the absence of root water uptake and plant transpiration are addressed first. The measured annual water losses in the bare soil are approximately 618 and 596 mm for compacted and non-compacted bare soil, respectively (Figure 4.11a). This compares favorably with the simulated annual evaporation of 608 and 561 mm for compacted and non-compacted bare soil, respectively (Figure 4.11b). However, the simulated total water losses (i.e., combining evaporation and drainage) are complemented by drained water which is 363 and 389 mm for compacted and non-compacted bare soil, respectively. Annual drainage from non-compacted bare soil is 26 mm larger than non-compacted bare soil. The simulated total water losses overestimate the measured water losses by over 300 mm/year, implying that evaporation and/or drainage are overestimated by the model. This is evident in the time-series of simulated and measured dielectric permittivity presented at 20 and 40 cm depth (Figures 4.7b and 4.7c). The simulated cumulative evaporation as a function of time (presented in Figure 4.11d) shows a very similar trend that the measured water losses as a function of time, suggesting that the model specially overestimates water drainage and may still offer a good prediction of evaporation. Annual excess in water losses related to enhanced evaporation of compacted bare soil with respect to non-compacted bare soil are 40 mm.

The measured annual water losses were 1101 and 954 mm for compacted and non-compacted ley, respectively. The simulated annual water losses were 1057 and 1039 mm for compacted and non-compacted ley, respectively. Contrary to what is observed for bare soil, the simulated total water losses in ley soils provide a good estimation of total water losses observed from TDR data (4.1% and 8.9% difference for the compacted and non-compacted ley, respectively) as observed in Figure 4.11c. However, the excess of water losses in compacted ley relative to non-compacted ley was much higher in the measured (147 mm/y) than in the simulated (16 mm/y) water losses. This is consistent with the resulting differences in simulated dielectric permittivity between compacted and non-compacted ley which are underestimated at 40 cm depth (Figure 4.8d).

In order to interpret the water losses in ley soil and separate the contributions of soil evaporation, transpiration and drainage for the two compaction states, we relied on (1) our proposed conceptual description of soil potential evapotranspiration based on the spatial distribution

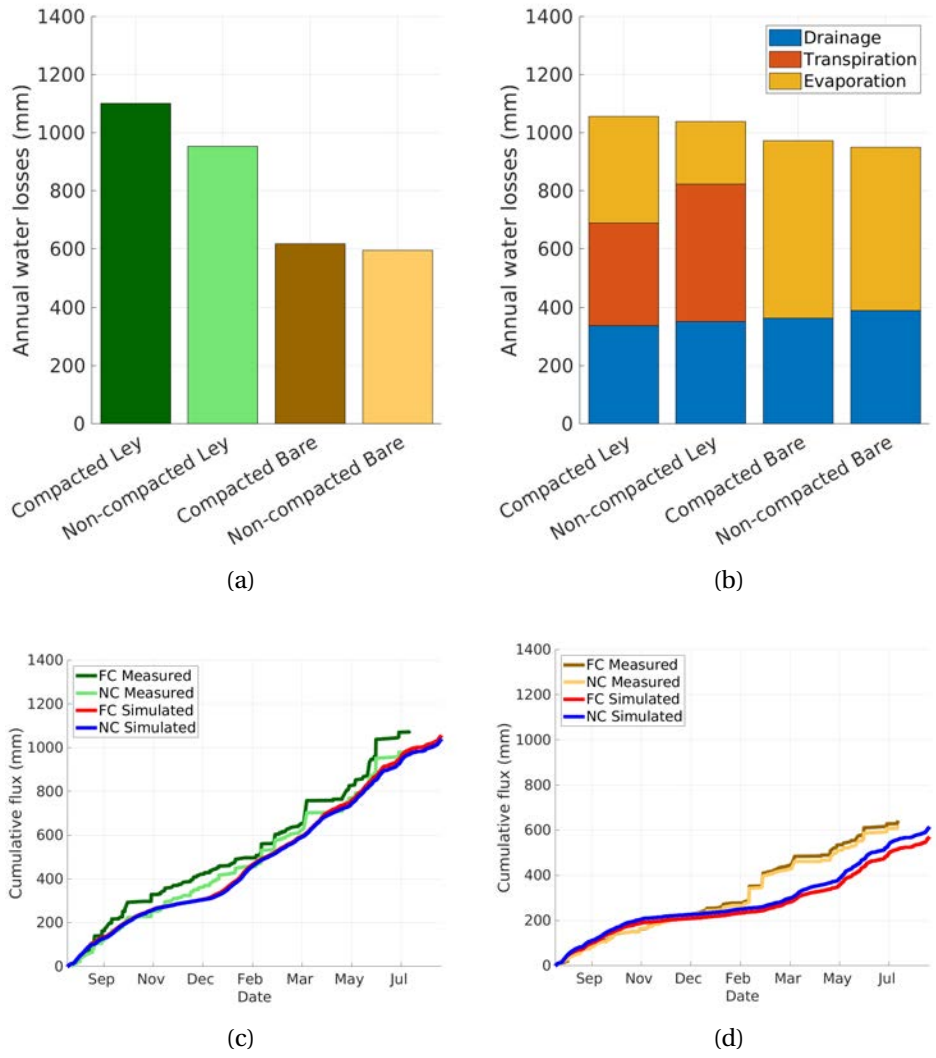

Figure 4.11 – (a) Measured total annual water losses in the top meter of soils (estimated from TDR data). (b) Total annual water losses in the top meter of soils resulting from the Hydrus simulations. The different soil fluxes are marked with different colors for each soil case. (c) Measured and simulated cumulative total water losses as a function of time for compacted and non-compacted ley. (d) Measured total water losses and simulated evaporation as a function of time for compacted and non-compacted bare soil. The time axis goes from the middle of 2017 to the middle of 2018

of water uptake and transpiration (equation 4.12) and (2) constrains for the plant water use derived from aboveground biomass observations. We note that the estimated evaporation depth for the non-compacted ley (L_C = 31 cm) was only 8 cm larger than root-density skin depth (λ_{RU} = 20 cm), implying that evaporation and root water uptake occur from the same soil volume for non-compacted ley. This is supported by TDR data at 40 cm depth, presenting relatively small variations of dielectric permittivity in the non-compacted ley (Figure 4.8). For this reason, we assume that there is no evaporation in the non-compacted ley during the growing season. The simulated evapotranspiration during the growing season (473 mm) can be fully attributed to transpiration (this is shown in Figure 4.11b). We estimate the total transpiration of compacted ley using information about aboveground biomass. The measured biomass imply that transpiration in compacted ley is 70% of the transpiration in the non-compacted ley, leading to an estimation of annual transpiration of 329 mm for the compacted ley.

The results above suggest that the increased water losses in the compacted soils are delivered by soil evaporation occurring only in compacted ley during the growing season. This adverse effect might be linked with a decrease in leaf area index (LAI) due to the reduced aboveground biomass in compacted ley (see *Assaeed et al.*, 1990). Using this information, the estimated annual evaporation were 386 mm and 215 for compacted and non-compacted ley, respectively. The model predicts an annual increase of 171 mm in evaporation for compacted ley relative to non-compacted ley. Herein, we interpret this result as the combination of two effects produced by soil compaction: (1) the increment in evaporation capabilities and (2) the reduced LAI in compacted soils due to increased mechanical resistance in soil that leads to a decrease in crop growth capabilities. Our observations and modeling suggest that soil compaction might have a large impact in soil-atmosphere water partitions. We offer an initial qualitative description and modeling that is consistent with our observations. Yet, this topic merits further and more detailed investigation.

4.6 Conclusions

We developed a coupled hydrogeophysical modeling scheme that accounts for soil-specific evaporation properties to study the influence of soil structure on soil moisture dynamics captured by geoelectrical data. The modeling scheme includes a new pedophysical model that allows to interpret electrical properties of structured soils based on macroporosity and connectivity of soil aggregates. The modeling scheme was used to interpret DC-resistivity monitoring data from a soil compaction experiment. The apparent electrical resistivity data revealed that compacted soils are less resistive at the same water content than for non-compacted soils and the monitoring results provided insights of the influence of soil structure on the soil water dynamics. Small scale point observations of TDR data revealed soil compaction-induced variations in soil water regime. Such effects were captured at the plot-scale with monitored DC-resistivity data. Using the pedophysical model, we interpreted the differences between compacted and non-compacted electrical resistivity signals as a decrease in macroporosity and its connectivity due to compaction. Higher water losses in compacted ley than in non-compacted ley revealed by TDR and DC-resistivity data suggested increased

evapotranspiration in compacted ley. Since increased biomass production in non-compacted ley implies higher transpiration, this suggests a considerable contribution of evaporation to water losses in the compacted ley. The model scheme was capable of reproducing the main differences in soil water dynamics of bare soil by considering a larger evaporation length and lower critical water content for Stage-I evaporation in compacted ley and bare soil. The differences in moisture dynamics of compacted and non-compacted ley were qualitatively well described but underestimated by the model. We stress that the partition of soil water in compacted vegetated soils deserves further investigation. Our proposed modeling scheme and newly proposed pedophysical model expands our monitoring tools and strategies to capture and interpret geoelectrical signatures of soil structure. It provides insights of how small differences in soil physical properties may induce significant changes in soil-atmosphere water (and energy) fluxes. By illustrating impacts of soil compaction on soil water dynamics at the plot-scale, the results presented in this work provide evidence that incorporating soil structure impacts on water dynamics is helpful for improving Earth system models.

Chapter 5

Conclusions and Outlook

This PhD thesis addresses the challenge of minimally-invasively characterization of soil structure at spatial scales that are larger than those provided by traditional techniques and with enhanced capabilities for *in-situ* monitoring. We proposed that harnessing geophysical methods, due to their ability to image spatial and temporal dynamics would help us to achieve this.

The disparity of scales between traditional *in-situ* point observations and laboratory-based characterization of soil structure and the larger scales relevant for soil agricultural management or land-surface models is a long-standing challenge in soil science (*Or*, 2020). We used monitoring and modeling of seismic and geoelectrical data in combination with soil water flow modeling to advance soil structure characterization at larger scales. Furthermore, we linked by pedophysical modeling plot-scale observations of seismic velocities and apparent electrical resistivity to small scale *in-situ* point observations: TDR, cone penetrometer and laboratory measurements. In order to evaluate the advances made in this thesis, we consider bellow contributions in the following (interconnected) categories: linking microscopic and macroscopic properties, conceptual models of spatial variations of soil properties, monitoring of soil structure-driven processes and larger-scale characterization of soil structure.

Linking microscopic and macroscopic properties. We developed pedophysical models that link macroscopic P-wave velocities and electrical resistivity to microscopic topological properties of soil structure. The P-wave velocity was linked to the contact area (A) between aggregates and, similarly, the electrical resistivity was linked to the connectivity between soil aggregates (represented by M_{soil}). The two pedophysical models involving either mechanical contact or electrical connectivity between soil aggregates are linked to each other as indicated in Figure 5.1).

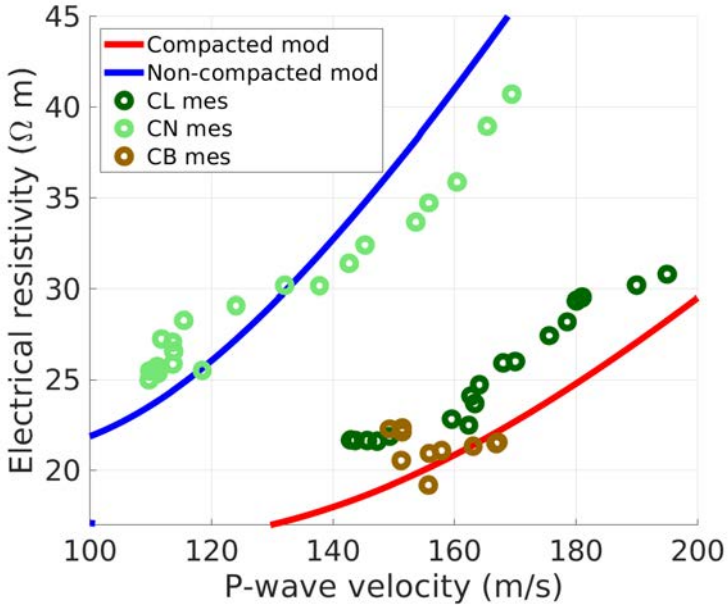

Figure 5.1 – Modeled and measured apparent resistivity against seismic velocities as a function of water content. The measured P-wave velocities correspond to the velocities of the first layer Chapter 3, while the apparent resistivities correspond to the j=1 in the Wenner-Schlumberger array in Chapter 4.

Conceptual models of spatial variations of soil properties. Conceptual models of how soil properties (e.g., porosity, saturated hydraulic conductivity) vary in space is essential to evaluate the large-scale impacts of soil structure on soil functioning and, ultimately, the corresponding geophysical data. In Chapter 4, we consider the saturated hydraulic conductivity, the total porosity and the macroporosity to be an exponentially decaying function of soil depth and use this to model water flow and compute geoelectrical data.

Monitoring of soil structure-driven processes. Our work mainly highlights strong links between measured geophysical data and soil water state. In Chapter 3, we observed a very strong correlation between S-wave velocities of seismic waves and water content derived from TDR probes despite that these methods probe very different soil volumes with a wavelength of ~1 m and ~0.1 m for the seismic method and TDR, respectively. Similarly, plot-scale apparent resistivity data presented in Chapter 4 were in agreement with observations of TDR data suggesting that water losses in compacted ley were considerably higher than in non-compacted ley. This suggests that soil compaction may strongly contribute to the depletion of groundwater resources by decreasing the recharge to aquifers.

Larger-scale characterization of soil structure. Both of the considered geophysical methods proved to be sensitive to soil compaction. The P-wave velocities of shallow seismic waves (i.e., propagating within a soil depth of 20 cm) in compacted soils presented an increase of ~30% (5 years after compaction) compared to non-compacted soils. This is qualitatively in good agreement with the increases observed in the averaged (5-15 cm) penetration resistance (~40%, 4 years after compaction) measured at a given point location. Similarly,

the apparent electrical resistivity of compacted soils was decreased by ~10% with respect to non-compacted soils. The methods offer complementary sensitivities to soil properties. Thus, a combined approach using both methods may help to discriminate the compaction state of a given field. For example, Figure 5.1 presents a crossplot of apparent resistivity data (j=1) and seismic velocities for compacted ley, non-compacted ley and compacted bare soil. Data were paired as values within a similar range of water content. Similarly, we added the corresponding modeled values using the model parameters inferred in Chapter 3 and 4. Clearly, data from compacted and non-compacted soils cluster in the proximity of their corresponding compacted and non-compacted modeled curves. This illustrates the potential of combined geophysical soil characterization using seismic and geoelectrical methods. This could circumvent the strong influence of water content as the level of compaction will determine the position of a data point in such a scatter plot.

5.1 Conclusions

When starting this PhD project, we performed a careful literature review from which we confirmed the potential of geophysical methods for sensing soil structure. Likewise, we identified several opportunities to systematically characterize of soil structure with geophysical methods: (1) improved pedophysical models relating soil structure and macroscopic geophysical properties; (2) improving the currently available monitoring techniques; (3) combining methods with complementary sensitivity to soil properties and (4) designing modeling tools to infer soil structure by its indirect influence in soil processes and related geophysical time-lapse signatures. Our review article (Chapter 2), hence, became the starting point establishing the basis for the efforts presented in Chapters 3 and 4. In the following, we highlight the main findings of those studies.

Geophysical data are sensitive to soil structure. Seismic and geoelectrical methods were selected for experimental testing to demonstrate their complementing sensitivities to the soil phases and their organization. We monitored seismic and geoelectrical signatures of soils with different compaction treatments and covers at a controlled experimental field site, in which a compaction event took place in 2014. The measured P-wave velocities carried a strong imprint of soil compaction. We observed considerably higher (~30%) P-wave velocities for compacted soils than for non-compacted soils five years after the compaction event. Similarly, the apparent electrical resistivity data revealed that compacted soils are typically less resistive (~15%) than non-compacted soils four years after the compaction event. In addition, dynamics of time-lapse electrical resistivity agreed with TDR water content dynamics revealing lower values of water storage in compacted ley and compacted bare soil during dry periods.

New pedophysical models linking soil structure to macroscopic geophysical properties. We developed new dual-domain pedophysical models for seismic and electrical properties of structured soils. The seismic model accounts for soil plastic deformation occurring in the contact area between aggregates during soil compaction. The inferred contact areas between aggregates at the field site are 2.9 times larger for compacted than for non-compacted soils. From these contact areas, we calculated volumetric strains (~3%) that were in agreement

with volumetric strains calculated from laboratory measurements of bulk density. The new pedophysical model of electric properties allows interpreting the observed reduction of electrical resistivity in compacted soils. We find that the main underlying mechanism is an enhanced ability of the soil frame to conduct electrical currents due to the reduction and disruption of macroporosity caused by compaction.

Integrative modeling allows mechanistic and quantitative interpretation of soil water dynamics. In the electrical resistivity study (Chapter 4), we developed a coupled hydrogeophysical modeling scheme that links geoelectrical signatures to a soil water regime that is dependent on soil structure. In addition, this modeling framework accounts for soil structure-specific evaporation. This allowed us to interpret higher water losses in compacted soils than in non-compacted soils as a consequence of increased evaporation in compacted soils due to the reduction of mesoporosity. We could reproduce qualitative differences in soil water dynamics of compacted and non-compacted soils by considering a larger evaporation length and lower critical water content for Stage-I evaporation in compacted soils. The modeling provided new insights about the water balance in compacted soils compared to their non-compacted counterparts.

There were no signs of complete soil compaction recovery. Our seismic and geoelectrical monitoring highlight persistent changes in physical properties several years after the prescribed compaction. Significantly higher P-wave velocities observed in the compacted plots suggested that the soils are still appreciably impacted by the compaction event and that soil structure recovery is a slow process. In addition, no significant differences were observed in P-wave velocities between soil cover (Ley vs. Bare soil), implying that the ley did not play a significant role in the recovery of soil mechanical properties. Similarly, relative differences in electrical properties between compacted and non-compacted soils have remained similar since the compaction event, thereby, offering no strong signs of soil recovery.

5.2 Outlook

Soil structure characterization at spatially relevant scales for management remains a major challenge. Our proposed modeling schemes and pedophysical models expand the monitoring tools and strategies available to capture and interpret geophysical signatures of soil structure. They provide the means to infer differences in soil structure (e.g., macroporosity and binding of soil constituents) with a strong impact on transport properties from small changes in macroscopic geophysical properties. This thesis is a first step towards geophysically-based characterization of soil structure. I hope that this work will motivate future efforts to improve our monitoring, imaging and modeling capabilities to characterize soil structure and its impact in physical processes. Below, I highlight some possible directions for future research:

- **Laboratory-based characterization of geophysical properties**
  This thesis did not laboratory-based characterization of geophysical properties in relation to soil structure. Designing and performing laboratory experiments for measuring geophysical properties of soil samples with controlled structure would be necessary to further develop geophysics-based soil structure characterization. For example, testing

the pedophysical models developed in this thesis would substantially improve our understanding of how geophysical properties sense soil structure.

- **Other geophysical methods and properties**
  The time-frame of a PhD thesis made it difficult to test all potentially interesting geophysical methods for soil structure characterization. As highlighted in Chapter 2, the induced polarization method might be highly sensitive to soil structure and merits further investigation in this context. Another example relates to seismic attributes that were not explored in this thesis, such as, velocity dispersion and attenuation. Due to their versatility for practical usage, movement and transportation, the ground penetrating radar (GPR) method and the electromagnetic induction (EMI) method could offer enhanced perspectives for soil structure characterization at large scales.
- **Survey design**
  After accumulating the necessary knowledge to sense soil structure with geophysical methods in relatively small (e.g., plot) scales, there is a need for measuring devices that act at much larger scales. Adapting unmanned aerial vehicle (UAV) for this task should be put at the center of development. GPR and EMI methods are the most suitable methods for this task. Their combined usage could help identifying zones with degraded soil structure that could be targeted for a more detailed assessment with other geophysical methods and laboratory analysis.
- **Effect of water content on S-wave (or surface wave) velocities**
  In Chapter 3, we observed a remarkably strong correlation between soil water content and S-wave velocities. This phenomena deserves further investigation and could lead to developments of new methods for measuring water content in soils.
- **Water partition in compacted vegetated soils**
  In Chapter 4, we observed a strong effect of soil compaction on the soil water regime of ley soil. The compacted ley was loosing considerably more water (~150 mm/year in average) than the non-compacted ley. We explained this effect as a difference in annual evaporation due to enhanced evaporative capabilities of the compacted soil. This effect deserves further investigation through a more detailed characterization of how water is partitioned in compacted soils.
- **Application to other soil types, vegetation and climates**
  In this thesis, we applied the developed frameworks to interpret data from structured agricultural soils. Yet, the methods are general and their application could be expanded to characterize other soil types, different vegetation types and under different climatic conditions. For example, it is possible that geophysical methods would offer valuable insights to understand soil structure dynamics and its impact on forest ecology.
- **Application to landscape scales for hydrologic and climatic modeling**
  Soil structure variations occurring at the pore scale have a strong impact on soil ecological functions and, ultimately, may influence climate change. Global hydrological and climatic modeling rely on information of soil properties that is currently incomplete and soil structure effects have not been accounted for in such models. Geophysical methods could contribute as an element for hierarchical upscaling of soil structure effect on soil functions from laboratory measurements to landscape scales sensed by remote sensing technologies.

Bibliography

Aeschbach-Hertig, W., and T. Gleeson (2012), Regional strategies for the accelerating global problem of groundwater depletion, *Nature Geoscience*, *5*(12), 853–861.

Aitkenhead, M., S. D. Allison, S. Assouline, P. Baveye, M. Berli, N. Brüggemann, P. Finke, M. Flury, T. Gaiser, G. Govers, T. Ghezzehei, P. Hallett, H. J. H. Franssen, J. Heppell, R. Horn, J. A. Huisman, D. Jacques, F. Jonard, S. Kollet, F. Lafolie, K. Lamorski, D. Leitner, A. Mcbratney, B. Minasny, C. Montzka, W. Nowak, Y. Pachepsky, J. Padarian, N. Romano, K. Roth, Y. Rothfuss, E. C. Rowe, A. Schwen, J. Šimůnek, A. Tiktak, J. V. Dam, S. E. A. T. M. V. D. Zee, H. J. Vogel, and J. A. Vrugt (2016), Modeling Soil Processes : Review , Key Challenges , and New Perspectives Brief History of Soil Modeling, *Vadose Zone Journal*, *15*, doi:10.2136/vzj2015.09.0131.

Algeo, J., R. L. Van Dam, and L. Slater (2016), Early-time GPR: a method to monitor spatial variations in soil water content during irrigation in clay soils, *Vadose Zone Journal*, *15*(11), doi:10.2136/vzj2016.03.0026.

Allred, B. J., J. J. Daniels, and M. R. Ehsani (Eds.) (2008), *Handbook of Agricultural Geophysics*, CRC Press.

André, F., C. van Leeuwen, S. Saussez, R. Van Durmen, P. Bogaert, D. Moghadas, L. de Resseguier, B. Delvaux, H. Vereecken, and S. Lambot (2012), High-resolution imaging of a vineyard in south of France using ground-penetrating radar, electromagnetic induction and electrical resistivity tomography, *Journal of Applied Geophysics*, *78*, 113–122, doi:10.1016/j.jappgeo.2011.08.002.

Annan, A. P. (2005), GPR methods for hydrogeological studies, in *Hydrogeophysics*, edited by Y. Rubin and S. S. Hubbard, chap. 7, pp. 185–213, Springer, Dordrecht, doi:10.1007/1-4020-3102-5_7.

Archie, G. (1942), The electrical resistivity log as an aid in determining some reservoir characteristics, *Petroleum Technology*, (October), 54–62, doi:10.2118/942054-G.

Asnaashari, A., R. Brossier, S. Garambois, F. Audebert, P. Thore, and J. Virieux (2013), Regularized seismic full waveform inversion with prior model information, *Geophysics*, *78*(2), R25–R36, doi:10.1190/geo2012-0104.1.

Assaeed, A. M., M. McGowan, P. D. Hebblethwaite, and J. C. Brereton (1990), Effect of soil compaction on growth, yield and light interception of selected crops, *Annals of Applied Biology*, *117*(3), 653–666, doi:https://doi.org/10.1111/j.1744-7348.1990.tb04831.x.

Assouline, S., K. Narkis, R. Gherabli, P. Lefort, and M. Prat (2014), Analysis of the impact of surface layer properties on evaporation from porous systems using column experiments and modified definition of characteristic length, *Water Resources Research*, *50*(5), 3933–3955, doi:10.1002/2013WR014489.

Bachrach, R., and A. Nur (1998), High-resolution shallow-seismic experiments in sand, Part I: Water table, fluid flow, and saturation, *Geophysics*, *63*(4), 1225–1233, doi:10.1190/1.1444423.

Bachrach, R., J. Dvorkin, and A. M. Nur (2000), Seismic velocities and Poisson's ratio of shallow unconsolidated sands, *Geophysics*, *65*(2), 559–564, doi:10.1190/1.1444751.

Bairlein, K., A. Hördt, and S. Nordsiek (2014), The influence on sample preparation on spectral induced polarization of unconsolidated sediments, *Near Surface Geophysics*, *12*, 667–677, doi:10.3997/1873-0604.2014023.

Behroozmand, A. A., K. Keating, and E. Auken (2014), A review of the principles and applications of the NMR technique for near-surface characterization, *Surveys in Geophysics*, *36*(1), 27–85, doi:10.1007/s10712-014-9304-0.

Bengough, A. G., and C. E. Mullins (1990), Mechanical impedance to root growth: a review of experimental techniques and root growth responses, *Journal of Soil Science*, *41*(3), 341–358, doi:https://doi.org/10.1111/j.1365-2389.1990.tb00070.x.

Bengough, A. G., B. M. McKenzie, P. D. Hallett, and T. A. Valentine (2011), Root elongation, water stress, and mechanical impedance: a review of limiting stresses and beneficial root tip traits, *Journal of Experimental Botany*, *62*(1), 59–68, doi:10.1093/jxb/erq350.

Berisso, F. E., P. Schjønning, T. Keller, M. Lamandé, A. Etana, L. W. De Jonge, B. V. Iversen, J. Arvidsson, and J. Forkman (2012), Persistent effects of subsoil compaction on pore size distribution and gas transport in a loamy soil, *Soil and Tillage Research*, *122*, 42–51, doi:10.1016/j.still.2012.02.005.

Berryman, J. G. (1995), Mixture theories for rock properties, *Rock physics & phase relations: A handbook of physical constants*, pp. 205–228, doi:10.1029/RF003p0205.

Berryman, J. G. (1999), Origin of Gassmann's equations, *Geophysics*, *64*(5), 1627–1629, doi:10.1190/1.1444667.

Besson, A., I. Cousin, A. Samouëlian, H. Boizard, and G. Richard (2004), Structural heterogeneity of the soil tilled layer as characterized by 2D electrical resistivity surveying, *Soil and Tillage Research*, *79*(2), 239–249, doi:10.1016/j.still.2004.07.012.

Besson, A., I. Cousin, A. Dorigny, M. Dabas, and D. King (2008), The temperature correction for the electrical resistivity measurements in undisturbed soil samples: Analysis of the existing conversion models and proposal of a new model, *Soil Science*, *173*(10), 707–720, doi:10.1097/SS.0b013e318189397f.

Besson, A., M. Séger, I. Cousin, G. Grandjean, K. Samyn, and S. Lambot (2010a), Inferences of soil characteristics by the Pedo-Transfert Functions approach, *Tech. Rep. March*, Report N FP7-DIGISOIL-D2.2.

Besson, A., I. Cousin, H. Bourennane, B. Nicoullaud, C. Pasquier, G. Richard, A. Dorigny, and D. King (2010b), The spatial and temporal organization of soil water at the field scale as described by electrical resistivity measurements, *European Journal of Soil Science*, *61*(1), 120–132, doi:10.1111/j.1365-2389.2009.01211.x.

Besson, A., M. Séger, G. Giot, and I. Cousin (2013), Identifying the characteristic scales of soil structural recovery after compaction from three in-field methods of monitoring, *Geoderma*, *204*, 130–139, doi:10.1016/j.geoderma.2013.04.010.

Beven, K., and P. Germann (2013), Macropores and water flow in soils revisited, *Water Resources Research*, *49*(February 2012), 3071–3092, doi:10.1002/wrcr.20156.

Bhowmick, S. (2017), Role of Vp/Vs and Poisson's ratio in the assessment of foundation(s) for important civil structure(s), *Geotechnical and Geological Engineering*, *35*(1), 527–534, doi:10.1007/s10706-016-0106-7.

Binley, A., and A. Kemna (2005), DC Resistivity and induced polarization methods, in *Hydrogeophysics*, edited by Y. Rubin and S. S. Hubbard, chap. 5, pp. 129–156, Springer, Dordrecht, doi:10.1007/1-4020-3102-5_5.

Binley, A., and L. Slater (2020), *Resistivity and Induced Polarization: Theory and Applications to the Near-Surface Earth*, Cambridge University Press.

Binley, A., S. S. Hubbard, J. A. Huisman, A. Revil, D. A. Robinson, K. Singha, and L. Slater (2015), The emergence of hydrogeophysics for improved understanding of subsurface processes over multiple scales, *Water Resources Research*, *51*(6), 3837–3866, doi:10.1002/2015WR017016.

Biot, M. A. (1962), Mechanics of deformation and acoustic propagation in porous media, *Journal of Applied Physics*, *33*(4), 1482–1498, doi:10.1063/1.1728759.

Bishop, A. W., and G. Blight (1963), Some aspects of effective stress in saturated and partly saturated soils, *Geotechnique*, *13*(3), 177–197, doi:10.1680/geot.1963.13.3.177.

Blainey, J. B., T. P. A. Ferré, and J. T. Cordova (2007), Assessing the likely value of gravity and drawdown measurements to constrain estimates of hydraulic conductivity and specific yield during unconfined aquifer testing, *Water Resources Research*, *43*(12), W12,408, doi:10.1029/2006WR005678.

Blanchy, G., C. W. Watts, J. Richards, J. Bussell, K. Huntenburg, D. L. Sparkes, M. Stalham, M. J. Hawkesford, W. R. Whalley, and A. Binley (2020), Time-lapse geophysical assessment of agricultural practices on soil moisture dynamics, *Vadose Zone Journal*, *19*(1), e20,080, doi:https://doi.org/10.1002/vzj2.20080.

Blazevic, L. A., L. Bodet, S. Pasquet, N. Linde, D. Jougnot, and L. Longuevergne (2020), Time-lapse seismic and electrical monitoring of the vadose zone during a controlled infiltration experiment at the Ploemeur hydrological observatory, France, *Water*, *12*(5), 1230, doi:10.3390/w12051230.

Blonquist Jr, J., S. B. Jones, I. Lebron, and D. Robinson (2006), Microstructural and phase configurational effects determining water content: Dielectric relationships of aggregated porous media, *Water Resources Research*, *42*(5), doi:10.1029/2005WR004418.

Blum, W. E., and H. Swaran (2004), Soils for sustaining global food production, *Journal of Food Science*, *69*(2), crh37–crh42, doi:https://doi.org/10.1111/j.1365-2621.2004.tb15490.x.

Bohlen, T. (2002), Parallel 3-D viscoelastic finite difference seismic modelling, *Computers and Geosciences*, *28*, 887–899, doi:10.1016/S0098-3004(02)00006-7.

Boizard, H., J. Peigné, M. C. Sasal, M. de Fátima Guimarães, D. Piron, V. Tomis, J.-F. Vian, S. Cadoux, R. Ralisch, J. Tavares Filho, D. Heddadj, J. De Battista, A. Duparque, J. C. Franchini, and J. Roger-Estrade (2017), Developments in the "profil cultural" method for an improved assessment of soil structure under no-till, *Soil and Tillage Research*, *173*, 92 – 103, doi:https://doi.org/10.1016/j.still.2016.07.007.

Börner, F. D., J. R. Schopper, and A. Weller (1996), Evaluation of transport and storage properties in the soil and groundwater zone from induced polarization measurements, *Geophysical Prospecting*, *44*(4), 583–601, doi:10.1111/j.1365-2478.1996.tb00167.x.

Bottinelli, N., P. Jouquet, Y. Capowiez, P. Podwojewski, M. Grimaldi, and X. Peng (2015), Why is the influence of soil macrofauna on soil structure only considered by soil ecologists?, *Soil & Tillage Research*, *146*(A), 118–124, doi:10.1016/j.still.2014.01.007.

Bouchand, P., J. Roger-Estrade, Y. Capowiez, G. Richard, and H. Boizard (2009), Experimental evidence for the role of earthworms in compacted soil regeneration based on field observations and results from a semi-field experiment, *Soil Biology and Biochemistry*, *41*, 711–717, doi:10.1016/j.soilbio.2009.01.006.

Breede, K. (2013), Characterization of effective hydraulic properties of unsaturated porous media using spectral induced polarization (SIP), Ph.D. thesis, Forschungszentrum Jülich GmbH.

Brie, A., F. Pampuri, A. F. Marsala, and O. Meazza (1995), Shear sonic interpretation in gas-bearing sands, in *SPE Annual Technical Conference and Exhibition. Society of Petroleum Engineers.*, pp. 701–710.

Bronick, C. J., and R. Lal (2005), Soil structure and management : a review, *Geoderma*, *124*(1-2), 3–22, doi:10.1016/j.geoderma.2004.03.005.

Brovelli, A., and G. Cassiani (2008), Effective permittivity of porous media: a critical analysis of the complex refractive index model, *Geophysical Prospecting*, *56*, 715–727, doi:10.1111/j.1365-2478.2008.00724.x.

Brunetti, C. U. o. L., N. Linde, and J. A. Vrugt (2017), Bayesian model selection in hydrogeophysics : Application to conceptual subsurface models of the South Oyster Baterial Transprt Site, Virginia, USA, *Advances in Water Resources*, *102*, 127–141, doi:10.1016/j.advwatres.2017.02.006.

Brus, D. J., and J. J. Van Den Akker (2018), How serious a problem is subsoil compaction in the Netherlands? A survey based on probability sampling, *Soil*, *4*(1), 37–45, doi:10.5194/soil-4-37-2018.

Brutsaert, W., and J. N. Luthin (1964), The velocity of sound in soils near the surface as a function of the moisture content, *Journal of Geophysical Research*, *69*(4), 643–652, doi:10.1029/JZ069i004p00643.

Burns, S., and P. Mayne (1996), Small-and high-strain measurements of in situ soil properties using the seismic cone penetrometer, *Transportation Research Record: Journal of the Transportation Research Board*, (1548), 81–88, doi:10.3141/1548-12.

Bussian, A. E. (1983), Electrical conductance in a porous medium, *Geophysics*, *48*(9), 1258–1268, doi:10.1190/1.1441549.

Campbell, R. B., C. A. Bower, and L. A. Richards (1948), Change of electrical conductivity with temperature and the relation of osmotic pressure to electrical conductivity and ion concentration for soil extracts, in *Soil Science Society of America Proceedings*, vol. 13, pp. 66–69.

Carminati, A., A. Kaestner, H. Flühler, P. Lehmann, D. Or, E. Lehmann, and M. Stampanoni (2007), Hydraulic contacts controlling water flow across porous grains, *Phys. Rev. E*, *76*, 026,311, doi:10.1103/PhysRevE.76.026311.

Carsel, R. F., and R. S. Parrish (1988), Developing joint probability distributions of soil water retention characteristics, *Water Resources Research*, *24*(5), 755–769, doi:10.1029/WR024i005p00755.

Carter, M. R., and E. G. Gregorich (2007), *Soil sampling and methods of analysis*, CRC press.

Cerveny, V. (2005), *Seismic Ray Theory*, Cambridge University Press.

Chen, Y., M. Irfan, T. Uchimura, G. Cheng, and W. Nie (2018), Elastic wave velocity monitoring as an emerging technique for rainfall-induced landslide prediction, *Landslides*, *15*(6), 1155–1172, doi:10.1007/s10346-017-0943-3.

Chen, Y. L., J. Palta, J. Clements, B. Buirchell, K. H. Siddique, and Z. Rengel (2014), Root architecture alteration of narrow-leafed lupin and wheat in response to soil compaction, *Field Crops Research*, *165*, 61–70, doi:10.1016/j.fcr.2014.04.007.

Ciampalini, A., F. André, F. Garfagnoli, G. Grandjean, S. Lambot, L. Chiarantini, and S. Moretti (2015), Improved estimation of soil clay content by the fusion of remote hyperspectral and proximal geophysical sensing, *Journal of Applied Geophysics*, *116*, 135–145, doi:10.1016/j.jappgeo.2015.03.009.

Colombi, T., S. Braun, T. Keller, and A. Walter (2017), Artificial macropores attract crop roots and enhance plant productivity on compacted soils, *Science of the Total Environment*, *574*, 1283–1293, doi:10.1016/j.scitotenv.2016.07.194.

Colombi, T., L. Chagas, A. Walter, and T. Keller (2018), Feedbacks between soil penetration resistance, root architecture and water uptake limit water accessibility and crop growth - A vicious circle, *Science of the Total Environment*, *626*, 1026–1035, doi:10.1016/j.scitotenv.2018.01.129.

Conrad, R. (1996), Soil microorganisms as controllers of atmospheric trace gases (h2, co, ch4, ocs, n2o, and no)., *Microbiology and Molecular Biology Reviews*, *60*(4), 609–640.

Corwin, D. L., and S. M. Lesch (2003), Application of soil electrical conductivity to precision agriculture, *Agronomy Journal*, *95*(3), 455–471, doi:10.2134/agronj2003.4550.

Cosenza, P., A. Ghorbani, C. Camerlynck, F. Rejiba, R. Guérin, and A. Tabbagh (2009), Effective medium theories for modelling the relationships between electromagnetic properties and hydrological variables in geomaterials: a review, *Near Surface Geophysics*, *7*(5-6), 563–578, doi:10.3997/1873-0604.2009009.

Costanza, R., R. d'Arge, R. De Groot, S. Farber, M. Grasso, B. Hannon, K. Limburg, S. Naeem, R. V. O'neill, J. Paruelo, et al. (1997), The value of the world's ecosystem services and natural capital, *Nature*, *387*(6630), 253–260.

Costanza, R., R. de Groot, P. Sutton, S. van der Ploeg, S. J. Anderson, I. Kubiszewski, S. Farber, and R. K. Turner (2014), Changes in the global value of ecosystem services, *Global Environmental Change*, *26*, 152 – 158, doi:https://doi.org/10.1016/j.gloenvcha.2014.04.002.

Curtis, T. P., W. T. Sloan, and J. W. Scannell (2002), Estimating prokaryotic diversity and its limits, *Proceedings of the National Academy of Sciences*, *99*(16), 10,494–10,499, doi:10.1073/pnas.142680199.

Dafflon, B., R. Oktem, J. Peterson, C. Ulrich, A. P. Tran, V. Romanovsky, and S. S. Hubbard (2017), Coincident aboveground and belowground autonomous monitoring to quantify covariability in permafrost, soil, and vegetation properties in Arctic tundra, *Journal of Geophysical Research: Biogeosciences*, *122*, 1321–1342, doi:10.1002/2016JG003724.

Day-Lewis, F., N. Linde, R. Haggerty, K. Singha, and M. A. Briggs (2017), Pore network modeling of the electrical signature of solute transport in dual-domain media, *Geophysical Research Letters*, *44*(10), 4908–4916, doi:10.1002/2017GL073326.

Day-Lewis, F. D., K. Singha, and A. M. Binley (2005), Applying petrophysical models to radar travel time and electrical resistivity tomograms : Resolution-dependent limitations, *Journal of Geophysical Research: Solid Earth*, *110*(B8), doi:10.1029/2004JB003569.

De Vries, D. A. (1963), Thermal properties of soils, in *Physiscs of Plant Environment*, edited by W. R. Van Wijk, pp. 210–235, North-Holland Publ. Co., Amsterdam.

Dexter, A. (1988), Advances in characterization of soil structure, *Soil and Tillage Research*, *11*(3-4), 199–238, doi:10.1016/0167-1987(88)90002-5.

Di Matteo, A., E. Pettinelli, and E. Slob (2013), Early-time GPR signal attributes to estimate soil dielectric permittivity: A theoretical study, *IEEE Transactions on Geoscience and Remote Sensing*, *51*(3), 1643–1654, doi:10.1109/TGRS.2012.2206817.

Dijkstra, E. W., et al. (1959), A note on two problems in connexion with graphs, *Numerische mathematik*, *1*(1), 269–271.

Doetsch, J., N. Linde, I. Coscia, S. A. Greenhalgh, and A. G. Green (2010), Zonation for 3D aquifer characterization based on joint inversions of multimethod crosshole geophysical data, *Geophysics*, *75*(6), G53–64, doi:10.1190/1.3496476.

Domenico, S. N. (1977), Elastic properties of unconsolidated porous sand reservoirs, *Geophysics*, *42*(7), 1339–1368, doi:10.1190/1.1440797.

Donohue, S., D. Forristal, and L. A. Donohue (2013), Detection of soil compaction using seismic surface waves, *Soil and Tillage Research*, *128*, 54–60, doi:10.1016/j.still.2012.11.001.

Doolittle, J. A., and E. C. Brevik (2014), The use of electromagnetic induction techniques in soils studies, *Geoderma*, *223*, 33–45, doi:10.1016/j.geoderma.2014.01.027.

Dou, S., and J. B. Ajo-Franklin (2014), Full-wavefield inversion of surface waves for mapping embedded low-velocity zones in permafrost, *Geophysics*, *79*(6), EN107–EN124, doi:10.1190/geo2013-0427.1.

Doussan, C., and S. Ruy (2009), Prediction of unsaturated soil hydraulic conductivity with electrical conductivity, *Water Resources Research*, *45*(10), 1–12, doi:10.1029/2008WR007309.

Doussan, C., L. Jouniaux, and J.-l. Thony (2002), Variations of self-potential and unsaturated water flow with time in sandy loam and clay loam soils, *Journal of Hydrology*, *267*, 173–185, doi:10.1016/S0022-1694(02)00148-8.

Durner, W. (1994), Hydraulic conductivity estimation for soils with heterogeneous pore structure, *Water Resources Research*, *30*(2), 211–223, doi:10.1029/93WR02676.

Dvorkin, J., M. Prasad, A. Sakai, and D. Lavoie (1999), Elasticity of marine sediments: Rock physics modeling, *Geophysical Research Letters*, *26*(12), 1781–1784, doi:10.1029/1999GL900332.

Evans, S. (1965), Dielectric properties of ice and snow–a review, *Journal of Glaciology*, *5*(42), 773–792, doi:10.3189/S0022143000018840.

Farahani, E., H. Emami, and T. Keller (2018), Impact of monovalent cations on soil structure. part ii. results of two swiss soils, *International Agrophysics*, *32*(1), 69–80.

Fatichi, S., D. Or, R. Walko, H. Vereecken, M. H. Young, T. A. Ghezzehei, T. Hengl, S. Kollet, N. Agam, and R. Avissar (2020), Soil structure is an important omission in Earth System Models, *Nature Communications*, *11*(1), 1–11, doi:10.1038/s41467-020-14411-z.

Faybishenko, B. A. (1995), Hydraulic behavior of quasi-saturated soils in the presence of entrapped air: Laboratory experiments, *Water Resources Research*, *31*(10), 2421–2435, doi:10.1029/95WR01654.

Feddes, R. A. (1982), *Simulation of field water use and crop yield*, Pudoc.

Flammer, I., A. Blum, A. Leiser, and P. Germann (2001), Acoustic assessment of flow patterns in unsaturated soil, *Journal of Applied Geophysics*, *46*(2), 115–128, doi:10.1016/S0926-9851(01)00032-5.

Follett, R. (2001), Soil management concepts and carbon sequestration in cropland soils, *Soil and Tillage Research*, *61*(1-2), 77–92, doi:10.1016/S0167-1987(01)00180-5.

Foster, T., N. Brozović, and A. P. Butler (2017), Effects of initial aquifer conditions on economic benefits from groundwater conservation, *Water Resources Research*, *53*(1), 744–762, doi:https://doi.org/10.1002/2016WR019365.

Foti, S., S. Parolai, D. Albarello, and M. Picozzi (2011), Application of surface-wave methods for seismic site characterization, *Surveys in Geophysics*, *32*(6), 777–825, doi:10.1007/s10712-011-9134-2.

Friedman, S. P. (2005), Soil properties influencing apparent electrical conductivity: a review, *Computers and electronics in agriculture*, *46*(1-3), 45–70, doi:10.1016/j.compag.2004.11.001.

Gallardo, L. a., and M. a. Meju (2003), Characterization of heterogeneous near-surface materials by joint 2D inversion of dc resistivity and seismic data, *Geophysical Research Letters*, *30*(13), doi:10.1029/2003GL017370.

García, X., and E. A. Medina (2006), Hysteresis effects studied by numerical simulations: Cyclic loading-unloading of a realistic sand model, *Geophysics*, *71*(2), F13–F20, doi:10.1190/1.2181309.

Garré, S., J. Koestel, T. Günther, M. Javaux, J. Vanderborght, and H. Vereecken (2010), Comparison of heterogeneous transport processes observed with electrical resisvity tomography in two soils, *Vadose Zone Journal*, *9*(2), 336–349, doi:10.2136/vzj2009.0086.

Garré, S., M. Javaux, J. Vanderborght, L. Pagès, and H. Vereecken (2011), Three-dimensional electrical resistivity tomography to monitor root zone water dynamics, *Vadose Zone Journal*, *10*, 412–424, doi:10.2136/vzj2010.0079.

Garré, S., I. Coteur, C. Wongleecharoen, T. Kongkaew, J. Diels, and J. Vanderborght (2013), Noninvasive monitoring of soil water dynamics in mixed cropping systems: a case study in Ratchaburi Province, Thailand, *Vadose Zone Journal*, *12*(2), doi:10.2136/vzj2012.0129.

Gassmann, F. (1951), Uber die elastizitat poroser medien, *Vierteljahrsschrift der Naturforschenden Gesellschaft in Zurich*, *96*, 1–23.

Gelman, A., and D. B. Rubin (1992), Inference from iterative simulation using multiple sequences, *Statistical Science*, *7*(4), 457–472, doi:10.1214/ss/1177011136.

Gerke, H. H., P. Germann, and J. Nieber (2010), Preferential and unstable flow: from the pore to the catchment scale, *Vadose Zone Journal*, *9*(2), 207–212, doi:10.2136/vzj2010.0059.

Ghezzehei, T. A., and D. Or (2001), Rheological properties of wet soils and clays under steady and oscillatory stresses, *Soil Science Society of America Journal*, *65*(3), 624–637, doi:10.2136/sssaj2001.653624x.

Ghezzehei, T. A., and D. Or (2003), Stress-induced volume reduction of isolated pores in wet soil, *Water Resources Research*, *39*(3), doi:10.1029/2001WR001137.

Ghorbani, A., P. Cosenza, S. Ruy, C. Doussan, and N. Florsch (2008), Non-invasive monitoring of water infiltration in a silty clay loam soil using Spectral Induced Polarization, *Water Resources Research*, *44*(8), 1–18, doi:10.1029/2007WR006114.

Glover, P. (2009), What is the cementation exponent? A new interpretation, *The Leading Edge*, *28*(1), 82–85, doi:10.1190/1.3064150.

Glover, P. W., M. J. Hole, and J. Pous (2000), A modified Archie's law for two conducting phases, *Earth and Planetary Science Letters*, *180*(3-4), 369–383.

Grandjean, G., I. Cousin, J. Thiesson, S. Lambot, B. Van Wesemael, A. Stevens, K. Samyn, A. Bitri, and S. Bernardie (2009a), From geophysical parameters to soil characteristics, *Tech. rep.*

Grandjean, G., A. Bitri, I. Cousin, S. Lambot, and F. Andre (2009b), Description of processing protocols for each sensor, *Tech. Rep. Report N FP7-DIGISOIL-D1 .2*.

Graves, A., J. Morris, L. Deeks, R. Rickson, M. Kibblewhite, J. Harris, T. Farewell, and I. Truckle (2015), The total costs of soil degradation in England and Wales, *Ecological Economics*, *119*, 399–413, doi:10.1016/j.ecolecon.2015.07.026.

Green, J. K., S. I. Seneviratne, A. M. Berg, K. L. Findell, S. Hagemann, D. M. Lawrence, and P. Gentine (2019), Large influence of soil moisture on long-term terrestrial carbon uptake, *Nature*, *565*(7740), 476, doi:10.1038/s41586-018-0848-x.

Gregory, A. S., C. W. Watts, W. R. Whalley, H. L. Kuan, B. S. Griffiths, P. D. Hallett, and A. P. Whitmore (2007), Physical resilience of soil to field compaction and the interactions with plant growth and microbial community structure, *European Journal of Soil Science*, *58*(6), 1221–1232, doi:10.1111/j.1365-2389.2007.00956.x.

Gregory, A. S., C. W. Watts, B. S. Griffiths, P. D. Hallett, H. L. Kuan, and A. P. Whitmore (2009), The effect of long-term soil management on the physical and biological resilience of a range of arable and grassland soils in England, *Geoderma*, *153*(1-2), 172–185, doi:10.1016/j.geoderma.2009.08.002.

Grote, K., S. Hubbard, and Y. Rubin (2003), Field-scale estimation of volumetric water content using ground-penetrating radar ground wave techniques, *Water Resources Research*, *39*(11), 1–14, doi:10.1029/2003WR002045.

Grote, K., C. Anger, B. Kelly, S. Hubbard, and Y. Rubin (2010), Characterization of soil water content variability and soil texture using GPR groundwave techniques, *Journal of Environmental & Engineering Geophysics*, *15*(3), 93–110, doi:10.2113/JEEG15.3.93.

Guimarães, R. M., M. Lamandé, L. J. Munkholm, B. C. Ball, and T. Keller (2017), Opportunities and future directions for visual soil evaluation methods in soil structure research, *Soil and Tillage Research*, *173*, 104–113, doi:10.1016/j.still.2017.01.016.

Gurevich, B., and J. M. Carcione (2000), Gassmann modeling of acoustic properties of sand-clay mixtures, *Pure and Applied Geophysics*, *157*(5), 811–827, doi:10.1007/PL00001119.

Håkansson, I., and J. Lipiec (2000), A review of the usefulness of relative bulk density values in studies of soil structure and compaction, *Soil and Tillage Research*, *53*(2), 71–85, doi:10.1016/S0167-1987(99)00095-1.

Håkansson, I., and R. C. Reeder (1994), Subsoil compaction by vehicles with high axle load—extent, persistence and crop response, *Soil and Tillage Research*, *29*(2), 277–304, doi:10.1016/0167-1987(94)90065-5.

Hamza, M. A., and W. K. Anderson (2005), Soil compaction in cropping systems: A review of the nature, causes and possible solutions, *Soil and Tillage Research*, *82*(2), 121–145, doi:10.1016/j.still.2004.08.009.

Hashin, Z., and S. Shtrikman (1963), A variational approach to the theory of the elastic behaviour of multiphase materials, *Journal of the Mechanics and Physics of Solids*, *11*(2), 127–140, doi:10.1016/0022-5096(63)90060-7.

Helliwell, J. R., C. J. Sturrock, K. M. Grayling, S. R. Tracy, R. J. Flaver, I. M. Young, W. R. Whalley, and S. J. Mooney (2013), Applications of X-ray computed tomography for examining biophysical interactions and structural development in soil systems: a review, *European Journal of Soil Science*, *64*(3), 279–297, doi:10.1111/ejss.12028.

Hirmas, D. R., D. Giménez, A. Nemes, R. Kerry, N. A. Brunsell, and C. J. Wilson (2018), Climate-induced changes in continental-scale soil macroporosity may intensify water cycle, *Nature*, *561*(7721), 100, doi:10.1038/s41586-018-0463-x.

Hobley, E. U., and B. Wilson (2016), The depth distribution of organic carbon in the soils of eastern australia, *Ecosphere*, *7*(1), doi:10.1002/ecs2.1214, e01214.

Holpp, M., T. Anken, J. Rek, R. Reiser, H. Oberholzer, P. Weisskopf, and O. Hensel (2010), Controlled traffic farming under Central European conditions., in *International Conference on Soil Mechanics and Geothecnical Engineering*.

Hubbard, S., and N. Linde (2011), Hydrogeophysics, in *Treatise on Water*, edited by P. Wilderer, chap. 2.15, pp. 401–434, Elsevier.

Ingeman-Nielsen, T., and F. Baumgartner (2006), CR1Dmod: A Matlab program to model 1D complex resistivity effects in electrical and electromagnetic surveys, *Computers & Geosciences*, *32*(9), 1411–1419.

Jarvis, N., J. Koestel, and M. Larsbo (2016), Understanding preferential flow in the vadose zone: recent advances and future prospects from pore to catchment scales, *Vadose Zone Journal*, *15*(12), doi:10.2136/vzj2016.09.0075.

Jayawickreme, D. H., E. G. Jobbágy, and R. B. Jackson (2014), Geophysical subsurface imaging for ecological applications, *New Phytologist*, *201*(4), 1170–1175, doi:10.1111/nph.12619.

Jensen, M. E., and H. R. Haise (1963), Estimating evapotranspiration from solar radiation, *Journal of the Irrigation and Drainage Division*, *89*, 15–41.

Johnson, D. L. (2001), Theory of frequency dependent acoustics in patchy-saturated porous media, *The Journal of the Acoustical Society of America*, *110*(2), 682–694, doi:10.1121/1.1381021.

Jonard, F., M. Mahmoudzadeh, C. Roisin, L. Weihermüller, F. André, J. Minet, H. Vereecken, and S. Lambot (2013), Characterization of tillage effects on the spatial variation of soil properties using ground-penetrating radar and electromagnetic induction, *Geoderma*, *207-208*, 310–322, doi:10.1016/j.geoderma.2013.05.024.

Jordanova, D., N. Jordanova, A. Atanasova, T. Tsacheva, and P. Petrov (2011), Soil tillage erosion estimated by using magnetism of soils - a case study from Bulgaria, *Environmental Monitoring Assessing*, *183*(1-4), 381–394, doi:10.1007/s10661-011-1927-8.

Jougnot, D., N. Linde, A. Revil, and C. Doussan (2012), Derivation of soil-specific streaming potential electrical parameters from hydrodynamic characteristics of partially saturated soils, *Vadose Zone Journal*, *11*(1), doi:10.2136/vzj2011.0086.

Jougnot, D., N. Linde, E. B. Haarder, and M. C. Looms (2015), Monitoring of saline tracer movement with vertically distributed self-potential measurements at the HOBE agricultural test site, Voulund, Denmark, *Journal of Hydrology*, *521*, 314–327, doi:10.1016/j.jhydrol.2014.11.041.

Keesstra, S. D., V. Geissen, K. Mosse, S. Piiranen, E. Scudiero, M. Leistra, and L. V. Schaik (2012), Soil as a filter for groundwater quality, in *Current Opinion in Environmental Sustainability*, chap. 4.5, pp. 507–516, doi:10.1016/j.cosust.2012.10.007.

Keller, T., M. Lamande, S. Peth, M. Berli, J. Delenne, W. Baumgarten, W. Rabbel, and F. Radjaı (2013a), An interdisciplinary approach towards improved understanding of soil deformation during compaction, *Soil and Tillage Research*, *128*, 61–80, doi:10.1016/j.still.2012.10.004.

Keller, T., M. Carizzoni, F. E. Berisso, M. Stettler, and M. Lamandé (2013b), Measuring the dynamic soil response during repeated wheeling using seismic methods, *Vadose Zone Journal*, *12*(3), 8830, doi:10.2136/vzj2013.01.0033.

Keller, T., T. Colombi, S. Ruiz, M. P. Manalili, J. Rek, V. Stadelmann, H. Wunderli, D. Breitenstein, R. Reiser, H. Oberholzer, S. Schymanski, A. Romero-Ruiz, N. Linde, P. Weisskopf, A. Walter, and D. Or (2017), Long-term Soil Structure Observatory for monitoring post-compaction evolution of soil structure, *Vadose Zone Journal*, *16*(4), doi:10.2136/vzj2016.11.0118.

Kemna, A., A. Binley, G. Cassiani, E. Niederleithinger, A. Revil, L. Slater, K. H. Williams, A. Flores Orozco, F.-h. Haegel, A. Hördt, S. Kruschwitz, V. Leroux, K. Titov, and E. Zimmermann (2012), An overview of the spectral induced polarization method for near-surface applications, *Near-Surface Geophysics*, *10*(6), 456–468, doi:10.3997/1873-0604.2012027.

Khalili, N., and M. Khabbaz (1998), A unique relationship of chi for the determination of the shear strength of unsaturated soils, *Geotechnique*, *48*(5), 681–7, doi:10.1680/geot.1998.48.5.681.

Kibblewhite, M. G., K. Ritz, and M. J. Swift (2008), Soil health in agricultural systems, *Biological Sciences*, *363*(1492), 685–701, doi:10.1098/rstb.2007.2178.

Klotzsche, A., F. Jonard, M. C. Looms, and J. V. D. Kruk (2018), Measuring soil water content with ground penetrating radar: a decade of progress, *Vadose Zone Journal*, *17*(1), doi:10.2136/vzj2018.03.0052.

Klute, A., and C. Dirksen (1986), *Hydraulic Conductivity and Diffusivity: Laboratory Methods*, chap. 28, pp. 687–734, John Wiley & Sons, Ltd, doi:https://doi.org/10.2136/sssabookser5.1.2ed.c28.

Koestel, J., A. Kemna, M. Javaux, A. Binley, and H. Vereecken (2008), Quantitative imaging of solute transport in an unsaturated and undisturbed soil monolith with 3-D ERT and TDR, *Water Resources Research*, *44*(12), doi:10.1029/2007WR006755.

Komatitsch, D., and R. Martin (2007), An unsplit convolutional perfectly matched layer improved at grazing incidence for the seismic wave equation, *Geophysics*, *72*(5), SM155–SM167, doi:10.1190/1.2757586.

Kowalsky, M. B., S. Finsterle, and Y. Rubin (2004), Estimating flow parameter distributions using ground-penetrating radar and hydrological measurements during transient flow in the vadose zone, *Advances in Water Resources*, *27*(6), 583–599, doi:10.1016/j.advwatres.2004.03.003.

Kramer, C., and G. Gleixner (2008), Soil organic matter in soil depth profiles: Distinct carbon preferences of microbial groups during carbon transformation, *Soil Biology and Biochemistry*, *40*(2), 425 – 433, doi:10.1016/j.soilbio.2007.09.016.

Kroener, E., M. Zarebanadkouki, A. Kaestner, and A. Carminati (2014), Nonequilibrium water dynamics in the rhizosphere: How mucilage affects water flow in soils, *Water Resources Research*, *50*(8), 6479–6495, doi:10.1002/2013WR014756.

Krueger, J., U. Franko, J. Fank, E. Stelzl, P. Dietrich, M. Pohle, and U. Werban (2013), Linking geophysics and soil function modeling - An application study for biomass production, *Vadose Zone Journal*, *12*(4), doi:10.2136/vzj2013.01.0015.

Kuhl, A. S., A. D. Kendall, R. L. V. Dam, and D. W. Hyndman (2018), Quantifying soil water and root dynamics using a coupled hydrogeophysical inversion, *Vadose Zone Journal*, *17*(1), doi:10.2136/vzj2017.08.0154.

Kutílek, M. (2004), Soil hydraulic properties as related to soil structure, *Soil and Tillage Research*, *79*(2), 175 – 184, doi:https://doi.org/10.1016/j.still.2004.07.006, soil Physical Quality.

Kyriakidis, P. C. (2004), A geostatistical framework for area-to-point spatial interpolation, *Geographical Analysis*, *36*(3), 259–289, doi:10.1111/j.1538-4632.2004.tb01135.x.

Laloy, E., and J. A. Vrugt (2012), High-dimensional posterior exploration of hydrologic models using multiple-try dream(zs) and high-performance computing, *Water Resources Research*, *48*(1), doi:10.1029/2011WR010608.

Lawrence, D. M., P. E. Thornton, K. W. Oleson, and G. B. Bonan (2007), The partitioning of evapotranspiration into transpiration, soil evaporation, and canopy evaporation in a gcm: Impacts on land–atmosphere interaction, *Journal of Hydrometeorology*, *8*(4), 862–880.

Lehmann, P., S. Assouline, and D. Or (2008), Characteristic lengths affecting evaporative drying of porous media, *Physical Review E*, *77*(5), 056,309.

Lehmann, P., O. Merlin, P. Gentine, and D. Or (2018), Soil texture effects on surface resistance to bare-soil evaporation, *Geophysical Research Letters*, *45*(19), 10–398.

Lehmann, P., S. Bickel, Z. Wei, and D. Or (2020), Physical constraints for improved soil hydraulic parameter estimation by pedotransfer functions, *Water Resources Research*, *56*(4), e2019WR025,963, doi:10.1029/2019WR025963, e2019WR025963 2019WR025963.

Lesmes, D., and S. Friedman (2005), Relationships between the electrical and hydrogeological properties of the rocks and soils, in *Hydrogeophysics*, edited by Y. Rubin and S. S. Hubbard, chap. 4, pp. 391–412, Springer.

Linde, N. (2014), Falsification and corroboration of conceptual hydrological models using geophysical data, *Wiley Interdisciplinary Reviews: Water*, *1*(2), 151–171, doi:10.1002/wat2.1011.

Linde, N., and J. Doetsch (2010), Joint inversion of crosshole GPR and seismic traveltime data joint inversion of crosshole GPR and seismic traveltime data, in *Advances in near-surface seismology and ground-penetrating Radar*, chap. 1, pp. 1–18, doi:10.1190/1.9781560802259.ch1.

Linde, N., and J. Doetsch (2016), Joint Inversion in hydrogeophysics and near-surface geophysics, in *Integrated Imaging of the Earth: Theory and Applications*, edited by M. Moorkamp, P. G. Lelièvre, N. Linde, and A. Khan, chap. 7, pp. 119–135, John Wiley & Sons, Inc., New Jersey.

Linde, N., A. Binley, A. Tryggvason, L. B. Pedersen, and A. Revil (2006), Improved hydrogeophysical characterization using joint inversion of cross-hole electrical resistance and ground-penetrating radar traveltime data, *Water Resources Research*, *42*(12), doi:10.1029/2006WR005131.

Lu, N., J. W. Godt, and D. T. Wu (2010), A closed-form equation for effective stress in unsaturated soil, *Water Resources Research*, *46*(5), doi:10.1029/2009WR008646.

Lu, P., M. Morris, S. Brazell, C. Comiskey, and Y. Xiao (2018), Using generative adversarial networks to improve deep-learning fault interpretation networks, *The Leading Edge*, *37*(8), 578–583, doi:10.1190/tle37080578.1.

Lu, Z. (2011), Feasibility of using a seismic surface wave method to study seasonal and weather effects on shallow surface soils, *Journal of Environmental & Engineering Geophysics*, *19*(2), 71–85, doi:10.2113/JEEG19.2.71.

Lu, Z., and J. M. Sabatier (2009), Effects of soil water potential and moisture content on sound speed, *Soil Science Society of America Journal*, *73*(5), 1614–1625, doi:10.2136/sssaj2008.0073.

Lu, Z., C. J. Hickey, and J. M. Sabatier (2004), Effects of compaction on the acoustic velocity in soils, *Soil Science Society of America Journal*, *68*(1), 7–16, doi:10.2136/sssaj2004.0007.

Lunne, T., J. J. Powell, and P. K. Robertson (1997), *Cone-penetration testing in geotechnical practice*, 352 pp., CRC Press, London, doi:10.1007/s11204-010-9072-x.

Lunt, I. A., S. S. Hubbard, and Y. Rubin (2005), Soil moisture content estimation using ground-penetrating radar reflection data, *Journal of Hydrology*, *307*(1-4), 254–269, doi:10.1016/j.jhydrol.2004.10.014.

Mandal, T., J. M. Tinjum, and T. B. Edil (2016), Non-destructive testing of cementitiously stabilized materials using ultrasonic pulse velocity test, *Transportation Geotechnics*, *6*, 97–107, doi:10.1016/j.trgeo.2015.09.003.

Manegold, E., and W. von Engelhardt (1933), Über kapillar-systeme, xii (4). die berechnung des stoffgehaltes heterogener gerüststrukturen, *Kolloid-Zeitschrift*, *63*(2), 149–154.

Markov, M., V. Levine, A. Mousatov, and E. Kazatchenko (2005), Elastic properties of double-porosity rocks using the differential effective medium model, *Geophysical Prospecting*, *53*(5), 733–754, doi:10.1111/j.1365-2478.2005.00498.x.

Márquez, C., V. Garcia, C. A. Cambardella, R. C. Schultz, and T. M. Isenhart (2004), Aggregate-size stability distribution and soil stability, *Soil Science Society of America Journal*, *68*(3), 725–735, doi:10.2136/sssaj2004.7250.

Martínez, I., A. Chervet, P. Weisskopf, W. G. Sturny, J. Rek, and T. Keller (2016), Two decades of no-till in the oberacker long-term field experiment: Part ii. soil porosity and gas transport parameters, *Soil and Tillage Research*, *163*, 130 – 140, doi:https://doi.org/10.1016/j.still.2016.05.020.

Mavko, G., T. Mukerji, and J. Dvorkin (2009), *The Rock Physics Handbook: Tools for Seismic Analysis of Porous Media*, second ed., Cambridge University Press.

Maximilian, J., S. Köhne, and Š. Jirka (2009), A review of model applications for structured soils : a) Water flow and tracer transport, *Journal of Contaminant Hydrology*, *104*(1-4), 4–35, doi:10.1016/j.jconhyd.2008.10.002.

Mayne, P. W., and G. J. Rix (1993), $G_{max} - qc$ relationships for clays, *Geotechnical Testing Journal*, *16*(1), 54–60.

Mayne, P. W., J. a. Schneider, and G. K. Martin (1999), Small-and large-strain soil properties from seismic flat dilatometer tests, in *Proc. 2nd Int. Symp. on Pre-Failure Deformation Characteristics of Geomaterials*, pp. 419–427.

McCarter, W. J. (1984), The electrical resistivity characteristics of compacted clays, *Géotechnique*, *34*(2), 263–267, doi:10.1680/geot.1984.34.2.263.

Menke, W. (2012), *Geophysical Data Analysis: Discrete Inverse Theory: MATLAB edition*, vol. 45, third ed., Academic press, Boston.

Mertens, J., H. Madsen, M. Kristensen, D. Jacques, and J. Feyen (2005), Sensitivity of soil parameters in unsaturated zone modelling and the relation between effective, laboratory and in situ estimates, *Hydrological Processes*, *19*(8), 1611–1633, doi:https://doi.org/10.1002/hyp.5591.

Meurer, K., J. Barron, C. Chenu, E. Coucheney, M. Fielding, P. Hallett, A. M. Herrmann, T. Keller, J. Koestel, M. Larsbo, E. Lewan, D. Or, D. Parsons, N. Parvin, A. Taylor, H. Vereecken, and N. Jarvis (2020), A framework for modelling soil structure dynamics induced by biological activity, *Global Change Biology*, *26*(10), 5382–5403, doi:https://doi.org/10.1111/gcb.15289.

Michot, D. (2003), Spatial and temporal monitoring of soil water content with an irrigated corn crop cover using surface electrical resistivity tomography, *Water Resources Research*, *39*(5), 1–20, doi:10.1029/2002WR001581.

Moysey, S. M. J., and Z. Liu (2012), Can the onset of macropore flow be detected using electrical resistivity measurements?, *Soil Science Society of America Journal*, *76*(1), 10–17, doi:10.2136/sssaj2010.0413.

Mualem, Y. (1976), A new model for predicting the hydraulic conductivity of unsaturated porous media, *Water Resources Research*, *12*(3), 513–522, doi:10.1029/WR012i003p00513.

Muñiz, E., R. K. Shaw, D. Gimenez, C. A. Williams, and L. Kenny (2016), Use of ground-penetrating radar to determine depth to compacted layer in soils under pasture, in *Digital Soil Morphometrics*, edited by A. Hartemink and B. Minasny, springer ed., pp. 411–421, Cham, doi:10.1007/978-3-319-28295-4_26.

Munkholm, L. (2000), *The spade analysis - a modification of the qualitative spade diagnosis for scientific use*, no. 28 in DIAS-report, Plant Production, Danish Institute of Agricultural Sciences.

Naveed, M., P. Moldrup, M. G. Schaap, M. Tuller, and R. Kulkarni (2016), Prediction of biopore- and matrix-dominated flow from X-ray CT-derived macropore network characteristics, *Hydrology and Earth System Sciences*, *20*(10), 4017–4030, doi:10.5194/hess-20-4017-2016.

Nawaz, M. F., G. Bourrié, and F. Trolard (2013), Soil compaction impact and modelling. A review, *Agronomy for Sustainable Development*, *33*(2), 291–309, doi:10.1007/s13593-011-0071-8.

Nelson, P. H. (1994), Permeability-porosity relationships in sedimentary rocks, *The Log Analyst*, *35*(03), 38–62.

Nuth, M., and L. Laloui (2008), Effective stress concept in unsaturated soils: Clarification and validation of a unified framework, *International Journal for Numerical and Analytical Methods in Geomechanics*, *32*(7), 771–801, doi:10.1002/nag.645.

Oades, J. M. (1993), The role of biology in the formation, stabilization and degradation of soil structure, *Geoderma*, *56*, 377–400, doi:10.1016/B978-0-444-81490-6.50033-9.

Oertel, C., J. Matschullat, K. Zurba, F. Zimmermann, and S. Erasmi (2016), Greenhouse gas emissions from soils - A review, *Chemie der Erde - Geochemistry*, *76*(3), 327–352, doi:10.1016/j.chemer.2016.04.002.

Oldeman, L. R. (1992), Global extent of soil degradation, in *Bi-Annual Report 1991-1992/ISRIC*, pp. 19–36, ISRIC.

Oleghe, E., M. Naveed, E. M. Baggs, and P. D. Hallett (2017), Plant exudates improve the mechanical conditions for root penetration through compacted soils, *Plant and Soil*, *421*(1-2), 19–30, doi:10.1007/s11104-017-3424-5.

Or, D. (1996), Wetting-induced soil structural changes: The theory of liquid phase sintering, *Water Resources Research*, *32*(10), 3041–3049, doi:10.1029/96WR02279.

Or, D. (2020), The tyranny of small scales—on representing soil processes in global land surface models, *Water Resources Research*, *56*(6), doi:https://doi.org/10.1029/2019WR024846.

Or, D., and T. A. Ghezzehei (2002), Modeling post-tillage soil structural dynamics: a review, *Soil and Tillage Research*, *64*(1-2), 41–59, doi:10.1016/S0167-1987(01)00256-2.

Or, D., and P. Lehmann (2019), Surface evaporative capacitance: How soil type and rainfall characteristics affect global-scale surface evaporation, *Water Resources Research*, *55*(1), 519–539, doi:10.1029/2018WR024050.

Or, D., and J. M. Wraith (1999), Temperature effects on soil bulk dielectric permittivity measured by time domain reflectometry: A physical model, *Water Resources Research*, *35*(2), 371–383.

Or, D., P. Lehmann, E. Shahraeeni, and N. Shokri (2013), Advances in soil evaporation physics — A Review, *Vadose Zone Journal*, *12*(4), doi:10.2136/vzj2012.0163.

Or, D., T. Keller, and W. H. Schlesinger (2021), Natural and managed soil structure: On the fragile scaffolding for soil functioning, *Soil and Tillage Research*, *208*, 104,912, doi:https://doi.org/10.1016/j.still.2020.104912.

Park, C. B., R. D. Miller, and H. Miura (2002), Optimum field parameters of an MASW survey, *Japanese Society of Exploration Geophysics (SEG-J) Extended Abstracts (22-23 May 2002). Tokyo, Japan*.

Park, C. B., R. D. Miller, J. Xia, and J. Ivanov (2007), Multichannel analysis of surface waves (MASW) - active and passive methods, *The Leading Edge*, *26*(1), 60–64, doi:10.1190/1.2431832.

Parker, R. L. (1984), The inverse problem of resistivity sounding, *Geophysics*, *49*(12), 2143–2158.

Parsekian, A. D., K. Singha, B. J. Minsley, W. S. Holbrook, and L. Slater (2015), Multiscale geophysical imaging of the critical zone, *Reviews of Geophysics*, *53*(1), 1–26, doi:10.1002/2014RG000465.

Pasquet, S., W. Holbrook, B. Carr, and K. Sims (2016), Geophysical imaging of shallow degassing in a yellowstone hydrothermal system, *Geophysical Research Letters*, *43*(23), 12–027, doi:10.1002/2016GL071306.

Peng, X., and R. Horn (2008), Time-dependent, anisotropic pore structure and soil strength in a 10-year period after intensive tractor wheeling under conservation and conventional tillage, *Journal of Plant Nutrition and Soil Science*, *171*(6), 936–944, doi:10.1002/jpln.200700084.

Perdok, U., B. Kroesbergen, and W. Hoogmoed (2002), Possibilities for modelling the effect of compression on mechanical and physical properties of various Dutch soil types, *Soil and Tillage Research*, *65*(1), 61–75, doi:10.1016/S0167-1987(01)00277-X.

Perroux, K. M., and I. White (1988), Designs for disc permeameters, *Soil Science Society of America Journal*, *52*(5), 1205–1215, doi:https://doi.org/10.2136/sssaj1988.03615995005200050001x.

Petersen, H., H. Fleige, W. Rabbel, and R. Horn (2005), Applicability of geophysical prospecting methods for mapping soil compaction variability of soil texture on farm land, *Journal of Plant Nutrition and Soil Science*, *168*(1), 68–79, doi:10.1002/jpln.200421282.

Porwollik, V., S. Rolinski, J. Heinke, and C. Müller (2019), Generating a rule-based global gridded tillage dataset, *Earth System Science Data*, *11*(2), 823–843, doi:10.5194/essd-11-823-2019.

Pride, S. (2005), Relationships between seismic and hydrological properties, in *Hydrogeophysics*, edited by Y. Rubin and S. S. Hubbard, chap. 9, Dordrecht.

Rabot, E., M. Wiesmeier, S. Schlüter, and H. Vogel (2018), Soil structure as an indicator of soil functions : A review, *Geoderma*, *314*, 122–137, doi:10.1016/j.geoderma.2017.11.009.

Ramankutty, N., A. T. Evan, C. Monfreda, and J. A. Foley (2008), Farming the planet: 1. geographic distribution of global agricultural lands in the year 2000, *Global Biogeochemical Cycles*, *22*(1), doi:https://doi.org/10.1029/2007GB002952.

Rapstine, T., P. Sava, and E. Arias (2017), Airbone seismic data acquisition using stereo vision, *Journal of Unmanned Vehicle Systems*, *6*(1), 31–42, doi:10.1139/juvs-2017-0019.

Reuss, A. (1929), Berechnung der fließgrenze von mischkristallen auf grund der plastizitätsbedingung für einkristalle., *ZAMM-Journal of Applied Mathematics and Mechanics/Zeitschrift für Angewandte Mathematik und Mechanik*, *9*(1), 49–58.

Revil, A., and L. M. Cathles (1999), Permeability of shaly sands, *Water Resources Research*, *35*(3), 651–662.

Revil, A., M. Karaoulis, T. Johnson, and A. Kemna (2012), Review: Some low-frequency electrical methods for subsurface characterization and monitoring in hydrogeology, *Hydrogeology Journal*, *20*(4), 617–658, doi:10.1007/s10040-011-0819-x.

Revil, A., A. Coperey, Z. Shao, N. Florsch, I. Fabricius, Y. Deng, J. Delsman, P. Pauw, M. Karaoulis, P. de Louw, E. van Baaren, W. Dabekaussen, A. Menkovic, and J. Gunnink (2017), Complex conductivity of soils, *53*, 7121–7147.

Rhoades, J. D., P. A. C. Raats, and R. J. Prather (1976), Effects of liquid-phase electrical conductivity, water content, and surface conductivity on bulk soil electrical conductivity, *Soil Science Society of America Journal*, *40*(5), 651–655, doi:10.2136/sssaj1976.03615995004000050017x.

Rhoades, J. D., N. A. Manteghi, P. J. Shouse, and W. J. Alves (1989), Soil electrical conductivity and soil salinity: New formulations and calibrations, *Soil Science Society of America Journal*, *53*(2), 433–439, doi:10.2136/sssaj1989.03615995005300020020x.

Richard, G., I. Cousin, J. F. Sillon, A. Bruand, and J. Guérif (2001), Effect of compaction on the porosity of a silty soil: influence on unsaturated hydraulic properties, *European Journal of Soil Science*, *52*(1), 49–58, doi:10.1046/j.1365-2389.2001.00357.x.

Richards, L. A. (1931), Capillary conduction of liquids through porous mediums, *Physics*, *1*(5), 318–333.

Robinson, D. A., A. Binley, N. Crook, T. P. A. Ferr, and V. J. S. Grauch (2008), Advancing process-based watershed hydrological research using near-surface geophysics: a vision for, and review of, electrical and magnetic geophysical methods, *Hydrological Processes*, *22*(18), 3604–3635, doi:10.1002/hyp.6963.

Romero-Ruiz, A., N. Linde, T. Keller, and D. Or (2018), A review of geophysical methods for soil structure characterization, *Reviews of Geophysics*, *56*(4), 672–697, doi:10.1029/2018RG000611.

Romero-Ruiz, A., N. Linde, L. Baron, S. G. Solazzi, T. Keller, and D. Or (2021), Seismic Signatures Reveal Persistence of Soil Compaction, submitted to Vadose Zone Journal.

Rosas-Carbajal, M., J.-C. Komorowski, F. Nicollin, and D. Gibert (2016), Volcano electrical tomography unveils edifice collapse hazard linked to hydrothermal system structure and dynamics, *Scientific Reports*, *6*(1), 1–11.

Rossi, R., M. Amato, A. Pollice, G. Bitella, J. J. Gomes, R. Bochicchio, and S. Baronti (2013a), Electrical resistivity tomography to detect the effects of tillage in a soil with a variable rock fragment content, *European Journal of Soil Science*, *64*(2), 239–248, doi:10.1111/ejss.12024.

Rossi, R., A. Pollice, M. P. Diago, M. Oliveira, B. Millan, G. Bitella, M. Amato, and J. Tardaguila (2013b), Using an automatic resistivity profiler soil sensor on-the-go in precision viticulture, *Sensors*, *13*(1), 1121–1136, doi:10.3390/s130101121.

Roth, K., R. Schulin, H. Fluhler, and W. Attinger (1990), Calibration of Time Domain Reflectometry for water content measurement using a composite dielectric approach, *Water Resources Research*, *26*(10), 2267–2273, doi:10.1029/WR026i010p02267.

Rubino, J. G., E. Caspari, T. M. Müller, M. Milani, N. D. Barbosa, and K. Holliger (2016), Numerical upscaling in 2-D heterogeneous poroelastic rocks: Anisotropic attenuation and dispersion of seismic waves, *Journal of Geophysical Research*, *121*, 6698–6721, doi:10.1002/2016JB013165.

Rücker, C., and T. Günther (2011), The simulation of finite ERT electrodes using the complete electrode model, *Geophysics*, *76*(4), F227–F238, doi:10.1190/1.3581356.

Rücker, C., T. Günther, and K. Spitzer (2006a), Three-dimensional modelling and inversion of dc resistivity data incorporating topography - I. Modelling, *Geophysical Journal International*, *166*(2), 495–505, doi:10.1111/j.1365-246X.2006.03010.x.

Rücker, C., T. Günther, and K. Spitzer (2006b), Three-dimensional modelling and inversion of dc resistivity data incorporating topography - I. Modelling, *Geophysical Journal International*, *166*(2), 495–505, doi:10.1111/j.1365-246X.2006.03010.x.

Ruiz, S., D. Or, and S. J. Schymanski (2015), Soil penetration by earthworms and plant roots-mechanical energetics of bioturbation of compacted soils, *PLOS One*, *10*(6), e0128,914, doi:10.1371/journal.pone.0128914.

Ryden, N., and M. J. S. Lowe (2004), Guided wave propagation in three-layer pavement structures, *The Journal of the Acoustical Society of America*, *116*(5), 2902–2913, doi:10.1121/1.1808223.

Ryden, N., and C. B. Park (2006), Fast simulated annealing inversion of surface waves on pavement using phase-velocity spectra, *Geophysics*, *71*(4), R49–R58, doi:10.1190/1.2204964.

Sabba, N., and O. Uyanik (2017), Prediction of reinforced concrete strength by ultrasonic velocities, *Journal of Applied Geophysics*, *141*, 13–23, doi:10.1016/j.jappgeo.2017.04.005.

Sakaguchi, A., T. Nishimura, and M. Kato (2005), The effect of entrapped air on the quasi-saturated soil hydraulic conductivity and comparison with the unsaturated hydraulic conductivity, *Vadose Zone Journal*, *4*(1), 139–144, doi:10.2136/vzj2005.0139.

Samouelian, A., I. Cousin, A. Tabbagh, A. Bruand, and G. Richard (2005), Electrical resistivity survey in soil science: A review, *Soil and Tillage Research*, *83*(2), 173–193, doi:10.1016/j.still.2004.10.004.

Schjønning, P., J. J. H. van den Akker, T. Keller, M. H. Greve, M. Lamandé, A. Simojoki, M. Stettler, J. Arvidsson, and H. Breuning-Madsen (2015), Driver-Pressure-State-Impact-Response (DPSIR) analysis and risk assessment for soil compaction-A European perspective, in *Advances in Agronomy*, vol. 133, edited by D. Sparks and S. Hallock, chap. Chapter 5, pp. 183–237, Elsevier, doi:10.1016/bs.agron.2015.06.001.

Schlüter, S., A. Sheppard, K. Brown, and D. Wildenschild (2014), Image processing of multiphase images obtained via X-ray microtomography: A review, *Water Resources Research*, *50*(4), 3615–3639, doi:10.1002/2014WR015256.

Schmitt, D. R. (2015), Geophysical properties of the near surface earth: Seismic properties, in *Treatise on Geophysics*, edited by L. Slater, pp. 43–87, Elsevier B.V., doi:10.1016/B978-0-444-53802-4.00190-1.

Séger, M., I. Cousin, A. Frison, H. Boizard, and G. Richard (2009), Characterisation of the structural heterogeneity of the soil tilled layer by using in situ 2D and 3D electrical resistivity measurements, *Soil and Tillage Research*, *103*(2), 387–398, doi:10.1016/j.still.2008.12.003.

Seladji, S., P. Cosenza, A. Tabbagh, J. Ranger, and G. Richard (2010), The effect of compaction on soil electrical resistivity: a laboratory investigation, *European Journal of Soil Science*, *61*(6), 1043–1055, doi:10.1111/j.1365-2389.2010.01309.x.

Sen, P. N. (1997), Resistivity of partially saturated carbonate rocks with microporosity, *Geophysics*, *62*(2), 415–425, doi:10.1190/1.1444152.

Sen, P. N., C. Scala, and M. H. Cohen (1981), A self-similar model for sedimentary rocks with application to the dielectric constant of fused glass beads, *Geophysics*, *46*(5), 781–795, doi:10.1190/1.1441215.

Shen, C. (2018), A trans-disciplinary review of deep learning research and its relevance for water resources scientists, *Water Resources Research*, *54*, doi:10.1029/2018WR022643.

Shen, J., J. M. Crane, J. M. Lorenzo, and C. D. White (2016), Seismic velocity prediction in shallow (< 30 m) partially saturated, unconsolidated sediments using effective medium theory, *Journal of Environmental and Engineering Geophysics*, *21*(2), 67–78, doi:10.2113/JEEG21.2.67.

Shin, H., W. R. Whalley, K. Attenborough, and S. Taherzadeh (2016), On the theory of Brutsaert about elastic wave speeds in unsaturated soils, *Soil and Tillage Research*, *156*, 155–165, doi:10.1016/j.still.2015.10.006.

Sihvola, A. (1999), *Electromagnetic mixing formulas and applications*, The Institution of Engineering and Technology, London.

Simunek, J., a. M. Šejna, H. Saito, M. Sakai, and M. T. V. Genuchten (2013), The HYDRUS-1D Software Package for Simulating the Movement of Water, Heat, and Multiple Solutes in Variably Saturated Media, Version 4.17, HYDRUS Software Series 3,, (June), 343.

Skalinski, M., and J. A. M. Kenter (2014), Carbonate petrophysical rock typing : Integrating geological attributes and petrophysical properties while linking with dynamic behaviour, *Geological Society, London, Special Publications*, *406*, SP406–6, doi:10.1144/SP406.6.

Slater, L. (2007), Near surface electrical characterization of hydraulic conductivity: from petrophysical properties to aquifer geometries - A review, *Surveys in Geophysics*, *28*(2-3), 169–197, doi:10.1007/s10712-007-9022-y.

Slater, L. D., and D. Lesmes (2002), IP interpretation in environmental investigations, *Geophysics*, *67*(1), 77, doi:10.1190/1.1451353.

Socco, L. V., S. Foti, and D. Boiero (2010), Surface-wave analysis for building near-surface velocity models — Established approaches and new perspectives, *Geophysics*, *75*(5).

Steduto, P., T. C. Hsiao, and E. Fereres (2007), On the conservative behavior of biomass water productivity, *Irrigation Science*, *25*(3), 189–207.

Steeples, D. W. (2005), Shallow seismic methods, in *Hydrogeophysics*, edited by Y. Rubin and S. Hubbard, chap. 8, pp. 215–251, Springer, Dordrecht.

Stemland, H. M., T. A. Johansen, and B. O. Ruud (2020), Potential use of time-lapse surface seismics for monitoring thawing of the terrestrial arctic, *Applied Sciences*, *10*(5), 1875, doi:10.3390/app10051875.

Stewart, B., S. Jalota, S. Kay, S. Komarneni, P. Malla, E. Murad, S. Prihar, and M. Summer (1990), *Advances in Soil Science*, Springer, New York.

Stirzaker, R., J. B. Passioura, and Y. Wilms (1996), Soil structure and plant growth : Impact of bulk density and biopores, *Plant and Soil*, (1988), 151–162.

Straubhaar, J., P. Renard, and G. Mariethoz (2016), Conditioning multiple-point statistics simulations to block data, *Spatial Statistics*, *16*, 53–71, doi:10.1016/j.spasta.2016.02.005.

Sudduth, K. A., N. R. Kitchen, W. J. Wiebold, W. D. Batchelor, G. A. Bollero, D. G. Bullock, D. E. Clay, H. L. Palm, F. J. Pierce, R. T. Schuler, and K. D. Thelen (2005), Relating apparent electrical conductivity to soil properties across the north-central USA, *Computers and Electronics in Agriculture*, *46*(1-3), 263–283, doi:10.1016/j.compag.2004.11.010.

Tabbagh, A., M. Dabas, A. Hesse, and C. Panissod (2000), Soil resistivity: a non-invasive tool to map soil structure horizonation, *Geoderma*, *97*(3-4), 393–404, doi:10.1016/S0016-7061(00)00047-1.

Telford, W. M., P. L. Geldart, and R. E. Sheriff (1990), *Applied Geophysics*, Cambridge University Press.

Toll, D., J. Mendes, D. Gallipoli, S. Glendinning, and P. Hughes (2012), Investigating the impacts of climate change on slopes: field measurements, *Geological Society, London, Engineering Geology Special Publications*, *26*(1), 151–161, doi:10.1144/EGSP26.17.

Topp, G. C., J. L. Davis, and A. P. Annan (1980), Electromagnetic determination of soil water content: measurements in coaxial transmission lines, *Water Resources Research*, *16*(3), 574–582, doi:10.1029/WR016i003p00574.

Tran, A. P., B. Dafflon, S. S. Hubbard, M. B. Kowalsky, P. Long, T. K. Tokunaga, and K. H. Williams (2016), Quantifying shallow subsurface water and heat dynamics using coupled hydrological-thermal-geophysical inversion, *Hydrology and Earth System Sciences*, *20*(9), 3477–3491, doi:10.5194/hess-20-3477-2016.

Tran, A. P., B. Dafflon, and S. S. Hubbard (2017), Coupled land surface – subsurface hydrogeophysical inverse modeling to estimate soil organic carbon content and explore associated hydrological and thermal dynamics in the Arctic tundra, *The Cryosphere*, pp. 2089–2109.

Tuller, M., and D. Or (2002), Preferential flow in structured soils- hydraulic functions derived from pore-scale processes, in *Proceedings of the 17th World Congress of Soil Science*, CONF, pp. 41–51.

Uyanik, O. (2010), Compressional and shear-wave velocity measurements in unconsolidated top-soil and comparison of the results, *International Journal of Physical Sciences*, *5*(7), 1034–1039, doi:10.5897/IJPS.

Uyanik, O. (2011), The porosity of saturated shallow sediments from seismic compressional and shear wave velocities, *Journal of Applied Geophysics*, *73*(1), 16 – 24, doi:https://doi.org/10.1016/j.jappgeo.2010.11.001.

Uyanik, O., and E. U. Ulugergerli (2008), Quality control of compacted grounds using seismic velocities, *Near Surface Geophysics*, *6*(5), 299–306, doi:https://doi.org/10.3997/1873-0604.2008004.

van Genuchten, M. T. (1980), A closed-form equation for predicting the hydraulic conductivity of unsaturated soils1, *Soil Science Society of America Journal*, *44*(5), 892, doi:10.2136/sssaj1980.03615995004400050002x.

Van Genuchten, M. T. (1987), A numerical model for water and solute movernent in and bellow the root zone, unpublished Research Report.

Van Looy, K., J. Bouma, M. Herbst, J. Koestel, B. Minasny, U. Mishra, C. Montzka, A. Nemes, Y. A. Pachepsky, J. Padarian, M. G. Schaap, B. Tóth, A. Verhoef, J. Vanderborght, M. J. van der Ploeg, L. Weihermüller, S. Zacharias, Y. Zhang, and H. Vereecken (2017), Pedotransfer functions in Earth system science: Challenges and perspectives, *Reviews of Geophysics*, *55*, 1199–1256, doi:10.1002/2017RG000581.

Vereecken, H., R. Kasteel, and T. Harter (2007), Upscaling hydraulic properties and soil water flow processes in heterogeneous soils, *Vadose Zone Journal*, *6*(1), 1–28, doi:10.2136/vzj2006.0055.

Vereecken, H., A. Schnepf, J. Hopmans, M. Javaux, D. Or, T. Roose, J. Vanderborght, M. Young, W. Amelung, M. Aitkenhead, S. Allison, S. Assouline, P. Baveye, M. Berli, N. Brüggemann, P. Finke, M. Flury, T. Gaiser, G. Govers, T. Ghezzehei, P. Hallett, and K. Lamorski (2016), Modeling soil processes: review, key challenges and new perspectives, *Vadose Zone Journal*, *15*(5), doi:10.2136/vzj2015.09.0131.

Wang, P., Z. Hu, Y. Zhao, and X. Li (2016), Experimental study of soil compaction effects on GPR signals, *Journal of Applied Geophysics*, *126*, 128–137, doi:10.1016/j.jappgeo.2016.01.019.

Wang, Z., H. Wang, and M. E. Cates (2001), Effective elastic properties of solid clays, *Geophysics*, *66*(2), 428–440, doi:10.1190/1.1444934.

Wathelet, M., J.-L. Chatelain, C. Cornou, G. D. Giulio, B. Guillier, M. Ohrnberger, and A. Savvaidis (2020), Geopsy: A user-friendly open-source tool set for ambient vibration processing, *Seismological Research Letters*, *91*(3), 1878–1889, doi:10.1785/0220190360.

Waxman, M. H., and L. J. M. Smits (1968), Electrical conductivities in oil-bearing shaly sands, *Society of Petroleum Engineers Journal*, *8*(02), 107–122, doi:10.2118/1863-A.

Webb, R. H. (2002), Recovery of severely compacted soils in the Mojave Desert, California, USA, *Arid Land Research and Management*, *15*(3), 291–305, doi:10.1080/153249802760284829.

Weller, A., L. Slater, and S. Nordsiek (2013), On the relationship between induced polarization and surface conductivity: Implications for petrophysical interpretation of electrical measurements, *Geophysics*, *78*(5), D315–D325.

Whiteley, J., J. Chambers, S. Uhlemann, P. Wilkinson, and J. Kendall (2019), Geophysical monitoring of moisture-induced landslides: a review, *Reviews of Geophysics*, *57*(1), 106–145.

Whiteley, J., J. Chambers, S. Uhlemann, J. Boyd, M. Cimpoiasu, J. Holmes, C. Inauen, A. Watlet, L. Hawley-Sibbett, C. Sujitapan, et al. (2020), Landslide monitoring using seismic refraction tomography–the importance of incorporating topographic variations, *Engineering Geology*, *268*, 105,525.

Whitmore, A. P., G. J. D. Kirk, and B. G. Rawlins (2015), Technologies for increasing carbon storage in soil to mitigate climate change, *Soil Use and Management*, *31*(S1), 62–71, doi: https://doi.org/10.1111/sum.12115.

Wu, Y., S. Nakagawa, T. J. Kneafsey, B. Dafflon, and S. Hubbard (2017), Electrical and seismic response of saline permafrost soil during freeze-thaw transition, *Journal of Applied Geophysics*, *146*, 16–26, doi:10.1016/j.jappgeo.2017.08.008.

Wunderlich, T., T. Petersen, S. Attia al Hagrey, and W. Rabbel (2013), Pedophysical models for resistivity and permittivity of partially water-saturated soils, *Vadose Zone Journal*, *12*(4), doi:10.2136/vzj2013.01.0023.

Xia, J., R. D. Miller, C. B. Park, J. A. Hunter, and J. B. Harris (2000), Comparing shear-wave velocity profiles from MASW with borehole measurements in unconsolidated sediments, Fraser River Delta, BC, Canada, *Journal of Environmental & Engineering Geophysics*, *5*(3), 1–13, doi:10.4133/JEEG5.3.1.

Young, I. M., E. Blanchart, C. Chenu, M. Dangerfield, C. Fragoso, M. Grimaldi, J. Ingram, and L. J. Monrozier (1998), The interaction of soil biota and soil structure under global change, *Global Change Biology*, *4*(7), 703–712, doi:10.1046/j.1365-2486.1998.00194.x.

Yunmin, C., K. Han, and C. Ren-peng (2005), Correlation of shear wave velocity with liquefaction resistance based on laboratory tests, *Soil Dynamics and Earthquake Engineering*, *25*, 461–469, doi:10.1016/j.soildyn.2005.03.003.

Zakri, T., J.-p. Laurent, and M. Vauclin (1998), Theoretical evidence for ' Lichtenecker ' s mixture formulae ' based on the effective medium theory, *Physics D: Applied Physics1*, *31*(13), 1589, doi:10.1088/0022-3727/31/13/013.

Zhang, W., T. H. Ricketts, C. Kremen, K. Carney, and S. M. Swinton (2007), Ecosystem services and dis-services to agriculture, *Ecological Economics*, *64*(2), 253–260, doi:10.1016/j.ecolecon.2007.02.024.

Zuo, Q., J. Shi, Y. Li, and R. Zhang (2006), Root length density and water uptake distributions of winter wheat under sub-irrigation, *Plant and Soil*, *285*(1/2), 45–55.

Appendix A

Long-term soil structure observatory for monitoring post-compaction evolution of soil structure

Thomas Keller, Tino Colombi, Siul Ruiz, Mervin Pogs Manalili, Jan Rek, Viktor Stadelmann, Hans Wunderli, Dani Breitenstein, René Reiser, Hansrudolf Oberholzer, Stanislaus Schymanski, Alejandro Romero-Ruiz, Niklas Linde, Peter Weisskopf, Achim Walter, and Dani Or.

Published[1] in *Vadose Zone Journal*

[1]Keller et al. (2017). Long-term soil structure observatory for monitoring post-compaction evolution of soil structure. *Vadose Zone Journal*, **16**(4) 1-16, doi:10.2136/vzj2016.11.0118

Published April 13, 2017

Original Research

Long-Term Soil Structure Observatory for Monitoring Post-Compaction Evolution of Soil Structure

Thomas Keller,* Tino Colombi, Siul Ruiz, Mervin Pogs Manalili, Jan Rek, Viktor Stadelmann, Hans Wunderli, Dani Breitenstein, René Reiser, Hansrudolf Oberholzer, Stanislaus Schymanski, Alejandro Romero-Ruiz, Niklas Linde, Peter Weisskopf, Achim Walter, and Dani Or

The projected intensification of agriculture to meet food targets of a rapidly growing world population are likely to accentuate already acute problems of soil compaction and deteriorating soil structure in many regions of the world. The key role of soil structure for soil functions, the sensitivity of soil structure to agronomic management practices, and the lack of reliable observations and metrics for soil structure recovery rates after compaction motivated the establishment of a long-term Soil Structure Observatory (SSO) at the Agroscope research institute in Zürich, Switzerland. The primary objective of the SSO is to provide long-term observation data on soil structure evolution after disturbance by compaction, enabling quantification of compaction recovery rates and times. The SSO was designed to provide information on recovery of compacted soil under different post-compaction soil management regimes, including natural recovery of bare and vegetated soil as well as recovery with and without soil tillage. This study focused on the design of the SSO and the characterization of the pre- and post-compaction state of the field. We deployed a monitoring network for continuous observation of soil state variables related to hydrologic and biophysical functions (soil water content, matric potential, temperature, soil air O_2 and CO_2 concentrations, O_2 diffusion rates, and redox states) as well as periodic sampling and in situ measurements of infiltration, mechanical impedance, soil porosity, gas and water transport properties, crop yields, earthworm populations, and plot-scale geophysical measurements. Besides enabling quantification of recovery rates of compacted soil, we expect that data provided by the SSO will help improve our general understanding of soil structure dynamics.

Core Ideas

- We provide long-term data on soil structure evolution following compaction.
- Treatments with and without plants and with and without tillage are included.
- Monitoring includes soil physical and biological properties and crop measures.
- Compaction decreased fluid transport capability and increased mechanical impedance.

T. Keller, M.P. Manalili, J. Rek, V. Stadelmann, R. Reiser, H. Oberholzer, and P. Weisskopf, Agroscope, Dep. of Agroecology and Environment, Reckenholzstrasse 191, CH-8046 Zürich, Switzerland; T. Keller, Swedish Univ. of Agricultural Sciences, Dep. of Soil and Environment, Box 7014, SE-75007 Uppsala, Sweden; T. Colombi and A. Walter, Swiss Federal Institute of Technology ETH, Institute of Agricultural Sciences, Crop Science, Universitätstrasse 2, CH-8092 Zürich, Switzerland; S. Ruiz, H. Wunderli, D. Breitenstein, S. Schymanski, and D. Or, Swiss Federal Institute of Technology, Institute of Terrestrial Ecosystems (ITES), Soil and Terrestrial Environmental Physics (STEP), Universitätstrasse 16, CH-8092 Zürich, Switzerland; A. Romero-Ruiz and N. Linde, Univ. of Lausanne, Institute of Earth Sciences, Applied and Environmental Geophysics Group, Bâtiment Géopolis, CH-1015 Lausanne, Switzerland. M.P. Manalili current address: Crop and Environmental Sciences Division, IRRI, Los Baños, Laguna, Philippines. *Corresponding author (thomas.keller@agroscope.admin.ch).

Vadose Zone J.
doi:10.2136/vzj2016.11.0118
Received 28 Nov. 2016.
Accepted 22 Feb. 2017.
Supplemental material online.

© Soil Science Society of America.
This is an open access article distributed under the CC BY-NC-ND license (http://creativecommons.org/licenses/by-nc-nd/4.0/).

Abbreviations: BS, bare soil; CEP, compaction of entire plot; CT, conventional tillage; CWT, compaction in wheel tracks; ERT, electrical resistivity tomography; FDR, frequency domain reflectometry; GPR, ground-penetrating radar; NOC, no compaction; NT, no-till; PG, permanent grass; SOC, soil organic carbon; SSO, Soil Structure Observatory.

Soil compaction due to agricultural operations is a serious threat to soil productivity and soil ecological functions in modern agriculture (Hamza and Anderson, 2005; Schjønning et al., 2015). The susceptibility of soil to compaction is a combination of inherent soil properties, soil moisture status at the time of field operations, soil and land management, and the machinery used. Soil compaction problems are therefore especially widespread in agriculture involving heavy machinery and/or moist soils; such is the case in large parts of Europe and North America or parts of South America and Australia. According to Jones et al. (2003), more than one third of European subsoils are highly susceptible to compaction, and Schjønning et al. (2015) suggested that a quarter of all European soils were compacted. Hamza and Anderson (2005) cited figures of compacted areas of 68 Mha (worldwide), 33 Mha (Europe), and 4 Mha (Australian wheat belt). The aggravation of soil compaction is linked with modern trends of steadily

increasing power and weight of agricultural vehicles and implements, which today may reach wheel loads in excess of 10 Mg for self-propelled harvesters or slurry spreaders (Schjønning et al., 2015). Economical and efficiency considerations suggest no slowing of this trend unless a technological breakthrough or a paradigm shift (e.g., small autonomous vehicles, fixed tracks) would occur. Considering the increasing pressures on agriculture for production of food, fiber, and biofuels, the continual degradation of soil resources due to compaction is expected to escalate in the future. Many modern agricultural vehicles induce stresses in the soil that exceed the mechanical strength of soils under most conditions, resulting in soil deformation and modification of the spatial arrangement of soil constituents and voids (pores), altering a critical component of soil structure. The reduction in pore volume and the change in pore structure (size distribution, connectivity, tortuosity) decrease transport capability (fluid and gas transport by advection and diffusion) and water storage capacity, increase mechanical resistance for root growth, change prevailing chemical reactions and the availability of nutrients (anoxic conditions), and modify physical habitats of soil organisms. These changes consequently affect biodiversity and a range of ecosystem services including the production of food, fiber, and fuel, water provision and purification, and atmospheric regulation (e.g., Zhang et al., 2007).

The real costs of soil compaction are borne by the cumulative loss of soil functionality (e.g., yield loss in agricultural systems) following a significant compaction event, integrated over the time period until a soil has effectively recovered to its pre-compaction functionality. Hence, quantifying compaction costs (and therefore the severity of compaction) requires knowledge about soil structure recovery rates after compaction. We differentiate between *instantaneous compaction impact* and *compaction damage* (Fig. 1), and define instantaneous compaction impact as the immediate effect of a compaction event on soil functions, whereas compaction damage relates to the compaction effect integrated over the structure recovery time. Considering the conceptual sketch in Fig. 1, we may describe compaction damage (CD) as

$$\mathrm{CD} = \int \left(\mathrm{CI} \left\{ 1 - \left[C_\mathrm{r}(t)\mathrm{d}t \right] \right\} \mathrm{d}t \right)$$

where CI is the immediate compaction impact (immediate change in a soil metric), C_r is the soil structure recovery rate (a function of time), and t is the elapsed time since compaction. The compaction damage can be expressed in terms of compaction costs, i.e., by valuation of ecosystem services, although this is not an easy exercise (e.g., Loomis et al., 2000; Farber et al., 2002). The costs of compaction relate to ecological costs but also to direct monetary value, e.g., for farmers in terms of reduced profit due to yield decline. A review of compaction costs was given by Chamen et al. (2015). We note that partial recovery times, e.g., 90% recovery, are typically used in ecological studies (e.g., MacNeil et al., 2015). Partial recovery times provide more useful estimates because simplistic recovery functions (e.g., logarithmic functions) may display unrealistic asymptotic behavior at large recovery times (Webb and Wilshire, 1980; Webb, 2002). While *recovery* describes a process, *resilience* is defined as the ability to recover a property, capacity, or function to its initial value when the disturbance (i.e., stress) is removed (e.g., Lal, 1993; Gregory et al., 2007). Resilience is typically quantified in terms of a resilience index that relates the initial impact (i.e., impact at time 0) to the effect at time x (e.g., Orwin and Wardle, 2004). Hence, resilience quantifies the amount of recovery at a certain time step after the disturbance.

Our knowledge regarding soil compaction recovery rates and recovery times is anecdotal and sketchy. Experimental evidence of compacted soil recovery periods from field studies suggests a wide range, from months (Drewry et al., 2004) and years (Culley et al., 1982; Blackwell et al., 1985; Langmaack et al., 1999; Radford et al., 2007; Besson et al., 2013) to decades (Håkansson and Reeder, 1994; Peng and Horn, 2008; Berisso et al., 2012) and centuries (Webb, 2002). In these studies, only a few properties and functions were addressed. Traditionally, crop yield has been the focus of such evaluations (e.g., Culley et al., 1982; Håkansson and Reeder, 1994), while more recent work has addressed soil structure and transport functions (e.g., Peng and Horn, 2008; Berisso et al., 2012; Besson et al., 2013) or earthworm abundance (Langmaack et al., 1999). Estimates of recovery rates based on laboratory studies (e.g., Arthur et al., 2013) are typically higher than those observed in field studies, thus potentially underestimating recovery times and compaction costs. The conflicting evidence of compaction recovery times, and the discrepancy in recovery rate estimates between

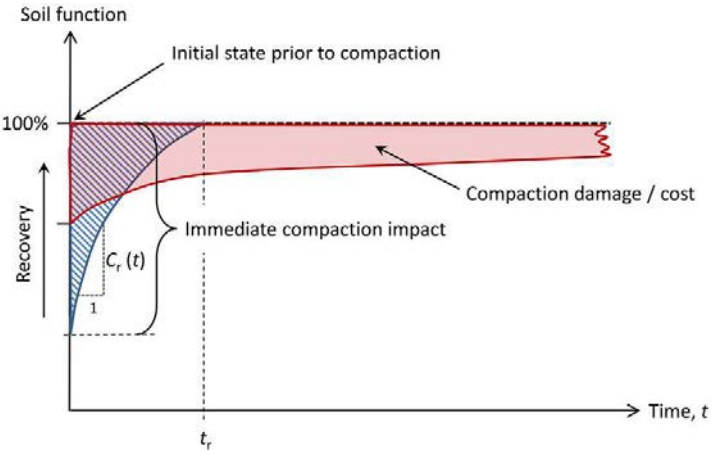

Fig. 1. Schematic figure showing immediate compaction impact, compaction recovery rate $C_\mathrm{r}(t)$, compaction recovery time t_r, and compaction damage. Case 1 in blue indicates a large immediate impact but a fast recovery, thus moderate damage (e.g., topsoil compaction), while Case 2 (red) shows a moderate immediate impact but slow recovery, thus large damage (e.g., subsoil compaction).

field and laboratory studies, is a manifestation of the partial and incomplete knowledge of the key processes involved in soil structure recovery and, more generally, soil structure dynamics. Although the relevant mechanisms are generally well established, their quantitative and predictive representation remain limited. The key natural mechanisms involved in soil structure recovery following compaction are grouped according to climatic and abiotic processes induced by wetting–drying and freezing–thawing phenomena, and biotic processes (root growth and root water uptake, burrowing of earthworms and other soil fauna, microbiological activity). Additionally, anthropogenic effects such as mechanical loosening and fragmentation by soil tillage play an important role in enhancing soil structure recovery. It is clear, however, that one-time tillage cannot simply reverse compaction effects, and it has been shown that compaction effects persist in the tilled layer for several years despite regular tillage (Arvidsson and Håkansson, 1996; Weisskopf et al., 2010).

A more definitive understanding of compacted soil recovery rates and times is not only needed for estimation of the real costs of compaction (see above and Fig. 1), but a more quantitative description of natural compaction recovery mechanisms and recovery pathways could also be used to develop site-specific soil management methods (or strategies) that accelerate compaction recovery (Dexter, 1991). More generally, improved understanding of soil structure dynamics due to biophysical processes could offer a path for harnessing biological processes to improve the physical and ecological conditions of soil for agricultural production (Dexter, 1991; Hallett et al., 2013). Protocols for enhancing soil structure recovery (and more generally, soil structure formation) are urgently needed, with the growing threat of soil compaction as a result of the intensification of agriculture to enhance food production.

A framework for combining in situ monitoring, modeling, and small-scale mechanistic experiments targeting the different compaction recovery processes is necessary to better understand the complex biophysical interactions and feedback mechanisms involved in soil structure dynamics. A major gap in our knowledge of soil structure dynamics as identified above is the discrepancy in temporal and spatial scales between laboratory investigations and field studies under natural climatic conditions and the lack of systematic field observations at the proper (i.e., years to decades) time scale. Consequently, research on soil structure evolution requires, among others, long-term field studies including adequate research infrastructure for monitoring.

To address these challenges, we designed a long-term field experiment for monitoring post-compaction evolution of soil structure, referred to as a soil structure observatory. Here we describe the objectives, the design, the implementation, and monitoring concept of our soil structure observatory and present the initial compaction effects.

The Soil Structure Observatory

Conceptual Approach, Rationale, and Motivation

An appropriate time (several years to decades) and spatial scale (plot scale or larger) is crucial for an adequate monitoring of soil structure recovery after compaction. Further key design factors include monitoring of climatic variables (precipitation, temperature, etc.), monitoring of soil state variables, and observations of soil and crop properties at regular intervals.

The general aim of the Soil Structure Observatory (SSO) is to provide long-term observation data on soil structure evolution after disturbance in the form of compaction. This will allow quantification of compaction recovery rates and times and therefore quantification of compaction costs (cf. Fig. 1). We aim at combining the data obtained from the SSO with modeling and small-scale mechanistic experiments to increase our understanding of soil structure dynamics and particularly soil structure recovery after compaction. The SSO may hereby serve as a platform for integrating the contemporary knowledge that is currently fragmented across temporal and spatial scales.

The SSO was designed to provide information on both the natural recovery of compacted soil structure and evaluation of soil management options (e.g., soil tillage) for accelerating soil structure (and function) recovery. Consequently, the SSO includes treatments with and without interference by farming operations. Moreover, we intended to isolate, as much as possible, predominantly physical natural recovery (i.e., without plants and limited soil fauna) from combined biological and physical natural recovery. Hence, treatments with and without plants and without any mechanical post-compaction disturbance were included in the SSO. In these treatments, it is important to prohibit any field traffic after the initial experimental compaction to study the natural recovery of soil structure after compaction. This substantially increases operational demands on the infrastructure (e.g., fencing) as well as workload in the field because all field operations have to be performed by hand. The SSO has been designed to test the following main hypotheses:

- Soil structure recovery is accompanied by measureable changes in soil biophysical properties and crop performance
- Biological activity increases the rate of soil structure recovery
- Tillage facilitates soil structure recovery
- Roots and soil mesofauna (e.g., earthworms) avoid compacted zones when possible (such as wheel tracks).

Study Site and Pre-compaction Field Management

The SSO was established on a deep gleyic Cambisol (IUSS Working Group WRB, 2006) with loamy soil texture (see Table 1) at the

Agroscope research institute in Zürich, Switzerland (47.4° N, 8.5° E; 444 m asl). The mean annual temperature is 9.4°C, and the mean annual precipitation is 1054 mm (data obtained from the Swiss Federal Office of Meteorology and Climatology, MeteoSwiss). The SSO is designed as a decade-long (or longer) observatory. Selected soil properties are presented in Tables 1 and 2.

The site (~1.5 ha) was sown with a grass mixture in April 2013, roughly 1 yr before initiating soil compaction in March 2014. We used the grass–white clover (*Trifolium repens* L.) mixture SM 442 (Suter et al., 2008) reinforced with an additional 4 kg ha^{-1} of lucerne (*Medicago sativa* L.). This grass mixture was chosen because it contains species with different root systems and depth-distributions of roots, and because it is known to be robust under a wide range of unfavorable soil physical conditions (e.g., water logging and O_2 stress). After sowing the mixture, no more traffic with agricultural machinery was allowed over the experimental area, except for a small self-propelled mower used for periodic cutting of the grass. The initiation of the ley 1 yr prior to initial compaction and the prohibition of any farm machinery traffic aimed at allowing the soil to "rest" before establishing the SSO.

A permanent meteorological station run by MeteoSwiss is located within 300 m from the experimental field, delivering hourly data on, among others, air temperature, precipitation, relative humidity, and global radiation.

Experimental Design

The SSO includes two experimental factors—compaction level and post-compaction soil management (see below)—and is based on a strip-plot design (Fig. 2) with three blocks (replicates). There are three compaction levels and four management treatments, as detailed below, amounting to a total of 36 plots. Each plot is 17 m long and 10 to 12 m wide. A one-time compaction was performed in the in-sown ley (see above) in March 2014, and the four post-compaction soil management treatments were immediately started thereafter. Thus, the (soil) conditions during compaction were the same (ley) in all treatments. No further experimental compaction is foreseen in the SSO.

Compaction Treatments

The SSO includes three compaction levels (Fig. 2): compaction of the entire plot area, i.e., track-by-track (CEP), compaction in wheel tracks (CWT), and control, i.e., no experimental compaction (NOC). The same compaction intensity (i.e., the same machinery and the same number of machinery passes) was applied in CEP and CWT.

Treatment CWT allows studying soil structure evolution under conditions where roots and soil organisms can avoid compacted zones (wheel tracks) (Capowiez et al., 2009), in comparison with processes under CEP, where the entire near-surface volume is compacted. Soil compaction recovery might be slower in the compacted zones under the wheel tracks if roots and soil organisms

Table 1. Basic soil properties at the Soil Structure Observatory, Zürich, Switzerland.

Block	Clay (<2 μm)	Silt (2–50 μm)	Sand (50–2000 μm)	Organic C	Particle density	pH ($CaCl_2$)	Cation exchange capacity
	g g^{-1}				Mg m^{-3}		cmol$_c$ kg^{-1}
0–0.2-m depth							
A	0.254 (0.014)†	0.518 (0.015)	0.228 (0.018)	0.018 (0.001)	2.56	6.3 (0.3)	17.4 (0.6)
B	0.273 (0.014)	0.486 (0.040)	0.241 (0.040)	0.017 (0.001)	2.62	7.1 (0.2)	17.8 (0.7)
C	0.275 (0.013)	0.464 (0.019)	0.261 (0.026)	0.015 (0.001)	2.61	7.2 (0.2)	17.6 (0.5)
0.3–0.5-m depth							
A	0.307 (0.018)	0.487 (0.017)	0.206 (0.030)	0.008 (0.000)	2.60	6.6 (0.3)	18.0 (0.6)
C	0.269 (0.038)	0.450 (0.026)	0.281 (0.054)	0.007 (0.004)	2.65	7.4 (0.2)	15.3 (2.6)

† Means and standard deviations (in parentheses) of 12 (topsoil) and eight (subsoil) sampling locations.

Table 2. Soil physical and biological properties prior to compaction, from samples taken during October 2013, i.e., 5 mo before the compaction event, including bulk density (BD), total porosity (TP), air-filled porosity at 100 hPa water suction ($\varepsilon_{a,100hPa}$), relative gas diffusion coefficient at 100 hPa water suction ($D_{p,100hPa}/D_0$), air permeability at 100 hPa water suction ($k_{a,100hPa}$), saturated hydraulic conductivity (K_{sat}), microbial biomass (MB, as microbial C [C_{mic}]), and basal respiration (BR).

Depth	BD	TP	$\varepsilon_{a,100hPa}$	$D_{p,100hPa}/D_0$	log $k_{a,100hPa}$	log K_{sat}	MB	BR
m	Mg m^{-3}	m^3 m^{-3}			log μm^2	log mm h^{-1}	mg C_{mic} kg^{-1}	μg CO_2–C g^{-1} h^{-1}
0.1	1.38 (0.01)†	0.47 (0.01)	0.09 (0.01)	0.019 (0.002)	1.29 (0.15)	2.08 (0.07)	482.5‡ (15.4)	0.55‡ (0.05)
0.3	1.52 (0.01)	0.42 (0.01)	0.06 (0.01)	0.010 (0.001)	0.93 (0.02)	2.18 (0.20)	161.8§ (0.81)	0.33§ (0.10)
0.6	1.53 (0.03)	0.42 (0.01)	0.04 (0.01)	0.005 (0.001)	0.43 (0.07)	1.63 (0.10)		

† Means and standard errors (in parentheses; n = 3 experimental blocks).
‡ 0–0.2-m depth.
§ 0.3–0.5-m depth.

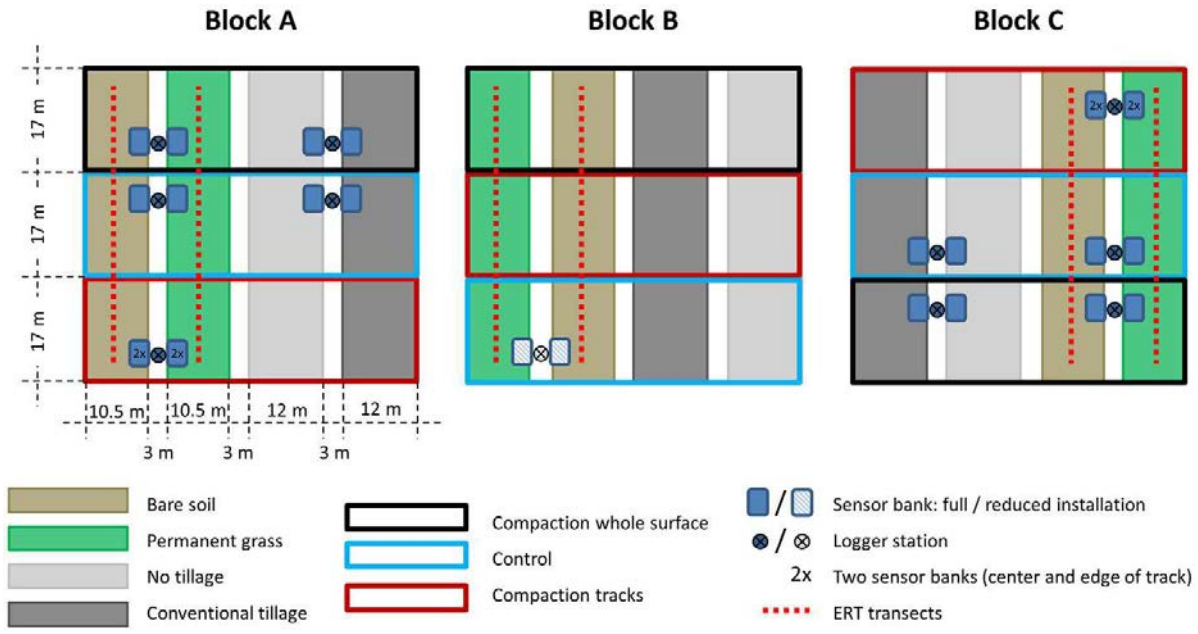

Fig. 2. Experimental design of the Soil Structure Observatory (SSO) in Zürich, Switzerland.

avoid these zones. On the other hand, it could be argued that recovery in CWT would be faster than in CEP because the compacted zone has a larger interface with uncompacted soil, from which recovery could be initiated. Treatment CWT would more often occur in practice; however, modern agricultural machinery (e.g., self-propelled sugarbeet harvesters, self-propelled forage harvesters, self-propelled slurry tankers) are equipped with offset steering and therefore track the entire surface area as in treatment CEP.

Post-compaction Soil Management and Cropping Systems

The SSO includes four post-compaction soil management–cropping systems: bare soil (BS), permanent grass (PG), crop rotation under no-till (NT), and crop rotation under conventional tillage (CT). No farming traffic and no mechanical disturbance are allowed in systems BS and PG; these systems therefore provide insights into uninterrupted natural processes of soil structure regeneration, with plants signifying normal biological activity (PG) and without plants suggesting reduced biological activity (BS). The two cropping systems (NT and CT) enable insights into soil structure recovery under common agricultural practices with minimal (NT) and conventional mechanical soil disturbance (CT).

Plants on the bare soil treatments (BS) are suppressed by periodic application of nonselective herbicides (glyphosate [*N*-(phosphonomethyl)glycine], glufosinate-ammonium [2-amino-4-(hydroxymethylphosphinyl)butanoic acid monoammonium salt]). The herbicide is applied manually using a knapsack sprayer with a 2.5-m swath width. The treatment PG represents a grass mixture that was established in spring 2013 (see above), i.e., the grass survived the compaction without any resowing. The grass is cut four to five times per year using a small self-propelled motor mower (total mass ~200 kg). The cut grass is then manually removed from the experimental area.

Triticale (×*Triticosecale*, cultivar Trado) was sown in the NT and CT plots on 3 Apr. 2014, i.e., 8 d after compaction. Glyphosate was applied to the BS and NT plots on 29 Mar. 2014 to control the ley that was established in 2013 (see above). The crop was sown without any prior tillage with a no-till drill in the NT plots, while the soil was moldboard plowed to about 0.25 m and harrowed to about the 0.06-m depth using a rotavator on 2 Apr. 2014 in the CT plots. Fertilization of the NT and CT plots is performed according to the Swiss fertilization recommendation (GRUDAF) (Flisch et al., 2009), and crop protection (weed and disease control) in NT and CT is done according to the principles of "integrated pest management" aiming to suppress pest populations below the economic injury level, largely relying on pesticides. The crop rotation for NT and CT, to date, is: triticale (×*Triticosecale*, 2014)–silage maize (*Zea mays* L., 2015)–winter wheat (*Triticum aestivum* L., 2016)–winter rapeseed (*Brassica napus* L., 2017).

Monitoring and Sampling Concept

Observations at the SSO include continuous monitoring of soil state variables (soil moisture, temperature, soil air CO_2 and O_2

concentrations, redox potential, and O_2 diffusion rates), for which a network of sensors was installed at various depths (0–1 m), and periodic sampling and measurements of soil physical, chemical, and biological properties, earthworm abundance, and crop measures. The monitoring and measurements cover different spatial scales: soil core, soil profile (e.g., root characteristics), and the plot scale (e.g., geophysical measurements, crop biomass). The observation scheme includes pre-compaction soil characterization (October 2013), measurements during the compaction event (March 2014), post-compaction soil characterization (March–May 2014), and post-compaction monitoring (April 2014 to date). An overview of all the measurements is provided in Supplemental Table S1.

Soil sampling and in situ measurements during pre-compaction soil characterization were performed at 12 randomly selected sampling or measuring locations per experimental block. Earthworm sampling was done at five randomly selected locations within each block. Geophysical measurements were performed in transects, with one electrical resistivity tomography (ERT) transect (48 electrodes, 1-m spacing) per block and three ground-penetrating radar (GPR) transects per block (one transect in the north–south direction and two in the east–west direction). Selected soil properties measured during the pre-compaction soil characterization are given in Table 2. The ERT and GPR results revealed only subtle lateral heterogeneities within and between transects, thereby indicating similar soil profiles across the SSO.

Post-compaction soil characterization was done 2 wk after compaction except for earthworm sampling, which was performed 2 mo after compaction. Three sampling or measuring locations were randomly selected in each NOC and CEP plot. For CWT, sampling or measuring was done at three positions, namely the track center, track edge, and between tracks, with three randomly selected sampling or measuring locations per plot for each position, amounting to a total of nine sampling or measuring locations in each CWT plot. Earthworms were sampled at two randomly selected locations per experimental block in the CEP and NOC plots.

Sampling and measurements during post-compaction monitoring will be performed at intervals of half a year (within the first 1–2 yr after compaction) to 1 yr (from the third year after compaction; and possibly larger time intervals at later stages). The sampling and measuring locations will be randomly selected within each plot. A minimum distance between plot edge and sampling and measuring locations of 1 m, as well as a minimum distance between previous and subsequent sampling and measuring locations of 1 m will be considered. The post-compaction monitoring includes fewer sampling or measuring locations than the post-compaction characterization and may not always include all sampling depths because recovery is expected to be slower at greater depths. Additional measurements such as greenhouse gas emissions could potentially be added later or for some periods of time.

Compaction Stresses in the Soil

During the compaction event, we measured soil mechanical stresses at the 0.2-, 0.4-, and 0.6-m depth using custom-made Bolling probes (Bolling, 1987), which are fluid-inclusion-type probes used to determine mean normal stress (Berli et al., 2006). These measurements were performed between the three experimental blocks (Fig. 2) to avoid damaging the experimental plots. The Bolling probes were installed as described by Keller et al. (2016). We acquired information from four field replicates, i.e., we installed the probes at four different locations within the field. We collected undisturbed soil samples (0.1-m diameter, 0.06-m height) at depths of 0.2, 0.4, and 0.6 m. Sampling locations were adjacent to the locations of soil stress measurements for determination of Poisson's ratio, ν, in the laboratory according to the method of Eggers et al. (2006) based on uniaxial confined and unconfined compression tests. The mean normal stress, σ_m, was then calculated from the Bolling probe pressure, p_i, and ν using Eq. [20] and [23] of Berli et al. (2006).

Monitoring Changes in Soil Surface Elevation Using Lidar

As part of the monitoring, we examined the potential of a modern lidar system for capturing soil surface elevation changes due to the prescribed compaction treatment and subsequent rebound. Such a system requires reference points of known position and elevation, so that measurements can be translated to surface elevation changes. Six ground screws (0.8 m in length; Krinner GmbH), serving as fixed points, were drilled into the soil at positions between the experimental plots. During measurements (scanning), spherical targets mounted on ~1.5-m-long aluminum rods are fixed to the ground screws, defining a fixed coordinate system (see also Friedli et al., 2016). Measurements were performed using a Faro Focus 3D S 120 laser scanner (Faro Technologies Inc.) that was mounted on a tripod at a height of about 3.5 m (Friedli et al., 2016). See Friedli et al. (2016) for more details on the scanner and the field setup.

An additional setup was used to perform scans immediately before compaction, immediately after trafficking, and 0.5, 1, and 2 h after trafficking, to quantify vertical surface displacements and potential rebound effects. Wooden square reference plates of 0.25 m^2 were placed into the center of two experimental plots (one plate per plot) after the vegetation was cut. Three spheres of 0.1-m diameter mounted on poles at a height of 0.75 m were arranged in a triangle and served as reference points to determine the displacement of the plates. The scanner was mounted on a tripod at a height of 3.5 m above the land surface. The horizontal distance from the scanner to the plates was 12.5 m, and the distance to the spheres was 1 m (one sphere) and 25 m (two far-off spheres). Scans were performed with a measuring rate of 244,000 scan points per second at half of the maximum resolution provided by the system. The distances between single scan points on the plates and the far-off spheres were 3.9 and 7.7 mm, respectively.

In Situ Sensors for Monitoring Physicochemical Soil State Variables

Sensor probe banks (Fig. 2) consisting of probes at various depths (Fig. 3) were installed post-compaction for continuous monitoring of the evolution of soil moisture states, soil temperature, soil air composition (O_2 and CO_2 concentrations), O_2 diffusion rates, and redox states. Installation started 5 d after the compaction event and was completed 10 d after the compaction event. Two banks were established in the CWT plots (Fig. 2): one in the center and one at the edge of a wheel track. The depths considered were 0.1, 0.2, and 0.4 m (all probes), and additionally 0.7 and 1 m (soil moisture probes). The probes were installed either horizontally from a pit or from above ground (Fig. 3). The distance between plot edge and sensing head was at least 0.6 m. In each bank, two to four replicate probes were installed per depth. Probes at the 0.1- and 0.2-m depths in the CT plots are removed and reinstalled at each tillage occasion. The sensor system was automated using CR800 and CR1000 dataloggers and AM16/32B multiplexers (all from Campbell Scientific Ltd.). Wired connection of the sensors to the dataloggers and multiplexers started as soon as the sensor probes were in the ground, but completion of the datalogging system took several weeks. Data are recorded every 30 min (for technical reasons, readings of redox potentials and O_2 diffusion rates are taken only every 8 h; see below) and automatically transferred via General Packet Radio Service (GPRS) communication to a database on a web server (WebDAVIS 3.0, Solexperts AG).

The soil moisture conditions are monitored by measuring soil water suction and soil water content. Soil water suction is measured with a combination of tensiometers (in-house production; Klute, 1986) and calibrated heat dissipation sensors (pF-Meter, ecoTech). The latter sensors yield indirect matric potential measurements and were installed due to the limited range of tensiometers in dry soil (tensiometers fail at water suctions >800 hPa). Soil water content is measured using in-house-produced three-prong time-domain reflectometry (TDR) probes (Jones et al., 2002) and frequency-domain reflectometry (FDR) profilers (EnviroScan, Sentek). The FDR profilers are easily removed from the soil, an operation that needs to be done in the two crop rotation treatments (CT and NT) during field operations (soil tillage, seeding). Some plots are equipped with both TDR and FDR sensors to allow cross comparisons. Two FDR profilers and two tensiometers per depth were installed in Block B at the end of summer 2013 (i.e., more than half a year before the compaction event). Apart from getting a "general feeling" for the soil water dynamics of the site, measurements from these probes were used to define an appropriate time for the compaction event (e.g., soil water content similar to the soil water content at the maximum Proctor density; ASTM, 1992; Aragón et al., 2000; Botta et al., 2008). Soil temperature is measured using standard copper-constantan thermocouples. Soil temperature dynamics affect biological activity and may also carry a structural signature (e.g., higher thermal conductivity for compacted layers).

Redox potentials (E_H) and O_2 diffusion rates (ODR) are monitored with a system consisting of Pt glass electrodes, calomel reference electrodes, and a brass anode, as detailed by Reiser et al. (2012). An 8-h logging interval, from one E_H–ODR data pair to the next, allows relaxation of the electrode polarization and regeneration of the depleted O_2 concentration near the Pt electrode.

Soil O_2 and CO_2 concentrations were initially measured manually at biweekly intervals according to a method described by Weisskopf et al. (2010). Porous polypropylene tubes of 0.5-m length were horizontally installed at the 0.1-, 0.2-, and 0.4-m depths for measurements of O_2 and CO_2 concentrations in the soil air using a CheckMate 9900 head space gas analyzer (PBI Dan-sensor A/S). Probes for continuous measurements were developed later.

Electrical Resistivity Tomography Monitoring and Ground Penetrating Radar

Repeated (two to three times per year) ERT measurements are performed in the SSO in an attempt to observe geophysical signatures of structural changes with time at the plot scale. Stainless steel electrodes were installed along transects (48 electrodes per transect; electrode spacing: 1 m) in the BS and PG plots, as indicated in Fig. 2. The electrodes were left in the ground to ensure that subsequent data acquisitions were acquired with exactly the same electrode geometry. This enables more consistent interpretations and makes it possible to use advanced time-lapse inversion strategies. The ERT data are acquired using a Syscal Switch Pro system (http://www.iris-instruments.com) in a Wenner-Schlumberger electrode configuration. The ERT data are inverted using the algorithm described by Günther et al. (2006) and implemented in the BERT software. Ground-penetrating radar measurements are performed using dual-frequency antennas operating at 300 and 800 MHz (UtilityScan DF by GSSI). The GPR data are analyzed using Reflexw (Sandmeier geophysical research) and in-house MATLAB scripts.

Soil Geochemical Properties

Soil samples are taken from the 0.0- to 0.2- and 0.3- to 0.5-m depth intervals. Soil texture is measured using the pipette method. Soil organic C (SOC) is determined by the wet combustion technique following ISO 10694. Soil pH was measured in $CaCl_2$. Total N is measured using the Dumas combustion method with an element analyzer (varioMAX CNAnalyser, Elementar Analysensysteme GmbH) (ISO 13878). The concentrations of exchangeable bases, i.e., Ca, K, Mg, Na, and P, are measured by the NH_4OAc method at pH 4.65. All analyses are performed according to Swiss standard protocols (Swiss Federal Research Stations, 1996).

Microbial Biomass

Soil samples are collected at two different depths, 0.0 to 0.2 and 0.3 to 0.5 m. Soil microbial biomass is obtained by two methods: as C_{mic} estimated according to Anderson and Domsch (1978) and as C_{mic}–SIR calculated from soil initial respiration (SIR) rates

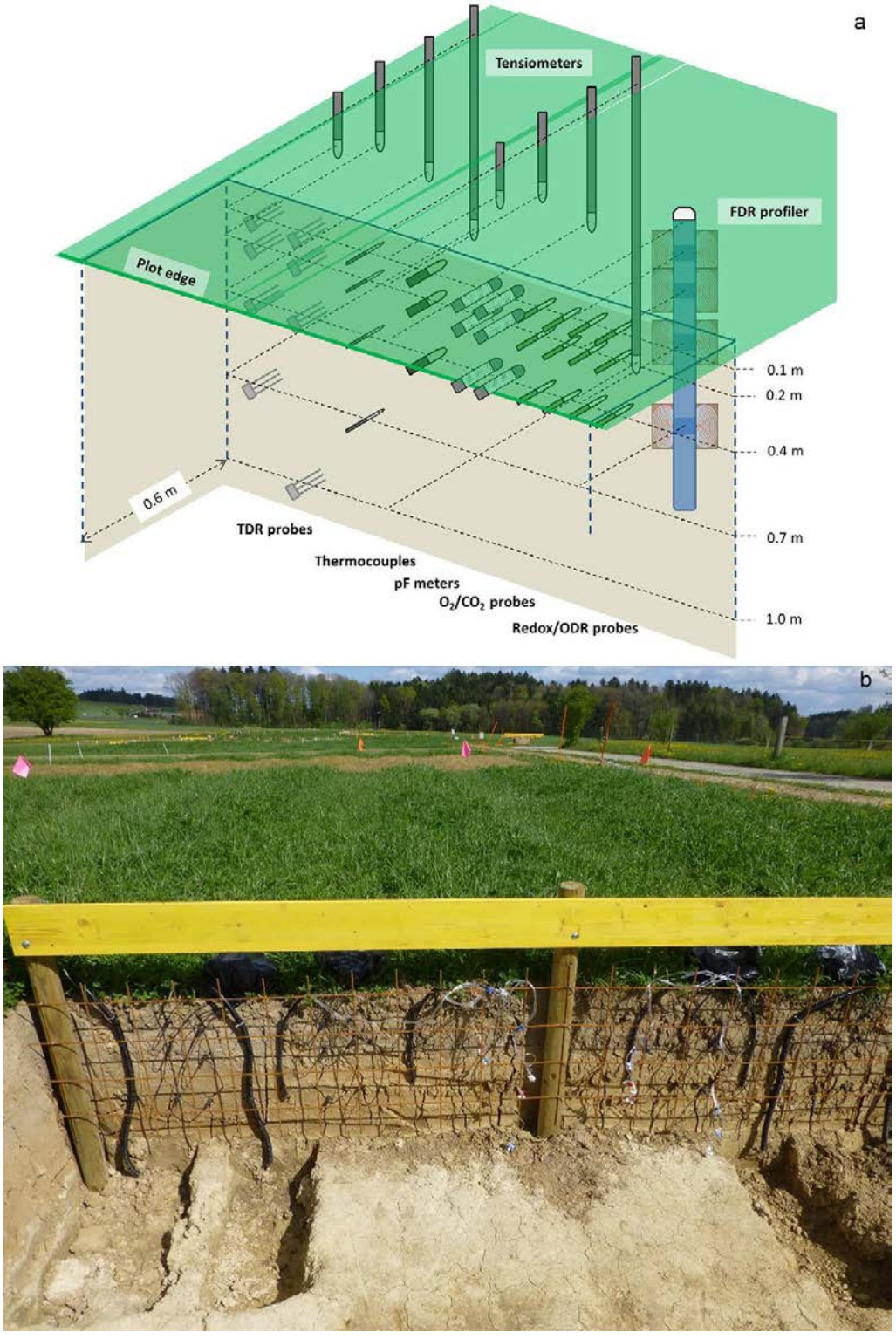

Fig. 3. (a) Schematic overview of a sensor bank, showing number and depths (0.1, 0.2, 0.4, 0.7, and 1.0 m) of the various sensor probes (but not necessarily the exact locations) installed from a profile wall at the plot edge through drilled holes of 0.6-m length; and (b) photo of a sensor bank where soil probes have been installed into the profile wall at various depths. The profile wall is at the plot edge.

according to Kaiser et al. (1992). Soil basal respiration is measured in preincubated samples (20 g soil dry matter for 7 d at 22°C) as CO_2 evolved during a period of 48 h (from the 24th to the 72nd h of incubation). All measurements are done according to the reference methods of the Swiss Agricultural Research Stations (Swiss Federal Research Stations, 1996).

Undisturbed Cylindrical Soil Cores for Characterization of Soil Structure

Undisturbed cylindrical soil cores (100 cm^3; diameter: 0.05 m; height: 0.05 m) are sampled at the 0.1-, 0.3-, and 0.6-m depth. The samples are stored at 2°C until measurements are done. On each sample, saturated hydraulic conductivity and air permeability and gas diffusivity at three levels of water suction (30, 100, and 300 hPa) are measured in the laboratory. Saturated hydraulic conductivity is measured using the constant-head method (Klute and Dirksen, 1986). Air permeability is obtained by measuring the air flow through the sample at an overpressure of 2 hPa, and gas diffusivity is measured in a one-chamber apparatus that uses O_2 as the diffusing gas assuming steady-state diffusion (Martínez et al., 2016). A subset of the soil core samples is scanned at 100 hPa water suction with X-ray micro-computed tomography (Phoenix Votmex x s 240, GE Sensing and Inspection Technologies GmbH) for visualization and characterization of soil pore architecture. The soil cores are dried in an oven at 105°C for at least 48 h after the various measurements, and the water content and bulk density are calculated.

Penetration Resistance and Water Infiltration

Penetrometer resistance is measured by means of a hand-pushed Eijkelkamp cone penetrometer (cone base area 1 cm^2, cone apex angle 60°) to a depth of 0.8 m. Two insertions are made at each sampling location.

Steady-state infiltration is measured at the soil surface using a disk permeameter (diameter: 0.2 m) (Perroux and White, 1988). Two infiltration measurements per sampling location are made. The infiltration rates are derived from the cumulative infiltration vs. time relationship.

Earthworm Abundance and Biomass

Earthworms are sampled in an area of 0.5 by 0.5 m using the following procedure. The top ~0.3 m of soil is excavated, and earthworms are collected by hand sorting. Then a 0.5% formaldehyde solution is applied to repel and thus extract earthworms from the subsoil (Kramer et al., 2008). Adults are determined to the species level, juveniles to ecological groups. Abundance and biomass are determined for each taxonomic group.

Crop Response Measurements

Both below- and aboveground crop properties are measured periodically. The root mass depth distribution for treatments PG, NT, and CT is obtained from sampling soil cores (0–0.75-m depth) and washing out roots (Colombi and Walter, 2016). Root architectural traits and root anatomy are measured for the NT and CT treatments as described by Colombi and Walter (2016). Aboveground measures include biomass in the PG plots (separately for grass and legumes) for the first and last cut of a season and plant height, leaf area index, and shoot dry biomass at different stages in NT and CT plots (Colombi and Walter, 2016). Crop productivity on a per-hectare basis, being either grain or silage yield, is determined by harvesting multiple rows of a defined length within the plots (NT and CT).

Initial Compaction Effects

Soil compaction was performed on the ley on 26 Mar. 2014 at an average water content close to field capacity using a self-propelled two-axle fully loaded agricultural self-propelled vehicle. The vehicle was equipped with 1050/50R32 tires inflated to 330 kPa. The wheel load, measured with portable vehicle scales (Radlastwaage WL 103, Haenni Instruments AG) on site, was 8.9 Mg on the front axle and 7.2 Mg on the rear axle (total vehicle mass: 32.2 Mg). Three vehicle passes (forward each time) were conducted on both CEP and CWT plots. The vehicle driving speed was maintained constant at 2 m s^{-1}.

Soil Moisture at Compaction

The soil moisture conditions on the day of compaction (26 Mar. 2014) were "ideal" for effective soil compaction (i.e., the soil water content was close to the water content at the maximum Proctor density; e.g., Aragón et al., 2000; Botta et al., 2008). We measured average soil water suctions, obtained from tensiometers, of 54, 60, 86, and 105 hPa at the 0.1-, 0.2-, 0.4-, and 0.7-m depths, respectively. For the same depths, the volumetric water contents, θ, obtained from FDR profilers, were 0.35, 0.32, 0.28 and 0.24 m^3 m^{-3}, respectively, corresponding to gravimetric water contents, w, of 0.26, 0.22, 0.18 and 0.15 g g^{-1}, respectively. These values are slightly above the "optimum water content," w_{opt}, associated with the maximum density obtained in a Proctor test: Naderi-Boldaji et al. (2016) obtained w_{opt} = 0.18 g g^{-1} from soil sampled at the 0.25-m depth in the immediate vicinity of the SSO (on the same field). This is identical to w measured at 0.4 m but slightly lower than w = 0.22 g g^{-1} that we measured at 0.2 m. Note that the optimum water content would be larger than the 0.18 g g^{-1} reported by Naderi-Boldaji et al. (2016) at the 0.1-m depth because of the higher SOC concentration in the topsoil, and lower than 0.18 g g^{-1} at 0.7 m because of the lower SOC concentration in the subsoil than at the 0.25-m depth. Hence, w at the time of the compaction event was close to w_{opt} at all considered depths.

Soil Stress, Surface Displacement, and Bulk Density

The mean normal stress under the agricultural vehicle decreased from ~150 kPa at 0.2 m to ~50 kPa at 0.5 m (Fig. 4a). The increase in bulk density (Fig. 4b) was large at 0.1 m (from ~1.3 to 1.5 Mg m^{-3}) and 0.3 m (from ~1.5 to 1.6 Mg m^{-3}), while there was only a small increase in bulk density at the 0.6-m depth. The depth of

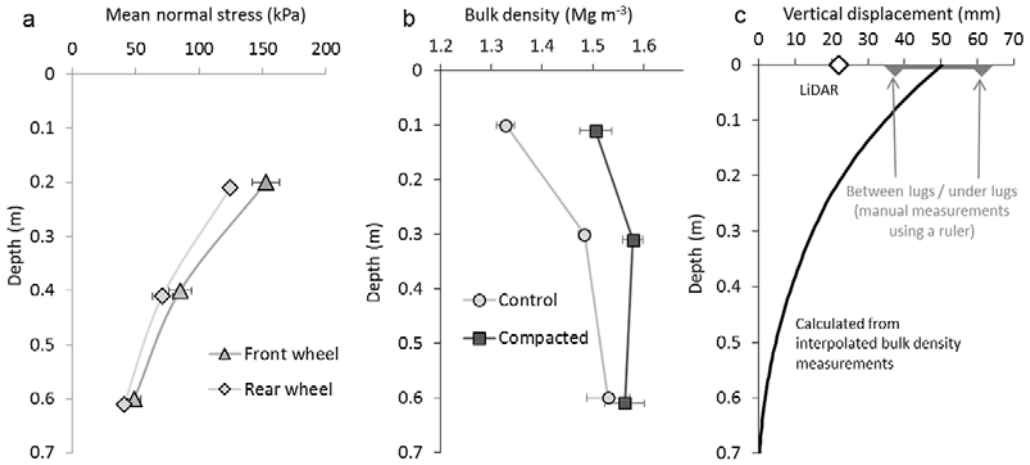

Fig. 4. (a) Mean normal stress under the agricultural vehicle (triangles: front wheel; rhombi: rear wheel) used for inflicting compaction; (b) average bulk density of uncompacted (circles) and compacted soil (squares), measured on samples collected 2 wk after the compaction event; and (c) vertical displacement estimated from measured changes in bulk density (curve) and surface displacement (rut depth) obtained from lidar measurements (rhombi) and from manual measurements using a ruler (gray horizontal bar indicating the range resulting from readings between tire lugs and under tire lugs).

compaction of about half a meter is consistent with the results presented by Keller et al. (2012), who analyzed data from a large number of trafficking experiments on various soil textures and found that vertical strain was observed when the vertical stress exceeded ~40 kPa. We calculated the vertical soil displacement from the measured changes in bulk density by interpolating between measuring depths, which resulted in a vertical displacement at the soil surface, i.e., rut depth, of 50 mm (Fig. 4c). This compared well with manual measurements using a ruler, from which we obtained rut depths between 37.5 (between tire lugs) and 61.3 mm (on tire lugs). The vertical surface displacement obtained from the lidar measurements (se above) was on average 22 mm. The smaller surface displacement is explained by the fact that the reference plates were lying on the highest points of the soil surface and thus measured the minimum vertical displacement. Lidar measurements at 0.5, 1, and 2 h after compaction did not reveal any rebound.

We estimated the maximum Proctor density, $\rho_{Proctor}$, using Eq. [8] of Naderi-Boldaji et al. (2016) and the soil textural data given in Table 1 to 1.66 and 1.70 Mg m^{-3} for the 0.1- and 0.3-m depths, respectively. The degree of compactness, DC, given as the ratio of the actual bulk density to $\rho_{Proctor}$, increased due to compaction from 78 to 90% at the 0.1-m depth, and from 88 to 94% at the 0.3-m depth. Critical limits of DC with respect to crop yield reported in the literature are 84 to 87% (Carter, 1990; Håkansson and Lipiec, 2000; Naderi-Boldaji and Keller, 2016). Using the relationship between DC and the Dexter (2004) soil quality index *S* developed by Naderi-Boldaji and Keller (2016), the DC values of the 0.1-m depth (topsoil) translate into *S* values of 0.044 (uncompacted) and 0.027 (compacted), indicating a shift from "good" soil physical quality to "poor" soil physical quality. These estimations suggest that the compaction inflicted in the SSO created soil physical conditions that are considered poor and expected to be limiting for crop development.

Soil Structure, Transport Properties, and Mechanical Impedance

The internal soil deformation and increase in bulk density (i.e., decrease in total porosity; see above) due to the trafficking by the agricultural vehicle caused significant changes to the soil pore structure and soil transport properties (Table 3). Figure 5 presents

Table 3. Impact of compaction on selected soil physical properties from samples taken on 11 Apr. 2014, i.e., 2 wk after the compaction event. "Uncompacted" represents mean values for the uncompacted (no experimental compaction) reference plots, while "Compacted" represents mean values for the plots with compaction of the entire plot area.

Soil property	Depth	Uncompacted	Compacted
	m		
Total porosity (m^3 m^{-3})	0.1	0.49 (0.01)†	0.42 (<0.01)
	0.3	0.44 (<0.01)	0.40 (<0.01)
	0.6	0.42 (<0.01)	0.41 (0.01)
Air-filled porosity at 100 hPa water suction (m^3 m^{-3})	0.1	0.10 (0.01)	0.04 (<0.01)
	0.3	0.07 (<0.01)	0.05 (<0.01)
	0.6	0.06 (<0.01)	0.05 (0.01)
Relative gas diffusion coefficient at 100 hPa water suction	0.1	0.024 (0.001)	0.006 (0.001)
	0.3	0.011 (0.001)	0.005 (<0.001)
	0.6	0.009 (0.001)	0.005 (<0.001)
Air permeability at 100 hPa water suction (μm^2)	0.1	56.9 (1.1)	3.2 (1.4)
	0.3	17.7 (1.0)	4.2 (1.2)
	0.6	10.9 (1.3)	3.0 (1.1)
Saturated hydraulic conductivity (mm h^{-1})	0.1	421.3 (1.1)	108.6 (1.2)
	0.3	194.9 (1.1)	78.2 (1.1)
	0.6	191.0 (1.3)	74.2 (1.2)
Soil surface water infiltration (mm h^{-1})	0	485.5 (50.9)	0.7 (0.6)

† Means and standard errors (in parentheses; n = 3 experimental blocks).

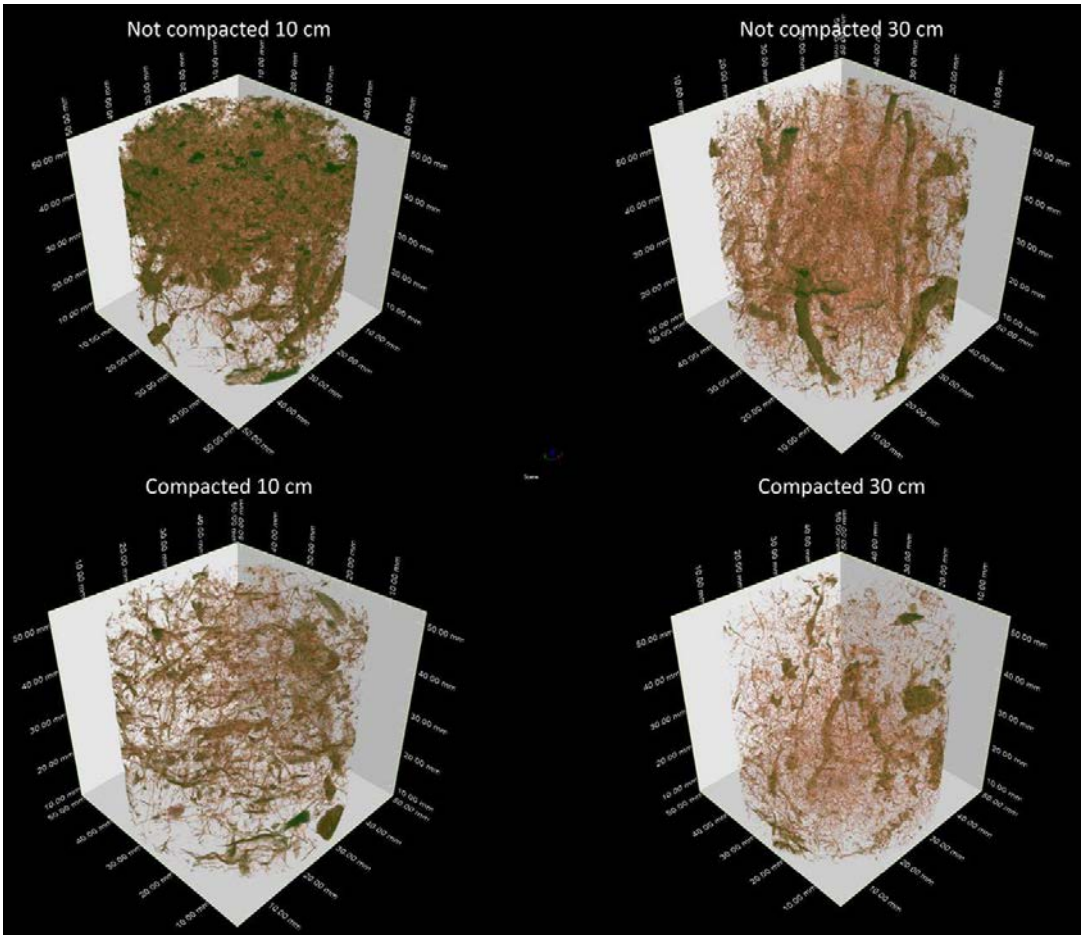

Fig. 5. Representative examples (100-cm^3 samples) of soil pore structure detectable on micro computed tomography images (voxel size 60 μm, corresponding to a minimum pore width of 120 μm) for uncompacted (top) and compacted bare soil (bottom) at the 0.1- (left) and 0.3-m depth (right), sampled 2 wk after the compaction event.

examples of the pore system (pores detectable on micro-computed tomography images, i.e., pore diameter > 120 μm) of compacted and uncompacted soil at the 0.1- and 0.3-m depths. The decrease in pore connectivity and in porosity is clearly visible at both depths, as also confirmed from measurements of air-filled porosity and gas transport properties (Fig. 6).

The decrease in porosity (Fig. 4b, 5, and 6a) drastically reduced the saturated hydraulic conductivity, K_{sat} (Fig. 6b), air permeability, k_a (Fig. 6c), and the relative gas diffusion coefficient, D_p/D_0 (Fig. 6d). The three different air-filled porosities per treatment and depth in Fig. 6c and 6d reflect measurements obtained at three water suction values (30, 100, and 300 hPa, respectively). A significant decrease in air-filled porosity and transport properties was measured at the 0.6-m depth (Fig. 6), although there was only a small increase in bulk density (Fig. 4b). This shows that soil functions related to pore size distribution and pore connectivity are more sensitive to compaction than macroscopic properties such as bulk density (Horn, 2003). Compaction did not affect the relationship between D_p/D_0 and ε_a (Fig. 6d), i.e., it did not affect the specific diffusivity ($c_D = D_p/D_0 \times \varepsilon_a^{-1}$), but D_p/D_0 was substantially decreased in the compacted soil due to lower ε_a. The slope of the log k_a vs. log ε_a relationship was slightly smaller for compacted soil (Fig. 6c), which would imply a slightly higher specific air permeability ($c_A = k_a \times \varepsilon_a^{-1}$) at small ε_a but a slightly lower c_A at high ε_a. During recovery, it may be expected that c_A and c_D initially increase and later decrease again (Jarvis, 2007; Mossadeghi-Björklund et al., 2016).

Water infiltration at the soil surface, measured by means of a disk permeameter, exhibited a more pronounced reduction due to compaction than K_{sat} in the soil profile. Infiltration rates decreased from 8 to 0.01 mm min^{-1}, i.e., a decrease of almost three orders of magnitude. In other words, immediately following compaction, the soil surface became nearly impervious, which could be attributed to the excessive smearing of the soil surface by the

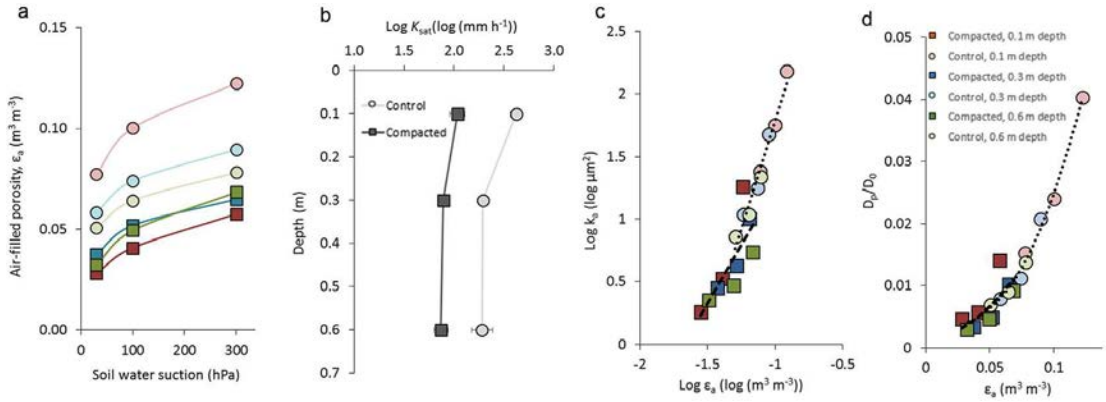

Fig. 6. Initial compaction effects on (a) air-filled porosity, ε_a, at different water suctions (circles: uncompacted; squares: compacted; red: 0.1-m depth, blue: 0.3-m depth, green: 0.6-m depth); (b) saturated hydraulic conductivity, K_{sat} (circles: uncompacted; squares: compacted); (c) air permeability, k_a, plotted as log k_a vs. log ε_a (circles: uncompacted; squares: compacted; red: 0.1-m depth, blue: 0.3-m depth, green: 0.6-m depth); and (d) relative gas diffusion coefficient, D_p/D_0, plotted as a function of ε_a (circles: uncompacted; squares: compacted; red: 0.1-m depth, blue: 0.3-m depth, green: 0.6-m depth). Note that the legends of Fig. 6d also apply to Fig. 6a and 6c. The data were obtained from soil cores sampled 2 wk after the compaction event. The data represent average values from the three treatments without tillage (i.e., bare soil, permanent grass, and no-till).

agricultural vehicle in addition to the effects of soil compaction. As a consequence, water ponded after rainfall in the compacted plots and in the wheel tracks. We measured an appreciable increase in mechanical resistance in the compacted topsoil (0–0.3-m depth) relative to the uncompacted soil. Penetration resistance was almost 2.5 MPa in the compacted soil at the 0.1- to 0.25-m depth, while the mechanical resistance at this depth was ~1.3 MPa in the uncompacted soil. Root elongation rates decrease with increasing soil penetration resistance (e.g., Dexter, 1987). A resistance of 2 MPa is often considered critical for root growth (Taylor et al., 1966; da Silva et al., 1994); it may correspond to a value where root elongation rates are about half of the maximum root elongation rate (Dexter, 1987).

Earthworms and Microbial Biomass

The earthworm population was drastically reduced due to compaction. The estimated biomass in the compacted plots was only 30% (epigeics) to 41% (anecics) of that in the uncompacted soil (Table 4). The decrease was probably caused by increased mortality rates during the compaction event (i.e., during loading; McKenzie et al., 2009), as well as less favorable living conditions after compaction. There were no immediate effects of soil compaction on microbial biomass and respiration. However, we expect microbial communities and hence microbial biomass and respiration to adapt to the changed soil physical conditions with time (Hartmann et al., 2013).

Electrical Resistivity Tomography

An example of a preliminary analysis is given for the bare soil in Block B (Fig. 7). In this figure, the relative difference between the estimated electrical resistivity on 7 Apr. 2014 (12 d after compaction) and 21 Mar. 2014 (before the compaction) is shown. The soil electrical resistivity decreased by 10 to 15% for the part of the block that had undergone CEP treatment, and decreases were also found under the wheel tracks for the CWT treatment. These results were obtained by an inversion process that smoothens actual variations in resistivity, which implies that the compaction-affected depth range is probably smaller than the approximately 0 to 1 m that is indicated in this figure.

Table 4. Earthworm biomass 5 mo before and 2 mo after compaction. Mean values of five samplings per block (2013) and six samplings per treatment (two per block) in 2014.

Ecophysiological category	2013	2014		
		Control	Compacted	Compacted/ control
	kg ha^{-1}			
Epigeic	106.7	114.7	34.6	0.30
Endogeic	499.2	476.2	154.8	0.33
Anecic	1581.5	1483.7	605.0	0.41
Total earthworm biomass	2187.3	2074.5	794.4	0.38

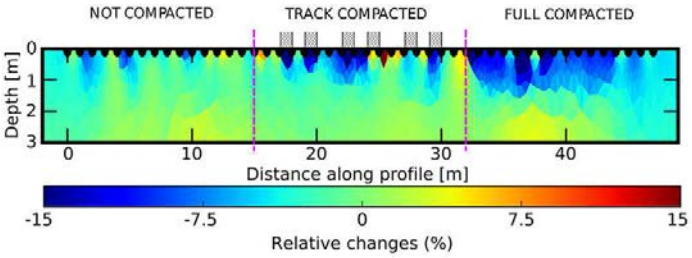

Fig. 7. Relative changes in inferred electrical resistivity between 7 Apr. 2014 (12 d after compaction) and 21 Mar. 2014 (5 d before compaction). The example shown is for bare soil in Block B. The patterns were similar for permanent grass and for the other blocks.

Outlook

The SSO aims at providing long-term data on the post-compaction soil structure evolution under contrasting post-compaction soil management regimes. The long-term time scale and tight intervals of observations (continuous measurements provided by various sensor probes in combination with regular sampling and in situ measurements) are crucial. We expect that the observations will allow quantification of recovery rates and recovery times of compacted soil and a better understanding of the (relative importance of the) recovery mechanisms, considering both natural biotic and abiotic mechanisms as well as soil tillage. Furthermore, we expect that the generated knowledge will help define strategies and guidelines for accelerating soil structure recovery, and more generally, improving soil structure in modern agriculture.

Sampling and in situ measurements have so far been done at half-yearly intervals after the compaction event, and sensor probes were installed in the weeks after the compaction event. Initial compaction increased the soil bulk density to about 0.5-m depth, decreased soil gas and water transport capability (air permeability, gas diffusivity, saturated hydraulic conductivity), and increased mechanical impedance. Water infiltration at the soil surface was drastically reduced (see also Fig. 8). Initial results from the post-compaction monitoring indicate projected recovery rates of years to decades, with different recovery rates for different properties and decreasing recovery rates with soil depth. Furthermore, the data indicate that soil tillage may immediately recover macroscopic soil total porosity but not soil functions (e.g., gas transport properties).

It would be highly desirable to establish similar SSOs under different soil and climatic conditions based on the concept outlined here. Additional SSOs could also include different compaction levels or different post-compaction soil management regimes. Data from other SSOs would increase our knowledge on how soil compaction recovery (and more generally, soil structure dynamics) is influenced by soil, climate, crops, and their interactions, allow estimates of compaction recovery rates and times across a wide range of soil and climatic conditions, and provide a wider basis for the development of soil management strategies.

Fig. 8. Ponding water after rainfall in (a) compacted plots and (b) wheel tracks of the bare soil treatment in April 2015 (i.e., 1 yr after compaction).

Acknowledgments

Financial support from the Swiss National Science Foundation (SNSF) through the National Research Program 68 "Soil Resources" is gratefully acknowledged (Project no. 406840-143061). We are thankful to Agroscope, Institute of Sustainability Sciences, for additional financial support. We thank Matthias Stettler (Bern University of Applied Sciences, School of Agricultural, Forest & Food Sciences HAFL, Zollikofen, Switzerland) for help with the soil stress measurements. Lina Grahm, Annika Tella, Annika Messmer, Dr. Ingrid Martínez, Marlies Sommer, Andrea Bonvicini, and Susanne Müller (Agroscope, Soil Fertility and Soil Protection, Zürich, Switzerland), Patrick Hagenbucher and Milad Aminzadeh (Swiss Federal Institute of Technology ETH, Soil and Terrestrial Environmental Physics STEP, Zürich, Switzerland), and Dr. Norbert Kirchgessner and Dr. Johannes Pfeifer (Swiss Federal Institute of Technology ETH, Crop Science, Zürich, Switzerland) are thanked for help with laboratory and field measurements. Dr. Peter Lehmann (Swiss Federal Institute of Technology ETH, Soil and Terrestrial Environmental Physics STEP, Zürich, Switzerland) is thanked for performing the randomization of sampling points. Philipp Walther, Fritz Käser, Stefan Schwarz, and Andres Sauter (Agroscope, trial support, Zürich, Switzerland) are thanked for performing the farming operations. Hans-Peter Müller, Hansueli Helbling, Theodor Neukom (Agroscope, Workshop, Zürich, Switzerland) and Beat Kürsteiner and Hubert Bollhalder (Agroscope, electronics workshop and support, Tänikon, Switzerland) are thanked for help with designing and constructing sensors and field installations.

References

Anderson, J.P.E., and K.H. Domsch. 1978. A physiological method for the quantitative measurement of microbial biomass in soil. Soil Biol. Biochem. 10:215–221. doi:10.1016/0038-0717(78)90099-8

Aragón, A., M.G. García, R.R. Filgueira, and Ya.A. Pachepsky. 2000. Maximum compactibility of Argentine soils from the Proctor test: The relationship with organic carbon and water content. Soil Tillage Res. 56:197–204. doi:10.1016/S0167-1987(00)00144-6

Arthur, E., P. Schjønning, P. Moldrup, M. Tuller, and L.W. de Jonge. 2013. Density and permeability of a loess soil: Long-term organic matter effect and the response to compressive stress. Geoderma 193–194:236–245. doi:10.1016/j.geoderma.2012.09.001

Arvidsson, J., and I. Håkansson. 1996. Do effects of soil compaction persist after ploughing? Results from 21 long-term field experiments in Sweden. Soil Tillage Res. 39:175–197. doi:10.1016/S0167-1987(96)01060-4

ASTM. 1992. Annual book of ASTM standards. ASTM Int., West Conshohocken, PA.

Berli, M., C.G. Eggers, M.L. Accorsi, and D. Or. 2006. Theoretical analysis of fluid inclusion for in situ soil stress and deformation measurements. Soil Sci. Soc. Am. J. 70:1441–1452. doi:10.2136/sssaj2005.0171

Berisso, F.E., P. Schjønning, T. Keller, M. Lamandé, A. Etana, L.W. de Jonge, et al. 2012. Persistent effects of subsoil compaction on pore characteristics and functions in a loamy soil. Soil Tillage Res. 122:42–51. doi:10.1016/j.still.2012.02.005

Besson, A., M. Séger, G. Giot, and I. Cousin. 2013. Identifying the characteristic scales of soil structural recovery after compaction from three in-field methods of monitoring. Geoderma 204–205:130–139. doi:10.1016/j.geoderma.2013.04.010

Blackwell, P.S., M.A. Ward, R.N. Lefevre, and D.J. Cowand. 1985. Compaction of a swelling clay soil by agricultural traffic: Effects upon conditions for growth of winter cereals and evidence for some recovery of structure. J. Soil Sci. 36:633–650. doi:10.1111/j.1365-2389.1985.tb00365.x

Bolling, I. 1987. Bodenverdichtung und Triebkraftverhalten bei Reifen: Neue Mess- und Rechenmethoden. Ph.D. diss. Technische Univ. München, München, Germany.

Botta, G.F., D. Rivero, M. Tourn, F.B. Melcon, O. Pozzolo, G. Nardon, et al. 2008. Soil compaction produced by tractor with radial and cross-ply tyres in two tillage regimes. Soil Tillage Res. 101:44–51. doi:10.1016/j.still.2008.06.001

Capowiez, Y., S. Cadoux, P. Bouchand, J. Roger-Estrade, G. Richard, and H. Boizard. 2009. Experimental evidence for the role of earthworms in compacted soil regeneration based on field observations and results from a semi-field experiment. Soil Biol. Biochem. 41:711–717. doi:10.1016/j.soilbio.2009.01.006

Carter, M.R. 1990. Relative measures of soil bulk density to characterize compaction in tillage studies on fine sandy loams. Can. J. Soil Sci. 70:425–433. doi:10.4141/cjss90-042

Chamen, W.C.T., A.P. Moxey, W. Towers, B. Balana, and P.D. Hallett. 2015. Mitigating arable soil compaction: A review and analysis of available cost and benefit data. Soil Tillage Res. 146:10–25. doi:10.1016/j.still.2014.09.011

Colombi, T., and A. Walter. 2016. Root responses of triticale and soybean to soil compaction in the field are reproducible under controlled conditions. Funct. Plant Biol. 43:114–128. doi:10.1071/FP15194

Culley, J.L.B., B.K. Dow, E.W. Presant, and A.J. MacLean. 1982. Recovery of productivity of Ontario soils disturbed by an oil pipeline installation. Can. J. Soil Sci. 62:267–279. doi:10.4141/cjss82-031

da Silva, A.P., B.D. Kay, and E. Perfect. 1994. Characterization of the least limiting water range. Soil Sci. Soc. Am. J. 58:1775–1781. doi:10.2136/sssaj1994.03615995005800060028x

Dexter, A.R. 1987. Mechanics of root growth. Plant Soil 98:303–312. doi:10.1007/BF02378351

Dexter, A.R. 1991. Amelioration of soil by natural processes. Soil Tillage Res. 20:87–100. doi:10.1016/0167-1987(91)90127-J

Dexter, A.R. 2004. Soil physical quality: I. Theory, effects of soil texture, density and organic matter and effects on root growth. Geoderma 120:201–214. doi:10.1016/j.geoderma.2003.09.004

Drewry, J.J., R.J. Paton, and R.M. Monaghan. 2004. Soil compaction and recovery cycle on a Southland dairy farm: Implications for soil monitoring. Aust. J. Soil Res. 42:851–856. doi:10.1071/SR03169

Eggers, C.G., M. Berli, M.L. Accorsi, and D. Or. 2006. Deformation and permeability of aggregated soft earth materials. J. Geophys. Res. 111:B10204. doi:10.1029/2005JB004123

Farber, S.C., R. Costanza, and M.A. Wilson. 2002. Economic and ecological concepts for valuing ecosystem services. Ecol. Econ. 41:375–392. doi:10.1016/S0921-8009(02)00088-5

Flisch, R., S. Sinaj, R. Charles, and W. Richner. 2009. Grundlagen für die Düngung im Acker- und Futterbau (GRUDAF). Agrarforschung Schweiz 16(2):6–31.

Friedli, M., N. Kirchgessner, C. Grieder, F. Liebisch, M. Mannale, and A. Walter. 2016. Terrestrial 3D laser scanning to track the increase in canopy height of both monocot and dicot crop species under field conditions. Plant Methods 12:9. doi:10.1186/s13007-016-0109-7

Gregory, A.S., C.W. Watts, W.R. Whalley, H.L. Kuan, B.S. Griffiths, P.D. Hallett, and A.P. Whitmore. 2007. Physical resilience of soil to field compaction and the interactions with plant growth and microbial community structure. Eur. J. Soil Sci. 58:1221–1232. doi:10.1111/j.1365-2389.2007.00956.x

Günther, T., C. Rücker, and K. Spitzer. 2006. Three-dimensional modeling and inversion of dc resistivity data incorporating topography: II. Inversion. Geophys. J. Int. 166:506–517. doi:10.1111/j.1365-246X.2006.03011.x

Håkansson, I., and J. Lipiec. 2000. A review of the usefulness of relative bulk density values in studies of soil structure and compaction. Soil Tillage Res. 53:71–85.

Håkansson, I., and R.C. Reeder. 1994. Subsoil compaction by vehicles with high axle load extent, persistence and crop response. Soil Tillage Res. 29:277–304. doi:10.1016/0167-1987(94)90065-5

Hallett, P.D., K.H. Karim, A.G. Bengough, and W. Otten. 2013. Biophysics of the vadose zone: From reality to model systems and back again. Vadose Zone J. 12(4). doi:10.2136/vzj2013.05.0090

Hamza, M.A., and W.K. Anderson. 2005. Soil compaction in cropping systems: A review of nature, causes and possible solutions. Soil Tillage Res. 82:121–145. doi:10.1016/j.still.2004.08.009

Hartmann, M., P.A. Niklaus, S. Zimmermann, S. Schmutz, J. Kremer, K. Abarenkov, et al. 2013. Resistance and resilience of the forest soil microbiome to logging-associated compaction. ISME J. 8:226–244. doi:10.1038/ismej.2013.141

Horn, R. 2003. Stress–strain effects in structured unsaturated soils on coupled mechanical and hydraulic processes. Geoderma 116:77–88. doi:10.1016/S0016-7061(03)00095-8

IUSS Working Group WRB. 2006. World reference base for soil resources: A framework for international classification, correlation and communication. World Soil Resour. Rep. 103. FAO, Rome.

Jarvis, N.J. 2007. A review of non-equilibrium water flow and solute transport in soil macropores: Principles, controlling factors and consequences for water quality. Eur. J. Soil Sci. 58:523–546. doi:10.1111/j.1365-2389.2007.00915.x

Jones, R.J.A., G. Spoor, and A.J. Thomasson. 2003. Vulnerability of subsoils in Europe to compaction: A preliminary analysis. Soil Tillage Res. 73:131–143. doi:10.1016/S0167-1987(03)00106-5

Jones, S.B., J.M. Wraith, and D. Or. 2002. Time domain reflectometry (TDR) measurement principles and applications. Hydrol. Processes 16:141–153. doi:10.1002/hyp.513

Kaiser, E.A., T. Mueller, R.G. Joergensen, H. Insam, and O. Heinemeyer. 1992. Evaluation of methods to estimate the soil microbial biomass and the relationship with soil texture and organic matter. Soil Biol. Biochem. 24:675–683. doi:10.1016/0038-0717(92)90046-Z

Keller, T., J. Arvidsson, P. Schjønning, M. Lamandé, M. Stettler, and P. Weisskopf. 2012. In situ subsoil stress–strain behavior in relation to soil precompression stress. Soil Sci. 177:490–497. doi:10.1097/SS.0b013e318262554e

Keller, T., S. Ruiz, J. Arvidsson, M. Stettler, and M. Berli. 2016. Determining soil stress beneath a tire: Measurements and simulations. Soil Sci. Soc. Am. J. 80:541–553. doi:10.2136/sssaj2015.07.0252

Klute, A., editor. 1986. Methods of soil analysis. Part 1. Physical and mineralogical methods. ASA and SSSA, Madison, WI.

Klute, A., and C. Dirksen. 1986. Hydraulic conductivity and diffusivity: Laboratory methods. In: A. Klute, editor, Methods of soil analysis. Part 1. 2nd ed. SSSA Book Ser. 5. SSSA and ASA, Madison, WI. p. 687–732.

Kramer, S., P. Weisskopf, and H.-R. Oberholzer. 2008. Status of earthworm populations after different compaction impacts and varying subsequent soil management practices. In: Soil tillage—New perspectives: 5th International Soil Conference ISTRO, Czech Branch, Brno. 30 June–2 July 2008. Int. Soil Tillage Res. Organ., the Netherlands. p. 249–256.

Lal, R. 1993. Tillage effects on soil degradation, soil resilience, soil quality, and sustainability. Soil Tillage Res. 27:1–8. doi:10.1016/0167-1987(93)90059-X

Langmaack, M., C. Wiermann, and S. Schrader. 1999. Interrelation between soil physical properties and Enchytraeidae abundances following a single compaction in arable soil. J. Plant Nutr. Soil Sci. 162:517–525. doi:10.1002/(SICI)1522-2624(199910)162:5<517::AID-JPLN517>3.0.CO;2-3

Loomis, J., P. Kent, L. Strange, K. Fausch, and A. Covich. 2000. Measuring the total economic value of restoring ecosystem services in an impaired river basin: Results from a contingent valuation survey. Ecol. Econ. 33:103–117. doi:10.1016/S0921-8009(99)00131-7

MacNeil, M.A., N.A.J. Graham, J.E. Cinner, S.K. Wilson, I.D. Williams, J. Maina, et al. 2015. Recovery potential of the world's coral reef fishes. Nature 520:341–344. doi:10.1038/nature14358

Martínez, I., A. Chervet, P. Weisskopf, W.G. Sturny, J. Rek, and T. Keller. 2016. Two decades of no-till in the Oberacker long-term field experiment: II. Soil porosity and gas transport parameters. Soil Tillage Res. 163:130–140. doi:10.1016/j.still.2016.05.020

McKenzie, B.M., S. Kühner, K. MacKenzie, S. Peth, and R. Horn. 2009. Soil compaction by uniaxial loading and the survival of the earthworm *Aporrectodea calignosa*. Soil Tillage Res. 104:320–323. doi:10.1016/j.still.2009.04.004

Mossadeghi-Björklund, M., J. Arvidsson, T. Keller, J. Koestel, M. Lamandé, M. Larsbo, and N. Jarvis. 2016. Effects of subsoil compaction on hydraulic properties and preferential flow in a Swedish clay soil. Soil Tillage Res. 156:91–98. doi:10.1016/j.still.2015.09.013

Naderi-Boldaji, M., and T. Keller. 2016. The degree of soil compactness is highly correlated with the physical quality index *S*. Soil Tillage Res. 159:41–46. doi:10.1016/j.still.2016.01.010

Naderi-Boldaji, M., P. Weisskopf, M. Stettler, and T. Keller. 2016. Predicting the relative density from on-the-go horizontal penetrometer measurements at some arable top soils in northern Switzerland. Soil Tillage Res. 159:23–32. doi:10.1016/j.still.2015.12.002

Orwin, K.H., and D.A. Wardle. 2004. New indices for quantifying the resistance and resilience of soil biota to exogenous disturbances. Soil Biol. Biochem. 36:1907–1912. doi:10.1016/j.soilbio.2004.04.036

Peng, X., and R. Horn. 2008. Time-dependent, anisotropic pore structure and soil strength in a 10-year period after intensive tractor wheeling under conservation and conventional tillage. J. Plant Nutr. Soil Sci. 171:936–944. doi:10.1002/jpln.200700084

Perroux, K.M., and I. White. 1988. Designs for disc permeameters. Soil Sci. Soc. Am. J. 52:1205–1215. doi:10.2136/sssaj1988.03615995005200050001x

Radford, B.J., D.F. Yule, D. McGarry, and C. Playford. 2007. Amelioration of soil compaction can take 5 years on a Vertisol under no till in the semi-arid subtropics. Soil Tillage Res. 97:249–255. doi:10.1016/j.still.2006.01.005

Reiser, R., J. Rek, M. Holpp, H.-R. Oberholzer, T. Keller, and P. Weisskopf. 2012. Soil aeration and redox conditions monitored in a controlled traffic farming field trial. In: 19th ISTRO Conference, Montevideo, Uruguay. September 2012. Int. Soil Tillage Res. Organ., the Netherlands.

Schjønning, P., J.J.H. van den Akker, T. Keller, M.H. Greve, M. Lamandé, A. Simojoki, et al. 2015. Driver–pressure–state–impact–response (DPSIR) analysis and risk assessment for soil compaction: A European perspective. Adv. Agron. 133:183–237. doi:10.1016/bs.agron.2015.06.001

Suter, D., E. Rosenberg, R. Frick, and E. Mosimann. 2008. Standardmischungen für den Futterbau, Revision 2009–2012. Agrarforschung Schweiz 15:1–12.

Swiss Federal Research Stations. 1996. Referenzmethoden der Eidgenössischen landwirtschaftlichen Forschungsanstalten: 2. Bodenuntersuchung zur Standortcharakterisierung. Agroscope Reckenholz-Tänikon ART, Zürich.

Taylor, H.M., G.M. Roberson, and J.J. Parker, Jr. 1966. Soil strength–root penetration relations for medium- to coarse-textured soil materials. Soil Sci. 102:18–22. doi:10.1097/00010694-196607000-00002

Webb, R.H. 2002. Recovery of severely compacted soils in the Mojave Desert, California, USA. Arid Land Res. Manage. 16:291–305. doi:10.1080/153249802760284829

Webb, R.H., and H.G. Wilshire. 1980. Recovery of soils and vegetation in a Mojave Desert ghost town, Nevada, U.S.A. J. Arid Environ. 3:291–303.

Weisskopf, P., R. Reiser, J. Rek, and H.-R. Oberholzer. 2010. Effect of different compaction impacts and varying subsequent management practices on soil structure, air regime and microbiological parameters. Soil Tillage Res. 111:65–74. doi:10.1016/j.still.2010.08.007

Zhang, W., T.H. Ricketts, C. Kremen, K. Carney, and S.M. Swinton. 2007. Ecosystem services and dis-services to agriculture. Ecol. Econ. 64:253–260. doi:10.1016/j.ecolecon.2007.02.024

Appendix B

Editor's Vox - The Geophysical Signatures of Soil Structure

Alejandro Romero-Ruiz, Niklas Linde, Thomas Keller and Dani Or.

Published[1] in *Eos* and herein slightly adapted to fit the theme of this thesis.

[1] Romero-Ruiz et al. (2019). The geophysical signatures of soil structure. *Eos*, **100**, doi:10.1029/2019EO112545

The authors of a recent review paper in Reviews of Geophysics describe how geophysical methods may offer new opportunities for soil structure characterization over varied spatial and temporal scales.

Figure B.1 – The tillaged (left) and vegetated (rigth) soils have a very different structure and functioning despite belonging to the same soil type. Quantitative characterization of soil structure over space and time remains a challenge. Credit: Free-photos

Soil is a vital natural resource that supports global food production and serves as a climate regulator but characterizing soil structure remains a challenge for scientists. A recent review article in Reviews of Geophysics explores how selected geophysical methods can offer insights into the variability of soil structure. Here the authors of the paper answer some questions about basic concepts and methodological developments in this field.

What is "soil structure"?

Soil structure refers to the spatial arrangement of the constituents (minerals and organic matter) and voids (pores) of soil. Soil structure may vary considerably, even within a localized area, due to variations in biological activity (e.g., plant roots, earthworms), mechanical disturbances (e.g., tillage, compaction, trampling), and natural cycles (e.g., wetting-drying or freezing-thawing).

Evidence suggests that biological activity is an important agent for soil structure formation and maintenance. For example, earthworms and decaying plant-roots introduce additional large pores ("biopores") to the primary pore-network of the soil (spaces between soil solid particles) and combine with bacterial activity to generate organic binding agents that attach soil particles to form aggregates stabilizing soil structure.

On the other hand, agricultural activities often degrade soil structure. For example, tillage operations fragment the soil, while soil compaction by heavy farm implements reduces and disrupts the pore network, especially biopores.

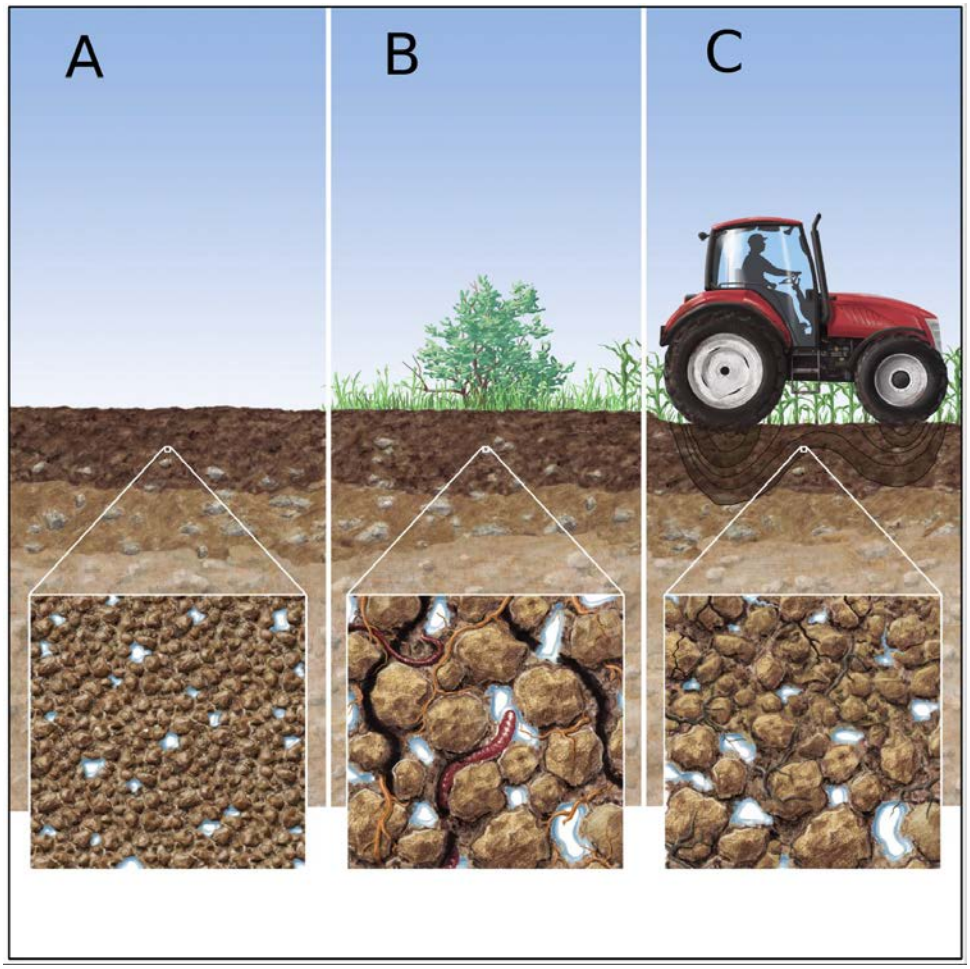

Figure B.2 – The same type of soil can have a very different structure depending on factors such as the presence of plant roots and earthworms (center) or compaction by agricultural machinery (right). Credit: *Romero-Ruiz et al.* (2018), Figure 1 https://doi.org/10.1029/2018RG000611

Why is soil structure important for soil functioning?

Soil has a range of ecological, agricultural and hydrological functions (such as carbon cycling, water cycling, plant growth) that rely on physical processes (such as water retention and transport, gas exchange, soil mechanical resistance, soil stability), and these are ultimately governed by soil structure.

The presence of soil biopores, for example, affects significantly the transport of water and gas, thereby increasing water and oxygen availability for plant roots and facilitating groundwater recharge. These preferential "flowpaths" can act as pathways to the groundwater and may also enable nutrient losses and pesticide leaching.

Conversely, when soil structure is degraded by compaction, there is a decrease in the water and oxygen available to plants and an increased difficulty for root growth. This also reduces the ability of soil to infiltrate moisture which may result in surface water runoff and soil erosion, as well as anoxic conditions that may lead to greenhouse gas emissions by anaerobic bacterial respiration.

Figure B.3 – Ponding water in compacted soils from farm fields. Credit: Gerd Altmann

Why is it so difficult to define and measure soil structure at relevant scales?

Soil structure is remarkably difficult to define rigorously. This is because a small change in the arrangement of soil constituents can have a significant impact on soil functioning; for example, a 1% change in macroporosity may induce several orders of magnitude changes in saturated hydraulic conductivity. Additionally, favorable soil structure for plant growth is determined by carbon spatial distribution and mechanical properties that are invisible to the eye.

Present methods for soil structure characterization are based on time-consuming destructive sampling, laboratory measurements or field assessment. In fact, most descriptions of soil structure are obtained under laboratory (not in-situ) conditions simplifying reality and resulting in a limited capacity to infer temporal variations and functioning under natural conditions. Similarly, certain aspects of the soil response to rainfall or other such factors become observable only at certain scales (such as the profile, plot or catchment). Alternative means to examine the spatial variability of soil structure at the profile scale are often subjective, empirical, highly invasive and incapable of addressing soil structure changes over time. However, geophysical methods have the potential of filling the scale-gap in soil structure characterization.

How could geophysical methods improve soil structure quantification?

Geophysical methods are used to study the interior of the Earth (e.g., composition and physical processes) and were developed mainly in the context of oil, gas and mineral exploration, and hydrologeology. They rely on natural or artificially created physical fields, typically measured at the surface of the Earth, to infer a spatial distribution of subsurface physical properties.

Our review examines how geoelectrical, electromagnetic and seismic methods have been used in soil studies and discusses how they can be used to infer soil structure by investigating signatures of soil structure captured by (1) geophysical properties and (2) monitored soil processes. These methods have the advantage of being non-invasive, providing information at larger integrative scales, and offering insights into the inherent variability of soil structure under field conditions.

Can you give some specific examples of how geophysical signatures capture soil structure?

The soil is composed of an heterogeneous mixture of minerals, water, air and organic matter. The properties inferred by geophysical methods are sensitive to (1) physical properties of the soil's individual components and (2) the way they are spatially distributed and how they connect.

Soil structure is expected to have strong signatures on electrical and seismic properties. The electrical conductivity of soils is governed by electrical flow and polarization mechanisms that strongly depend on the soil pore network and, thus, carries information related to pore sizes, connectivity, and tortuousity. A well connected pore network will increase the ability of soil to conduct electricity and a similar effect is expected in the presence of large pores saturated with water. Meanwhile, seismic methods and seismic velocities can be used to interpret the stability of soil structure, compaction, aggregation and, in general, mechanical aspects that are not visible with geoelectrical methods.

What are the main opportunities and challenges in geophysical applications to soil structure?

We still have an incomplete knowledge of how soil structure affects geophysical properties. This is partly because the established theoretical relationships between soil properties and geophysical properties are based on a simplified conceptualization of soil structure. Further theoretical development of specific "pedophysical" models and their associated experimental verification are needed to advance the field.

Likewise, the systematic inference of soil structure by geophysical time-lapse responses is an attractive topic for future research. Our review highlights possible ways of combining geophysical, hydro-mechanical and biological modeling to obtain quantitative information about soil structure. Choosing the best approach for such integrative framework remains a largely unexplored and challenging task. The multiple influences of soil properties on geophysical properties can lead to ambiguous interpretations. This shortcoming can be partly overcome by using combinations of geophysical data types (sensitive to different properties) and other more traditional measurements.

Finally, adapting geophysical survey configurations to soil investigations (shallow depths and extensive land areas) is a challenging methodological task. Our review describes how geophysical measuring devices, monitoring strategies, and data integration approaches could emerge to fulfill the spatial demands in soil structure characterization.

Alejandro Romero-Ruiz

+41 78 235 8757 | alejandro.romeroruiz@unil.ch | dob: 31.07.1991

Education

University of Lausanne — Lausanne, Switzerland
PhD in Environmental Sciences - Graduate assistant, Institute of Earth Sciences — *2016 – Present*

- Thesis:Geophysical Methods for Field-Scale Characterization of Soil Structure
  Director: Dr. Niklas Linde
  Co-Director: Dr. Dani Or

Center of Scientific Research and Higher Education of Ensenada — Ensenada, Mexico
Master in Applied Geophysics, Earth Sciences Division — *2013 – 2015*

- Thesis: Joint inversion of acoustic waveform and magnetic anomaly using fuzzy c-means clustering
  Director: Dr. Luis Gallardo Delgado
  Co-Director: Dr. Jonas de Basabe Delgado

Autonomous University of Zacatecas — Zacatecas, Mexico
Bachelor in Physics, Institute of Physics — *2008 – 2012*

- Thesis: Non-resonant tunneling through triple electrostatic barrier graphene systems
  Director: Dr. Isaac Rodriguez-Vargas
  Co-Director: Dr. Jesus Madrigal-Melchor

Conference presentations

Seismic characterization of soil structure-field observations and modeling — December 2019
AGU Fall Meeting — *San Francisco, United States*

Field-based geophysical characterization of soil structure — May 2019
EGU General Assembly — *Vienna, Austria*

Geophysical Methods in Soil Structure Characterization — April 2018
EGU General Assembly — *Vienna, Austria*

Borehole constrained inversion of geophysical data based on fuzzy clustering — April 2018
21st European Meeting of Environmental and Engineering Geophysics — *Turin, Italy*

Publications

Romero-Ruiz, A., Linde, N., Baron, L., Keller, T., & Or, D. (2020). Influence of soil structure on soil water dynamics revealed by geolectrical monitoring. *Manuscript in preparation.*

Romero-Ruiz, A., Linde, N., Baron, L., Solazzi, S., Keller, T., & Or, D. (2020). Seismic Signatures Reveal Persistence of Soil Compaction. *Submitted to Vadose Zone Journal.*

Romero-Ruiz, A., Linde, N., Keller, T., & Or, D. (2018). A review of geophysical methods for soil structure characterization. Reviews of Geophysics, 56(4), 672-697.

Keller, T., Colombi, T., Ruiz, S., Manalili, M. P., Rek, J., Stadelmann, V., Wunderli, H., Breitenstein, D., Reiser, R., Oberholzer, H., Schymanski, S., **Romero-Ruiz, A.**, Linde, L., Weisskopf, P., Walter, A., and Or, D. (2017). Long-term soil structure observatory for monitoring post-compaction evolution of soil structure. Vadose Zone Journal, 16(4), 1-16.

Workshops and summer schools

Hydrogeophysical inversion and data assimilation — June 2019
VIU Graduate Seminar - Venice International University — *Venice, Italy*

Data assimilation — May 2019
PhD School Water-Earth Systems - University of Neuchâtel — *Neuchâtel, Switzerland*

Flow and transport in porous and fractured media June 2018
4th Cargèse summer school - L'Institut d'Etudes Scientifiques de Cargèse *Cargèse, France*

Reservoir property modeling using MPS and advanced geostatistics June 2017
PhD School Water-Earth Systems - University of Neuchâtel *Neuchâtel, Switzerland*

Model Calibration and Uncertainty Analysis Using PEST February 2017
PhD School Water-Earth Systems - University of Neuchâtel *Neuchâtel, Switzerland*

Languages and programing skills

Languages: English, Spanish (mother tongue), French (intermediate)
OS: Linux, Windows
Programing languages: Fortran, C/C++, Matlab, Python, LaTeX

References

Niklas Linde · niklas.linde@unil.ch
Institute of Earth Sciences, Faculty of Geosciences and Environment, University of Lausanne, Lausanne, Switzerland

Dani Or · dani.or@env.ethz.ch
Soil and Terrestrial Environmental Physics, Department of Environmental Systems Science, ETH Zürich, Zürich, Switzerland